COLLECTIVE MOTION IN ACTIVE MATTER

— From Microscopic Models to Macroscopic Dynamics —

FLORIAN PETER THÜROFF

Department of Physics
Arnold Sommerfeld Center for Theoretical Physics
Ludwig-Maximilians-Universität München

München 2014

COLLECTIVE MOTION IN ACTIVE MATTER

— From Microscopic Models to Macroscopic Dynamics —

Dissertation
an der Faultät für Physik
der Ludwig-Maximilians-Universität
München

vorgelegt von

Florian Peter Thüroff
aus Hof / Saale

München, den 20. Mai 2014

Florian Peter Thüroff: *Collective Motion in Active Matter,* From Microscopic Models to Macroscopic Dynamics, © Mai 2014

GUTACHTER:

Prof. Dr. Erwin Frey (Erstgutachter)
Prof. Dr. Holger Stark (Zweitgutachter)

TAG DER MÜNDLICHEN PRÜFUNG:

25. Juli 2014

A happy family is but an earlier heaven.

— George Bernard Shaw

Dedicated to my beloved family.

ZUSAMMENFASSUNG

Die vorliegende Arbeit befasst sich mit verschiedenen Aspekten der Ausbildung selbst-organisierter, kollektiver Bewegung in aktiv getriebenen Systemen.

Teil i der Arbeit adressiert den Grenzfall niedriger Dichten und untersucht den Übergang zu langreichweitiger, kollektiver Bewegung auf der Grundlage binärer Teilchen-Stöße. Sämtliche Ergebnisse dieses Teils der Arbeit beruhen auf Analysen der berühmten Boltzmann Gleichung, die 1872 von Ludwig Boltzmann vorgeschlagen wurde um das "Wärmegleichgewichts unter Gasmolekülen" zu studieren [23], und die in den letzten Jahren einige Popularität im Zusammenhang mit der Beschreibung aktiver Systeme gewonnen hat.

In diesem Zusammenhang untersuchen wir zunächst den Einfluss von Teilchenzahlerhaltung auf die Entstehung kollektiver Bewegung in getriebenen Systemen. Dazu vergleichen wir zwei unterschiedliche kinetische Modelle, von denen sich eines auf die Beschreibung abgeschlossener Systeme, das andere auf die Modellierung von Systemen in Kontakt mit einem Teilchenreservoir bezieht. Zwischen beiden Modellvarianten manifestiert sich ein wichtiger qualitativer Unterschied am Übergang zur kollektiven Bewegung. Für Systeme die sich im Kontakt mit einem Teilchenreservoir befinden existiert am Übergang zur geordneten Phase eine stabile Lösung räumlich homogener kollektiver Bewegung. Im Gegensatz hierzu ist die Entstehung kollektiver Bewegung in teilchenzahlerhaltenden Systemen durch die Ausbildung räumlich inhomogener, dichteseparierter Zustände gekennzeichnet, die sich im Allgemeinen in der Form polarer Dichtewellen manifestiert. Während das Auftauchen solcher Dichtewellen bereits in vorherigen Arbeiten eingehend diskutiert wurde, ergeben sich aus unseren Diskussionen zur Teilchenzahlerhaltung wichtige qualitative Erkenntnisse, auf deren Grundlage wir ein

mechanistisches Bild zur Entstehung derartiger dichteseparierter Zustände zeichnen.

In einem nächsten Schritt gehen wir der Frage nach, inwiefern die eigentliche Physik dissipativer Zweiteilchenstöße mit der Ausbildung langreichweitiger polarer Ordnung in aktiven Systemen in Übereinklang zu bringen ist. Dazu stellen wir zunächst eingehende numerische Streustudien zweier kollidierender getriebener Teilchen an und konstruieren eine kinetische Beschreibung auf Grundlage der Ergebnisse aus diesen Streustudien. Anhand dieses maßgeschneiderten kinetischen Modells untersuchen wir den Zusammenhang zwischen der Physik binärer Teilchenstöße und der Fähigkeit entsprechender Systeme kollektive Zustände mit langreichweitiger polarer Ordnung hervorzubringen. Insgesamt setzt sich unsere Arbeit mit der Anwendbarkeit der aktiven Boltzmann Gleichung im Zusammenhang mit physikalisch wechselwirkenden Teilchensystemen kritisch auseinander und diskutiert Grenzen in der Beschreibung Cluster bildender Systeme.

Nachdem sich die beiden vorhergehenden Arbeiten auf analytische Verfahren zur Untersuchung der Boltzmann Gleichung konzentrierten, wenden wir uns im letzten Abschnitt des ersten Teils der vorliegenden Arbeit einer von uns neu entwickelten, numerischen Lösungsmethode der Boltzmann Gleichung für aktive Systeme zu. Aufgrund ihrer komplexen mathematischen Struktur ist die Boltzmann Gleichung analytischen Methoden nur bedingt zugänglich. Insbesondere blieben bisherige Verfahren zur Untersuchung der aktiven Boltzmann Gleichung auf Systemparameter in der unmittelbaren Umgebung des Ordnungsübergangs beschränkt. Im Gegensatz dazu diskutieren wir in dieser Arbeit ein alternatives Vorgehen zur Lösung der Boltzmann Gleichung, welches auch noch tiefer in der geordneten Phase keiner prinzipiellen Beschränkung unterworfen ist. Wir verwenden diese neu entwickelte Methode zur systematischen Untersuchung der Entwicklung kollektiver Ordnung anhand eines generischen Modells aktiv getriebener Teilchen. Im Rahmen dieser Untersuchungen stoßen wir auf verblüffende Ähnlichkeiten zwischen dem Übergang zu polarer Ordnung in derartigen aktiven Systemen und dem Übergang zwischen flüssigem und gasförmigem Zustand in

Gleichgewichtssystemen. Weiterhin ergeben unsere numerischen Lösungen neue faszinierende Muster kollektiver Bewegung, die sich sowohl hinsichtlich ihrer Form als auch im Hinblick auf ihre globale Ordnungsstruktur von den bisher diskutierten polaren Dichtewellen unterscheiden.

Während in Teil i der vorliegenden Arbeit das Studium aktiver Systeme bei niedrigen Dichten im Fokus stand, beschäftigt sich Teil ii der Arbeit mit dem umgekehrten Grenzfall hoher Teilchendichten. Konkret untersuchen wir die Ausbildung kollektiver Migration in konfluenten Einfachschichten adhäsiver Zellverbände. Die Migrationsdynamik von Zellen spielt eine wesentliche Rolle in einer Vielzahl medizinisch relevanter Vorgänge, angefangen bei grundlegenden biologischen Prozessen in frühen Stadien der Embryonalentwicklung, bis hin zu pathologischen Veränderungen somatischer Gewebe, wie der Entstehung und Entwicklung von Krebs. Die Dynamik von Zellen und Zellverbänden wird maßgeblich bestimmt durch eine Reihe hoch komplexer Zellfunktionen, die es einzelnen Zellen erlauben verschiedene mechanische und chemische Signale in ihrer jeweiligen Umwelt zu verarbeiten und mit anderen Zellen entsprechend zu kommunizieren. Vielzahl und Komplexität dieser Zellfunktionen stellen dabei ein erhebliches Hindernis dar, wenn es darum geht die wesentlichen Eigenschaften kollektiver Zellmigration sinnvoll zu modellieren. Bisherige Arbeiten in dieser Richtung befassen sich im Wesentlichen mit der detaillierten Modellierung subzellulärer Grundlagen einzelner, für die Zellmigration maßgeblicher Zellfunktionen, oder mit phänomenologischen, makroskopischen Ansätzen zur Beschreibung ganzer Gewebeschichten.

Hier beschreiten wir einen Mittelweg zwischen den beiden vorgenannten Modellierungsebenen und entwickeln ein zelluläres Automatenmodell zur Simulation beliebiger Systemgrößen. Wie wir zeigen werden ist unser Simulationsmodell in der Lage, Form und Migrationsverhalten selbst einzelner Zellen sinnvoll zu reproduzieren. Gleichzeitig ist das Modell effizient genug, Systeme bestehend aus bis zu $\mathcal{O}(10^4)$ Zellen zu simulieren und damit wichtige Beiträge im Zusammenhang mit der Dynamik von Geweben zu leisten.

Wir verwenden unser Simulationsmodell zunächst um die Entstehung und Eigenschaften kollektiver Zellmigration in kleinen Zellgruppen in kreisförmig beschränkten Umgebungen zu untersuchen. Dieses, auch experimentell sehr gut zugängliche System (siehe unten), eignet sich hervorragend zur Identifikation einschlägiger Zellfunktionen im Zusammenhang mit der Entstehung und Aufrechterhaltung persistenter Gruppenmigration. Des Weiteren untersuchen wir den Einfluss von Zellwachstum und aktiver Zellbewegung auf die Grenzflächendynamik einer anfänglich eingeschränkten Gewebsschicht während ihrer Migration in den freien Raum. Dieses letztgenannte Migrationsszenario bildet den Kern zahlreicher experimenteller gewebedynamischer Untersuchungen und dient als weiterverbreitetes Modell zur Untersuchung von Wundheilungsprozessen.

Schließlich arbeiten wir im zweiten Abschnitt dieses Teils der vorliegenden Arbeit mit der experimentellen Arbeitsgruppe von Prof. Joachim O. Rädler (LMU München) zusammen und verdeutlichen anhand von Experimenten an kleinen Gruppen von MDCK Zellen auf kreisförmigen Inseln den Einfluss von Systemgröße und Zellkonfigurationen auf die Persistenz kollektiver Zellrotationen. Insbesondere zeigt ein im Rahmen dieser Arbeit angestellter, direkter Vergleich zwischen experimentellen Messungen und entsprechenden Simulationsresultaten gute Übereinstimmung zwischen beiden Datensätzen.

Die vorliegende Arbeit gliedert sich wie folgt. Nachdem wir zu Beginn der Arbeit eine allgemeine Einführung in das Feld aktiver Systeme geben, unterteilen wir den Rest der Arbeit in die beiden oben dargestellten Teile. Dabei stellen wir jedem der beiden Teile jeweils ein kurzes Kapitel voran, um die zentralen technischen Methoden der nachfolgenden Studien einzuführen (Kapitel 1 und 5). Die nachfolgenden Kapitel besprechen dann die durchgeführten Forschungsarbeiten und untergliedern sich ihrerseits jeweils in vier Unterabschnitte: Der erste Unterabschnitt bespricht den wissenschaftlichen Ausgangspunkt der jeweiligen Forschungsarbeit und führt auf deren zentrale Fragestellung hin. Im zweiten Unterabschnitt diskutieren wir die wesentlichen Ergebnisse der entsprechenden Forschungsarbeit, und geben, davon ausgehend, einen kurzen Ausblick auf zukünftige Fragen

und Anwendungen im dritten Unterabschnitt. Das Originalmanuskript der jeweiligen Arbeit ist dann im vierten und letzten Unterabschnitt abgedruckt. Einen Überblick über alle dieser Doktorarbeit zugrundeliegenden publizierten, eingereichten und in Vorbereitung befindlichen Manuskripte gibt das Literaturverzeichnis (Research Articles) am Anfang der vorliegenden Niederschrift.

ABSTRACT

The present work discusses different aspects underlying the emergence of self-organized, collective motion in active systems.

Part i of this thesis addresses the limiting case of low density systems, and investigates the transition toward collective motion on the basis of binary particle collisions. The results of part i of this thesis are all based on the famous Boltzmann equation, which has been proposed by Ludwig Boltzmann in 1872 to study the equilibrium properties of gases [23], and which has gained considerable popularity in recent years to describe the behavior of active systems.

In this context, we first investigate the influence of particle number conservation on the emergence of collective motion in systems of self-propelled particles. To this end, we compare two archetypical modeling approaches, describing the spatiotemporal evolution of systems in which the total number of particles is conserved, and of systems which are in contact with a particle reservoir, respectively. Both modeling paradigms predict qualitatively different transitions to large scale collective motion. For systems in contact with a particle reservoir, we obtain stable solutions corresponding to states of spatially homogeneous polar order. In contrast, in systems where the total number of particles is conserved, the emergence of macroscopic order is accompanied by the formation of density segregated structures, which usually manifest themselves in the form of solitary polar waves. While the emergence of such wave patterns has already been reported in previous works, we suggest a mechanistic explanation for the emergence of these density segregated patterns on the basis of our previous investigations.

In the next project, we address the question to which extent the actual physics of dissipative, binary collisions between actively propelled particles is compatible with the emergence of large scale polar order. To this end, we perform thorough numer-

ical scattering studies of collisions between two self-propelled rod-like particles, and use the corresponding results to set up a kinetic framework which incorporates the most pertinent features of binary particle collisions. This kinetic model, in turn, serves as a basis to investigate the propensity of active systems to elicit states of macroscopic polar order as a function of the physics of binary particle collisions. Our work gives a critical assessment of the Boltzmann equation approach to active particle systems, and discusses limitations in the context of cluster forming systems.

So far, our studies on active systems have largely been based on analytical tools to investigate the Boltzmann equation. In the last chapter of part i of this thesis, we follow an alternative route and propose a novel numerical scheme to directly solve the active Boltzmann equation. Due to the inherent mathematical complexity of the Boltzmann equation, progress in the investigation of this equation on the basis of analytical approaches alone has been limited substantially. In particular, previous approaches to treat the Boltzmann equation in the context of active systems have largely been limited to parameter regions in the immediate vicinity of the ordering transition. In contrast, the validity of the numerical procedure we propose in our work is not principally restricted to the onset of collective motion and, therefore, allows for the study of active systems even deeper inside the ordered phase. We use our computational model to give a detailed investigation of the emergence of collective motion in an archetypical model system for self-propelled polar particles. Strikingly, we find that the transition toward collective motion in such systems bears striking similarities to liquid-gas transitions in equilibrium systems. Moreover, our numerical solutions exhibit the emergence of novel density-segregated patterns of collective motion, which are different from the familiar solitary wave patterns both, with respect to shape and with respect to their global ordering structure.

While in part i of this thesis we studied active systems at low densities, part ii of the present work addresses the opposite limit of high densities. To be specific, our focus will be on the emergence of collective migration in confluent monolayers of adhesive cells. The migration dynamics of cells plays a pivotal role in

a number of medically relevant situations, ranging from fundamental biological processes in the early stages of embryonic development to the pathological transformation of somatic tissues in cancer progression. The dynamics of single cells and of tissues are governed by a variety of highly complex cell functions, which allow cells to sense and process mechanical and chemical stimuli from their respective environments, and to establish crosstalk between cells. At the same time, the sheer number and complexity of such cellular functions severely hinders scientific progress in deciphering the essential drivers behind the formation and control of collective cell behaviors. Previous works in this direction have largely been focused on the subcellular basis of essential cell functions underlying single cell migration, or on phenomenological approaches to describe the migratory dynamics at the scale of entire tissues.

Here, we focus on a mesoscopic modeling approach, which lies in between these antipodal modeling paradigms, and propose a cellular automaton model, which lends itself to the simulation of arbitrary system sizes. We will show that our simulation model is capable to reproduce cell shapes and dynamics down to the level single individuals. At the same time, our model is computationally efficient enough to allow for the simulation of currently up to $\mathcal{O}(10^4)$ cells, and can, therefore, contribute substantially even to the study of whole tissues.

In a first step, we use our simulation model to study the emergence of collective cell migration in small groups of adhesive cells in circular confinement. Besides being amenable to direct experimental measurement (see below), this setup is ideally suited to identify the most pertinent cell functions in the context of the emergence and maintenance of persistent, collective group migration. Moreover, we address the influence of cell growth and cell motility on the boundary layer dynamics of an initially confined tissue as it migrates to invade free space. This latter migration scenario has been used in a number of previous experimental works as a popular model system to study the dynamics of tissues during wound healing.

Eventually, in chapter 7 of this thesis, we collaborate with the experimental group of Prof. Joachim O. Rädler (LMU München)

to highlight the influence of cell number and cell configuration on the persistency of collective cell rotation in small groups of MDCK cells in circular confinement. In the framework of this study, we also compare our numerical simulations to experimental measurements and find good agreement.

This thesis is structured as follows. After giving a general introduction to the field of active systems, we divide the rest of this work in two parts, as outlined above. Each of these two parts is prefaced by a chapter (chapters 1 and 5) containing a general discussion of the technical and methodological basis of subsequent works. The following chapters then discuss the various research articles (manuscripts) which form the basis of this thesis. Each of these chapters, in turn, is subdivided into four sections: In the first section, we discuss the starting point of the single research projects and introduce the core scientific question underlying the respective work. The second section, then contains a brief summary and discussion of the main results of the corresponding work, while section three gives an outlook on potential future questions and applications. Finally, in section four we provide a reprint of the original research article or manuscript. A list containing all published and submitted articles, as well as all manuscripts in preparation which are part of this PhD thesis can be found under the "Research Articles" heading at the beginning of this thesis.

RESEARCH ARTICLES

PUBLISHED

[TWF14] Florian Thüroff, Christoph A. Weber, and Erwin Frey. Numerical treatment of the boltzmann equation for self-propelled particle systems. *Phys. Rev. X*, 4:041030, 2014.

[TWF13] Florian Thüroff, Christoph A. Weber, and Erwin Frey. Critical Assessment of the Boltzmann Approach to Active Systems. *Phys. Rev. Lett.*, 111(19):190601, 2013.

[WTF13] Christoph A. Weber, Florian Thüroff, and Erwin Frey. Role of particle conservation in self-propelled particle systems. *New J. Phys.*, 15(4):045014, 2013.

SUBMITTED

[STFR14] Felix Segerer, Florian Thüroff, Erwin Frey, and Joachim O. Rädler. Cell Number and Local Arrangement Affect Collective Rotation on Micropatterns. *Submitted to Phys. Rev. Lett.*, 2014.

IN PREPARATION

[TRS+14] Florian Thüroff, Matthias Reiter, Felix Segerer, Joachim O. Rädler, and Erwin Frey. Bridging the gap between single cell migration and collective dynamics. *In preparation*, 2014.

It is the supreme art of the teacher to awaken joy in creative expression and knowledge.

— Albert Einstein

ACKNOWLEDGMENTS

Die vorliegende Arbeit fasst die Früchte meiner etwa vierjährigen Arbeit als Doktorand am Lehrstuhl von Prof. Erwin Frey zusammen. Seine unermüdliche Unterstützung, seine wissenschaftliche Intuition und nicht zuletzt seine just grenzenlose Geduld sind die wesentlichen Tragpfeiler, die Arbeiten wie diese erst zu ihrer vollen Reife bringen. Aus diesen und unzähligen weiteren Gründen geht mein besonderer Dank an meinen Doktorvater Erwin Frey, den ich im Laufe der vielen Jahre unserer Zusammenarbeit nicht nur als Wissenschaftler außerordentlich zu schätzen gelernt habe.

Im gleichen Zusammenhang verdient mein hoch geschätzter Kollege und enger Freund Christoph Weber meine besondere Anerkennung und tief empfundenen Dank. Unsere stets vertrauensvolle und von gegenseitigem Respekt geprägte Zusammenarbeit bildet den Kern sämtlicher im ersten Teil der Arbeit vorgestellter Projekte. Sein kreativer Einfluss und sein beneidenswerter Blick für globalere Zusammenhänge hinterlässt bleibende Eindrücke.

Wichtige Teile des zweiten Teils meiner Doktorarbeit entstanden aus einer Kollaboration mit Prof. Joachim Rädler, sowie seinen Mitarbeitern Felix Segerer und Dr. Alicia Piera Alberola. Ihnen möchte ich für die stets freundschaftliche und vertrauensvolle Atmosphäre danken, die unsere Zusammenarbeit immer geprägt hat.

Danke sagen möchte ich ebenfalls Jonas Denk und Matthias Reiter, die diese Arbeit korrekturgelesen haben und mit denen ich die Ehre hatte bzw. habe an spannenden Projekten zu arbeiten. Die Zusammenarbeit mit ihnen war mir nicht nur aufgrund ihrer großen Begabung stets eine außerordentliche Freude.

Bedanken möchte ich mich auch ganz grundsätzlich bei all meinen Kolleginnen und Kollegen am Lehrstuhl für die ausgesprochen freundschaftliche und kollegiale Atmosphäre die sie schaffen. Ich habe es als großes Privileg empfunden Teil einer solch außergewöhnlichen Gruppe zu sein.

Nicht zuletzt Danke sagen möchte ich Familie und Freunden, die mir, bewusst oder unbewusst, die fraglos wichtigste Stütze in der gesamten Zeit meiner Promotion und weit darüber hinaus waren, sind und hoffentlich immer bleiben werden. Euch nur im vorliegenden Rahmen meinen Dank auszusprechen würde der Sache nicht gerecht. Ich gehe hierzu geeignetere Wege.

CONTENTS

INTRODUCTION

I don't know anything,
but I do know that everything is interesting
if you go into it deeply enough.

— Richard P. Feynman

To maintain order, life depends on function. Function, in turn, relies on a constant "consumption" of energy and is itself based on well ordered structure. The whole narrative is, therefore, ultimately circular and the existence of life is inextricably linked to the *self-organized* emergence of order as has already been recognized by Kant in the 18th century [70]. In nature, self-organization of order manifests itself in a large variety of different processes, ranging from the formation of subcellular structures like the aster shaped mitotic spindle [122] to collective decision making like the synchronization of activity in groups of sheep [52].

In this thesis, our focus is on the emergence of self-organized patterns in the form of collective motion in active matter. According to the conventional use of the term, "active matter" refers to systems with an input and dissipation of energy at the scale of the constituent particles, such that each particle can be considered actively propelled [113, 153, 83]. This working definition applies to a large number of systems like bacterial or artificial microswimmers [75, 42, 170, 171], or simply vertically agitated granular particles [164, 74, 37], to name but a few. In such active systems, particle propulsion in conjunction with dissipative interactions sets the stage for the emergence of large scale patterns of coherent particle motion. The phenomenon of collective motion can be observed on vastly different length scales and in a large variety of different systems, including driven biopolymers [26, 124, 123, 125, 135], collections of swimming or gliding bacteria [39, 4, 132, 166, 106, 157], cellular flows in extended tissues [43, 111, 148, 109, 143, 128], insect groups [25, 18], and schools of fish [81]; see also Fig. 1.

To come to grips with their basic features, active systems are often associated with different classes of active matter modeling approaches, where each modeling class emphasizes different key aspects behind the formation of coherent dynamics. Probably at

Figure 1.: Examples of collective motion in active matter. *Left:* Swarming of motile *M. xanthus* bacteria (scale bar: 50 μm; image taken from Ref. [163], licensed under CC BY). *Right:* Collective motion in a flock of starlings (image by John Holmes, source: geograph.org.uk, licensed under CC BY-SA).

the most basic level, a distinction can be made between "wet" and "dry" active systems [83]. The theoretical description of wet active systems takes into account both, the dynamics of active particles and the transfer of momentum between fluid and active particles. Examples pertaining to this modeling class include bacterial suspensions and microswimmers [39, 132, 170, 171], or pattern formation processes in systems of driven filaments [123]. In such wet systems, hydrodynamic interactions among the active particles or between active particles and confining walls in general constitute an important determinant of the system's overall dynamical behavior. In contrast, in dry active systems solvent mediated interactions only have a negligible effect on the dynamical processes of interest, which themselves are mostly driven by direct interactions between the constituent active particles. In these cases, surrounding fluids or substrate surfaces can simply be modeled as "momentum sinks" and active particle motions can be considered overdamped. Typical examples falling under this kind of modeling paradigm include shaken granules [22, 98, 7, 74, 73, 37, 38, 155], cells crawling over a substrate [139], or flocks of birds [10].

In this thesis, our focus is on dry active systems, where patterns of collective motion essentially emerge from a competition

between the order creating effects of particle-particle interactions and the randomizing effects of noise. Theoretical work in this direction has been pioneered by Vicsek and coworkers [152], who implemented this general notion in terms of a two-dimensional agent based model which can be summarized as follows; see also Fig. 2(a). Each agent is modeled as a point like particle with a position coordinate $\mathbf{x}$ and an orientation θ. Particle interactions are implemented such that at each time step, particles seek to align their current orientation θ to the average direction of all particles with position vectors within some finite range r. To add an element of stochasticity, these particle alignments are assumed to be subject to noise which is captured in the form of (unbiased) random errors made in the measurement of average angles. This model, which came to be known as the "Vicsek model", strongly resembles the so-called XY model, which has been used extensively to study the emergence of ferromagnetic order in equilibrium systems [29]. The key difference between both models lies in the fact that in the Vicsek model particles are *active*, i.e. they move at a constant, *non-zero* speed relative to a stationary substrate, such that particle motions are along the respective particle orientations, whereas in the XY model, each "magnetic needle" is attached to a lattice site and (directly) interacts only with a fixed set of neighboring magnetic needles; cf. Fig. 2. This seemingly innocuous variation entails striking consequences in terms of the system's macroscopic ordering behavior and thus elucidates the dramatic consequences brought about by particle activity: The XY model obeys the Mermin-Wagner theorem [93] which states that in systems with a continuous symmetry no long range magnetic order can be established in two spatial dimensions (or below) at finite temperatures (i.e. non-zero noise levels). Intriguingly, the Vicsek model eludes the Mermin-Wagner theorem[1] and indeed supports the formation of long range orientational order even at finite noise levels, provided the density of particles is sufficiently high such that the ordering effects of particle interactions outcompete the effects of noise.

1 It must be stressed that the Vicsek model must not be seen as a counter example invalidating the Mermin-Wagner theorem, since the latter only applies to the case of equilibrium systems.

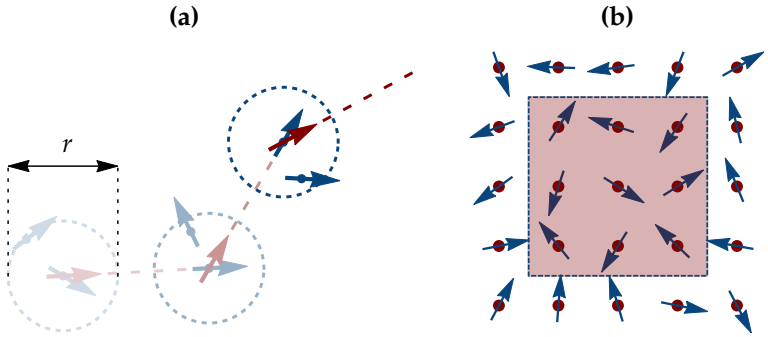

Figure 2.: Modeling the emergence of orientational order. **(a)** Illustration of a particle's sample trajectory (red dashed line) in the Vicsek model. Darker colors indicate more recent events. At each time step, the particle aligns it current orientation (blue arrows) to the average orientation (red arrows) of all particles within a range r. Over growing periods of time, the particle will have interacted with an ever increasing number of particles. This circumstance sets the stage for the development of long range order. **(b)** Illustration of the XY model. "Magnetic needles" (arrows) are located at fixed spatial positions, and direct magnetic interactions are confined to each needle's local neighborhood (shaded area). According to the Mermin-Wagner theorem [93], no long range magnetic order will develop in two dimensions (or below) at finite temperatures.

Inspired by the unexpected ordering behavior of the Vicsek model, Toner and Tu [145] proposed a phenomenological continuum model to highlight the theoretical basis of flocking. Specifically, they attributed the emergence of genuine long range order in Vicsek like systems to the fact that each agent interacts with an ever changing set of "collision partners" rather than with a fixed neighborhood of particles, as would be the case in the XY model. Thus, particle motility renders the range of particle interactions time dependent and, hence, stabilizes the emergence of polar order [145]. The hydrodynamic model set up by Toner and Tu combines features of magnets and fluids and exhibits remarkable non-equilibrium properties like different propagation speeds of velocity and density fluctuations along the direction of

the flock's orientation, as a result of the absence of Galilean invariance [149, 147, 83]. Moreover, generic hydrodynamic approaches to active systems predict the emergence of anomalously large density fluctuations [147, 113, 83]. In the meantime, such "giant number fluctuations" have also been observed in a number of experimental [166, 37, 106] and numerical studies [32, 30, 31, 155].

In recent years, progress toward a better understanding of the emergence of collective motion in dry active systems has been made in a number of different contexts using a variety of different approaches. For instance, the Vicsek model has been generalized to include the effects of particle cohesion [57] and repulsion [30, 154], and has been adapted to study the effect of nematic particle interactions where the alignment of particles is along a common axis rather than along a common direction [32]. In addition to the rule based approach of the Vicsek model, microscopic simulations explicitly accounting for particle interaction forces have been implemented to study the swarming behavior and clustering of self-propelled colloidal particles [105, 158, 60]. Likewise, the phenomenological approaches to the macroscopic dynamics of active systems have been complemented by microscopic derivations of the hydrodynamic equations both, in the context of polar [20, 4, 21, 64, 108] and nematic symmetries [17, 16, 107, 19].

The focus of this thesis will be on polar systems. The emergence of polar order in active matter can be discussed on the basis of two alternative modeling assumptions. On the one hand, the emergence of polar ordered structures in systems like vibrated granular rods or disks [22, 98, 7, 74, 73, 37, 38, 155], or certain bacterial colonies [4, 106] is driven by dissipative excluded volume interactions. More generally, for a large class of active systems aligning interactions are "short ranged" and occur only among particles in close spatial vicinity. This particular class of interactions has come to be referred to as *metric interactions* and includes the standard Vicsek model as defined above, which implements the notion of metric interactions in the form of a finite alignment range r. On the other hand, the alignment of "particles" in many of the more highly evolved systems, including, e.g., flocks of birds [10], or pedestrians and human crowds [97], have been

argued to rely on qualitatively different alignment interactions to establish states of collective motion. One possible approach to account for the more complex decision making processes underlying the alignment rules in such systems is to assume *metric-free interactions*, where the alignment occurs between "neighboring particles" in a topological, rather than metric sense [53, 33, 108]. Interestingly, metric and metric-free modeling paradigms lead to qualitatively different predictions concerning the transition to collective motion. In closed systems with metric interactions among the constituent particles, the transition to polar order is discontinuous and is accompanied by the formation of density segregated patterns (typically in the form of polar waves), while a spatially homogeneous state of collective motion is observed only well beyond the actual onset of order [31]. In contrast, systems governed by metric-free interactions have been reported to undergo a continuous transition to a spatially homogeneous state of collective motion and to be devoid of the instabilities which cause metric systems to elicit density segregated patterns across the ordering transition [53, 33, 108].

Part i of this thesis is devoted to a detailed investigation of the emergence of polar order in systems with metric interactions. Our studies will be based on a Boltzmann equation approach, which has been employed previously in a number of different contexts including the study of pattern formation of microtubules [5, 6, 168], swimming bacteria [4], and "Vicsek like" systems [20, 21]. The Boltzmann equation approach to active matter systems will be reviewed in chapter 1, where a technical introduction to the corresponding kinetic framework, as well as a strategy to treat the active Boltzmann equation analytically are discussed. In chapter 2, we study the significance of particle conservation in the context of self-propelled particle systems and discuss its impact on the qualitative properties of those systems at the onset of collective motion [WTF13]. In chapter 3, we consider the actual microscopic basis of dissipative excluded volume interactions among rod-like particles and use a binary collision theory to investigate how the physics of such microscopic interactions translates to the system's dynamics on macroscopic scales [TWF13]. Finally, in chapter 4, we go beyond the onset of collec-

tive motion, and present an in-depth study of the development of collective motion by means of a newly developed numerical scheme to solve the Boltzmann equation [TWF14].

While the studies presented in part i of this thesis address the macroscopic, collective dynamics in systems which can be considered "sufficiently dilute" such that their dynamics is governed by binary particle interactions, part ii of this thesis investigates the emergence of cohort migration patterns in groups and tissues of adhesive cells. In such systems, coupling effects between neighboring cells are strong and a description of cell-cell interactions in terms of a low density binary theory is likely to miss the essential physical aspects determining the system's collective behavior. In this sense, groups and tissues of adhesive cells pertain to the opposite limit of high density systems which call for alternative modeling approaches to identify and study the basic mechanisms determining their dynamical behavior.

Cell migration both, in the context of solitary cells [95, 36] and in the context of collective cell migration [119, 47, 66] plays a pivotal role in a large number of biological processes. A variety of developmental processes, like the migration of border cells during *Drosophila* oogenesis [118] and the formation of blood vessels [131], as well as numerous diseases, most notably the formation of metastases during cancer progression [47], rely on the motility of cells. In contrast to the picture conveyed by generic modeling approaches like the Vicsek model, the migratory response of cells is controlled by a variety of cellular functions, which allow the cell to integrate a number of environmental factors, including chemical signals [9, 50, 141, 142, 140], and mechanical stimuli [143].

Progress toward a more detailed understanding of the biochemical as well as physical basis of cell migration has been made by means of a number of experimental model systems. Keratocyte cells, for instance, are a widely used model system, investigated in a number of experimental studies [112, 11, 71] and modeled in various theoretical approaches [120, 85, 72, 95, 99, 96, 130, 169, 100, 84, 129, 36, 167] to address the properties and subcellular basis of single cell migration. Conversely, wound healing assays, where a confluent tissue layer invades freely available

space [43, 111, 148, 109, 143, 3, 128] are a commonly used experimental setup to study collective cell migration in extended tissues. At intermediate scales, micropatterns are used to assess the impact of spatial confinement on the dynamics of cells [24, 63, 67, 41, 82, 144, 151, 40, 80, 79, 150].

Despite a continuously growing body of experimental data, a mechanistic picture highlighting the connection between single cell functions and the emergence of large scale patterns of collective cell migration remains largely elusive. Specifically, while large amounts of theoretical work concentrate either on the subcellular basis of such cell functions or on a coarse grained picture of tissue level cellular flows, a plain connection between these two levels of description remains to be established. In part ii of this thesis, we present possible steps in this direction and propose a simulation model which is specifically designed to bridge the gap between the basic cellular functions determining the single cell's migratory response, and the emergent modes of collective migration both in small cell groups and in extended tissues made up of several thousand cells. The core framework underlying our simulations is based on the cellular Potts model, which has been introduced by Graner and Glazier [56, 55] to study cell sorting due to differential cell adhesion. In the meantime, the general framework of the cellular Potts model has been applied in a number of different contexts including detailed studies of the subcellular basis of single cell migration [85, 84], as well as tissue level applications like the growth and evolution of tumors [137]. In chapter 5, we review the basic properties of the cellular Potts model as initially proposed by Graner and Glazier [56, 55] in order to provide a frame of reference for subsequent discussions of the simulation model used in this thesis to study the emergence of collective cell migration. Chapter 6 presents both, a non-technical outline of the basic ideas behind our simulation model, as well as an extensive study of the emergence of persistent cell migration ranging from the dynamical behavior of single cells, over the cohort migration of confined cell groups to the expansion dynamics of cell tissues invading free space [TRS+14]. The technical details of our simulation model are discussed in Appendix B. Finally, in chapter 7, we collaborate with the group

of Prof. Joachim O. Rädler (LMU München) and compare our simulation data to experimental measurements on collectively rotating MDCK cells on circular micropatterns [STFR14].

Part I

BOLTZMANN EQUATION APPROACH TO ACTIVE MATTER SYSTEMS

1

A PRIMER ON THE ACTIVE BOLTZMANN EQUATION

Part i of this thesis addresses the dynamics and the emergence of spatiotemporal patterns of collective motion in *dry active systems*. In contrast to our discussions in part ii, our focus here is on systems whose dynamics is governed by binary particle interactions, and which can, ipso facto, be considered "sufficiently dilute". In analogy to the theory of dilute gases, the effects of binary interactions in active systems have been successfully captured by means of kinetic equations whose mathematical structure is identical to the Boltzmann equation [23, 62, 126], and which we will henceforth refer to as "*Boltzmann equation approach to active matter*" or "*active Boltzmann equation*". The present chapter briefly reviews the active Boltzmann equation, and highlights common strategies to treat this kinetic equation by means of analytical methods. The general framework outlined here will serve as a basis for the works discussed in chapters 2 – 4. Since this thesis is concerned with the emergence of *polar* order in active systems, we will restrict our following discussion to the case of polar particle interactions. For applications of the Boltzmann approach to nematic systems, we refer the interested reader to Refs. [107, 19].

In the following, we will consider two-dimensional model systems of self-propelled rod-shaped[1] particles of length L with the following general properties; cf. Fig. 3 and Refs. [20, 21, WTF13, TWF13]: (i) Particles are assumed to move in an overdamped environment and to be driven by a force with fixed magnitude, acting along the particles long axis. As a result, particle speeds,

1 We include circular particle shapes as a special case where the particles' aspect ratio equals one.

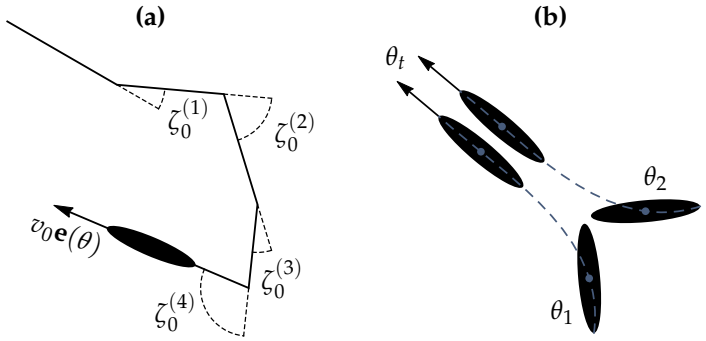

Figure 3.: Basic model assumptions. **(a)** Single particle trajectories. Particles are assumed to travel at constant speed v and to perform run-and-tumble like movements. Tumbling events are assumed to occur at a constant rate λ and to cause particle orientations to change by a random amount ζ_0 (the $\zeta_0^{(i)}$ represent one particular sample of the random variable ζ_0). **(b)** Binary particle collisions. Particles are assumed to be subject to excluded volume interactions (collisions). We assume polar binary collisions during which the two colliding particles with pre-collision orientations θ_1 and θ_2 align to a common post-collision orientation θ_t (which is a model-specific function of the pre-collision angles). In addition, we assume each binary collision event to be subject to noise (not depicted).

v, can be considered constant and each particle's state is completely determined by its two-dimensional position vector $\mathbf{x}$, and its orientation θ. (ii) Due to a noisy background and / or noisy propelling machineries, particles are assumed to follow run-and-tumble like trajectories. This type of motion is modeled via a constant tumbling rate λ, at which particle orientations θ are being shuffled by some random amount ζ_0 [cf. Fig. 3(a)],

$$\theta \xrightarrow{\lambda} \theta + \zeta_0 \qquad (\text{modulo } 2\pi), \tag{1}$$

where the random variable ζ_0 is assumed to be drawn from a zero mean Gaussian distribution with variance σ_0^2. (iii) Interactions among particles are modeled in the form of polar aligning, binary particle collisions. At the level of the active Boltzmann

equation, such collisions will be captured in the form of simple "collision rules", i.e. mappings between the particles' pre- and post-collision orientations [cf. Fig. 3(b)],

$$(\theta_1, \theta_2) \xrightarrow{\Gamma} (\theta_1' = \theta_t + \zeta, \theta_2' = \theta_t + \zeta). \tag{2}$$

Here, $\theta_{1/2}$ and $\theta_{1/2}'$ denote the pre- and post-collision orientations of the two colliding particles, respectively, θ_t denotes the target angle which is a function of the pre-collision angles $\theta_{1/2}$, and the Gaussian random variable ζ (zero mean; variance σ^2) captures the effects of noise during each binary collision. Moreover, Γ denotes the "scattering cross section" and quantifies the rate of binary collisions between particles with relative pre-collision orientations $|\theta_1 - \theta_2|$; cf. Fig. 4.

By means of these modeling assumptions, we can write down the following form of the active Boltzmann equation, which governs the spatiotemporal evolution of the system's one-particle distribution function[2] $f(\mathbf{x}, \theta, t)$ [20, 21]:

$$\partial_t f(\mathbf{x}, \theta, t) + v\, \mathbf{e}(\theta) \cdot \nabla f(\mathbf{r}, \theta, t) = I_\mathrm{d} + I_\mathrm{c}, \tag{3a}$$

where $\mathbf{e}(\theta)$ denotes the unit vector in the direction of θ. The left hand side of Eq. (3) simply captures the convective contribution to the dynamics of $f(\mathbf{x}, \theta, t)$ due to ballistic particle motions with constant speed v. The right hand side of this equation captures the effects due to particle tumbling (in the following also referred to as "diffusion"; I_d), and due to binary particle collisions (I_c). The former effect of (rotational) particle diffusion is described by means of the diffusion integral

$$I_\mathrm{d} = \lambda \left\langle \int_{-\pi}^{\pi} d\phi f(\phi)[\delta(\theta - \phi - \zeta_0) - \delta(\theta - \phi)] \right\rangle_{\zeta_0}, \tag{3b}$$

2 The one-particle distribution function $f(\mathbf{x}, \theta, t)$ is defined such that $f(\mathbf{x}, \theta, t)\, d^2\mathbf{x}\, d\theta$ counts the number of particles inside an "infinitesimal" phase space volume element $d^2\mathbf{x}\, d\theta$ centered about $(\mathbf{x}, \theta)$. In the context of the spatial coordinate $\mathbf{x}$, "infinitesimal volume element" refers to a volume element which is small compared to the system's overall spatial dimensions, but still large enough to contain a large number of particles.

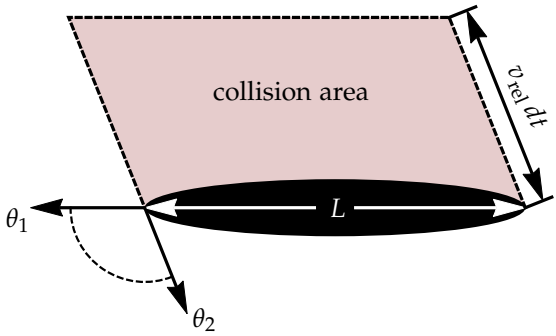

Figure 4.: Geometrical basis of the scattering cross section Γ for long, slender rods (a more careful derivation of the scattering cross section for rods of arbitrary aspect ratio is given in section 2.4). During the time interval $[t, t+dt]$, the depicted rod of length L and orientation θ_1 collides with all rods of orientation θ_2 whose head positions at time t lie within the red shaded "collision area". Here, $v_{\mathrm{rel}} = v\,|\mathbf{e}(\theta_1) - \mathbf{e}(\theta_2)|$ denotes the relative velocity between rods of orientations θ_1 and θ_2, respectively. The scattering cross section $\Gamma(L, |\theta_1 - \theta_2|)$ is, therefore, equal to the collision area divided by the length of the (infinitesimal) time interval, dt.

while binary particle interactions are formulated by means of the collision integral

$$I_{\mathrm{c}} = \Big\langle \int_{-\pi}^{\pi} d\theta_1 \int_{-\pi}^{\pi} d\theta_2\, \Gamma(L, |\theta_1 - \theta_2|) f(\theta_1) f(\theta_2) \times \Big[\delta\big(\theta - \theta_t(\theta_1, \theta_2) - \eta\big) - \delta\big(\theta - \theta_1\big)\Big] \Big\rangle_{\zeta}. \tag{3c}$$

In Eqs. (3b) and (3c) the spatial coordinate $\mathbf{x}$ is not displayed explicitly, since no spatial integrations are involved in these expressions which only act on the particles' angular degrees of freedom.

Both integrals, I_d and I_c can be read as a sum of terms quantifying the gain and loss of particles (per unit time and per unit area) inside the phase space element $d^2\mathbf{x}\,d\theta$ centered about $(\mathbf{x}, \theta)$, respectively. In the case of rotational diffusion, this phase space

element gains one particle, if some particle at position $\mathbf{x}$ happens to enter the angular element $[\theta, \theta + d\theta]$ through tumbling [first term in Eq. (3b)]. Conversely, this same phase space elements loses one particle, if some some particle at position $\mathbf{x}$ and orientation $\phi \in [\theta, \theta + d\theta]$ will tumble [second term in Eq. (3b)]. Similarly, the number of particles inside this phase space element increases by two[3], if any two particles at $\mathbf{x}$ are scattered into the angular element $[\theta, \theta + d\theta]$ by a binary collision [first term in Eq. (3c)], and it loses one particle if some particle at $\mathbf{x}$ is scattered out of the angular element $[\theta, \theta + d\theta]$ [second term in Eq. (3c)].

The particular form used to implement binary particle interactions in the kinetic framework set up in Eqs. (3) deserves some additional remarks. The analytic form of the collision integral, Eq. (3c), follows from an adaption of the "Stoßzahlansatz" [126] to the case of active particle systems with properties as outlined above. In particular, the use of a product of two one-particle distribution functions, $f(\theta_1)f(\theta_2)$, in place of the (joint) two-particle distribution function $f_2(\theta_1, \theta_2)$ in the integrand of Eq. (3c) expresses the "*molecular chaos assumption*", which posits that particle correlations prior to binary collisions can be neglected. The molecular chaos assumption is a key ingredient of the kinetic framework discussed in the present part of this thesis, as it is inextricably linked to the Boltzmann equation as outlined in Eqs. (3). Without the molecular chaos assumption, Eqs. (3) would have to be complemented by additional equations governing the evolution of $f_2(\theta_1, \theta_2)$, which usually leads to an infinite hierarchy of equations which is of rather limited use in actual calculations[4]. When the molecular chaos assumption holds, the rate of particle collisions, as quantified by the scattering cross section $\Gamma(L, |\theta_1 - \theta_2|)$, can be calculated by means of purely geometrical considerations; cf. Fig. 4.

As will be detailed in chapter 4, the active Boltzmann equation (3) is amenable to direct numerical treatment. To proceed an-

3 It might appear that the gain of two particles should be reflected by a factor of 2 in front of the first delta function in Eq. (3c). However, this factor of 2 is implicitly contained in Eq. (3c), since each pair of collision angles θ_1 and θ_2 is counted twice.

4 If the system's dynamics can be described by means a Hamiltonian, this hierarchy of equations is known as the BBGKY hierarchy [62].

alytically, however, this partial integro-differential equation has to be simplified to allow for a (largely qualitative) investigation of the system's dynamics. While actual applications of such analytical approaches will be discussed in chapters 2 and 3, our focus here will be on a brief outline of the general strategy commonly employed to map the active Boltzmann equation (3) to a set of equations for the system's slow, hydrodynamic variables; also cf. [5, 20, 6, 4, 21, 108, 107].

The general procedure to arrive at a hydrodynamic description of the system, starting from the kinetic formulation in Eqs. (3) consists of two steps. In step one, the integrals on the right hand side of the active Boltzmann equation are eliminated by Fourier transforming the entire equation with respect to the angular coordinate θ. To this end, let

$$\hat{f}_k(\mathbf{x}, t) = \int_{-\pi}^{\pi} d\theta \, e^{ik\theta} f(\mathbf{x}, \theta, t) \tag{4}$$

denote the Fourier transform of the one-particle distribution function $f(\mathbf{x}, \theta, t)$. Then the Fourier transform of Eqs. (3) reads

$$\begin{aligned} &\partial_t \hat{f}_k + \frac{v}{2}\left[\partial_x(\hat{f}_{k+1} + \hat{f}_{k-1}) - i\partial_y(\hat{f}_{k+1} - \hat{f}_{k-1})\right] = \\ &-\lambda\left(1 - e^{-(k\sigma_0)^2/2}\right)\hat{f}_k + \sum_{n=-\infty}^{\infty} \mathcal{I}_{n,k}\,\hat{f}_n \hat{f}_{k-n}, \end{aligned} \tag{5}$$

where the matrix $\mathcal{I}_{n,k}$ denotes the Fourier space representation of the collision kernel of the integrals defined in Eq. (3c), and depends on the specific choice for the target angle mapping $\theta_t(\theta_1, \theta_2)$; cf. section 2.4 and Appendix A.

In polar systems, the slow, hydrodynamic variables are given by the particle density $\rho(\mathbf{x}, t)$ and the momentum density $\boldsymbol{\tau}(\mathbf{x}, t)$. According to the definition of the Fourier transform of the one-particle distribution function, Eq. (4), these slow hydrodynamic variables are directly related to the zeroth and first Fourier mode[5]

5 The order parameters corresponding to higher symmetries are encoded in higher Fourier modes. For instance, $\hat{f}_2(\mathbf{x}, t)$ is directly related to the nematic field tensor [107].

in the hierarchy of equations (5). More precisely, identifying $\mathbb{R}^2 \leftrightarrow \mathbb{C}$, we get

$$\rho(\mathbf{x}, t) \equiv \hat{f}_0(\mathbf{x}, t), \tag{6a}$$
$$\boldsymbol{\tau}(\mathbf{x}, t) \equiv v\,\hat{f}_1(\mathbf{x}, t). \tag{6b}$$

Unfortunately, according to Eqs. (5), the actual dynamics of $\rho(\mathbf{x}, t)$ and $\boldsymbol{\tau}(\mathbf{x}, t)$ are coupled to an infinite number of higher order Fourier modes and, therefore, cannot be assessed without further simplification. Step two of the general procedure to derive a hydrodynamic description, therefore, involves an "appropriate" truncation of this hierarchy, in order to attain a closed set of equations for the hydrodynamic filed variables $\rho(\mathbf{x}, t)$ and $\boldsymbol{\tau}(\mathbf{x}, t)$. Possible truncations schemes, which can be shown to yield a meaningful description of the system's hydrodynamics at the onset of collective motion, will be discussed in chapters 2 and 3 and rely on the assumption that all Fourier modes beyond the second order mode remain small across the transition to collective motion. We emphasize, however, that so far no well-controlled and systematic truncation scheme has been proposed, which would allow for an actual control of the error made in truncating the set of equations (5). Rather, the design of the truncation schemes used to make progress starting from the hierarchy of equations (5), largely relies on physical intuition and usually differs between systems with different collision symmetries; cf., e.g., Refs. [21] and [107]. To benchmark analytical studies based on the general strategy outlined above, it is, therefore, highly important to approach the actual solution of the active Boltzmann equation (3) by alternative means. A possible route in this direction will be discussed in chapter 4, where we propose a numerical framework to solve the active Boltzmann equation in real space, rather than in Fourier space.

2

PARTICLE CONSERVATION IN SELF-PROPELLED PARTICLE SYSTEMS

2.1 STARTING POINT OF THE PROJECT

The emergence of collective motion in systems of self-propelled particles is among the most frequently studied phenomena in active matter research. Although a large number of different modeling classes can be distinguished (cf. discussion in the introduction), this thesis especially focuses on dry systems with polar collisions among constituent particles. This particular modeling class has been the subject of intensive research both, in the context of agent based simulation approaches [152, 35, 149, 57, 31, 53] and in terms of analytical models [145, 146, 20, 4, 21, 94, 44, 108]. These studies convey a largely unified picture concerning the emergence of macroscopic polar order: Decreasing the strength of noise relative to the frequency of particle collisions causes systems to transition from a completely disordered, isotropic gas state toward a spatially homogeneous, polar ordered state. While in systems with metric interactions among particles this transition is first order and proceeds via the formation of density segregated polar structures at intermediate noise strengths [57, 31], a "direct", continuous transition to a spatially homogeneous state of collective motion has been reported in systems with metric-free interactions [53, 33, 108].

A detailed picture describing the emergence of collective motion in the former case of metric interactions has been obtained by means of agent based simulations [57]. There, it was demonstrated that the formation of macroscopically extended polar wave structures is preceded by the formation of polar clusters even at

noise levels, where the overall polarity in the system remains zero. The emergence of these clusters leads to superdiffusive particle trajectories, which can be pictured as a succession of ballistic flights when particles are caged by a polar cluster, interspersed by purely diffusive episodes when particles are free. Similar superdiffusive behavior has been observed in previous experiments on bacterial systems [161], and was discussed to be caused by the same collective clustering effects [59, 162, 58].

In our work *"Role of particle conservation in self-propelled particle systems"* [WTF13], we derive a mechanistic picture of polar order formation in self-propelled particle systems with metric interactions in terms of a simple kinetic model which builds on the simulation results described above [57]. Specifically, we highlight the importance of particle conservation in the formation of density segregated polar structures near the ordering transition, and assess the impact of particle shape in the framework of a Boltzmann equation based description. A brief survey over the modeling approach adopted in this work, as well as an outline of the main results of our work is given in the subsequent section 2.2. In section 2.3, we comment on the range of applicability of our kinetic approach and highlight potential future questions. A fully comprehensive account of our work can be found in section 2.4.

2.2 SUMMARY OF MAIN RESULTS

To implement the particle based picture of the transition to collective motion described in the previous section, we proceed as follows. First, we observe that particles can be roughly classified according to whether or not they are part of a larger polar cluster. Particles which are caged inside such a cluster are referred to as *"cluster particles"*, particles moving freely around in space are referred to as *"single particles"*. Both classes are assumed to exchange particles via the following processes; cf. Fig. 5: (i) Binary collisions between *single particles* lead to the nucleation of polar (two particle) clusters and, therefore, "converts" two *single particles* into two *cluster particles*. (ii) Conversely, clusters are assumed to "evaporate" at a constant rate ϵ, which leads to the

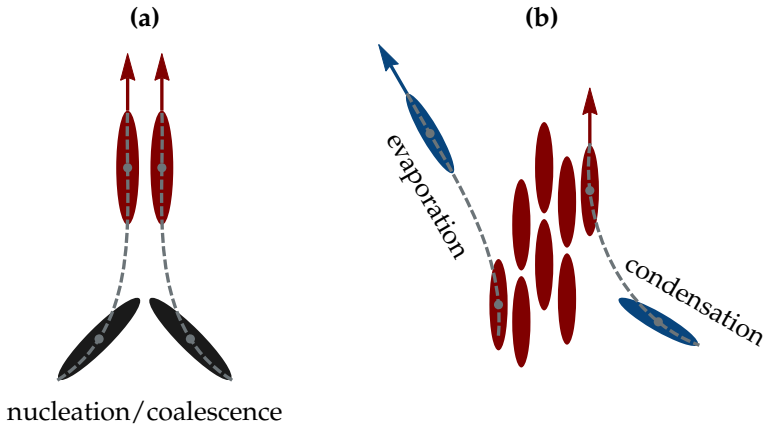

Figure 5.: Illustration of collision and conversion processes in our kinetic model. *Single particles* are shown in blue, *cluster particles* in red. Black particles can refer to either particle class. **(a)** Collisions among *single particles* lead to cluster "nucleation"; cluster "coalescence" is modeled via collisions among *cluster particles*. **(b)** Existing clusters lose particles to the *single particle* class by "evaporation" (assumed to occur at a constant rate ϵ), and gain particles from the *single particle* class by particle "condensation".

conversion of a *cluster particle* into a *single particle*. (iii) If a collision occurs between a *single particle* and a *cluster particle*, the *single particle* is assumed to align to the direction of the *cluster particle* and will be converted to become a member of this cluster (particle "condensation"). (iv) Finally, if two *cluster particles* collide, they are assumed to align and to form a new cluster (cluster "coalescence").

On the level of the active Boltzmann equation as reviewed in chapter 1, the description above can be formulated in terms of the one particle distribution functions for the class of *single particles*, $s(\mathbf{x}, \theta, t)$, and the class of *cluster particles*, $c(\mathbf{x}, \theta, t)$, respectively:

$$\partial_t s(\mathbf{x}, \theta, t) + v\, \mathbf{e}(\theta) \cdot \nabla s(\mathbf{x}, \theta, t) = \dot{s}(\mathbf{x}, \theta, t), \tag{7a}$$

$$\partial_t c(\mathbf{x}, \theta, t) + v\, \mathbf{e}(\theta) \cdot \nabla c(\mathbf{x}, \theta, t) = \dot{c}(\mathbf{x}, \theta, t). \tag{7b}$$

The source terms $\dot{s}(\mathbf{x},\theta,t)$ and $\dot{c}(\mathbf{x},\theta,t)$ on the right hand sides of these equations read

$$\begin{aligned}\dot{s} &= \lambda\left[\mathcal{D}_s^{(+)}(\theta)-\mathcal{D}_s^{(-)}(\theta)\right]+\epsilon\mathcal{D}_c^{(+)}(\theta)\\ &\quad -\mathcal{C}_s^{(-)}(\theta)-\mathcal{A}[s,c;\theta], \qquad (8a)\\ \dot{c} &= -\epsilon\mathcal{D}_c^{(-)}(\theta)\\ &\quad +\mathcal{C}_s^{(+)}(\theta)+\mathcal{C}_c^{(+)}(\theta)+\mathcal{A}[c,s;\theta]-\mathcal{C}_c^{(-)}(\theta)\,, \qquad (8b)\end{aligned}$$

where terms due to particle diffusion are gathered in the first lines of Eqs. (8), and collision integrals are displayed in the second lines. Here, particle diffusion within the class of *single particles* is assumed to occur at a rate λ, while tumbling of particles within the group of *cluster particles* is assumed to occur at a much lower rate $\epsilon \ll \lambda$ due to stabilization effects by the surrounding cluster. The diffusion integrals $\mathcal{D}_f^{(\pm)}$ ($f \in \{s,c\}$) read

$$\mathcal{D}_f^{(-)}(\theta)=f(\theta); \quad \mathcal{D}_f^{(+)}(\theta)=\langle f(\theta-\vartheta_0)\rangle_0\,, \qquad (9a)$$

where $\langle\dots\rangle_0$ denotes an average over zero-mean Gaussian random variable ϑ_0. Note that no actual diffusion occurs within the class of *cluster particles*. When *cluster particles* tumble, they leave the cluster and become *single particles*. In the meantime, *cluster particles* move fully ballistic. This is in accordance with the particle based picture underlying the observed superdiffusive behavior of self-propelled particles [58, 57], which we described in the previous section. The collision integrals $\mathcal{C}_f^{(+)}$ ($f \in \{s,c\}$) describing collisions among *cluster particles* ($f \equiv c$) or among *single particles* ($f \equiv s$), respectively, read

$$\begin{aligned}\mathcal{C}_f^{(+)}(\theta) &= \left\langle \int d\mathcal{I}\, f(\theta')f(\theta'')\,\delta\!\left(\frac{\theta'+\theta''}{2}+\vartheta-\theta\right)\right\rangle, \qquad (9b)\\ \mathcal{C}_f^{(-)}(\theta) &= \int d\mathcal{I}\, f(\theta')f(\theta'')\delta(\theta'-\theta), \qquad (9c)\end{aligned}$$

where $\langle\dots\rangle$ denotes an average with respect to the zero-mean Gaussian random variable ϑ with variance σ^2. Finally, the align-

ment integrals $\mathcal{A}[f,g;\theta]$ ($f,g \in \{s,c\}$), describing the condensation of *single particles* to clusters, read

$$\mathcal{A}[f,g;\theta] = \int d\mathcal{I}\, f(\theta')g(\theta'')\delta(\theta'-\theta). \tag{9d}$$

In Eqs. (9b) – (9d), we abbreviated

$$\int d\mathcal{I}\,(\dots) \equiv \int_{-\pi}^{\pi} d\theta' \int_{\theta'-\pi}^{\theta'+\pi} d\theta''\, \Gamma(L,d,|\theta'-\theta''|)\,(\dots)\,,$$

where $\Gamma(L,d,|\theta'-\theta''|)$ is the scattering cross section, which we derive in section 2.4, taking into account variable particle diameters d and lengths L (see also Fig. 4).

Equations (9) comprise our kinetic modeling approach. To assess the influence of particle conservation on the transition to collective motion, we investigate two distinct model variants, both of which are based on the kinetic description in Eqs. (9): First, we consider a *canonical* model in which the total number of particles

$$N = \int d^2\mathbf{x}\,\rho = \int d^2\,\mathbf{x}(\rho_s+\rho_c)$$

($\rho_s = \int d\theta\, s(\theta,\mathbf{x})$: density of *single particles*; $\rho_c = \int d\theta\, c(\theta,\mathbf{x})$: density of *cluster particles*) is assumed to be constant. This situation corresponds to the standard modeling approaches which we referred to in the previous section. Secondly, we consider a *grand canonical* model in which the local density of single particles is assumed to be fixed, $\rho_s = \text{const}$. This scenario is motivated by recent experimental approaches including, e.g., typical gliding assays [26, 124, 123, 125, 135] where the collective motion of filaments is confined to a two-dimensional carpet of molecular motors which itself is in contact with a three-dimensional bulk reservoir of filaments.

A detailed hydrodynamic level analysis of these model variants of Eqs. (9) is given in section 2.4. Here we restrict ourselves to presenting a brief summary of our main results.

Considering the low-density / high noise parameter regime, where a spatially homogeneous, isotropic state constitutes a stable solution to our kinetic model, we investigate the composition of the system in terms of *single particles* and *cluster particles*.

We find that both modeling variants, the *canonical* and the *grand canonical* model, exhibit a crossover to a *cluster particle* dominated regime at a particle shape dependent packing fraction

$$\bar{p} \simeq \frac{3\pi}{8v} \frac{\epsilon L}{2 + L/d} \qquad (L/d \gg 1), \tag{10}$$

which fully agrees with previous numerical observations on cluster forming systems [105].

While Eq. (10) holds true for both modeling variants, *canonical* and *grand canonical* model exhibit qualitatively different behaviors across the threshold to collective motion, highlighting the significance of particle conservation in the pattern selection processes in active systems. The analysis of the *canonical* model reveals the familiar longitudinal instability which is responsible for the formation of density segregated patterns across the transition to collective motion. This same instability, however, is *absent* in the *grand canonical* model. Remarkably, our results suggest that the *grand canonical* model transitions directly toward a spatially homogeneous state of collective motion at intermediate collision noise levels σ. For low collision noise levels, we find a very weak hybrid shear / splay instability which quickly restabilizes for parameters only slightly away from the transition line.

The overall situation is probably best illustrated by inspecting the dispersion relations for the momentum and density modes characterizing the transition from a spatially homogeneous and isotropic state toward the formation of polar order. The corresponding modes are shown in Fig. 6(a) for the *canonical* model, and in Fig. 6(b) for the *grand canonical* model. In the *canonical* model, conservation of the total number of particles implies a marginally stable mode at wavenumber $q = 0$. This, in turn leads to positive growth rates of density modes with wave numbers $q \gtrsim 0$ at the onset of collective motion. There, the fastest growth of the density mode is observed at some (parameter dependent) wave number $\hat{q} > 0$ which hints at the initial formation of structures of finite size $\sim \hat{q}^{-1}$. In contrast, the constraint of conservation of particle number is lifted in the *grand canonical* model, in which, therefore, the density modes remain stable across the ordering transition. At the onset of collective motion, only the

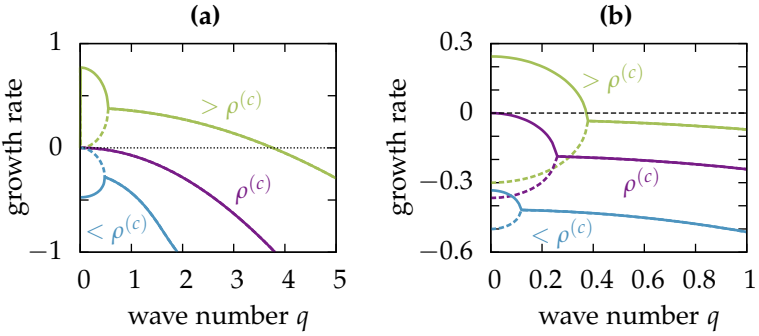

Figure 6.: Dispersion relations of the growth rates of momentum (solid lines) and density modes (dashed lines) for a spatially homogeneous, isotropic base state in the vicinity of the transition to collective motion. The different curves correspond to overall densities $\rho = \rho_c + \rho_s$ below, at, and above the transition density $\rho^{(c)}$ (indicated in the figures). **(a)** *Canonical* model. Due to particle conservation, the density mode is marginally stable at $q = 0$ and grows for $q \gtrsim 0$ and $\rho \gtrsim \rho^{(c)}$. **(b)** *Grand canonical* model. Particle conservation does not apply and the density modes are stable across the transition to collective motion.

momentum modes possess positive growth rates with the fastest growing mode at $q = 0$, hinting at the emergence of a spatially homogeneous polar ordered state.

We conclude this brief summary of our main results by discussing the following mechanistic picture which helps illuminate the significance of particle conservation in active systems in the context of the emergence (or absence) of density segregated structures. To this end, consider the effect of a local perturbation in the particle density ρ in the *grand canonical* model. Since the density of the isotropic sea of *single particles*, ρ_s, is constant by assumption, this perturbation translates into a corresponding perturbation of the density of polar ordered *cluster particles*, ρ_c. In a stationary state, the particle currents between both particle classes balance and we have, according to our kinetic model (working with appropriately rescaled densities; cf. section 2.4):

$$\left(\rho_s^0 + \rho_c\right) \rho_s^0 = \rho_c. \tag{11}$$

Here the left hand side of this equation captures the particle current from the class of *single particles* into the class of *cluster particles* by cluster nucleation (first term) and particle condensation (second term), and the right hand side captures the reverse current due to cluster evaporation. As can be seen from Eq. (11), increasing (decreasing) the local value of ρ_c results in a net current out of (into) the class of *cluster particles*. The balance equation (11), therefore, implies a negative feedback which counteracts local density fluctuations, and which explains the absence of a corresponding density triggered (longitudinal) instability.

Proceeding along the same line of arguments for the *canonical* model, we find the exact opposite behavior. In the *canonical* model, ρ_s must not be considered constant. To assess the effects of local density fluctuations in the context of the *canonical* model, we therefore rewrite Eq. (11) in terms of the total particle density $\rho = \rho_c + \rho_s$ and the density difference $\eta \equiv \rho_c - \rho_s > 0$ (this inequality holds for all parameters inside the polar ordered regime),

$$\rho(\rho - \eta) = \rho + \eta. \tag{12}$$

Now, consider a local increase (decrease) of the total density ρ at constant η. This perturbation leads to a net particle current into (out of) the class of *cluster particles*. Since, at the same time, *cluster particles* are the carriers of macroscopic momentum, this implies that particle enriched regions pick up further momentum and, in turn, gather even more particles. Conversely, regions deprived of particles lose momentum which implies impaired capabilities to gather new particles. In the case of the *canonical* model, therefore, the balance equation (12) implies a positive feedback such that small density perturbations tend to be amplified as a result of overall particle conservation. This, in turn, provides a possible mechanistic explanation concerning the occurrence of a (density triggered) longitudinal instability and the emergence of density segregated patterns at the onset of collective motion.

2.3 OUTLOOK

The kinetic modeling approach discussed in sections 2.2 and 2.4 incorporates the formation of clusters of coherently moving particles into a strictly binary kinetic theory. We have shown that this model predicts a crossover to a cluster dominated state even below the transition to collective motion, and is thus consistent with corresponding observations made in the context of the agent based simulations in Ref. [57]. Moreover, the dependence of the clustering crossover density on particle shape, Eq. (10), predicted by our approach agrees with the microscopic simulations of Ref. [105] on rod-like particles with excluded volume interactions. This suggests that our kinetic model appropriately captures the main features of particle clustering at low densities, where no macroscopic order has been established.

We emphasize, however, that it is impossible to assess effects beyond binary particle interactions and the assumption of molecular chaos using the kinetic model introduced above; cf. discussions in chapter 1 and section 3.3. Our model is, therefore, unlikely to properly capture effects due to particle clustering at larger densities, where both, kinetic [20, 21, WTF13] and agent based approaches [152, 35, 57, 31] would predict macroscopic polar order to emerge. In particular, both modeling paradigms do not distinguish between interactions among free particles and interactions among particles caged in clusters, which clearly oversimplifies collision processes between clusters. The actual effects of cluster formation on the establishment of genuine large scale collective motion, remain largely elusive. For instance, in recent experiments on *M. xanthus* mutants [106] no state of global polar order has been observed, despite the formation of large polar clusters of coherently moving bacteria.

Moreover, according to our kinetic model, particle shape only implies a shift in characteristic density scales, but does not have any observable impact on the qualitative features of our model at the hydrodynamic level. Yet, recent microscopic simulations on self-propelled rod-like particles indicate that particle aspect ratios also impact the pattern selection processes at large enough densities [158].

The emergence of dense clusters of coherently moving particles thus introduces new interesting and challenging questions in the context of collective motion in active systems at large densities. The kinetic modeling approach discussed here is suitable in situations where the emergence of collective motion is primarily driven by binary particle interactions. Systems in which the formation of order is dominated by the formation of densely packed clusters of particles, however, lie beyond the scope of this approach, which is tailored to sufficiently dilute systems. Alternative theoretical modeling approaches are needed for these cases, to fully assess the significance of these fascinating structures; cf. Refs. [61, 104].

New Journal of Physics
The open access journal for physics

Role of particle conservation in self-propelled particle systems

Christoph A Weber[1], **Florian Thüroff**[1] **and Erwin Frey**[2]
Arnold Sommerfeld Center for Theoretical Physics and Center for NanoScience, Department of Physics, Ludwig-Maximilians-Universität München, Theresienstraße 37, D-80333 Munich, Germany
E-mail: frey@lmu.de

New Journal of Physics **15** (2013) 045014 (31pp)
Received 2 November 2012
Published 22 April 2013
Online at http://www.njp.org/
doi:10.1088/1367-2630/15/4/045014

Abstract. Actively propelled particles undergoing dissipative collisions are known to develop a state of spatially distributed coherently moving clusters. For densities larger than a characteristic value, clusters grow in time and form a stationary well-ordered state of coherent macroscopic motion. In this work we address two questions. (i) What is the role of the particles' aspect ratio in the context of cluster formation, and does the particle shape affect the system's behavior on hydrodynamic scales? (ii) To what extent does particle conservation influence pattern formation? To answer these questions we suggest a simple kinetic model permitting us to depict some of the interaction properties between freely moving particles and particles integrated in clusters. To this end, we introduce two particle species: single and cluster particles. Specifically, we account for coalescence of clusters from single particles, assembly of single particles on existing clusters, collisions between clusters and cluster disassembly. Coarse graining our kinetic model, (i) we demonstrate that particle shape (i.e. aspect ratio) shifts the scale of the transition density, but does not impact the instabilities at the ordering threshold and (ii) we show that the validity of particle conservation determines the existence of a longitudinal instability, which tends

[1] These authors contributed equally to this work.
[2] Author to whom any correspondence should be addressed.

to amplify density heterogeneities locally, and in turn triggers a wave pattern with wave vectors parallel to the axis of macroscopic order. If the system is in contact with a particle reservoir, this instability vanishes due to a compensation of density heterogeneities.

Contents

1. Introduction

The emergence of collective motion is a ubiquitous phenomenon in nature, encountered in a great variety of actively propelled systems [1–3]. Coherently moving groups have been observed over a broad range of length scales, spanning from micrometer-sized systems [4–10] over millimeter large granules [11–13] to large groups of animals [14]. The fact that the capability of synchronizing movements between agents is shared even among fundamentally different systems has called for abstract modeling approaches, aiming at identifying the essential properties of these systems both in terms of analytical descriptions [15–28] and by means of agent-based simulation techniques [29–39].

Theoretically, the emergence of collective motion has mostly been studied in the context of particle conserving systems. There are, however, a number of experimental systems in which the assumption of particle conservation is questionable. In typical gliding assays [4–6, 9, 10], for instance, collective motion of filaments is observed on a two-dimensional 'motor carpet' which itself is in contact with a three-dimensional bulk reservoir of filaments. However, the impact of particle conservation on the formation of patterns of collective motion remains largely elusive.

Here, we address the significance of constraints for particle number by highlighting the differences in the collective properties between particle conserving systems and those in contact

with a particle reservoir. Our focus will be on the comparison of two archetypical scenarios, which we will refer to as the *canonical* (particle conserving) and the *grand canonical* (violating particle conservation) scenarios, respectively.

To this end, we will resort to a kinetic approach, which has been set up previously by Aranson and Tsimring [16] to describe pattern formation in a system of interacting microtubules, and which has been extended to the case of self-propelled spheres by Bertin *et al* [17, 22]. In the following, we will extend this description in accordance with a physical picture of collective motion that has been developed over the last decade based on observations in agent-based simulations of locally interacting, particle conserving systems [31, 32, 37, 39]. Among the most pertinent phenomena that have been reported in the context of these studies is the formation of intricate local structures pervading these systems in the vicinity of the ordering transition. Densely packed cohorts of coherently moving particles—subsequently referred to as *clusters*—incessantly 'nucleate' and 'evaporate' on local scales, even below threshold, rendering the system isotropic and homogeneous only in the limit of macroscopic length scales. Individual particles exhibit superdiffusive behavior in this regime, performing quasi-ballistic 'flights' as long as they are part of a cluster, and conventional particle diffusion if they are not. Above threshold, collective motion manifests itself on macroscopic scales in the form of coherently moving and dense bands, which are submersed in an isotropic low-density 'particle sea'. Spatially homogeneous flowing states, in contrast, are observed only well beyond the ordering threshold [31]. Moreover, particle geometry was demonstrated to play an essential role in the context of clustering dynamics, with higher aspect ratios facilitating the formation of clusters of coherently moving particles [37].

In the light of the above, we suggest a simplified modeling framework to incorporate the intricate role of clusters on the ordering behavior, which will be presented in greater technical detail in the following section. Particles interact via binary collisions with a scattering cross section that is explicitly derived as a function of particle shape. Depending on whether a given particle is part of a cluster or not, it will be associated with one of two distinct particle classes, which we will refer to as the class of *cluster particles* and the class of *single particles*, respectively. *Single particles* are 'converted' to *cluster particles* by 'condensation' every time a *single particle* collides with a cluster. Conversely, *cluster particles* are 'converted' back to *single particles* by an 'evaporation' process which we assume to occur at some constant (possibly particle shape dependent [37]) rate. Moreover, in the absence of interactions, *cluster particles* will be assumed to move ballistically, whereas *single particles* will be assumed to perform random walks. Taken together, the conversion dynamics and the class specificity of particle motion provide a simple way of implementing the typical superdiffusive behavior of individual particles, which was alluded to above. To assess the importance of particle conservation in the context of pattern formation, we will analyze two variants of this model. Firstly, we study closed systems in which the total number of particles is conserved (*canonical* scenario) and where, consequently, the denser cluster phase grows at the expense of the single phase. Secondly, we examine open systems in contact with a particle reservoir (*grand canonical* scenario), where the particle current out of the single phase is compensated so as to retain the density of the isotropic sea of *single particles* at a constant level; cf figure 1.

Our work is structured as follows. In section 2 the modeling framework for the *canonical* and *grand canonical* models is introduced and the model equations are discussed in detail. The corresponding hydrodynamic equations are derived in section 3 by means of an appropriate truncation scheme in Fourier space. Therein, we also give explicit expressions of

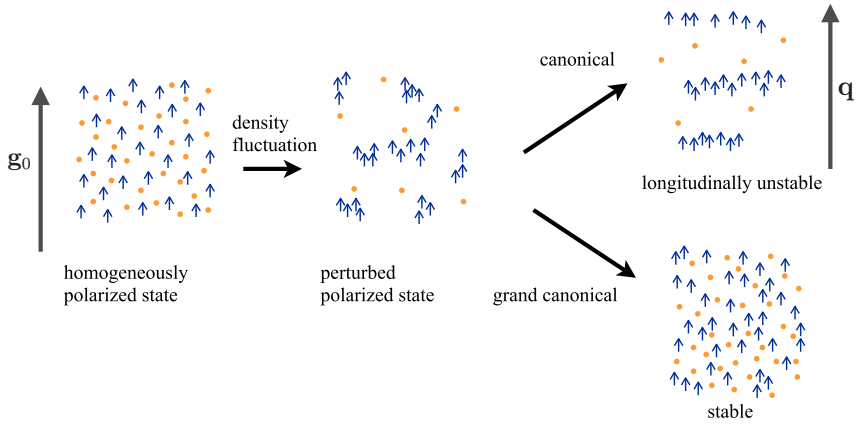

Figure 1. Illustration of the *canonical* and *grand canonical* modeling framework, highlighting the quintessential differences in the context of pattern formation. In the homogeneously polarized state (left), the *cluster particles* density (blue arrows) constitutes the system's macroscopic net momentum $\mathbf{g}_0$, while some fraction of the system's particles, the *single particles* (orange dots), exhibit zero net momentum. Spatial perturbations of both density fields lead to two fundamentally different outcomes: (i) In the case of a closed system obeying total particle conservation (*single particles* + *cluster particles*), termed as the *canonical* model, the homogeneously polarized state is longitudinally unstable, with a wave vector $\mathbf{q}$ parallel to the polarized state $\mathbf{g}_0$, potentially enforcing a wave-like pattern. (ii) In contrast, open systems turn out to be stable against this kind of density fluctuation.

the kinetic coefficients as a function of the particles' aspect ratio and velocity, noise level and density for *single particles* and *cluster particles*. Section 4 is devoted to the analysis of the homogeneous equations. The dynamic's stationary fixed points are determined and the phase boundary between the isotropic and homogeneous states is calculated. Section 5 deals with the implications of the inhomogeneous equations in the framework of a linear stability analysis, which are concluded in section 6.

2. A coarse-grained kinetic model

We consider rod-like particles of length L and diameter d moving in two dimensions with a constant velocity v. A particle's state is determined by its position $\mathbf{x}$ and the orientation θ of its velocity vector. To describe the time evolution of the system, we adopt a kinetic approach [16–18, 22].

On mesoscopic scales, the system's spatio-temporal evolution is then governed by Boltzmann-like equations for the one-particle distribution functions within the classes of *single*

particles and *cluster particles*, respectively. Interactions enter this description by means of collision integrals. The kernel of these integrals involves both a measure for the rate of collisions, as well as a 'collision rule' implementing a mapping between pre- and post-collisional directions θ and θ' of each of the two partaking particles. Here, we are led to consider a simplified model of binary particle interactions, which builds on the distinction between *single particles* and *cluster particles*. The details of this model will be described in the following section.

2.1. Reaction equations

Let $S(\theta)$ and $C(\theta)$ refer to a particle moving in the direction of θ and being associated with the class of *single particles* or *cluster particles*, respectively. In the absence of interactions, *single particles* are assumed to perform a persistent random walk, which we model as a succession of ballistic straight flights, interspersed by self-diffusion ('tumble') events. These tumble events are assumed to occur at a constant rate λ and reorient the particle's orientation θ by a random amount ϑ_0:

$$S(\theta) \xrightarrow{\lambda} S(\theta' = \theta + \vartheta_0). \tag{1}$$

For simplicity we assume ϑ_0 to be Gaussian distributed,

$$p_0(\vartheta_0) = \frac{1}{\sqrt{2\pi\sigma_0^2}} \exp\left(-\vartheta_0^2/2\sigma_0^2\right), \tag{2}$$

with σ_0 denoting the standard deviation. On time scales much larger than λ^{-1}, this tumbling behavior can be described as conventional particle diffusion, with the particles' diffusion constant being a function of λ and σ_0 [40].

When two *single particles* $S(\theta_1)$ and $S(\theta_2)$ collide, they are assumed to assemble a cluster, i.e. each of the two particles becomes a *cluster particle* (see figure 2(a)):

$$S(\theta_1) + S(\theta_2) \to C(\bar{\theta} + \vartheta) + C(\bar{\theta} + \vartheta), \tag{3}$$

where[3]

$$\bar{\theta}(\theta_1, \theta_2) = \tfrac{1}{2}(\theta_1 + \theta_2) \tag{4}$$

denotes the average of both pre-collisional angles θ_1 and θ_2, and where ϑ is a random variable which we, again, assume to be Gaussian distributed:

$$p(\vartheta) = \frac{1}{\sqrt{2\pi\sigma^2}} \exp\left(-\vartheta^2/2\sigma^2\right). \tag{5}$$

The rate of binary collisions, such as equation (3), is determined by a particle-shape-dependent *differential scattering cross section*, which will be discussed below; see section 2.2 and appendix A.

Collisions involving *cluster particles* are distinct from *single particle* events. Due to the close spatial proximity of particles within each cluster, these collisions correspond to many-particle interactions. Needless to say, a detailed description of cluster formation and the ensuing particle dynamics represents a highly complex matter, requiring explicit consideration of such

[3] To make sure that $\bar{\theta}$ points into the 'right' direction (i.e. $|\bar{\theta} - \theta_{1/2}| \leqslant \pi/2$), we choose $\theta_1 \in (-\pi, \pi]$ and $\theta_2 \in (\theta_1 - \pi, \theta_1 + \pi]$.

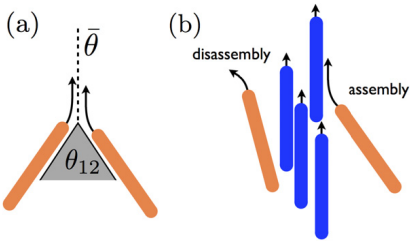

Figure 2. (a) Illustration of two *single particle* species (light orange) with a pre-collisional relative angle of θ_{12}, colliding such that they align collinear to the average angle $\bar{\theta}$. Both particles become a cluster species after the collision. (b) Right: illustration of a possible scenario where a single particle joins a cluster by perfectly aligning to the cluster particles (blue). Left: a particle leaves the cluster by a random change of its direction at a characteristic rate ϵ.

many-particle interactions. For simplicity, we will resort to the following simplified interaction picture. We assume that (binary) collisions between *single particles* and *cluster particles* lead to a condensation process during which the *single particle* aligns to the *cluster particle* without changing the direction of the cluster as a whole:

$$S(\theta_1) + C(\theta_2) \rightarrow C(\theta_2) + C(\theta_2). \tag{6}$$

Equation (6) thus captures the net effect of collisions between *single particles* and *cluster particles*, during which multiple collisions, involving neighboring particles belonging to the same cluster, stabilize the cluster's direction; cf figure 2(b) for an illustration.

Collisions among *cluster particles* is an even more intricate process, since they actually depend on the size and shape of both colliding clusters, and in general involve multi-particle interactions. In the framework of a Boltzmann-like description, correlations in the particle distribution are neglected and only binary interactions are considered. The frequency of interactions is determined by a geometrical construction called the 'Boltzmann cylinder', assuming that particle positions are homogeneously distributed on local scales. With regard to many-particle interactions during collisions among *cluster particles*, we thus have to resort to some kind of simplified, binary collision picture. Since our kinetic model lacks any direct notion of cluster size or shape, we will stick to the assumption that, on average, collisions between *cluster particles* are devoid of any directional bias, leading to the same type of collision rule as for *single particles*:

$$C(\theta_1) + C(\theta_2) \rightarrow C(\bar{\theta} + \vartheta) + C(\bar{\theta} + \vartheta). \tag{7}$$

Again, ϑ constitutes a Gaussian-distributed random variable given in (5). Moreover, due to external (e.g. thermal background) and internal (e.g. noisy propelling mechanism) noise, *cluster particles* evaporate to become *single particles*. In analogy to the self-diffusion of *single particles*, we thus introduce a rate[4] ϵ characterizing the following evaporation process:

$$C(\theta) \xrightarrow{\epsilon} S(\theta' = \theta + \vartheta_0). \tag{8}$$

[4] As has been pointed out in [37], this rate may depend on particle shape.

Also in this case, the strength of the angular changes is Gaussian distributed according to (2), and for simplicity we use the same standard deviation σ_0 as for the *single particles*' persistent random walk. As discussed above, *cluster particles* are strongly caged due to their close proximity to neighboring, collinearly moving particles. Reorientations of *cluster particles* due to noise are therefore strongly counteracted by realigning particle collisions, rendering *cluster particles* considerably less susceptible to random fluctuations than *single particles*. Hence, we assume

$$\epsilon \ll \lambda, \tag{9}$$

which is consistent with the observations in agent-based simulations slightly below the ordering transition [31], finding coherently moving clusters in an unpolarized background of randomly moving particles. In this regime individual particles exhibit superdiffusive behavior, performing quasi-ballistic 'flights' as long as they are part of a cluster, and conventional particle diffusion if they are not.

2.2. Constitutive equations

Building on the modeling framework defined above, we now set up a kinetic description for the *canonical* model. We denote by $s(\theta, \mathbf{x}, t)$ and $c(\theta, \mathbf{x}, t)$ the one-particle distribution functions within the class of *single particles* and *cluster particles*, respectively, i.e. $s(\theta, \mathbf{x}, t)\,\mathrm{d}\theta\,\mathrm{d}^2x$ gives the number of *single particles* located in an infinitesimal region $[\mathbf{x}, \mathbf{x}+\mathrm{d}\mathbf{x}]$ with orientations in the interval $[\theta, \theta+\mathrm{d}\theta]$ (and likewise for $c(\theta, \mathbf{x}, t)\,\mathrm{d}\theta\,\mathrm{d}^2x$). Both one-particle distribution functions are subject to convection due to the propelling velocity $\mathbf{v}$ of each particle. Moreover, local fluctuations in the one-particle distribution functions due to self-diffusion and collision events are to be accounted for. We thus arrive at the following set of Boltzmann-like equations for the *canonical* model:

$$\partial_t s(\theta, \mathbf{x}, t) + \mathbf{v}\cdot\nabla s(\theta, \mathbf{x}, t) = \dot{s}(\theta, \mathbf{x}, t), \tag{10a}$$

$$\partial_t c(\theta, \mathbf{x}, t) + \mathbf{v}\cdot\nabla c(\theta, \mathbf{x}, t) = \dot{c}(\theta, \mathbf{x}, t), \tag{10b}$$

where the source terms $\dot{s}(\theta, \mathbf{x}, t)$ and $\dot{c}(\theta, \mathbf{x}, t)$ read

$$\dot{s} = \lambda\left[\mathcal{D}_s^{(+)}(\theta) - \mathcal{D}_s^{(-)}(\theta)\right] + \epsilon\mathcal{D}_c^{(+)}(\theta) - \mathcal{C}_s^{(-)}(\theta) - \mathcal{A}[s, c; \theta], \tag{11a}$$

$$\dot{c} = -\epsilon\mathcal{D}_c^{(-)}(\theta) + \mathcal{C}_s^{(+)}(\theta) + \mathcal{C}_c^{(+)}(\theta) + \mathcal{A}[c, s; \theta] - \mathcal{C}_c^{(-)}(\theta). \tag{11b}$$

They give the net number of *single particles* and *cluster particles* entering the phase space region $\mathrm{d}\omega = [\mathbf{x}, \mathbf{x}+\mathrm{d}\mathbf{x}] \times [\theta, \theta+\mathrm{d}\theta]$ per unit time and unit area, respectively. The various terms correspond to gain (superscript $^{(+)}$) and loss (superscript $^{(-)}$) of particles by the following processes.

1. *Self-diffusion and evaporation*. In these cases the source terms are products of the corresponding rates and probability densities, with

$$\mathcal{D}_f^{(-)}(\theta) = f(\theta) \tag{12}$$

denoting the probability density for a particular species f to have a certain angle θ, and

$$\mathcal{D}_f^{(+)}(\theta) = \langle f(\theta - \vartheta_0)\rangle_0 \tag{13}$$

denoting the transition probability from $\theta' = \theta - \vartheta_0$ to θ averaged over all ϑ_0 with respect to the Gaussian weight (2). Note that, here and in the following, the argument of f is understood modulo 2π.

2. *Collisions within the same class of particles*. The collision integrals, representing the processes defined in equations (3) and (7), are given by standard expressions [16–18, 22]

$$\mathcal{C}_f^{(+)}(\theta) = \left\langle \int \mathrm{d}\mathcal{I}\, f(\theta')\, f(\theta'')\, \delta(\bar{\theta}(\theta', \theta'') + \vartheta - \theta) \right\rangle, \tag{14a}$$

$$\mathcal{C}_f^{(-)}(\theta) = \int \mathrm{d}\mathcal{I}\, f(\theta')\, f(\theta'')\delta(\theta' - \theta). \tag{14b}$$

Here $\langle \ldots \rangle$ denotes an average over $\vartheta \in (-\infty, \infty)$ with respect to the Gaussian weight (5) and the average angle $\bar{\theta}$ is given in equation (4). The integral measure

$$\int \mathrm{d}\mathcal{I}\,(\ldots) \equiv \int_{-\pi}^{\pi} \mathrm{d}\theta' \int_{\theta'-\pi}^{\theta'+\pi} \mathrm{d}\theta''\, \Gamma(L, d, |\theta' - \theta''|)\,(\ldots) \tag{15}$$

contains the *differential scattering cross section*

$$\Gamma(L, d, |\theta' - \theta''|) = 4\, \mathrm{d}v \left| \sin\left(\frac{\theta' - \theta''}{2}\right) \right| \left[1 + \frac{(L/d) - 1}{2} \left| \sin(\theta' - \theta'') \right| \right] \tag{16}$$

characterizing the frequency of collisions (i.e. hard-core interactions) between rod-like particles. The scattering function Γ itself carries all information concerning the shape of the particles and is a function of the relative orientation of the colliding particles. Reminiscent of the Boltzmann scattering cylinder, Γ can be derived on the basis of purely geometric considerations assuming that all spatial coordinates within the cylinder are equally probable; for details see appendix A.

3. *Assembly events of a single particle joining a cluster*. These events, represented by (6), occur through binary collisions between *single particles* and *cluster particles* and are thus represented by an analogous integral expression:

$$\mathcal{A}[f, g; \theta] = \int \mathrm{d}\mathcal{I}\, f(\theta')g(\theta'')\delta(\theta' - \theta). \tag{17}$$

3. Derivation of hydrodynamic equations

In order to reduce our kinetic description to a set of hydrodynamic equations valid on large length and time scales, we follow the well-established procedure of Aranson and Tsimring [16] and Bertin *et al* [17, 22], and analyze the angular dependence of equations (10*a*) and (10*b*) in Fourier space. Due to the 2π-periodicity in θ, the one-particle distribution functions can be expanded in Fourier series

$$s(\theta, \mathbf{x}, t) = \frac{1}{2\pi} \sum_{n=-\infty}^{\infty} s_n(\mathbf{x}, t) \mathrm{e}^{-\mathrm{i}n\theta}, \tag{18a}$$

$$c(\theta, \mathbf{x}, t) = \frac{1}{2\pi} \sum_{n=-\infty}^{\infty} c_n(\mathbf{x}, t) \mathrm{e}^{-\mathrm{i}n\theta}, \tag{18b}$$

where

$$s_n(\mathbf{x}, t) = \int_{-\pi}^{\pi} \mathrm{d}\theta\, \mathrm{e}^{\mathrm{i}n\theta} s(\theta, \mathbf{x}, t), \tag{19a}$$

$$c_n(\mathbf{x},t) = \int_{-\pi}^{\pi} \mathrm{d}\theta\, \mathrm{e}^{\mathrm{i}n\theta} c(\theta,\mathbf{x},t). \tag{19b}$$

Upon identifying $\mathbb{R}^2 \leftrightarrow \mathbb{C}$, e.g. $\mathbf{v} \leftrightarrow v\,\mathrm{e}^{\mathrm{i}\theta}$ ($v = |\mathbf{v}|$), the zeroth and first Fourier modes are directly connected to the hydrodynamic densities ρ_s (*single particle* density) and ρ_c (*cluster particle* density), and the corresponding current densities $\mathbf{g}_s$ and $\mathbf{g}_c$, i.e.

$$\rho_s(\mathbf{x},t) = s_0(\mathbf{x},t), \tag{20a}$$

$$\rho_c(\mathbf{x},t) = c_0(\mathbf{x},t), \tag{20b}$$

$$\mathbf{g}_s(\mathbf{x},t) \equiv \rho_s(\mathbf{x},t)\,\mathbf{u}_s(\mathbf{x},t) = v\,s_1(\mathbf{x},t), \tag{20c}$$

$$\mathbf{g}_c(\mathbf{x},t) \equiv \rho_c(\mathbf{x},t)\,\mathbf{u}_c(\mathbf{x},t) = v\,c_1(\mathbf{x},t). \tag{20d}$$

In equations (20*c*) and (20*d*), the '=' signs indicate identification of vectors and complex numbers. The quantities $\mathbf{u}_{s/c}$ denote the velocities of the macroscopic flow fields established by *single particles* and *cluster particles*, respectively. Also note that the second Fourier components are proportional to the nematic order parameter within the respective class of particles (as reflected by the symmetry of $\mathrm{e}^{\mathrm{i}2\theta}$ under $\theta \to \theta + \pi$). Using equations (18*a*) and (18*b*), the Boltzmann-like equations (10*a*) and (10*b*) transform to

$$\partial_t s_k + \frac{v}{2}[\partial_x\,(s_{k+1} + s_{k-1}) - \mathrm{i}\partial_y\,(s_{k+1} - s_{k-1})]$$
$$= -\lambda s_k + \mathrm{e}^{-(k\sigma_0)^2/2}\,(\lambda s_k + \epsilon c_k) - \sum_{n=-\infty}^{\infty} I_{n,0}\,(s_n + c_n)\,s_{k-n}, \tag{21a}$$

$$\partial_t c_k + \frac{v}{2}[\partial_x\,(c_{k+1} + c_{k-1}) - \mathrm{i}\partial_y\,(c_{k+1} - c_{k-1})]$$
$$= -\epsilon c_k + \sum_{n=-\infty}^{\infty} [I_{n,0}(s_n c_{k-n} - c_n c_{k-n}) + \mathrm{e}^{-(k\sigma)^2/2} I_{n,k}\,(s_n s_{k-n} + c_n c_{k-n})], \tag{21b}$$

where the collision integrals $I_{n,k}$ are defined as follows:

$$I_{n,k} = \frac{1}{2\pi}\int_{-\pi}^{\pi} \mathrm{d}\phi\,\Gamma(L,d,|\phi|)\cos\left[\left(n - \frac{k}{2}\right)\phi\right]. \tag{22}$$

Note, in particular, that $I_{0,0}$ gives the *total scattering cross section*.

3.1. Truncation scheme

Equations (21*a*) and (21*a*) constitute an infinite set of coupled equations in Fourier space, which are fully equivalent to the Boltzmann-like equations (10a) and (10*b*). To derive a closed set of hydrodynamic equations, we need to consider some additional assumptions, allowing us to truncate this infinite Fourier space representation.

Here, our focus will be on virtually isotropic systems in the vicinity of an ordering transition breaking rotational symmetry. In this case, deviations of the one-particle distribution functions from the constant distribution $\sim 1/2\pi$ are small and contributions from large wavenumbers in the Fourier series (21*a*) and (21*a*) are negligible. We further consider sufficiently dilute systems, in which the number of (binary) particle collisions per unit time and area [$\sim (\rho_c + \rho_s)^2\, I_{0,0}$] is much smaller than the corresponding number of *single particle*

Table 1. Summary of relevant collision integrals $I_{n,k}$ as a function of the aspect ratio $\xi = L/d$, where L and d denote particle length and diameter, and where v is the particle velocity. The quantities $I_{n,k}/I_{0,0}$ depend only weakly on the aspect ratio ξ. In particular, the signs of $I_{n,k}/I_{0,0}$ do not change with ξ, leaving all our present conclusions made on the basis of the kinetic coefficients qualitatively unchanged.

Integral	$I_{0,0}$	$I_{1,0}/I_{0,0}$	$I_{1,1}/I_{0,0}$	$I_{2,0}/I_{0,0}$	$I_{2,1}/I_{0,0}$
Value	$\frac{8\,dv(2+\xi)}{3\pi}$	$-\frac{4+\xi}{5(2+\xi)}$	$\frac{3}{16}\frac{8+\pi(\xi-1)}{2+\xi}$	$\frac{6-13\xi}{35(2+\xi)}$	$\frac{3}{16}\frac{\pi(1-\xi)-8}{2+\xi}$

diffusion events [$\sim \lambda\,\rho_s$]. Together with $\epsilon \ll \lambda$ (equation (9)), stating that disassembly from a cluster is strongly hindered by particle caging, allows us to treat *single particle* diffusion as a fast process. The *single particle* phase thus acts as an isotropic sea of particles where particle orientations (but not necessarily particle densities) are equilibrated, and hence the net hydrodynamic flow vanishes ($\mathbf{u}_s = 0$). Finally, from a dimensional analysis of equations (19*a*) and (19*b*), together with (20*c*) and (20*d*), one finds $c_k/\rho_c \sim \mathcal{O}(|\mathbf{u}_c|^k/v^k)$. Near the onset of order, where $|\mathbf{u}_c|/v \ll 1$, we only consider the density (c_0) and polarity (c_1) of *cluster particles*, and use the stationary equation for c_2 as a closure relation, neglecting all contributions from higher order coefficients.

In summary, we resort to the following truncation scheme, leading to a set of hydrodynamic equations, valid near the onset of the ordering transition:

$$s_k = 0, \quad \forall |k| > 0, \tag{23a}$$

$$c_k = 0, \quad \forall |k| > 2. \tag{23b}$$

3.2. Derivation of the hydrodynamic equations

With the above truncation scheme, (21*a*) and (21*b*) reduce to

$$\partial_t s_0 = \epsilon c_0 - I_{0,0}\left(s_0^2 + s_0 c_0\right), \tag{24a}$$

$$\partial_t c_0 = -v\left[\partial_x \Re(c_1) + \partial_y \Im(c_1)\right] - \partial_t s_0, \tag{24b}$$

$$\begin{aligned}\partial_t c_1 = -\frac{v}{2}[\partial_x(c_2 + c_0) - \mathrm{i}\partial_y(c_2 - c_0)] + [(2\,\mathrm{e}^{-\sigma^2/2} I_{1,1} - I_{1,0} - I_{0,0})c_0 - \epsilon + I_{0,0} s_0]c_1 \\ + [2\,\mathrm{e}^{-\sigma^2/2} I_{2,1} - I_{1,0} - I_{2,0}]c_1^* c_2,\end{aligned} \tag{24c}$$

$$\begin{aligned}\partial_t c_2 = -\frac{v}{2}[\partial_x + \mathrm{i}\partial_y]c_1 + [(2\,\mathrm{e}^{-2\sigma^2} I_{1,0} - I_{2,0} - I_{0,0})c_0 - \epsilon + I_{0,0} s_0]c_2 \\ + [\mathrm{e}^{-2\sigma^2} I_{0,0} - I_{1,0}]c_1 c_1,\end{aligned} \tag{24d}$$

where we used $f_{-k} = f_k^*$, since $f(\theta) \in \mathbb{R}$ ($f \in \{s, c\}$), and where $\Re(a)$ ($\Im(a)$) denotes the real (imaginary) part of a. Moreover, as can be seen from the definition in (22), the collision integrals $I_{n,k}$ only depend on the value $|n - k/2|$, whence only five of the collision integrals appearing in the above equations are independent. These integrals as a function of the particle's aspect ratio are evaluated and summarized in table 1. Also note that the entire set of equations (24*a*)–(24*d*) is

independent of the fast *single particle* diffusion time scale λ^{-1} (and, hence, also of the diffusion noise parameter σ_0). In our present approach, λ has only a conceptual meaning in maintaining a well-mixed particle bath within the class of *single particles*.

For given particle densities, the time scales governing the dynamics of the polar and nematic order parameter fields, represented by c_1 and c_2, are given by the linear coefficients in the second line of (24*c*) and (24*d*), respectively. As will be detailed in section 4.2, the onset of collective motion is hallmarked by a change in sign of the linear coefficient in (24*c*), implying a diverging time scale for the dynamics of the polarity field. On the other hand, the time scale for c_2 is finite for all densities, which implies that the relaxation of the nematic order parameter field is fast compared to the polarity field. This allows us to set $\partial_t c_2 \approx 0$ in (24*d*).

In the following, it will be convenient to write down equations in dimensionless form. To this end, we construct the following characteristic scales: time and space will be measured in units of the cluster evaporation time and length scale

$$\hat{\tau}_\mathrm{e} = \epsilon^{-1} \quad \text{and} \quad \hat{\ell}_\mathrm{e} = v/\epsilon. \tag{25}$$

From the cluster evaporation time scale $\hat{\tau}_\mathrm{e}$ and the *total scattering cross section* $I_{0,0}$, we can construct the characteristic density scale

$$\hat{\rho}_b = \frac{1}{I_{0,0}\,\hat{\tau}_\mathrm{e}}. \tag{26}$$

The *single particle* and *cluster particle* phases constantly exchange particles at rates that are determined by cluster evaporation (ϵ) on the one hand (*cluster particles* $\rightarrow$ *single particles*) and cluster nucleation due to particle collisions on the other hand (*single particles* $\rightarrow$*cluster particles*) which occur with a rate $\sim\rho\, I_{0,0}$. Therefore the characteristic density scale $\hat{\rho}_b$ marks the particle density, where both rates balance. In particular, $\rho/\hat{\rho}_b = (\rho_s + \rho_c)/\hat{\rho}_b$ gives the rate of inter-particle collisions relative to cluster evaporation events. Thus, the numerical quantity $\rho/\hat{\rho}_b$ provides a direct measure expressing the competition between the randomizing effects of noise and the order creating effects of particle collisions, hallmarking the onset (and maintenance) of collective motion [29].

We thus arrive at the following rescaling scheme:

$$t \rightarrow t \cdot \hat{\tau}_\mathrm{e}, \tag{27a}$$

$$\mathbf{x} \rightarrow \mathbf{x} \cdot \hat{\ell}_\mathrm{e}, \tag{27b}$$

$$\rho_{s/c} \rightarrow \rho_{s/c} \cdot \hat{\rho}_b, \tag{27c}$$

$$\mathbf{g} \rightarrow \mathbf{g} \cdot \hat{\rho}_b\, \frac{\hat{\ell}_\mathrm{e}}{\hat{\tau}_\mathrm{e}}, \tag{27d}$$

$$I_{n,k} \rightarrow I_{n,k} \cdot \frac{1}{\hat{\rho}_b\, \hat{\tau}_\mathrm{e}}, \tag{27e}$$

where the characteristic scales for momentum ($\mathbf{g}$) and scattering cross section ($I_{n,k}$) have been constructed from those of time, space and density. In this rescaling the momentum current density is equal to one if the corresponding fluid element with a characteristic density $\hat{\rho}_b$, for which cluster evaporation and nucleation balance, is convected with the particle velocity v.

Then, upon eliminating c_2 from (24*c*) as discussed above, and using the relations between Fourier modes and hydrodynamic fields (for details see appendix B), (20*a*)–(20*d*),

equations (24*a*)–(24*d*) give rise to the hydrodynamic equations corresponding to the *canonical model*. In rescaled variables they read

$$\partial_t \rho_s = \rho_c - (\rho_s + \rho_c)\,\rho_s, \tag{28a}$$

$$\partial_t \rho_c = -\nabla\cdot\mathbf{g} - \rho_c + (\rho_s + \rho_c)\,\rho_s, \tag{28b}$$

$$\begin{aligned}\partial_t \mathbf{g} = {} & -\nu_1\mathbf{g} - \frac{\mu\kappa}{\nu_2}\mathbf{g}^2\mathbf{g} - \frac{1}{2}\nabla\rho_c + \frac{1}{4\nu_2}\nabla^2\mathbf{g} + \frac{\zeta_+}{\nu_2}(\mathbf{g}\cdot\nabla)\mathbf{g} + \frac{\zeta_-}{\nu_2}[(\nabla\cdot\mathbf{g})\mathbf{g} - \frac{1}{2}\nabla(\mathbf{g}^2)] \\ & + \frac{\mu}{\nu_2^2}[\mathbf{g}(\mathbf{g}\cdot\boldsymbol{\partial}[\rho_c,\rho_s]) - \frac{1}{2}\mathbf{g}^2\boldsymbol{\partial}[\rho_c,\rho_s]] + \frac{1}{4\nu_2^2}[(\nabla\cdot\mathbf{g})\boldsymbol{\partial}[\rho_c,\rho_s] \\ & - (\nabla\mathbf{g} + \nabla\mathbf{g}^t)\boldsymbol{\partial}[\rho_c,\rho_s]],\end{aligned} \tag{28c}$$

where

$$\boldsymbol{\partial}[f,g] = \left(\partial_f \nu_2\right)\nabla f + \left(\partial_g \nu_2\right)\nabla g, \tag{29}$$

and where we have introduced the following abbreviations:

$$\nu_1 = 1 - (\rho_s - \rho_c) + (I_{1,0} - 2e^{-\sigma^2/2} I_{1,1})\rho_c, \tag{30a}$$

$$\nu_2 = 1 - (\rho_s - \rho_c) + (I_{2,0} - 2e^{-2\sigma^2} I_{1,0})\rho_c, \tag{30b}$$

$$\mu = \mathrm{e}^{-2\sigma^2} - I_{1,0}, \tag{30c}$$

$$\kappa = I_{1,0} + I_{2,0} - 2\,\mathrm{e}^{-\sigma^2/2} I_{2,1}, \tag{30d}$$

$$\zeta_\pm = -\mu \pm \frac{\kappa}{2}. \tag{30e}$$

Equations (28*a*)–(28*c*) capture the evolution of our *canonical* model system on a hydrodynamic level. More specifically, (28*a*) and (28*b*) describe the spatio-temporal evolution of the particle densities ρ_s and ρ_c. Since, by the assumptions underlying our model, no macroscopic flow of *single particles* can build up, only the density of *cluster particles* (ρ_c) is subject to convection. This implies that the genuine hydrodynamic momentum field $\mathbf{g} = \mathbf{g}_c + \mathbf{g}_s \equiv \mathbf{g}_c$ is carried solely by the subset of cluster particles. Therefore we omit the subscript c in (28*b*) and (28*c*) and denote $\mathbf{g} \equiv \mathbf{g}_c$. The dynamics of both densities is, moreover, driven by source terms, as determined by the reactions discussed in section 2.1. The gain and loss parts in these source terms of ρ_c and ρ_s are exactly balanced, such that the total density $\rho = \rho_c + \rho_s$ is conserved. As an aside we note that any distinction between *single particles* and *cluster particles* is a purely conceptual matter. Experimentally, only the total density ρ and the momentum field $\mathbf{g}$ are accessible.

Equation (28*c*), governing the evolution of the current density $\mathbf{g}$, can be interpreted as a generalization of the Navier–Stokes equation to active systems. The terms on the right-hand side of (28*c*) can be given by the following interpretation. In the first line, the first two terms account for the local dynamics of $\mathbf{g}$. They play a crucial role in establishing and maintaining a state of macroscopic flow, as will be detailed below. The Navier–Stokes equation itself, which conserves momentum, is devoid of these terms. In formal analogy to the Navier–Stokes equation, the density gradient in the first line together with the last term in the second line can be interpreted as a pressure gradient. This effective pressure is given by $\frac{1}{2}(\rho_c + \frac{\zeta_-}{\nu_2}\mathbf{g}^2)$, when neglecting the

density dependence of ν_2. The last term in the first line is analogous to the shear stress term in the Navier–Stokes equation, with a kinematic viscosity $\sim \nu_2^{-1}$. The second line in (28*c*) is a generalization of the convection term to systems not obeying Galilean invariance, where all combinations of ∇ and factors second order in $\mathbf{g}$ transforming as vectors are allowed [41]. Finally, the last two lines describe couplings of the current density $\mathbf{g}$ and gradients thereof to density gradients. Note that the density gradients in these coupling terms are all of the same generic structure (29).

As already noted, the *canonical* model equations (28*a*)–(28*c*) conserve the total number of particles. To make this explicit, we define

$$\rho \equiv \rho_c + \rho_s, \tag{31a}$$

$$\eta \equiv \rho_c - \rho_s, \tag{31b}$$

where ρ denotes the overall particle density and η measures the density difference between the two particle classes. The *canonical* model equations then attain the following form:

$$\partial_t \rho = -\nabla \cdot \mathbf{g}, \tag{32a}$$

$$\partial_t \eta = -\nabla \cdot \mathbf{g} + \rho^2 - (\rho + 1)\eta - \rho, \tag{32b}$$

$$\begin{aligned}\partial_t \mathbf{g} = &-\nu_1 \mathbf{g} - \frac{\mu\kappa}{\nu_2}\mathbf{g}^2\mathbf{g} - \frac{1}{4}\nabla(\rho+\eta) + \frac{1}{4\nu_2}\nabla^2\mathbf{g} + \frac{\zeta_+}{\nu_2}(\mathbf{g}\cdot\nabla)\mathbf{g} + \frac{\zeta_-}{\nu_2}\left[(\nabla\cdot\mathbf{g})\mathbf{g} - \frac{1}{2}\nabla\left(\mathbf{g}^2\right)\right] \\ &+ \frac{\mu}{\nu_2^2}\left[\mathbf{g}(\mathbf{g}\cdot\boldsymbol{\partial}[\rho,\eta]) - \frac{1}{2}\mathbf{g}^2\boldsymbol{\partial}[\rho,\eta]\right] + \frac{1}{4\nu_2^2}[(\nabla\cdot\mathbf{g})\boldsymbol{\partial}[\rho,\eta] - (\nabla\mathbf{g} + \nabla\mathbf{g}^t)\boldsymbol{\partial}[\rho,\eta]].\end{aligned} \tag{32c}$$

The equation governing ρ expresses the overall conservation of particle number, whereas the source terms of equations (28*a*) and (28*b*) combine to determine the local dynamics of the relative density η in (32*b*).

Now we turn to the *grand canonical* model, where the *single particle* phase is coupled to a particle reservoir, resulting in a situation where *single particles* constitute an isotropic sea of particles that is maintained at a constant density ρ_s^0. Particle number conservation is now violated, and the only non-trivial density dynamics takes place within the phase of *cluster particles*. The hydrodynamic equations corresponding to the *grand canonical* model can be obtained immediately by setting in (28*a*)–(28*c*) the density of *single particles* to a constant value, yielding

$$\rho_s = \rho_s^0 = \text{const.}, \tag{33a}$$

$$\partial_t \rho_c = -\nabla \cdot \mathbf{g} - \rho_c + \left(\rho_s^0 + \rho_c\right)\rho_s^0, \tag{33b}$$

$$\begin{aligned}\partial_t \mathbf{g} = &-\nu_1 \mathbf{g} - \frac{\mu\kappa}{\nu_2}\mathbf{g}^2\mathbf{g} - \frac{1}{2}\nabla\rho_c + \frac{1}{4\nu_2}\nabla^2\mathbf{g} + \frac{\zeta_+}{\nu_2}(\mathbf{g}\cdot\nabla)\mathbf{g} + \frac{\zeta_-}{\nu_2}\left[(\nabla\cdot\mathbf{g})\mathbf{g} - \frac{1}{2}\nabla\left(\mathbf{g}^2\right)\right] \\ &+ \frac{\mu\partial_{\rho_c}\nu_2}{\nu_2^2}\left[\mathbf{g}(\mathbf{g}\cdot\nabla\rho_c) - \frac{1}{2}\mathbf{g}^2\nabla\rho_c\right] + \frac{\partial_{\rho_c}\nu_2}{4\nu_2^2}[(\nabla\cdot\mathbf{g})\nabla\rho_c - (\nabla\mathbf{g} + \nabla\mathbf{g}^t)\nabla\rho_c].\end{aligned} \tag{33c}$$

One final remark is in order. The rescaling scheme introduced in equations (27*a*)–(27*e*) renders both the *canonical* and *grand canonical* model equations virtually independent of particle shape.

While these equations exhibit a weak dependence on the particles' aspect ratio L/d (via the rescaled collision integrals $I_{n,k}$), this dependence introduces only minor quantitative effects, which are negligible for all present purposes. To a good approximation we can thus set $L/d = 1$ while working with dimensionless variables, and assess the effects entailed by particle shape by restoring original units. Within our present approach, the effects of particle shape are purely quantitative, causing a numerical shift in the characteristic scales, but leaving the qualitative features of the problem unaffected. Deep within the ordered phase, i.e. for large densities, we indeed find a qualitative change of the ensuing hydrodynamic instability, as detailed in section 5. Nevertheless, this statement has to be taken with a grain of salt because corresponding threshold densities are far beyond the validity of the hydrodynamic equations.

4. Spatially homogeneous systems

To investigate the implications of the hydrodynamic equations, we start with the simplest case by analyzing spatially homogeneous solutions. These considerations will provide the basis for the study of spatially inhomogeneous systems, which will be the subject of section 5. Dropping all gradients, the hydrodynamic equations for spatially homogeneous systems for the *canonical* model read

$$\partial_t \rho = 0, \tag{34a}$$

$$\partial_t \eta = \rho^2 - (\rho + 1)\eta - \rho, \tag{34b}$$

$$\partial_t \mathbf{g} = -\nu_1 \mathbf{g} - \frac{\mu\kappa}{\nu_2}\mathbf{g}^2\mathbf{g}. \tag{34c}$$

For the *grand canonical* model we obtain

$$\partial_t \rho_c = -\rho_c + \left(\rho_s^0 + \rho_c\right)\rho_s^0, \tag{35a}$$

$$\partial_t \mathbf{g} = -\nu_1 \mathbf{g} - \frac{\mu\kappa}{\nu_2}\mathbf{g}^2\mathbf{g}. \tag{35b}$$

In both cases, the density dynamics decouples from the momentum current dynamics and can be addressed separately.

In this section, our focus is on the stationary properties of the *canonical* and *grand canonical* models, respectively. While the dynamical approach to the stationary state is model dependent, the system's composition in terms of *single particles* and *cluster particles*, for given total density ρ, in the limit $t \to \infty$ is identical in both cases (refer to (28*a*)–(28*b*) and (33*a*)–(33*b*)). Since, moreover, the momentum current densities $\mathbf{g}$ obey identical dynamical equations, the ensuing analysis of the stationary state is equal for both models.

4.1. Crossover to clustering

To assess the density difference between the *cluster particle* and the *single particle* phase η, we calculate the dynamical fixed point η^* of (34*b*), attracting the dynamics of $\eta(t)$ in the long time limit $t \to \infty$:

$$\eta^*(\rho) = \frac{\rho^2 - \rho}{\rho + 1}. \tag{36}$$

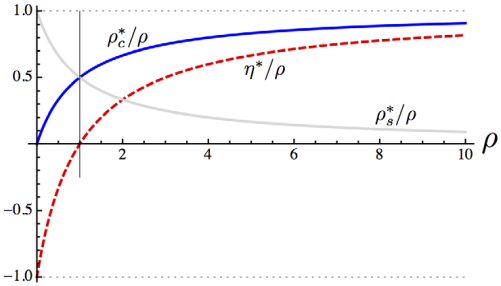

Figure 3. Fixed points of the homogeneous equations for the *grand canonical* and *canonical* models: the stationary relative density η^*/ρ, as well as the stationary cluster and single particle density, ρ_c^*/ρ and ρ_s^*/ρ, respectively. The larger the ρ, the more the cluster particles existing in the system. The vertical line corresponds to the density $\bar{\rho}$ above which the number of *cluster particles* exceeds the number of *single particles*. Note that $\rho_s < 1$ holds for all finite values of the total particle density ρ. (This is of particular relevance in the context of the *grand canonical* model, where ρ_s can be considered as a control parameter.)

The defining equations (31*a*)–(31*b*) can be used to determine the corresponding (stationary) fixed point densities of *single particles* (ρ_s^*) and *cluster particles* (ρ_c^*) as a function of the total density ρ. Figure 3 summarizes these findings. Upon increasing the total density ρ, the ratio η^*/ρ continuously grows from $\eta^*/\rho = -1$ at $\rho = 0$, asymptotically approaching $\eta^*/\rho = 1$ as $\rho \to \infty$. Based on the sign of η^*, two density regimes can be distinguished. In the low-density regime ($\rho \ll 1$, $\eta^* < 0$), particle collisions, underlying the formation of clusters, occur at much smaller rates than cluster evaporation events. Only a small fraction of all particles organize themselves in clusters, leading to a relatively dense population of *single particles* and a correspondingly small density of *cluster particles*. In the high-density regime ($\rho \gg 1$, $\eta^* > 0$), the situation is reversed: large overall densities imply frequent particle collisions and, consequently, cluster formation and cluster growth dominate over cluster evaporation. In this regime, the number of *cluster particles* exceeds the number of *single particles*.

The crossover between the *single particle* dominated low-density regime and the *cluster particle* dominated high-density regime occurs at the crossover density $\bar{\rho} = \hat{\rho}_b = 1$, where both the *single particle* and the *cluster particle* populations are of equal size (i.e. $\eta^*(\bar{\rho}) = 0$). The relation between the crossover density to clustering, and the geometrical shape of the constituent particles has been addressed previously in [37], based on agent-based simulations and a mean-field-type analytical analysis. Using our definition of the crossover density $\bar{\rho}$, we can establish the corresponding relation simply by restoring original units (equation (26)). Using packing fraction $\bar{p} \simeq \bar{\rho}\, Ld$ instead of particle density, and assuming for the sake of simplicity $L/d \gg 1$, which allows us to estimate the particle surface $A_0 \simeq Ld$, we find that

$$\bar{p} \simeq \frac{\epsilon\, Ld}{I_{0,0}} = \frac{3\pi}{8v}\frac{\epsilon L}{2 + L/d}, \tag{37}$$

which correctly reproduces the findings of [37] (taking into account that the cluster evaporation rate is assumed to be proportional to the inverse particle length, $\epsilon \propto L^{-1}$). For the sake of completeness, we note that the definition of the clustering crossover density in [37] is based on the cluster size distribution, and thus does not necessarily coincide with our definition. We stress, however, that in our description the scaling structure in equation (37) is completely generic. It is an immediate consequence of the characteristic scales of our model and of the fact that the rescaled hydrodynamic model equations are (virtually) independent of particle shape. The structure of equation (37) is thus robust under an arbitrary redefinition of the (rescaled) crossover density $\bar{\rho}$.

4.2. Homogeneous equations for momentum current density

Having examined the composition of the system in terms of *single particle* and *cluster particle* densities, we now turn to a discussion of the spatially homogeneous solutions for the momentum current density $\mathbf{g}$. Due to rotational invariance of (34*c*), only the magnitude $g = |\mathbf{g}|$ of the momentum current density, but not its direction, evolves in time. We can thus concentrate on the scalar equation

$$\partial_t g = -\nu_1\, g - \frac{\mu\kappa}{\nu_2}\, g^3, \tag{38}$$

which leads to the following fixed points g^* as the attractor of the dynamics of g in the limit of long times:

$$g^* = \begin{cases} 0 & \text{for } \nu_1 > 0, \\ g_0 = \sqrt{-\frac{\nu_1\nu_2}{\mu\kappa}} & \text{for } \nu_1 < 0. \end{cases} \tag{39}$$

It can be shown that the coefficient in front of the cubic term in (38) is indeed strictly positive for all control parameters of density ρ and noise σ consistent with $\nu_1 < 0$, ensuring the existence of the non-trivial fixed point in the second line of (39).

Depending on the sign of the linear coefficient ν_1, two parameter regimes can thus be distinguished. Parameters leading to $\nu_1 > 0$ render stable an overall homogeneous and isotropic state with vanishing macroscopic flow $\mathbf{g} = 0$. Upon crossing the *phase boundary*

$$\nu_1(\rho, \sigma) = 0 \tag{40}$$

in parameter space, the isotropic solution gets unstable and a macroscopic current density of non-zero amplitude builds up. In equation (40) we used the fact that the density difference η, in the stationary limit, is a function of the total density ρ; cf equation (36). Hence, in the limit of long times, ν_1 is a function of the total density ρ and the noise parameter σ, only.

Using the definition of the coefficient ν_1, equation (30*a*), we can readily calculate the shape of the phase boundary in the $\sigma\rho$-plane:

$$\sigma_c(\rho) = \sqrt{-2\,\ln\left(\frac{2}{3} + \rho^{-2}\right)} \quad (\rho \geqslant \sqrt{3}), \tag{41}$$

where we used $I_{1,0} = -\frac{1}{3}$ and $I_{1,1} = \frac{1}{2}$. The corresponding phase diagram is shown in figure 4.

To conclude this section, we note that the analysis of spatially homogeneous systems corroborates the general physical picture of active systems, which was alluded to in the introduction (e.g. cf [31]). Even in the absence of noise, $\sigma = 0$, for which the threshold

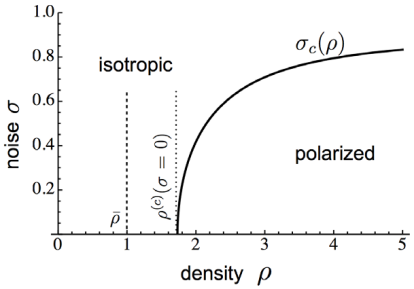

Figure 4. Phase diagram given by the homogeneous equations for the *canonical* and *grand canonical* models. For noise values smaller than the critical value, $\sigma < \sigma_c$, the isotropic state becomes unstable, giving rise to a state of collective motion of non-zero macroscopic momentum current. For $\sigma > \sigma_c$ the isotropic state ($g_0 = 0$) represents a stable solution. The vertical dotted line indicates the transition density $\rho^{(c)}$ at zero collision noise $\sigma = 0$, and the vertical dashed line corresponds to the crossover density $\bar{\rho}$, above which the number of *cluster particles* exceeds the number of *single particles*.

density $\rho^{(c)}$ is lowest, the fully isotropic state $\mathbf{g} = 0$ remains stable up to a critical density $\rho^{(c)}(\sigma = 0) = \sqrt{3}\,\bar{\rho}$, which lies well beyond the density $\bar{\rho}$ indicating the crossover to clustering. We thus extract the following physical picture; cf figure 4. For low densities, $\rho < \bar{\rho}$, cluster evaporation dominates over cluster assembly via particle collisions and clusters form only transiently. The system most closely resembles a structureless, isotropic 'sea of particles'. At intermediate densities, $\bar{\rho} < \rho < \rho^{(c)}$, particle collisions are more frequent. The emergence of clusters is now a virtually persistent phenomenon, with cluster evaporation occurring at a lower rate than cluster formation and growth. Yet, the collision rates between clusters (i.e. collisions among *cluster particles*) are still too low to orchestrate macroscopic order, leading to an overall isotropic 'sea of clusters'. Finally, for large densities, $\rho > \rho^{(c)}$, the frequency of collisions among clusters is high enough to establish collective motion even on macroscopic scales.

5. Stability of inhomogeneous hydrodynamic equations

From our discussions hitherto, we have ascertained that the isotropic, homogeneous state ($\rho = \text{const.}$ and $\mathbf{g} = 0$) becomes unstable for sufficiently large densities. Yet, from a purely homogeneous analysis we cannot say anything about the spatial structure of such a macroscopic broken-symmetry state. Nor can we be sure that the isotropic and homogeneous solution for $\rho < \rho^c(\sigma)$ is indeed stable with respect to spatially inhomogeneous perturbations. In this section, we therefore test the linear stability of the homogeneous isotropic and non-isotropic base states with respect to wave-like perturbations of arbitrary wavenumber. Unlike the homogeneous model equations, the full hydrodynamic model equations are different for both the *canonical* and *grand canonical* models, implying different dispersion relations describing the growth of such wave-like perturbations. We will thus analyze both models separately, and show that particle conservation does indeed influence pattern formation in essential respects.

5.1. Linearization about stationary, spatially homogeneous base states

We start by linearizing the hydrodynamic equations for the *canonical* model. In the *canonical* model, the total number of particles is conserved, and the appropriate base state reads (cf section 4)

$$\rho = \rho_{\mathrm{h}} = \text{const.}, \tag{42a}$$

$$\eta = \eta^*(\rho_{\mathrm{h}}) = \frac{\rho_{\mathrm{h}}^2 - \rho_{\mathrm{h}}}{\rho_{\mathrm{h}} + 1}, \tag{42b}$$

$$\mathbf{g} = \mathbf{g}_{\mathrm{h}} \in \left\{ 0,\ g_0 = \sqrt{-\frac{\nu_1}{\mu\kappa}\nu_2} \right\} \hat{\mathbf{e}}_g, \tag{42c}$$

where $\hat{\mathbf{e}}_g$ denotes the unit vector in the direction of the homogeneous polarization, and where all fields of the base states are assumed to be constant in both space and time. We are going to investigate the linear stability of the solutions (42*a*)–(42*c*) against wave-like perturbations, employing the following ansatz:

$$\rho(\mathbf{x}, t) = \rho_h + \delta\rho(\mathbf{x}, t), \tag{43a}$$

$$\eta(\mathbf{x}, t) = \eta^* + \delta\eta(\mathbf{x}, t), \tag{43b}$$

$$\mathbf{g}(\mathbf{x}, t) = \mathbf{g}_{\mathrm{h}} + \delta\mathbf{g}(\mathbf{x}, t), \tag{43c}$$

where the perturbations are plane waves

$$\delta\rho(\mathbf{x}, t) = \delta\rho_0\, \mathrm{e}^{st + \mathrm{i}\mathbf{q}\cdot\mathbf{x}}, \tag{44a}$$

$$\delta\eta(\mathbf{x}, t) = \delta\eta_0\, \mathrm{e}^{st + \mathrm{i}\mathbf{q}\cdot\mathbf{x}}, \tag{44b}$$

$$\delta\mathbf{g}(\mathbf{x}, t) = \delta\mathbf{g}_0\, \mathrm{e}^{st + \mathrm{i}\mathbf{q}\cdot\mathbf{x}}. \tag{44c}$$

In the equations above, $\mathbf{q}$ denotes the wave vector and s is the growth rate. Inserting this ansatz into the hydrodynamic equations (32*a*)–(32*c*), we obtain the following eigenvalue problem:

$$s\,\delta\rho_0 = -\mathrm{i}\mathbf{q}\cdot\delta\mathbf{g}_0, \tag{45a}$$

$$s\,\delta\eta_0 = (2\rho_{\mathrm{h}} - \eta^* - 1)\,\delta\rho_0 - (1 + \rho_{\mathrm{h}})\,\delta\eta_0 - \mathrm{i}\mathbf{q}\cdot\delta\mathbf{g}_0, \tag{45b}$$

$$\begin{aligned} s\,\delta\mathbf{g}_0 = {} & \left[\frac{\partial_\rho \nu_2\, \mu}{\nu_2^2} \left(\kappa\, \mathbf{g}_{\mathrm{h}}^2\, \mathbf{g}_{\mathrm{h}} + (\mathbf{g}_{\mathrm{h}}\cdot\mathrm{i}\mathbf{q})\, \mathbf{g}_{\mathrm{h}} - \frac{\mathrm{i}\mathbf{q}}{2}\, \mathbf{g}_{\mathrm{h}}^2 \right) - \partial_\rho \nu_1\, \mathbf{g}_{\mathrm{h}} - \frac{\mathrm{i}\mathbf{q}}{4} \right] \delta\rho \\ & + \left[\frac{\partial_\eta \nu_2\, \mu}{\nu_2^2} \left(\kappa\, \mathbf{g}_{\mathrm{h}}^2\, \mathbf{g}_{\mathrm{h}} + (\mathbf{g}_{\mathrm{h}}\cdot\mathrm{i}\mathbf{q})\, \mathbf{g}_{\mathrm{h}} - \frac{\mathrm{i}\mathbf{q}}{2}\, \mathbf{g}_{\mathrm{h}}^2 \right) - \partial_\eta \nu_1\, \mathbf{g}_{\mathrm{h}} - \frac{\mathrm{i}\mathbf{q}}{4} \right] \delta\eta \\ & + \left[\frac{\zeta_+}{\nu_2}\, (\mathrm{i}\mathbf{q}\cdot\mathbf{g}_{\mathrm{h}}) - \frac{\mathbf{q}^2}{4\nu_2} - \nu_1 - \frac{\mu\kappa}{\nu_2}\mathbf{g}_{\mathrm{h}}^2 \right] \delta\mathbf{g}_0 - \frac{2\mu\kappa}{\nu_2}\mathbf{g}_{\mathrm{h}}\, (\mathbf{g}_{\mathrm{h}}\cdot\delta\mathbf{g}_0) \\ & + \frac{\zeta_-}{\nu_2}[\mathbf{g}_{\mathrm{h}}(\mathrm{i}\mathbf{q}\cdot\delta\mathbf{g}_0) - \mathrm{i}\mathbf{q}\,(\mathbf{g}_{\mathrm{h}}\cdot\delta\mathbf{g}_0)]. \end{aligned} \tag{45c}$$

Unlike the *canonical* model, the *grand canonical* model conserves the number of *single particles*, but not the total number of particles. The appropriate base state in this case reads

$$\rho_s = \text{const.}, \tag{46a}$$

$$\rho_c = \rho_c^*(\rho_s) = \frac{\rho_s^2}{1-\rho_s}, \tag{46b}$$

$$\mathbf{g} = \mathbf{g}_\mathrm{h} \in \left\{0,\ g_0 = \sqrt{-\frac{\nu_1\nu_2}{\mu\kappa}}\right\}\hat{\mathbf{e}}_g. \tag{46c}$$

We investigate the linear stability of these solutions, using a perturbation ansatz analogous to equations (43*a*)–(44*c*):

$$\rho_c(\mathbf{x},t) = \rho_c^* + \delta\rho_c(\mathbf{x},t), \tag{47a}$$

$$\mathbf{g}(\mathbf{x},t) = \mathbf{g}_h + \delta\mathbf{g}(\mathbf{x},t), \tag{47b}$$

with

$$\delta\rho_c(\mathbf{x},t) = \delta\rho_c^0\,\mathrm{e}^{\mathrm{st}+\mathrm{i}\mathbf{q}\cdot\mathbf{x}}, \tag{48a}$$

$$\delta\mathbf{g}(\mathbf{x},t) = \delta\mathbf{g}_0\,\mathrm{e}^{\mathrm{st}+\mathrm{i}\mathbf{q}\cdot\mathbf{x}}. \tag{48b}$$

Inserting this ansatz into equations (33*a*)–(33*c*), we obtain

$$s\,\delta\rho_c^0 = (\rho_s - 1)\,\delta\rho_c^0 - \mathrm{i}\mathbf{q}\cdot\delta\mathbf{g}_0, \tag{49a}$$

$$\begin{aligned} s\,\delta\mathbf{g}_0 = {} & \left[\frac{\partial_{\rho_c}\nu_2\,\mu}{\nu_2^2}\left(\kappa\,\mathbf{g}_\mathrm{h}^2\,\mathbf{g}_\mathrm{h} + (\mathbf{g}_\mathrm{h}\cdot\mathrm{i}\mathbf{q})\,\mathbf{g}_\mathrm{h} - \frac{\mathrm{i}\mathbf{q}}{2}\mathbf{g}_\mathrm{h}^2\right) - \partial_{\rho_c}\nu_1\mathbf{g}_\mathrm{h} - \frac{\mathrm{i}\mathbf{q}}{2}\right]\delta\rho_c^0 \\ & + \left[\frac{\zeta_+}{\nu_2}(\mathrm{i}\mathbf{q}\cdot\mathbf{g}_\mathrm{h}) - \frac{\mathbf{q}^2}{4\nu_2} - \nu_1 - \frac{\mu\kappa}{\nu_2}\mathbf{g}_\mathrm{h}^2\right]\delta\mathbf{g}_0 - \frac{2\mu\kappa}{\nu_2}\mathbf{g}_\mathrm{h}\,(\mathbf{g}_\mathrm{h}\cdot\delta\mathbf{g}_0) \\ & + \frac{\zeta_-}{\nu_2}\Big[\mathbf{g}_\mathrm{h}(\mathrm{i}\mathbf{q}\cdot\delta\mathbf{g}_0) - \mathrm{i}\mathbf{q}\,(\mathbf{g}_\mathrm{h}\cdot\delta\mathbf{g}_0)\Big]. \end{aligned} \tag{49b}$$

5.2. *Stability of the disordered state* $g_0 = 0$

We start by considering the homogeneous and isotropic base states, which was shown to be stable against spatially homogeneous perturbations for $\rho < \rho^{(c)}(\sigma)$; cf section 4.2. To assess the stability of this state with respect to perturbations of arbitrary (non-zero) wave vectors in the *canonical* model, we use the linearized hydrodynamic equations (45*a*)–(45*c*) with $g_h = 0$. The resulting eigenvalue problem is most conveniently expressed in matrix form:

$$s\begin{pmatrix}\delta\rho_0\\ \delta\eta_0\\ \delta g_0\end{pmatrix} = \begin{pmatrix}0 & 0 & -\mathrm{i}q\\ 2\rho_\mathrm{h} - \eta^* - 1 & -(1+\rho_\mathrm{h}) & -\mathrm{i}q\\ -\mathrm{i}q/4 & -\mathrm{i}q/4 & -\nu_1 - q^2/(4\nu_2)\end{pmatrix}\begin{pmatrix}\delta\rho_0\\ \delta\eta_0\\ \delta g_0\end{pmatrix}. \tag{50}$$

The corresponding eigenvalue problem for the *grand canonical* model is found from equations (49*a*)–(49*b*), and attains the following form:

$$s\begin{pmatrix}\delta\rho_c^0\\ \delta g_0\end{pmatrix} = \begin{pmatrix}(\rho_s - 1) & -\mathrm{i}q\\ -\mathrm{i}q/2 & -\nu_1 - q^2/(4\nu_2)\end{pmatrix}\begin{pmatrix}\delta\rho_c^0\\ \delta g_0\end{pmatrix}. \tag{51}$$

For $\mathbf{g}_\mathrm{h} = 0$, (45*c*) or (49*b*), respectively, implies $\mathbf{q} \parallel \delta\mathbf{g}_0$, allowing us to replace the vectors $\mathbf{q}$ and $\delta\mathbf{g}_0$ by their respective magnitudes q and δg_0. We solved both eigenvalue problems numerically for arbitrary wavenumbers $q > 0$ with the results shown in figure 5. Note that in

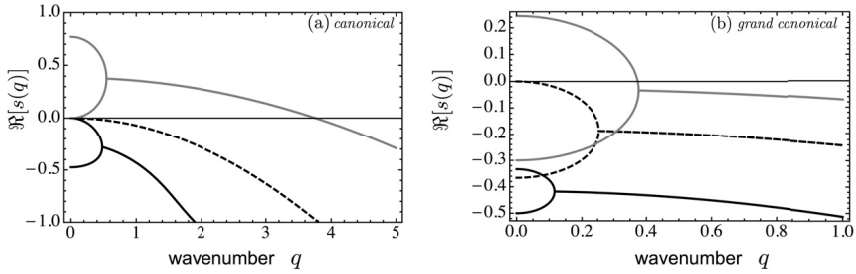

Figure 5. Fastest growth rate of $\Re[s(q)]$ as a function of the wavenumber $q = |\mathbf{q}|$ for the *canonical* (a) and *grand canonical* models (b), each for $\sigma = 0$. The disordered state is stable for all wavenumbers q if $\rho < \rho^{(c)}(\sigma)$. The marginal case, $\rho = \rho^{(c)}(\sigma)$, is dashed. An instability (gray) occurs for densities larger than the corresponding homogeneous critical density $\rho^{(c)}(\sigma)$. Similar behavior is found for $\sigma \neq 0$.

both models the real parts of all eigenvalues are negative for all wavenumbers $q > 0$, provided the particle density $\rho < \rho^{(c)}$. The spatially homogeneous, isotropic state is thus stable against small perturbations with *arbitrary* wave vectors.

For densities $\rho > \rho^{(c)}$, in contrast, a narrow band of positive eigenvalues emerges in both models, located at wavenumbers $q \ll 1$. Equations (50) and (51) evaluated at $q = 0$ return nothing but the linearized versions of the homogeneous hydrodynamic equations, (34*a*)–(34*c*) and (35*a*)–(35*b*). To gain new insights, we will therefore examine the limit $q \to 0$ and consider the eigenvalues of the above coefficient matrices to leading order in the wavenumber q.

In this limit of small wavenumbers, the *grand canonical* coefficient matrix, given in (51), approaches diagonal form and the dynamics of density fluctuations $\delta\rho_c^0$ and momentum current density fluctuations δg_0 practically decouple. Since $\rho_s < 1$ (cf figure 3), the first eigenvalue $s_1^{(\mathrm{GC})} = \rho_s - 1 + \mathcal{O}(q^2)$ is strictly negative and density fluctuations decay exponentially. The second eigenvalue, $s_2^{(\mathrm{GC})} = -\nu_1 + \mathcal{O}(q^2)$, is positive at small wavenumbers, leading to an instability in the momentum current density against long-wavelength fluctuations.

In the case of the *canonical* model (50), the coefficient matrix approaches block diagonal form in the limit of small wavenumbers. Again, the dynamics of momentum current density fluctuations δg_0 practically decouples from density fluctuations ($\delta\rho_0$ and $\delta\eta_0$), with momentum current density fluctuations being amplified by virtue of a positive eigenvalue $s_3^{(\mathrm{C})} = -\nu_1 + \mathcal{O}(q^2)$ at small wavenumbers. In contrast to the *grand canonical* model, however, particle conservation entails a marginally stable mode $s_1^{(C)}(q = 0) = 0$, which turns positive for $q \gtrsim 0$: $s_1^{(C)} \propto q^2$ (the remaining eigenvalue $s_2^{(\mathrm{C})} = -(1 + \rho_\mathrm{h}) + \mathcal{O}(q^2)$ is strictly negative).

To sum up, the study of the linear stability of the homogeneous, isotropic state against spatially inhomogeneous perturbations of arbitrary wave vectors strongly suggests that particle conservation plays a vital role in the context of pattern formation. Both models exhibit spontaneous symmetry breaking by establishing a state of macroscopic collective motion. In the canonical model, in addition, conservation of total particle number entails a marginally stable density mode at $q = 0$ which is absent in the *grand canonical* model. This mode, in turn, gives

rise to a density instability at small, non-zero wavenumbers, accompanying the spontaneous symmetry breaking event for $\rho > \rho^{(c)}$. We note, however, that, at this point of the discussions, the existence of a narrow band of unstable modes at small wavenumbers does not allow for any conclusions concerning the structure of the macroscopic density and momentum current density for $\rho > \rho^{(c)}$. We will address this issue in greater detail in the following section.

5.3. Stability of the broken symmetry state $g_0 > 0$

Both the *canonical* and *grand canonical* models exhibit spontaneous symmetry breaking for overall densities $\rho > \rho^{(c)}(\sigma)$. To shed light on the spatial structure of this broken symmetry state, we start from the most simple case of a spatially homogeneous state of collective motion, and examine its stability with respect to wave-like perturbations in the hydrodynamic particle and momentum current densities. Without loss of generality, we assume that the direction of the macroscopic momentum current density coincides with the x-direction and choose $\mathbf{g}_\mathrm{h} = g_0\,\hat{\mathbf{e}}_x$. The wave vector $\mathbf{q}$ of the perturbation fields is assumed to make an angle ψ with the macroscopic momentum current density $\mathbf{g}_\mathrm{h}$, yielding $\psi = \angle(\mathbf{q}, \mathbf{e}_x)$ and $\mathbf{q} = q\,(\cos(\psi), \sin(\psi))$ with $q = |\mathbf{q}|$.

The linearized *canonical* model equations (45*a*)–(45*c*) then attain the following form:

$$s\,\delta\rho_0 = -\mathrm{i}q\cos(\psi)\delta g_{x,0} - \mathrm{i}q\sin(\psi)\delta g_{y,0}, \tag{52a}$$

$$s\,\delta\eta_0 = (2\rho_\mathrm{h} - \eta^*(\rho_\mathrm{h}) - 1)\,\delta\rho_0 - (1+\rho_0)\,\delta\eta_0 - \mathrm{i}q\cos(\psi)\delta g_{x,0} - \mathrm{i}q\sin(\psi)\delta g_{y,0}, \tag{52b}$$

$$\begin{aligned} s\,\delta g_{x,0} = {} & \left[\frac{1}{2}\mathrm{i}q\cos(\psi)\left(g_0^2\frac{\mu}{\nu_2^2}\partial_\rho\nu_2 - \frac{1}{2}\right) - g_0\left(\partial_\rho\nu_1 - \frac{\mu\kappa}{\nu_2^2}g_0^2\partial_\rho\nu_2\right)\right]\delta\rho_0 \\ & + \left[\frac{1}{2}\mathrm{i}q\cos(\psi)\left(g_0^2\frac{\mu}{\nu_2^2}\partial_\eta\nu_2 - \frac{1}{2}\right) - g_0\left(\partial_\eta\nu_1 - \frac{\mu\kappa}{\nu_2^2}g_0^2\partial_\eta\nu_2\right)\right]\delta\eta_0 \\ & + \left(\mathrm{i}q\cos(\psi)\frac{\zeta_+}{\nu_2}g_0 - \frac{q^2}{4\nu_2} - \frac{2\mu\kappa}{\nu_2}g_0^2\right)\delta g_{x,0} + \mathrm{i}q\frac{\zeta_-}{\nu_2}\sin(\psi)g_0\delta g_{y,0}, \end{aligned} \tag{52c}$$

$$\begin{aligned} s\,\delta g_{y,0} = {} & -\frac{1}{2}\mathrm{i}q\sin(\psi)\left(g_0^2\frac{\mu}{\nu_2^2}\partial_\rho\nu_2 + \frac{1}{2}\right)\delta\rho_0 - \frac{1}{2}\mathrm{i}q\sin(\psi)\left(g_0^2\frac{\mu}{\nu_2^2}\partial_\eta\nu_2 + \frac{1}{2}\right)\delta\eta_0 \\ & - \mathrm{i}q\sin(\psi)\frac{\zeta_-}{\nu_2}\,g_0\,\delta g_{x,0} + \left(\mathrm{i}q\cos(\psi)\frac{\zeta_+}{\nu_2}g_0 - \frac{q^2}{4\nu_2}\right)\delta g_{y,0}. \end{aligned} \tag{52d}$$

The corresponding equations for the *grand canonical* model read

$$s\,\delta\rho_c^0 = (\rho_s - 1)\,\delta\rho_c^0 - \mathrm{i}q\cos(\psi)\delta g_{x,0} - \mathrm{i}q\sin(\psi)\delta g_{y,0}, \tag{53a}$$

$$\begin{aligned} s\,\delta g_{x,0} = {} & \left[\frac{1}{2}\mathrm{i}q\cos(\psi)\left(g_0^2\frac{\mu}{\nu_2^2}\partial_{\rho_c}\nu_2 - 1\right) - g_0\left(\partial_{\rho_c}\nu_1 - \frac{\mu\kappa}{\nu_2^2}g_0^2\partial_{\rho_c}\nu_2\right)\right]\delta\rho_c^0 \\ & + \left(\mathrm{i}q\cos(\psi)\frac{\zeta_+}{\nu_2}g_0 - \frac{q^2}{4\nu_2} - \frac{2\mu\kappa}{\nu_2}g_0^2\right)\delta g_{x,0} + \mathrm{i}q\frac{\zeta_-}{\nu_2}\sin(\psi)g_0\,\delta g_{y,0}, \end{aligned} \tag{53b}$$

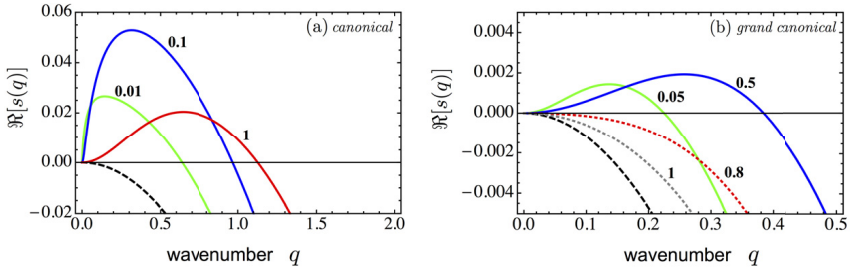

Figure 6. Largest growth rate of $\Re[s(q)]$ as a function of the wavenumber q for $\sigma = 0$ and several values for the total particle density ρ. The marginal $\rho = \rho^{(c)}$ is dashed. Further values are $\rho = \rho^{(c)} + \Delta$ with Δ indicated in the figure. (a) *Canonical model:* for $\rho > \rho^{(c)}$, longitudinal perturbations ($\psi = 0$) are unstable. (b) *Grand canonical model:* transversal ($|\psi| = \pi/2$) perturbations are unstable closely above the critical density $\rho^{(c)}$ (refer to the green and blue curve corresponding to $\Delta \in \{0.05, 0.5\}$). For larger densities, i.e. $\Delta > 0.7$ for $\sigma = 0$, the transversal instability re-stabilizes again (dotted curves, $\Delta \in \{0.8, 1\}$). However, the density regime hosting this transversal instability vanishes completely for noise values larger than σ_r, as illustrated in figure 7.

$$s\,\delta g_{y,0} = -\frac{1}{2}\mathrm{i}q\sin(\psi)\left(g_0^2\frac{\mu}{\nu_2^2}\partial_{\rho_c}\nu_2 + 1\right)\delta\rho_c^0 - \mathrm{i}q\sin(\psi)\frac{\zeta_-}{\nu_2}\,g_0\,\delta g_{x,0} + \left(\mathrm{i}q\cos(\psi)\frac{\zeta_+}{\nu_2}g_0 - \frac{q^2}{4\nu_2}\right)\delta g_{y,0}. \tag{53c}$$

In equations (52*a*)–(53*c*) we used $-\nu_1 - \frac{\mu\kappa}{\nu_2}\,g_0^2 = 0$, which directly follows from the definition of g_0, given in equation (39). We numerically solved both eigenvalue problems in the immediate vicinity of the ordering transition line $\rho = \rho^{(c)}(\sigma)$.

In the case of the *canonical* model, we find that the most unstable mode occurs for longitudinal perturbations, i.e. perturbations with wave vectors parallel to the direction of macroscopic motion, $\mathbf{q} \parallel \mathbf{g}_0$ ($\psi = 0$). Figure 6(a) shows the corresponding eigenvalues as functions of the wavenumber q for a set of density values slightly beyond $\rho = \rho^{(c)}$. Further inspection of the coupling coefficients in equations (52*a*)–(52*d*) reveals that this longitudinal instability only affects the amplitude of $\mathbf{g}$ leaving the direction unchanged. For $\psi = 0$, the dynamics of $\delta g_{y,0}$ decouples and momentum current density fluctuations perpendicular to the direction of macroscopic motion decay exponentially,

$$\delta g_{y,0} = s_4^{(\mathrm{c})}\,\delta g_{y,0}, \tag{54}$$

with a rate

$$\Re\left[s_4^{(\mathrm{c})}\right] = -\frac{q^2}{4\nu_2} < 0, \tag{55}$$

which approaches zero for $q \to 0$, as expected for a broken symmetry variable. To assess the nature of the instability in greater detail, we calculated the eigenvector corresponding to the

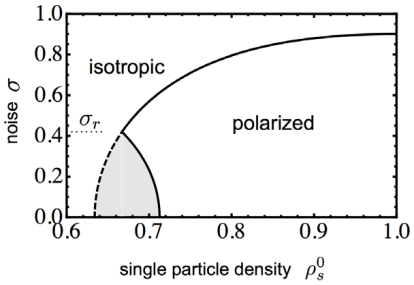

Figure 7. Phase diagram determined from the homogeneous equations of the *grand canonical* model, as a function of noise level σ and single particle density ρ_s^0, now complemented by the results obtained from the stability analysis of the linearized inhomogeneous equations: whereas longitudinal perturbations decay within the homogeneous phase boundary, there is a zone (gray shaded) where transversal modes become linearly unstable. The width of this zone gradually decreases for increasing noise values σ, and vanishes completely above some critical noise value σ_r (horizontally dotted line).

most unstable longitudinal mode (evaluated at the most unstable wavenumber). It turns out that this eigenvector has approximately equally large components along the remaining fluctuation amplitudes $\delta g_{x,0}$, $\delta\rho_0$ and $\delta\eta_0$. This is consistent with our previous findings, indicating that the density mode, which was alluded to in section 5.2 and which turns unstable at $\rho = \rho_c$, renders the state of homogeneous collective motion unstable to fluctuations of the magnitude of the momentum current density. We further note that this picture is in agreement with previous numerical [31] and analytical [22] results (cf figure 1).

The stability regions of the *grand canonical* model strongly deviate from the above picture. Setting $\psi = 0$ (longitudinal perturbations), we calculated the largest eigenvalue $s_{\max}^{(\mathrm{GC})}$ of the linear system of equations (53*a*)–(53*c*):

$$\Re\left[s_{\max}^{(\mathrm{GC})}\right] = -\frac{(1-\rho_s)\,q^2}{4\left[(1-\rho_s)^2 + \rho_s^2\left(\frac{14}{15} + \frac{2}{3}\,\mathrm{e}^{-2\sigma^2}\right)\right]}, \tag{56}$$

which is always negative since $\rho_s < 1$. In contrast to the *canonical* model, longitudinal perturbations thus always decay exponentially fast in the *grand canonical* model. For perturbations in transverse directions, in contrast, a positive eigenvalue can be found for sufficiently low noise levels $\sigma < \sigma_r$, with the fastest growing modes possessing wave vectors $\mathbf{q} \perp \mathbf{g}_0$. Figure 6(b) shows the eigenvalue of the most unstable modes, which occur for $\sigma = 0$. To assess the implications of this instability for the dynamics of the various fluctuation amplitudes, we numerically examined the eigenvector corresponding to the positive eigenvalue, evaluated at the most unstable wavenumber. For densities in the vicinity of the ordering transition, we find that this eigenvector has approximately equal components in both momentum current density fluctuation amplitudes, $\delta g_{x,0}$ and $\delta g_{y,0}$, but an essentially vanishing component along the direction of density fluctuations $\delta\rho_c^0$. The corresponding instability can thus be classified as a hybrid shear/splay instability, leaving the spatially homogeneously distributed particle density virtually unaffected.

Three remarks are in order. Firstly, for noise values $\sigma_c(\rho \to \infty) > \sigma > \sigma_r$, the state of homogeneous collective motion becomes linearly stable with respect to arbitrary perturbations, including transverse perturbations. Secondly, even the most unstable eigenvalues 'restabilize' for densities that are in the vicinity of the ordering transition threshold, which is depicted in figure 7. Finally, a restabilization can also be 'observed' for the longitudinal instability in the *canonical* model. In this case, however, the restabilization occurs for relatively large densities and thus lies outside the range of validity of the linearized equations (52*a*)–(52*d*).

6. Discussion and conclusion

To conclude, we discuss and summarize our main findings. To study the onset of collective motion in active media, we started out with a simplified model for a system of self-propelled rod-like particles of variable aspect ratio. Collective motion was assumed to be established in a completely self-organized fashion solely by means of interactions among the constituent particles and in the absence of any external alignment fields. These interactions were assumed to occur via binary, inelastic particle collisions, during which the rods align their direction of motion. Moreover, interactions were assumed to be subject to noise, which we controlled by a single model parameter σ. To assess some of the structural properties of such systems, we associated each of the particles with one of two classes: *single particles* and *cluster particles*, each with the corresponding density fields denoted as ρ_s and ρ_c. The class of *cluster particles* hosts all particles belonging to some coherently moving group of particles, which we referred to as cluster. The rest of the particles can be imagined to make up an isotropic sea of particles and are associated with the class of *single particles*. Using this classification scheme, we implemented simple interaction rules, representing cluster nucleation, cluster growth and cluster evaporation; the latter is assumed to occur at some fixed rate ϵ.

To illuminate the self-organization of collective motion, we set up an analytical, kinetic description of such systems, focusing on two archetypical modeling frameworks. Firstly, we considered isolated systems in which the total number of constituent particles is a conserved quantity. This case was referred to as the *canonical* model. Secondly, we examined open systems, which we referred to as the *grand canonical* model. Open systems are in contact with a particle reservoir which keeps the density of *single particles* at a constant level.

Inspecting the corresponding hydrodynamic equations, we were able to establish the following physical picture, portraying the formation of collective motion via dissipative particle interactions. For both the *canonical* and the *grand canonical* model, we identified two characteristic density scales $\bar{\rho}$ and $\rho^{(c)}(\sigma)$, with $\rho^{(c)}(\sigma) > \bar{\rho}$, which allowed us to distinguish three density regimes.

For low densities, $\rho < \bar{\rho}$, the rate at which particles collide is much smaller than the rate at which clusters disassemble. In terms of a particle-based picture, this regime corresponds to a situation where particle clusters are unstable, evaporating shortly after their nucleation. In the stationary state, the vast majority of particles populates the *single particle* phase, rendering the system homogeneous and isotropic even on mesoscopic scales. This low-density regime terminates at the characteristic density $\bar{\rho}$, where both classes exchange particles at equal rates.

In the contiguous regime of intermediate densities, $\bar{\rho} < \rho < \rho^{(c)}$, the overall rate of cluster formation and growth outstrips the rate at which clusters evaporate, and the majority of particles becomes organized in clusters. Translated to a particle-based notion, clusters grow to finite sizes and persist over macroscopic time scales. Clusters of coherently moving particles now

dominate the physical picture on mesoscopic scales. Yet, interactions among clusters are too rare to establish a macroscopic state of collective motion. On hydrodynamic length scales, the system can be viewed as a homogeneous and isotropic sea of clusters.

For densities exceeding the critical density, $\rho > \rho^{(c)}(\sigma)$, collisions within the cluster phase occur at sufficiently high rates, and macroscopic collective motion emerges. The homogeneous and isotropic state, which has been shown to be stable within the two preceding regimes, thus gets unstable and rotational symmetry is spontaneously broken. Resorting to a particle-based image, we can imagine the mean cluster size to reach a 'percolation threshold', leading to coagulation and net alignment between clusters.

While the qualitative features of the *canonical* and the *grand canonical* model are the same in the low and the intermediate density regimes, the establishment of collective motion in the high-density regime differs in important respects in both models. We found that in the *grand canonical* model, a broadly extended region in parameter space exists, where a spatially homogeneous state of macroscopic collective motion exists and is actually stable. Except density, the key parameter controlling the stability of a spatially homogeneous flowing state is the noise amplitude σ. For low noise levels the homogeneous flowing state gets unstable toward transverse perturbations (i.e. perturbations with wave vectors $\mathbf{q}$ perpendicular to the direction of the macroscopic flow). We note, however, that these instabilities are remarkably weak, i.e. the corresponding growth rates are smaller than those of the longitudinal instability in the *canonical* model by a factor of $\sim$10 (cf figure 7), and 'restabilization' of the spatially homogeneous flowing state occurs upon increasing the density only slightly beyond the threshold $\rho^{(c)}(\sigma)$. Interestingly, this transverse instability vanishes altogether, if angular diffusion is slightly enhanced upon increasing σ. Hence, for intermediate values of σ, the system directly establishes a homogeneous state of collective motion, which is stable against arbitrary perturbations of small magnitude. Finally, if the noise is too strong, order is destroyed and the system remains isotropic even for arbitrarily large densities. This last statement is, of course, shared among all active systems [29], particle conserving or not, and thus applies equally well to the *canonical* model.

In the case of the *canonical* model, a spatially homogeneous base state is unstable toward longitudinal perturbations (i.e. perturbations with wave vectors $\mathbf{q}$ parallel to the direction of the macroscopic flow) for all values of the noise parameter σ. Both the magnitude of the macroscopic velocity field and the particle density are prone to this kind of instability. This is in agreement with previous analytical [22] and numerical [31] results for particle conserving systems, where the emergence of solitary wave structures has been reported in the vicinity of the ordering transition $\rho \gtrsim \rho^{(c)}(\sigma)$. The longitudinal instability thus seems to be a quite generic feature of particle conserving systems with hard core interactions. For an interesting counter example we refer the reader to [26], where a particle conserving system with topological interactions has been studied.

We can now combine our findings for both the *canonical* and the *grand canonical* model to offer the following mechanistic explanation concerning the emergence of the longitudinal instability. The prerequisite, underlying the establishment of coherent motion, is embodied by two basic processes: cluster nucleation by collisions among *single particles* and cluster growth by alignment of *single particles* to clusters. Only if, by virtue of these processes, the concentration of *cluster particles* grows sufficiently large, clusters are able to synchronize their movements by coagulation and macroscopic collective motion emerges.

Now consider the effect of a density fluctuation in an otherwise homogeneous state of macroscopic collective motion. In the *grand canonical* model, where the density of *single*

particles is kept fixed by virtue of a particle reservoir, this fluctuation occurs within the class of *cluster particles*. We can use the right-hand side of equation (35*a*) to assess the implications of such a fluctuation on the local composition of the system in terms of *cluster particles* and *single particles*:

$$(\rho_s^0 + \rho_c)\rho_s^0 = \rho_c. \tag{57}$$

Note that this equation captures the balance of the two particle currents between the *single particle* and the *cluster particle* phase in the stationary limit. As can be seen from this equation, locally enhancing the density of *cluster particles* implies a net current from the *cluster particle* phase into the *single particle* phase, thus counteracting the effect of the original density fluctuation. Conversely, locally diminishing the density of *cluster particles* leads to the opposite effect. Density fluctuations are thus damped in the *grand canonical* model and do not impact the macroscopic velocity field, which is set up by the *cluster particles*.

Exactly the opposite happens in the particle conserving *canonical* model. Again, consider a spatially homogeneous base state of macroscopic collective motion. Particles are then distributed among the phases of *cluster particles* and *single particles* as determined by the balance equation (cf (34*b*))

$$\rho(\rho - \eta) = \rho + \eta, \tag{58}$$

where the left-hand side describes cluster nucleation and condensation, and the right-hand side corresponds to cluster evaporation. This can be seen by using the definitions of the relative density $\eta = \rho_c - \rho_s$ and the total particle density $\rho = \rho_s + \rho_c$. Now, consider a fluctuation in the total density ρ, where, for the sake of simplicity, we assume the relative density η to remain constant. In regions where the fluctuation leads to an increase in the total density by a factor $k > 1$, we have

$$k\rho(k\rho - \eta) > k\rho + \eta. \tag{59}$$

Hence, the particle current into the *cluster particle* phase grows. As a consequence, the local value of the momentum current density increases, since the *cluster particles* are the 'carriers' of the macroscopic momentum. In contrast, in regions where the fluctuation decreases the total density by a factor $k' < 1$, we have

$$k'\rho(k'\rho - \eta) < k'\rho + \eta. \tag{60}$$

There the *cluster particle* phase gets depleted and the local magnitude of the momentum current density declines. As a result, high-density regions move at faster speeds than low-density regions, gathering more and more particles on their way through the system. Conversely, lower density regions continually lose particles to the faster high-density structures. In particle conserving systems, every density fluctuation thus automatically triggers a corresponding fluctuation in the momentum current density, which in turn amplifies the density fluctuation. As a result of this process, high-density bands of collectively moving *cluster particles* might emerge [31]. These bands are interspersed by regions where the particle density has fallen below the critical density $\rho^{(c)}$ (and possibly below $\bar{\rho}$), leading to local destruction of clusters and collective motion.

We close by adding some remarks on the importance of the particles' shape on the establishment of collective motion on hydrodynamic scales. We found that the impact of particle shape on the macroscopic properties of such systems is purely quantitative in the framework of our present study: varying the particles' aspect ratio results in a shift of the characteristic density

scales $\bar{\rho}$ and $\rho^{(c)}(\sigma)$, which we quantified in equation (37). Qualitatively, our conclusions concerning the macroscopic properties of these systems remain unaffected by a change in the particles' aspect ratio. Note that, in our approach, the aspect ratio basically determines the total scattering cross section and thus 'merely' impacts the rate at which particles collide. We stress, however, that in real systems particle shape is likely to have a profound impact on the entire physical picture of particle interactions, and not just on their rate. The study of those effects lies outside the scope of our present work and would be an interesting topic for future research.

Acknowledgments

The authors thank Simon Weber and Jonas Denk for discussions and a critical reading of our paper. Financial support from the DFG in the framework of the SFB 863 and the German Excellence Initiative via the program Nanosystems Initiative Munich (NIM) is gratefully acknowledged. This research was also supported in part by the National Science Foundation under grant no. NSF PHY11-25915.

Appendix A. Derivation of the Boltzmann collision cylinder for driven rods

In the framework of our Boltzmann-like description, binary collisions, such as equations (3), (6) and (7), occur with a certain rate Γ depending on particle shape (L and d), relative angle of both collision partners $\theta_{12} = |\theta_1 - \theta_2|$ and the constant velocity v. The quantity $\Gamma(L, d, \theta_{12})$ characterizes the collision area per unit time—more commonly referred to as a Boltzmann collision cylinder. On the scale of the Boltzmann equation, binary collisions occur locally, say in an infinitesimal volume element centered at $\mathbf{r}$. Assume that particle 1 has an orientation θ_1. Then, $\Gamma(L, d, \theta_{12})\,\mathrm{d}t$ gives the area around particle 1 in which every particle with orientation θ_2 will collide during a time interval $[t, t + \mathrm{d}t]$ with particle 1. As a consequence, $\Gamma(L, d, \theta_{12})\, f(\mathbf{r}, \theta_1, t)\, f(\mathbf{r}, \theta_2, t)\mathrm{d}\theta_1\, \mathrm{d}\theta_2$ equals the number of collisions per unit time and unit area at time t, with $f(\mathbf{r}, \theta, t)$ denoting the one-particle distribution function.

To determine $\Gamma(L, d, \theta_{12})$, we take a microscopic point of view. Since the model employed in this work assigns to each particle a velocity vector pointing along its rod axis, we can distinguish 'head' and 'tail'. Referring to figure A.1, without loss of generality we assume $\pi - \theta_{12} \equiv \theta \in [0, \pi]$ (negative relative angles lead to the same result), and consider the blue rod, with the position of its head indicated by the blue dot. All rods of relative orientation $\theta_{12} = \theta_1 - \theta_2$, and with their heads lying in the area $S = A \cup S_1 \cup S_2$ at time t, will collide with the blue rod during the time interval $[t, t + \mathrm{d}t]$. Since A, S_1 and S_2 are disjoint,

$$|S| = |B| + |S_1| + |S_2|, \tag{A.1}$$

where $|X|$ denotes the area of the region X. The respective areas are given by

$$|A| = \mathrm{d}t\, v_{\mathrm{rel}}\, (L - d)|\sin\theta| = \mathrm{d}t\, v_{\mathrm{rel}}\, (L - d)|\sin\theta_{12}| \tag{A.2}$$

and

$$|S_2| + |S_1| = \mathrm{d}t\, v_{\mathrm{rel}}\, d \int_{-\theta}^{\pi-\theta} \mathrm{d}\phi\, \sin(\phi + \theta) = 2\,\mathrm{d}t\, v_{\mathrm{rel}}\, d. \tag{A.3}$$

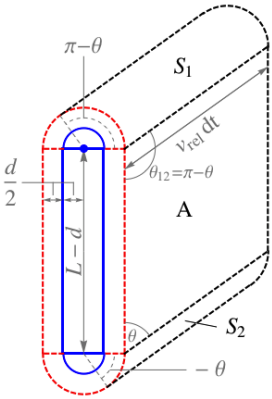

Figure A.1. Illustration of the collision cylinder in the rest frame of the blue rod. The red lines indicate the excluded volume due to the finite expansion of the rods. The quantity v_{rel} denotes the magnitude of the relative velocity of those rods making a relative angle $\theta_{12} = \pi - \theta$ with the blue rod's axis, and is given by $v_{\mathrm{rel}} = v|\hat{\mathbf{e}}(\theta) - \hat{\mathbf{e}}(0)| = 2v|\sin(\theta_{12}/2)|$.

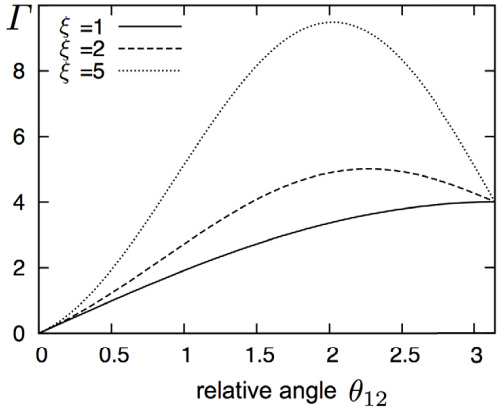

Figure A.2. $\Gamma(L, d, \theta_{12})$ as a function of the relative angle θ_{12} for different values of aspect ratio ξ. For the figure, we chose for particle width $d = 1$ and for particle velocity $v = 1$. Increasing the aspect ratio L/d, the most probable collision approaches $\theta_{12} = \pi/2$, whereas for $L/d = 1$ the most probable collision is the head–head collision with $\theta_{12} = \pi$.

Returning to the laboratory frame we have $v_{\rm rel} = v|\hat{\mathbf{e}}(\theta_1) - \hat{\mathbf{e}}(\theta_2)| = 2\,v|\sin(\theta_{12}/2)|$. Noting that $\Gamma = |S|/\mathrm{d}t$ (cf equation (A.1)), we find that

$$\Gamma(L, d, \theta_{12}) = 4v\,d\,\left|\sin\left(\frac{\theta_{12}}{2}\right)\right|\left(1 + \frac{L/d - 1}{2}\,|\sin\theta_{12}|\right). \tag{A.4}$$

In figure A.2, $\Gamma(L, d, \theta_{12})$ is shown as a function of relative angle θ_{12} for different particle lengths, whereby the particle width d is kept fixed. Increasing L/d shifts the most probable collision from $\theta_{12} = \pi$ for $L/d = 1$ (the case of a sphere; $\theta_{12} = \pi$ leads to the largest value of the relative velocity) toward $\theta_{12} = \pi/2$ for $L/d \to \infty$ (limiting case of a needle; largest target area for $\theta_{12} = \pi/2$).

Appendix B. Derivation of the gradient terms in the hydrodynamic equations

To assist the reader in tracing back the emergence of the gradient terms in the hydrodynamic equations (28*a*)–(28*c*) (and, likewise, in equations (32*a*)–(32*c*) and (33*a*)–(33*c*)), we briefly summarize the main steps in the derivation of these equations. All gradient terms in the hydrodynamic equations ultimately arise from the convection term in the first line of equation (24*c*) and the closure relation obtained by quasi-statically approximating (24*d*). Here we collect all such (complex) gradient terms and give a brief derivation of their vector-analytic counterparts. As in the main text, we identify $\mathbb{C}$ and $\mathbb{R}^2$, i.e.

$$f = f_x + \mathrm{i}f_y \in \mathbb{C} \leftrightarrow \mathbf{f} = \begin{pmatrix} f_x \\ f_y \end{pmatrix} \in \mathbb{R}^2. \tag{B.1}$$

To distinguish (genuinely) complex from purely real quantities, we assume $f \in \mathbb{C}$ and $\rho \in \mathbb{R}$ in the following.

$(\partial_x + \mathrm{i}\partial_y)\rho$:

Using (B.1) we immediately obtain

$$(\partial_x + \mathrm{i}\partial_y)\rho \equiv \nabla\rho. \tag{B.2}$$

$(\partial_x - \mathrm{i}\partial_y)(\partial_x + \mathrm{i}\partial_y)f$:

By straightforward expansion we find

$$(\partial_x - \mathrm{i}\partial_y)(\partial_x + \mathrm{i}\partial_y)f = (\partial_x^2 + \partial_y^2)f \equiv \nabla^2\mathbf{f}. \tag{B.3}$$

$(\partial_x - \mathrm{i}\partial_y)f^2$:

Decomposing f into real and imaginary parts and expanding, we find

$$\begin{aligned}(\partial_x - \mathrm{i}\partial_y)(f_x^2 - f_y^2 + 2if_xf_y) &= \partial_x f_x^2 - \partial_x f_y^2 + 2\partial_y(f_xf_y) + \mathrm{i}\left[\partial_y f_y^2 - \partial_y f_x^2 + 2\partial_x(f_xf_y)\right] \\ &\equiv 2\left[\partial_i(f_if_j) - \frac{1}{2}\delta_{ij}\partial_i\mathbf{f}^2\right]\mathbf{e}_j \\ &= 2\mathbf{f}(\nabla\cdot\mathbf{f}) + 2(\mathbf{f}\cdot\nabla)\mathbf{f} - \nabla\mathbf{f}^2,\end{aligned} \tag{B.4}$$

where $\mathbf{e}_j$ denotes the jth Cartesian unit vector.

$[(\partial_x + \mathrm{i}\partial_y)f][(\partial_x - \mathrm{i}\partial_y)\rho]$:

Expanding and collecting real and imaginary parts, we find

$$[(\partial_x + \mathrm{i}\partial_y) f][(\partial_x - \mathrm{i}\partial_y)\rho] = \partial_x f_x \partial_x \rho - \partial_y f_y \partial_x \rho + \partial_x f_y \partial_y \rho + \partial_y f_x \partial_y \rho + \mathrm{i}(-\partial_x f_x \partial_y \rho + \partial_y f_y \partial_y \rho + \partial_x f_y \partial_x \rho + \partial_y f_x \partial_x \rho).$$

Thus,

$$[(\partial_x + \mathrm{i}\partial_y) f][(\partial_x - \mathrm{i}\partial_y)\rho] \equiv ((\partial_i f_j)\partial_i \rho + (\partial_j f_i)\partial_i \rho)\mathbf{e}_j - (\nabla \cdot \mathbf{f})\nabla\rho = [(\nabla \mathbf{f}) + (\nabla \mathbf{f})^t]\nabla\rho - (\nabla \cdot \mathbf{f})\nabla\rho. \tag{B.5}$$

$f^2(\partial_x - \mathrm{i}\partial_y)\rho$:

We find

$$f^2(\partial_x - \mathrm{i}\partial_y)\rho = f_x^2 \partial_x \rho - f_y^2 \partial_x \rho + 2 f_x f_y \partial_y \rho + i(-f_x^2 \partial_y \rho + f_y^2 \partial_y \rho + 2 f_x f_y \partial_x \rho).$$

Hence,

$$f^2(\partial_x - \mathrm{i}\partial_y)\rho \equiv 2 f_i f_j \partial_j \rho \, \mathbf{e}_i - \mathbf{f}^2 \nabla\rho = 2\mathbf{f}(\mathbf{f} \cdot \nabla\rho) - \mathbf{f}^2 \nabla\rho. \tag{B.6}$$

References

[1] Ramaswamy S 2010 The mechanics and statistics of active matter *Annu. Rev. Condens. Matter Phys.* **1** 323–45

[2] Aranson I S and Tsimring L S 2009 *Granular Patterns* (New York: Oxford University Press)

[3] Marchetti M C, Joanny J-F, Ramaswamy S, Liverpool T B, Prost J, Rao M and Aditi R Simha 2012 Soft active matter arXiv:1207.2929 [cond-mat.soft]

[4] Butt T, Mufti T, Humayun A, Rosenthal P B, Khan S, Khan S and Molloy J E 2010 Myosin motors drive long range alignment of actin filaments *J. Biol. Chem.* **285** 4964–74

[5] Schaller V, Weber C A, Semmerich C, Frey E and Bausch A 2010 Polar patterns in propelled filaments *Nature* **467** 73–7

[6] Schaller V, Weber C, Frey E and Bausch A R 2011 Polar pattern formation: hydrodynamic coupling of driven filaments *Soft Matter* **7** 3213–8

[7] Zhang H P, Be'er A, Florin E-L and Swinney H L 2010 Collective motion and density fluctuations in bacterial colonies *Proc. Natl Acad. Sci. USA* **107** 13626–30

[8] Dombrowski C, Cisneros L, Chatkaew S, Goldstein R E and Kessler J O 2004 Self-concentration and large-scale coherence in bacterial dynamics *Phys. Rev. Lett.* **93** 098103

[9] Schaller V, Weber C A, Hammerich B, Frey E and Bausch A R 2011 Frozen steady states in active systems *Proc. Natl Acad. Sci. USA* **108** 19183–8

[10] Sumino Y, Nagai K H, Shitaka Y, Tanaka D, Yoshikawa K, Chaté H and Oiwa K 2012 Large-scale vortex lattice emerging from collectively moving microtubules *Nature* **483** 448–452

[11] Deseigne J, Dauchot O and Chaté H 2010 Collective motion of vibrated polar disks *Phys. Rev. Lett.* **105** 098001

[12] Deseigne J, Léonard S, Dauchot O and Chaté H 2012 Vibrated polar disks: spontaneous motion, binary collisions, and collective dynamics *Soft Matter* **8** 5629–39

[13] Kudrolli A, Lumay G, Volfson D and Tsimring L S 2008 Swarming and swirling in self-propelled polar granular rods *Phys. Rev. Lett.* **100** 058001

[14] Ballerini M *et al* 2008 Empirical investigation of starling flocks: a benchmark study in collective animal behaviour *Animal Behav.* **76** 201–15

[15] Toner J and Tu Y 1995 Long-range order in a two-dimensional dynamical XY model: how birds fly together *Phys. Rev. Lett.* **75** 4326–9

[16] Aranson I S and Tsimring L S 2005 Pattern formation of microtubules and motors: inelastic interaction of polar rods *Phys. Rev.* E **71** 050901

[17] Bertin E, Droz M and Grégoire G 2006 Boltzmann and hydrodynamic description for self-propelled particles *Phys. Rev.* E **74** 022101
[18] Aranson I S, Sokolov A, Kessler J O and Goldstein R E 2007 Model for dynamical coherence in thin films of self-propelled microorganisms *Phys. Rev.* E **75** 040901
[19] Baskaran A and Cristina Marchetti M 2008 Hydrodynamics of self-propelled hard rods *Phys. Rev.* E **77** 011920
[20] Baskaran A and Cristina Marchetti M 2008 Enhanced diffusion and ordering of self-propelled rods *Phys. Rev. Lett.* **101** 268101
[21] Holm D D, Putkaradze V and Tronci C 2008 Kinetic models of oriented self-assembly *J. Phys. A: Math. Theor.* **41** 344010
[22] Bertin E, Droz M and Grégoire G 2009 Hydrodynamic equations for self-propelled particles: microscopic derivation and stability analysis *J. Phys. A: Math. Theor.* **42** 445001
[23] Holm D D, Putkaradze V and Tronci C 2010 Double-bracket dissipation in kinetic theory for particles with anisotropic interactions *Proc. R. Soc. Lond.* A **466** 2991–3012
[24] Mishra S, Baskaran A and Cristina Marchetti M 2010 Fluctuations and pattern formation in self-propelled particles *Phys. Rev.* E **81** 061916
[25] Ihle T 2011 Kinetic theory of flocking: derivation of hydrodynamic equations *Phys. Rev.* E **83** 030901
[26] Peshkov A, Ngo S, Bertin E, Chaté H and Ginelli F 2012 Continuous theory of active matter systems with metric-free interactions *Phys. Rev. Lett.* **109** 098101
[27] Peshkov A, Aranson I S, Bertin E, Chaté H and Ginelli F 2012 Nonlinear field equations for aligning self-propelled rods *Phys. Rev. Lett.* **109** 268701
[28] Wensink H H, Dunkel J, Heidenreich S, Drescher K, Goldstein R E, Löwen H and Yeomans J M 2012 Meso-scale turbulence in living fluids *Proc. Natl Acad. Sci. USA* **109** 14308–13
[29] Vicsek T, Czirók A, Ben-Jacob E, Cohen I and Shochet O 1995 Novel type of phase transition in a system of self-driven particles *Phys. Rev. Lett.* **75** 1226–9
[30] Czirók A and Vicsek T 2000 Collective behavior of interacting self-propelled particles *Physica* A **281** 17–29
[31] Grégoire G and Chaté H 2004 Onset of collective and cohesive motion *Phys. Rev. Lett.* **92** 025702
[32] Chaté H, Ginelli F, Grégoire G and Raynaud F 2008 Collective motion of self-propelled particles interacting without cohesion *Phys. Rev.* E **77** 046113
[33] Chaté H, Ginelli F, Grégoire G, Peruani F and Raynaud F 2008 Modeling collective motion: variations on the Vicsek model *Eur. Phys. J.* B **64** 451–6
[34] Grossman D, Aranson I S and Ben Jacob E 2008 Emergence of agent swarm migration and vortex formation through inelastic collisions *New J. Phys.* **10** 023036
[35] Baglietto G and Albano E V 2009 Nature of the order–disorder transition in the Vicsek model for the collective motion of self-propelled particles *Phys. Rev.* E **80** 050103
[36] Ginelli F, Peruani F, Bär M and Chaté H 2010 Large-scale collective properties of self-propelled rods *Phys. Rev. Lett.* **104** 184502
[37] Peruani F, Deutsch A and Bär M 2006 Nonequilibrium clustering of self-propelled rods *Phys. Rev.* E **74** 030904
[38] Peruani F, Klauss T, Deutsch A and Voss-Boehme A 2011 Traffic jams, gliders and bands in the quest for collective motion of self-propelled particles *Phys. Rev. Lett.* **106** 128101
[39] Weber C A, Schaller V, Bausch A R and Frey E 2012 Nucleation-induced transition to collective motion in active systems *Phys. Rev.* E **86** 030901
[40] Lovely P S and Dahlquist F W 1975 Statistical measures of bacterial motility and chemotaxis *J. Theor. Biol.* **50** 477–96
[41] Toner J, Tu Y and Ramaswamy S 2005 Hydrodynamics and phases of flocks *Ann. Phys.* **318** 170–244

3

A CRITICAL ASSESSMENT OF THE BOLTZMANN APPROACH

3.1 STARTING POINT OF THE PROJECT

Over the past decades, progress in our understanding of the phenomenon of collective motion in active systems has largely been made in terms of generic models [152, 35, 57, 5, 20, 31, 21, 53, 54, 108, 107, 19]. Generic approaches typically classify different active systems according to their symmetry properties and focus on simplified models, designed to highlight those symmetries. On the level of kinetic descriptions, Bertin et al. [20, 21] have introduced a binary collision model to investigate the macroscopic properties of systems of self-propelled particles with polar interactions. As a blueprint to capture the polar symmetry of particle collisions, they proposed a "half-angle alignment rule" and assumed particles with pre-collision orientations θ_1 and θ_2 to align along a common orientation $\theta_t = (\theta_1 + \theta_2)/2$ (plus noise). Similar alignment rules have been used previously to describe pattern formation of microtubules [5, 6].

In the meantime, recent experimental setups, including actin and microtubule gliding assays [26, 124, 123, 125, 135] and vibrated granules [22, 98, 7, 74, 73, 37, 38, 155], allow for a direct assessment of binary collision process between particles. Studies in this direction [155, 60, 136, TWF13] reveal significant differences between the assumptions underlying generic modeling approaches as described above, and the actual physics of binary collisions observed in experiments. First, the relationship between pre- and post-collision orientations of rod-shaped parti-

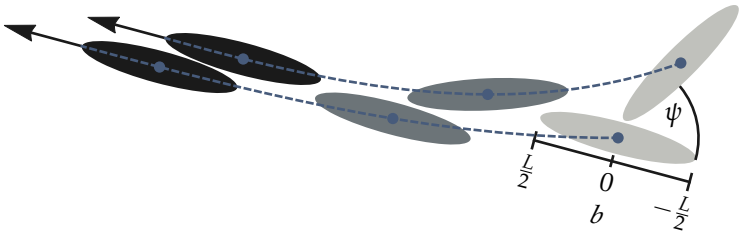

Figure 7.: Illustration of a dissipative polar collision process with an alignment weight deviating from the half-angle alignment rule. Depicted here is a collision configuration with relative pre-collision particle orientation ψ and impact parameter $b \approx 0$, such that the angular momentum exerted on the lower rod is virtually zero. For small ψ, such collisions typically lead to polar alignment with an alignment weight $w(\psi, b) \approx 1$, i.e. with the upper rod aligning to the direction of the lower rod. Trajectories of rods' centers of mass are indicated by dashed lines.

cles strongly depends on the collision parameter and typically exhibits deviations from the simplified half-angle alignment rule. Secondly, "indifferent" collisions between particles which do not lead to particle alignment at all are frequently observed.

According to the kinetic picture conveyed by the popular half-angle alignment rule, polar order in self-propelled particle systems is established and maintained by sufficiently frequent binary particle collisions, which incessantly act to diminish orientational spreads between particles and, therefore, efficiently counteract the randomizing effects of noise. The experimental and numerical evidence, alluded to above, however, introduces new questions. Both, the observed deviations of the post-collision angles from their optimal values (given by the half-angle collision rule) and the occurrence of indifferent collisions corrupt the efficiency of binary collisions to generate polar order. It is thus far from obvious to which extent this simple kinetic picture alone can actually account for the emergence of polar ordered structure as reported in experiments [124, 37, 38, 135].

Our work *"Critical Assessment of the Boltzmann Approach to Active Systems"* [TWF13], revolves around the following central question: "With no additional assumptions to be made, does the integrated effect of binary particle interactions in active systems suffice to establish a state of collective motion on macroscopic scales"? The following section 3.2 contains a brief discussion of the key concepts used to answer this question and summarizes our main findings. An outlook on open questions and potential future projects in given in section 3.3. Details on this work can be found in the appended paper, section 3.4, and in Appendix A.

3.2 SUMMARY OF MAIN RESULTS

To assess the question of whether or not binary particle collisions alone can account for the emergence of large scale polar structures in active systems, we proceed in two steps. First, to extract the qualitative features of binary particle collisions under "realistic" conditions, we simulate a microscopic model of self-propelled rod-shaped particles in an overdamped environment, assuming excluded volume interactions. Specifically, we consider two archetypical models corresponding to stiff and semi-flexible rods, respectively. Within each model, we conduct detailed scattering studies by preparing different pre-collision angles $\psi = \theta_1 - \theta_2$ and collision parameters b (cf. Fig. 7), and recording the resulting post-collision angles θ_1' and θ_2'.

Figure 8(a) illustrates the results of the scattering study for the case of self-propelled stiff rods. We observe perfect polar particle alignment, $\theta_1' = \theta_2' \equiv \theta'$, if particles are well aligned before the collision (small values of ψ), and indifferent scattering outcomes, $\psi' \equiv \theta_1' - \theta_2' = \psi$, if pre-collision particle alignment is poor [large values of ψ; white region in Fig. 8(a)]. To quantify particle alignments in the polar region of the scattering diagram, Fig. 8(a), we introduce the "alignment weight function"

$$w(\psi) \equiv \left\langle \frac{\theta' - \theta_2}{\psi} \right\rangle_b \qquad (\psi \neq 0). \tag{13}$$

For the half-angle alignment rule, the alignment weight function reduces to $w(\psi) = \text{const.} = 1/2$. Thus, $w(\psi)$ quantifies the devi-

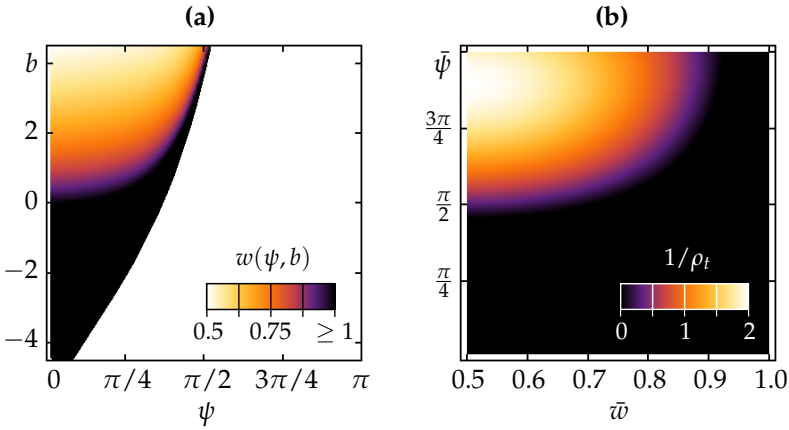

Figure 8.: **(a)** Binary scattering study for rigid, rod-shaped particles in overdamped environments. The color code indicates the value of the microscopic alignment function $w(\psi, b) \equiv (\theta' - \theta_2)/\psi$ ($\psi \neq 0$). White region: Indifferent collision events (no polar alignment). **(b)** Transition density ρ_t (color code) as a function of the alignment range $\bar{\psi}$ and the effective alignment parameter $\bar{w}$ at noise levels $\sigma = \sigma_0 = 0.5$. Black region: Parameters are incompatible with the formation of polar order due to binary collisions.

ations of observed alignment processes from the half-angle alignment rule.

To work out the consequences of the scattering results presented in Fig. 8(a) in the context of the system's macroscopic ordering dynamics, we generalize the Boltzmann equation approach introduced in chapter 1, to incorporate the effects of alignment weights $w(\psi) \neq 1/2$ and the occurrence of indifferent scattering events. To this end, we redefine the collision integrals I_c on the right hand side of the Boltzmann equation

$$\partial_t f(\mathbf{r}, \theta, t) + v_0 \mathbf{e}(\theta) \cdot \nabla f(\mathbf{r}, \theta, t) = I_\mathrm{d} + I_\mathrm{c}. \tag{14a}$$

according to[1]

$$I_c = \left\langle \int_{-\pi}^{\pi} d\phi \int_{-\bar{\psi}}^{\bar{\psi}} d\psi \, \mathcal{S}(L,d,\psi) f(\phi) f(\phi+\psi) \times \left[\delta(\theta-\phi-w(\psi)\psi-\eta)-\delta(\theta-\phi)\right] \right\rangle_{\eta}. \quad (14b)$$

The diffusion integral is assumed to take its familiar form and reads

$$I_d = \lambda \left\langle \int_{-\pi}^{\pi} d\phi f(\phi)[\delta(\theta-\phi-\varphi)-\delta(\theta-\phi)] \right\rangle_{\varphi}, \quad (14c)$$

where λ denotes the tumbling rate as introduced in chapter 1. In Eq. (14b), the "alignment range" $\bar{\psi} \leq \pi$ reflects the limited extension of the occurrence of polar events in Fig. 8(a), and the target angle $\theta_t = \phi + w(\psi) \cdot \psi$ is determined by the (experimentally measurable) alignment weight function $w(\psi)$. Again, the random variables η and φ are included to account for the effects of noise in collision events and free particle motions and are assumed to be drawn from zero-mean Gaussian distributions with variances σ^2 and σ_0^2, respectively.

Equations (14) can then be used to determine the transition density ρ_t, beyond which the spatially homogeneous, disordered solution $f(\mathbf{r},\theta,t)$ becomes linearly unstable toward the formation of polar ordered structures. We find

$$\rho_t[w(\psi);\bar{\psi}] = \frac{1-e^{-\sigma_0^2/2}}{\mathcal{I}_{0,1}[w(\psi);\bar{\psi}]+\mathcal{I}_{1,1}[w(\psi);\bar{\psi}]}, \quad (15)$$

where $\mathcal{I}_{n,k}$ denotes the Fourier space representation of the kernel of the collision integral, Eq. (14b); cf. Appendix A. We emphasize that the expression for the transition density, Eq. (15), is exact and can, therefore, be used to quantify the efficiency of binary collisions with alignment weight function $w(\psi)$ and alignment range

1 To be consistent with our presentation in the appended paper, section 3.4, here we use v_0 (rather than v) to denote the constant propelling speed, $\mathbf{r}$ (rather than $\mathbf{x}$) to denote the spatial position vector, $\mathcal{S}$ (rather than Γ) to denote the scattering cross section, and η and φ to denote the random variables associated with collision and diffusion noise, respectively.

$\bar{\psi}$ to elicit polar order on macroscopic scales. To facilitate further analysis, we organize the space of alignment weight functions $w(\psi)$ into distinct equivalence classes according to the specific value of the transition density $0 < \rho_t < \infty$. Specifically, it can be shown that each such equivalence class contains (and, thus, can be represented by) one and only one constant member function $w(\psi) = \text{const.} \equiv \bar{w} \geq 1/2$; cf. section 3.4 and Appendix A.

This then allows us to investigate the transition density ρ_t as a function (rather than a functional) of the "effective alignment weight" $\bar{w}$ and of the alignment range $\bar{\psi}$. We arrive at the following key results. First of all, alignment weight functions represented by an effective alignment weight $\bar{w} \geq 1$ are incompatible with finite (non-negative) values of the transition density ρ_t. Polar collisions with such alignment weight functions are, therefore, incapable to elicit polar structures of macroscopic extent even in the limiting case of vanishing collision noise levels $\sigma = 0$. For increasing collision noise levels $\sigma > 0$, the range of effective alignment weights compatible with the formation of macroscopic polar order narrows even further. In addition, even for perfect half-angle alignment, $\bar{w} = 1/2$, the transition density ρ_t diverges if alignment ranges $\bar{\psi}$ fall short of a (noise specific) threshold value. The mere occurrence of indifferent events can, therefore, lead to a complete breakdown of polar order due to binary collisions.

These observations help clarify the simple kinetic picture of polar order formation, alluded to in section 3.1, in the context of more realistic collision processes. According to this picture, polar order emerges whenever the order creating effects of particle interactions dominate over the randomizing effects of noise by virtue of sufficiently frequent collisions. This notion of order formation necessarily requires a finite amount of net alignment of particles per collision event. Quite generally, net alignment in particle interactions is lost if the collision noise gets too violent. Imperfections in particle alignment, as indicated by deviations of the effective alignment parameter from its optimal value $\bar{w} = 1/2$, can be seen as an additional source of noise during each polar collision event, such that polar order formation breaks down if these deviations become too large. Similarly, decreasing alignment ranges $\bar{\psi}$ implicitly amplify the effects of collision

noise by increasing the mean noise amplitude $\propto \sigma$ relative to the alignment corridor $\propto \bar{\psi}$. The overall situation is illustrated in Fig. 8(b), where the transition density ρ_t (color code) is plotted against the effective alignment weight $\bar{w}$ and the alignment range $\bar{\psi}$ for $\sigma = 0.5$.

3.3 OUTLOOK

Our results indicate that the simple kinetic paradigm, emphasizing the competition between collision-mediated alignment and noise, implies significant restrictions on actual collision processes in terms of alignment efficiency per collision event in order to be applicable. In particular, it turns out that none of the scattering diagrams recorded for our *in silico* models which we discussed earlier in this section, is compatible with the formation of polar order, despite the fact that particles undergo perfect alignment during polar collision events. This suggests to consider alternative mechanisms of the formation of polar ordered structures which lie beyond the kinetic approach discussed in this chapter. Quite recently, numerical studies [105, 165, 156, 158, 27] and experiments on bacterial systems [166, 106] highlight the importance of the formation and growth of clusters of tightly entangled particles. In such systems, the emergence of ordered structures rests on a buildup of correlation effects between particles which are inconsistent with the molecular chaos assumption underlying the Boltzmann equation. Alternative approaches are needed to account for such clustering effects and to assess their importance in the formation of large scale ordered structures [61, 104].

On the other hand, recently performed microscopic simulations indicate that a properly "renormalized", yet strictly binary Boltzmann equation approach, as presented in this thesis, is appropriate to describe the ordering behavior in a collection of propelled, soft colloidal particles [60]. Taken together, these results therefore strongly suggest to make a distinction between cluster forming systems (for which it is still unclear whether long range polar order would actually emerge in the first place [106]) and "Vicsek like" systems in which the formation of genuine long range order is primarily driven by local particle in-

teractions. In the former case of cluster forming systems, approaches based on the Boltzmann equation would typically break down due to the limitations entailed by the molecular chaos assumption. In the latter case of "Vicsek like" systems, however, the Boltzmann equation approach has proven highly successful [5, 20, 6, 4, 168, 21, 108, 107, 19, 60, WTF13, TWF14] and, therefore, constitutes a valuable and highly flexible tool to assess the physical properties of this kind of systems on macroscopic length and time scales, as will be detailed in the following chapter 4.

Critical Assessment of the Boltzmann Approach to Active Systems

Florian Thüroff, Christoph A. Weber, and Erwin Frey*

Department of Physics, Arnold Sommerfeld Center for Theoretical Physics and Center for NanoScience, Ludwig-Maximilians-Universität München, Theresienstrasse 37, D-80333 Munich, Germany

(Received 9 April 2013; revised manuscript received 17 July 2013; published 4 November 2013)

Generic models of propelled particle systems posit that the emergence of polar order is driven by the competition between local alignment and noise. Although this notion has been confirmed employing the Boltzmann equation, the range of applicability of this equation remains elusive. We introduce a broad class of mesoscopic collision rules and analyze the prerequisites for the emergence of polar order in the framework of kinetic theory. Our findings suggest that a Boltzmann approach is appropriate for weakly aligning systems but is incompatible with experiments on cluster forming systems.

DOI: 10.1103/PhysRevLett.111.190601 PACS numbers: 05.70.Ln, 05.20.Dd, 47.45.Ab, 64.60.Cn

The emergence of large-scale collective motion is one of the most intriguing features, which is shared among a large variety of active systems [1–11]. This apparent universality has led to considerable theoretical efforts aiming at the identification of general physical principles underlying collective motion in active systems [12–16]. There is a general consensus that an antagonism between dynamic processes favoring alignment between the particles' velocities and noise is the basic mechanism which triggers a phase transition from an isotropic to a polar ordered state. The computational model by Vicsek *et al.* [17] adapts this idea and implements it as an update rule in the spirit of a cellular automaton: each particle aligns parallel to the average of all particles' orientations within some finite neighborhood.

On a more microscopic scale, Bertin *et al.* [18] have formulated the dynamics of propelled particle systems in the framework of kinetic theory. Collisions between particles are described by a half-angle alignment rule; i.e., one assumes that particles line up parallel to their average orientation upon binary collisions. While, similar to the Vicsek model, this rule phenomenologically accounts for the dissipative character of collisions, it is not rooted in a microscopic analysis of actual collision processes between active particles. In the meantime there are, however, a range of well-characterized experimental model systems including actin and microtubule gliding assays [2,4], and shaken granular particles [8,19], which are amenable to a quantitative analysis at the scale of collisions between individual particles. These studies highlight that actual collisions differ from generic interaction rules in two important respects: (i) the postcollision particle orientations are not symmetric with respect to the average of the precollision directions, but depend on both the relative orientation and relative position of the colliding particles before the collision [Fig. 1]; (ii) frequently, one finds "indifferent" collision events where collisions do not change the relative orientations of the collision partners [8,19]. Therefore, the region of configuration space supporting aligning collisions is restricted, and it is thus far from obvious whether binary, dissipative interactions actually contribute to the formation of order in active systems. This raises an important question: with no additional assumptions to be made, does the integrated effect of binary particle interactions in active systems suffice to establish a state of collective motion on macroscopic scales?

To address this question, we investigate the physics of binary collisions between propelled rodlike particles and its impact on the emergence of polar order within the framework of kinetic theory. Our starting point is a numerical analysis of the collision process between propelled rodlike particles. The goal is to motivate a broad class of mesoscopic collision rules comprising the most pertinent features of the dissipative collisions. Integrating this collision rule into a Boltzmann equation, we give a systematic study of the ordering capabilities of active systems in terms of the underlying collision dynamics. Our findings suggest that a kinetic description based on binary particle interactions is suitable to capture ordering processes which

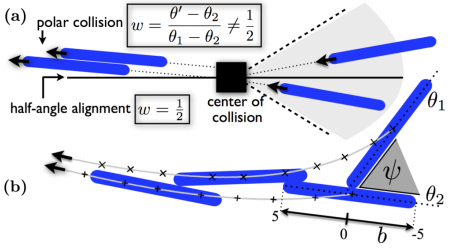

FIG. 1 (color online). (a) Rod interactions within an angular alignment range $\tilde{\psi}$ (grey shaded) lead to polar alignment, whose direction typically deviates from the half-angle alignment $w = \frac{1}{2}$ [w is directly given by Eq. (1)]. (b) Simulated example trajectory for a model of propelled rigid rods (relative angle $\psi \approx \pi/3$, impact parameter $b \approx 0$ in units of rod diameter, $w(\pi/3, 0) \approx 1.3$).

proceed via a gradual reduction in the spread of particle orientations, but fails if collective motion patterns emerge from clustering processes. Within our kinetic framework, we demonstrate that the presence of noise in the collision process (collision noise) imposes a "minimum efficiency requirement" on the underlying microscopic collision dynamics if collective motion is to be observed. Finally, we address the system's spatiotemporal behavior using a numerical solution of the underlying kinetic equations [20]. We demonstrate that, for a large class of generic collision rules, the formation of wavelike patterns, as previously observed in agent-based simulations (see, e.g., Ref. [21]), is a robust feature accompanying the transition to collective motion and rendering this phase transition discontinuous.

Two microscopic scenarios.—To quantify binary particle collisions, we performed numerical simulations for two exemplary models of propelled rodlike particles (length $L = 10$, diameter $d = 1$) moving in a two-dimensional over-damped environment (for details, see Supplemental Material [22]). Specifically, we considered hard-core rigid, propelled rods as in [23], and a bead-spring model for propelled stiff polymers with a finite bending modulus, interacting by a short-ranged polar alignment interaction. Each particle is driven by a constant propelling force, pointing along the long axis of the rod or parallel to the polymer's contour. We performed scattering studies by preparing the particles with different relative precollision orientations $\psi = \theta_1 - \theta_2 \in [0, \pi]$ ($\theta_{1/2}$: precollision rod orientations) and different impact parameters b (measuring the location of impact along the "target particle's" contour; cf. Fig. 1), and observe the resulting relative postcollision orientations $\psi' = \theta_1' - \theta_2'$ ($\theta_{1/2}'$: postcollision rod orientations). The corresponding results are summarized in Figs. 2(a) and 2(b).

Although quantitative differences are manifest, there are distinct qualitative features which equally apply to both scattering studies: collisions may be classified either as "indifferent", where the relative scattering angle remains

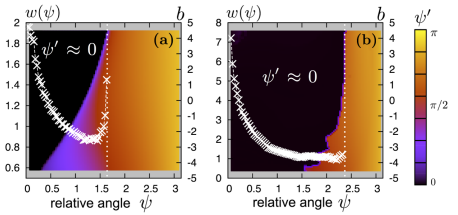

FIG. 2 (color online). Binary scattering plot: relative postcollision angle $\psi' = \theta_1' - \theta_2'$ (scale bar), versus impact parameter b and relative precollision angle ψ, for propelled hard rods (a), and stiff polymers (b). The mesoscopic alignment weight $w(\psi)$ and the alignment range $\bar{\psi}$ are indicated as crosses and vertical dotted lines, respectively. $L = 10$; for simulation details and videos refer to Supplemental Material [22].

virtually unchanged ($\psi' \approx \psi$) [24], or "polar alignment" events with $\theta_1' = \theta_2' =: \theta'$, i.e., $\psi' = 0$. These two regimes are delineated by a rather sharp boundary denoted as $\psi_{\max}(b)$, which is the maximum value of ψ in the regime where $\psi' \approx 0$. For simplicity, we will approximate this boundary by a single angle $\bar{\psi} = \max_b \psi_{\max}(b)$ which we term the effective alignment range [indicated by vertical dotted lines in Figs. 2(a) and 2(b)]. Within the alignment range ($\psi \le \bar{\psi}$), the postcollision angle θ' is an intricate function of the precollision angles and the impact parameter. Due to rotational invariance, it is of the form $\theta' = w(\psi, b)\theta_1 + [1 - w(\psi, b)]\theta_2$, where $w(\psi, b)$ can be interpreted as microscopic alignment weight characteristic for the respective model; cf. Fig. 1(a). Since we are aiming at a Boltzmann approach which does not resolve length scales comparable to the size of single particles, we adopt a mean-field approach and average over all impact parameters to introduce a mesoscopic alignment weight $w(\psi) := \langle w(\psi, b)\rangle_b$. It defines the relative magnitude of the precollision angles in the postcollision angle:

$$\theta' = w(\psi)\theta_1 + [1 - w(\psi)]\theta_2. \tag{1}$$

Taken together, the alignment range $\bar{\psi}$ and the alignment weight $w(\psi)$ constitute a generalized mesoscopic collision rule. It accounts for indifferent scattering events as well as deviations from half-angle alignment ($w = \frac{1}{2}$). Figure 2 shows the actual form of both quantities for the particular examples discussed above. Next, abstracting from the two particular examples given, we explore the consequences of such generalized collision rules for the ordering propensity of active matter.

Analytical formulation.—The Boltzmann equation for driven particles in two spatial dimensions takes the following general form [18]:

$$\partial_t f(\vec{r}, \theta, t) + v_0 \vec{e}(\theta) \cdot \nabla f(\vec{r}, \theta, t) = I_d + I_c. \tag{2a}$$

Here, $f(\vec{r}, \theta, t)$ is the one-particle distribution function, and v_0 and $\vec{e}(\theta)$ denote the magnitude and direction of the velocity vector of freely moving particles, respectively. I_d accounts for rotational particle diffusion with Gaussian-distributed angular increments φ [with standard deviation σ_0] occurring with a rate λ [25]

$$I_d = \lambda \left\langle \int_{-\pi}^{\pi} d\phi f(\phi)[\delta(\theta - \phi - \varphi) - \delta(\theta - \phi)] \right\rangle_{\varphi}. \tag{2b}$$

The collision integral

$$I_c = \left\langle \int_{-\pi}^{\pi} d\phi \int_{-\bar{\psi}}^{\bar{\psi}} d\psi \mathcal{S}(L, d, \psi) f(\phi) f(\phi + \psi) \times [\delta(\theta - \phi - w(\psi)\psi - \eta) - \delta(\theta - \phi)] \right\rangle_{\eta}, \tag{2c}$$

quantifies binary scattering events and depends on the mesoscopic collision rule. In Eq. (2c), $\mathcal{S}(L, d, \psi) = 4v_0 d|\sin(\psi/2)|(1 + (L/d - 1)|\sin\psi|/2)$ denotes the

"differential scattering cross section" [26]. We have also included stochastic effects by adding a Gaussian-distributed angle η [with standard deviation σ] to the postcollision angle.

To calculate the onset of polar order we analyze Eq. (2) in terms of Fourier modes $\hat{f}_k = \int_{-\pi}^{\pi} d\theta e^{ik\theta} f(\theta)$:

$$\partial_t \hat{f}_k + \frac{v_0}{2}[\partial_x(\hat{f}_{k+1} + \hat{f}_{k-1}) - i\partial_y(\hat{f}_{k+1} - \hat{f}_{k-1})] = -\lambda(1 - e^{-(k\sigma_0)^2/2})\hat{f}_k + \sum_{n=-\infty}^{\infty} I_{n,k}\hat{f}_n\hat{f}_{k-n}, \quad (3)$$

where the Fourier coefficients of the collision kernel $I_{n,k}$ are given in [22]. The first two Fourier components, are related to the (hydrodynamic) particle density $\rho = \hat{f}_0$ and the momentum density $\vec{\tau} = \rho\vec{u} = v_0\hat{f}_1$, where $\vec{u}$ denotes the hydrodynamic velocity. We are interested in the regime close to the transition from an isotropic state, $f(\vec{r}, \theta, t) = (1/2\pi)$, toward a polar state. For our base states, we then assume $|\vec{u}| \ll v_0$ and, consequently, $|\hat{f}_k| = \mathcal{O}[(|\vec{u}|/v_0)^k] \ll 1$. We are thus able to truncate Eqs. (3) by setting $\hat{f}_k \approx 0$ for all $k > 2$ [18,27]. Since the instability of the isotropic state toward formation of collective order occurs at zero wave number [22], we may restrict ourselves to spatially homogeneous systems and drop all spatial derivatives:

$$\partial_t \rho = 0, \quad (4a)$$

$$\partial_t \boldsymbol{\tau} = -\nu_1 \boldsymbol{\tau} + \nu_2^{-1}[I_{1,2}(I_{-1,1} + I_{2,1})]\boldsymbol{\tau}^2\boldsymbol{\tau}, \quad (4b)$$

where $\nu_k = 1 - e^{-(k\sigma_0)^2/2} - \rho(I_{0,k} + I_{k,k})$. In Eqs. (4), variables have been rescaled: $t \to t/\lambda$, $\rho \to \rho\lambda/\bar{S}$, $\boldsymbol{\tau} \to \boldsymbol{\tau} v_0\lambda/\bar{S}$, $I_{n,k} \to I_{n,k}\bar{S}$ with $\bar{S} = (2\pi)^{-1}\int_{-\bar{\psi}}^{\bar{\psi}} S(L, d, \psi) d\psi$ the "total scattering cross section" for polar collisions. In these units, ρ measures the frequency of collisions relative to the frequency of self-diffusion, λ. Depending on the alignment range $\bar{\psi}$, ν_2 might turn negative, in which case Eqs. (4) would have to be complemented by equations for higher order broken-symmetry variables, like the nematic tensor [28]. Here, we restrict ourselves to the discussion of the polar case, where $\nu_2 > 0$. Then, Eq. (4a) simply expresses conservation of particle number, and Eq. (4b) captures the formation of collective motion via spontaneous breaking of rotational symmetry.

The isotropic state $\boldsymbol{\tau} = 0$ becomes unstable at a threshold density ρ_t, determined by $\nu_1(\rho_t) = 0$:

$$\rho_t[w(\psi); \bar{\psi}] = \frac{1 - e^{-\sigma_0^2/2}}{I_{0,1}[w(\psi); \bar{\psi}] + I_{1,1}[w(\psi); \bar{\psi}]}. \quad (5)$$

Importantly, the analytical form of ρ_t, Eq. (5), is exact, i.e., independent of the particular scheme used to truncate the Fourier space Boltzmann equation [Eq. (3)], and establishes a direct connection between the microscopic details of particle collisions and the location of the phase boundary toward collective motion. Subsequent quantitative investigations of this connection are greatly facilitated by the fact that the functional space of all alignment weight functions $w(\psi)$ can be organized in terms of equivalence classes, using the equivalence relation $w_1(\psi) \sim w_2(\psi)$ if and only if $\rho_t[w_1(\psi)] = \rho_t[w_2(\psi)]$. It can be shown [22] that each such equivalence class contains one and only one constant alignment weight function $\bar{w}$, which can be determined from any (e.g., experimentally measured) $w(\psi)$ by inverting the relation $\rho_t[w(\psi)] = \rho_t[\bar{w}]$. In what follows, we will refer to $\bar{w}$ as "effective alignment weight" and use it as a convenient "parameterization" of the functional space of all alignment weight functions. The symmetry of the Boltzmann equation [Eq. (2)] with respect to $\bar{w} \to 1 - \bar{w}$, allows us to consider $\bar{w} \geq 0.5$ without loss of generality.

Analytical results.—Figure 3(a) shows the threshold density ρ_t as a function of the effective alignment weight $\bar{w}$ and different noise strengths σ.

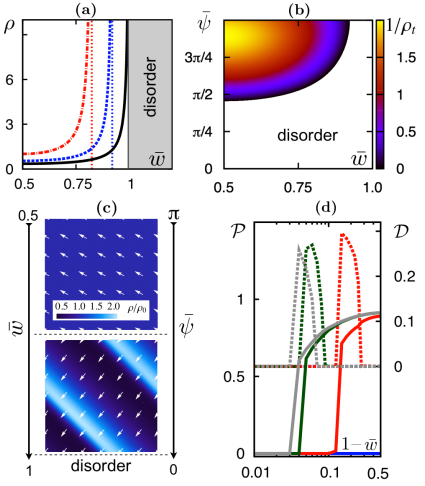

FIG. 3 (color online). (a) Transition density $\rho_t(\bar{w})$: curves from left to right (dash-dotted, dashed, solid) correspond to $\sigma = \{0.7, 0.5, 0\}$ with $\bar{\psi} = \pi$. (b) $\rho_t^{-1}(\bar{w}, \bar{\psi})$ for $\sigma = 0.5$. Parameters for (a) and (b): $L/d = 1$, $\sigma_0 = 0.5$. Stationary numerical solution of Eq. (2): (c) Snapshots of observed polar patterns (periodic boundary conditions; arrows: normalized, local polarization) for $\bar{\psi} = 3\pi/4$: homogeneously distributed density field (top, $\bar{w} = 0.8$) and polar-wave pattern (bottom, $\bar{w} = 0.92$, relative density differences are indicated, see color bar). (d) Total polarity $\mathcal{P}$ (solid lines) and spatial density variance $\mathcal{D}$ (dashed lines) versus $\bar{w}$ (from left to right: grey-green-red-blue correspond to $\bar{\psi} = \{\pi, 3\pi/4, \pi/2, \pi/4\}$). For $\psi = \pi/4$ (blue), $\mathcal{D} = 0$ and $\mathcal{P} = 0$ for all $\bar{w}$. Parameters for (c) and (d): $\rho_0 = 0.15$, $\sigma = \sigma_0 = 0.15$, $L/d = 1$.

For deterministic collisions, $\sigma = 0$, the transition density ρ_t is finite over the range $\bar{w} < 1$, and diverges as $\bar{w} \to 1$ [solid curve in Fig. 3(a)]. In the latter limit, the postcollision angle coincides with one of the precollision angles, cf. Eq. (1). This type of binary collision is on average equivalent to a specular reflection: due to particle exchange symmetry, two particles with precollision angles θ_1 and θ_2 are both either scattered into θ_1 (↗↖→↖↖) or θ_2 (↗↖→↗↗), with equal probability. Since two-particle correlations are not taken into account in the Boltzmann equation, we have $1/2(↖↖ + ↗↗) \equiv ↖↗$, which amounts to a specular reflection. This "alignment–reflection duality" carries over to arbitrary collision processes ($\bar{w} \neq 1$), and is inextricably linked to the Boltzmann equation due to the molecular chaos assumption. As a consequence, polar order cannot build up from a disordered state for effective alignment weights $\bar{w} \geq 1$. In the light of this discussion, the parameter $\bar{w} - 1 \equiv \delta$ can be reinterpreted as an angular dispersion factor: while for $\delta = 0$, the angular distribution remains invariant, any deviation from an isotropic distribution is amplified by collisions for $\delta < 0$, and polar order develops. Angular dispersion factors $\delta > 0$ (i.e., $\bar{w} > 1$) have the opposite effect. Obviously, the threshold density ρ_t also diverges for $\bar{\psi} \to 0$ (data not shown), which corresponds to the limiting case where all collisions are indifferent, i.e., to noninteracting particles.

The above picture is to be modified upon adding stochasticity to the collisions, $\sigma > 0$. Then, the poles of ρ_t are increasingly shifted toward the limiting case of optimal alignment conditions, i.e., $(\bar{w}, \bar{\psi}) = (\frac{1}{2}, \pi)$ [Figs. 3(a) and 3(b)]. Surprisingly, to compensate for the disaligning effect of collision noise, one needs both, a smaller angular dispersion δ, and a larger alignment range $\bar{\psi}$. Even for half-angle alignment, $\bar{w} = \frac{1}{2}$, any stochasticity during the collision process immediately sets a lower bound for the alignment range $\bar{\psi}$, which cannot be abrogated by increasing the density; cf. Fig. 3(b). In other words, the presence of collision noise imposes a "minimum efficiency requirement" on microscopic particle interactions for the emergence of polar order.

The popular half-angle alignment rule thus overestimates the effect of binary collisions on the buildup of orientational order. This is indeed the case for the two paradigmatic scenarios of propelled rods and stiff polymers discussed above: using the microscopic scattering data $\psi_{\max}(b)$ and $w(\psi, b)$ from our simulations, we computed the transition density ρ_t by means of Eq. (5). To get a precise estimate, we explicitly accounted for the functional dependence of the collision integrals on the microscopic alignment weight $w(\psi, b)$, only assuming uniformly distributed collision parameters b. Interestingly, the ensuing threshold densities for both models turn out to be negative. The failure of these models to establish a state of polar order suggests to reconsider the range of applicability of the Boltzmann approach to active systems. In fact, recent numerical and experimental work on similar systems [23,29,30] highlights the importance of nucleation and growth of clusters as a driving force behind the formation of large scale nonisotropic structures. Within these clusters, however, correlation effects become important which are incompatible with the alignment–reflection duality alluded to above. Thus, while the Boltzmann approach is well suited to capture the emergence of order via a gradual reduction in the spread of particle orientations, it breaks down if ordering proceeds via the formation of clusters.

Numerical solution of the Boltzmann equation.—To address the impact of $\bar{w}$ and $\bar{\psi}$ on the system's capability to form patterns, we numerically solved the Boltzmann equation [Eq. (2)] using a constant alignment weight, $w(\psi) = \bar{w}$ [20,22]. We tested that the numerical solution reproduces the phase boundary obtained from our analytical calculations, Eq. (5) (data not shown). In accordance with previous agent-based simulations [21] and with expectations from analytical considerations [18], we observe stable traveling wave patterns emerging from random initial conditions for $\rho \gtrsim \rho_t(\bar{w}, \bar{\psi})$, and with typical asymmetrical wave front profiles; cf. snapshot Fig. 3(c) and videos in the Supplemental Material [22]. Figure 3(d) illustrates the onset of ordering upon varying the effective alignment weight $\bar{w}$ at a fixed overall density $\rho_0 > \rho_t[\bar{w} = 0.5, \bar{\psi} = \pi]$, fixed noise parameters, and a set of alignment ranges $\bar{\psi}$: crossing the transition point (at $\rho_t[\bar{w}, \bar{\psi}] = \rho_0$), we observe a growth of the system's total polarity $\mathcal{P} = \overline{\boldsymbol{\tau}(\vec{r})}$ [overbar: spatial average], which is accompanied by the formation of traveling wave patterns in a parameter window adjacent to the ordering transition. As a simple indicator for wavelike patterns, we use the variance of the spatial density $\mathcal{D} = \overline{(\rho(\vec{r}) - \overline{\rho})^2}/\overline{\rho}^2$ measured at times where the traveling wave patterns become stationary. The emergence of wavelike patterns in the transition region toward polar order seems to be a generic consequence of linear collision rules, i.e., constant alignment weight functions $w(\psi) = \bar{w} = \text{const}$.

Contrary to what can be expected from the spatially homogeneous dynamics, Eq. (4b), our numerical solutions [Fig. 3(d)] indicate that the development of spatial inhomogeneities in the form of traveling wave fronts causes the polar order parameter $\mathcal{P}$ to undergo a discontinuous jump. This indicates a first-order phase transition toward polar order, rather than a second-order transition. An analogous transition behavior is observed upon varying the density ρ at constant values for the collision parameters (not shown). Whether or not a more complicated, nonlinear collision dynamics alters this behavior poses an interesting question for future work.

We acknowledge support by the Deutsche Forschungsgemeinschaft in the framework of the SFB 863 "Forces in Biomolecular Systems" and the German

Excellence Initiatives via the program "NanoSystems Initiative Munich (NIM)". This research was also supported in part by the National Science Foundation under Grant No. NSF PHY11-25915. F. Thüroff and C. A. Weber contributed equally to this work.

*frey@lmu.de

[1] T. Butt, T. Mufti, A. Humayun, P. B. Rosenthal, S. Khan, S. Khan, and J. E. Molloy, J. Biol. Chem. **285**, 4964 (2009).
[2] V. Schaller, C. Weber, C. Semmrich, E. Frey, and A. R. Bausch, Nature (London) **467**, 73 (2010).
[3] V. Schaller, C. Weber, E. Frey, and A. R. Bausch, Soft Matter **7**, 3213 (2011).
[4] Y. Sumino, K. H. Nagai, Y. Shitaka, D. Tanaka, K. Yoshikawa, H. Chaté, and K. Oiwa, Nature (London) **483**, 448 (2012).
[5] C. Dombrowski, L. Cisneros, S. Chatkaew, R. E. Goldstein, and J. O. Kessler, Phys. Rev. Lett. **93**, 098103 (2004).
[6] H. P. Zhang, A. Be'er, E.-L. Florin, and H. L. Swinney, Proc. Natl. Acad. Sci. U.S.A. **107**, 13 626 (2010).
[7] J. Deseigne, O. Dauchot, and H. Chaté, Phys. Rev. Lett. **105**, 098001 (2010).
[8] J. Deseigne, S. Leonard, O. Dauchot, and H. Chaté, Soft Matter **8**, 5629 (2012).
[9] A. Kudrolli, G. Lumay, D. Volfson, and L. S. Tsimring, Phys. Rev. Lett. **100**, 058001 (2008).
[10] M. Ballerini *et al.*, Animal Behaviour **76**, 201 (2008).
[11] V. Schaller, C. A. Weber, B. Hammerich, E. Frey, and A. R. Bausch, Proc. Natl. Acad. Sci. U.S.A. **108**, 19 183 (2011).
[12] I. S. Aranson and L. S. Tsimring, *Granular Patterns* (Oxford University press, New-York, 2009), Chap. 9.
[13] K. Kruse, J. F. Joanny, F. Jülicher, J. Prost, and K. Sekimoto, Eur. Phys. J. E **16**, 5 (2005).
[14] T. Vicsek and A. Zafeiris, Phys. Rep. **517**, 71 (2012).
[15] S. Ramaswamy, Annu. Rev. Condens. Matter Phys. **1**, 323 (2010).
[16] M. C. Marchetti, J. F. Joanny, S. Ramaswamy, T. B. Liverpool, J. Prost, M. Rao, and R. A. Simha, Rev. Mod. Phys. **85**, 1143 (2013).
[17] T. Vicsek, A. Czirok, E. Ben-Jacob, I. Cohen, and O. Shochet, Phys. Rev. Lett. **75**, 1226 (1995).
[18] E. Bertin, M. Droz, and G. Grégoire, Phys. Rev. E **74**, 022101 (2006); J. Phys. A **42**, 445001 (2009).
[19] C. A. Weber, T. Hanke, J. Deseigne, S. Léonard, O. Dauchot, E. Frey, and H. Chaté, Phys. Rev. Lett. **110**, 208001 (2013).
[20] F. Thüroff, C. A. Weber, and E. Frey (to be published).
[21] H. Chaté, F. Ginelli, G. Grégoire, and F. Raynaud, Phys. Rev. E **77**, 046113 (2008).
[22] See Supplemental Material at http://link.aps.org/supplemental/10.1103/PhysRevLett.111.190601 for videos and more information.
[23] F. Peruani, A. Deutsch, and M. Bär, Phys. Rev. E **74**, 030904 (2006).
[24] Since indifferent events do, in general, change the mean orientation of the particles, they could be described by an effective noise term, which will be neglected here.
[25] The argument of $f(\phi)$ is understood modulo 2π.
[26] C. A. Weber, F. Thüroff, and E. Frey, New J. Phys. **15**, 045014 (2013).
[27] I. S. Aranson and L. S. Tsimring, Phys. Rev. E **71**, 050901 (2005).
[28] A. Peshkov, I. S. Aranson, E. Bertin, H. Chate, and F. Ginelli, Phys. Rev. Lett. **109**, 268701 (2012).
[29] C. A. Weber, V. Schaller, A. R. Bausch, and E. Frey, Phys. Rev. E **86**, 030901 (2012).
[30] F. Peruani, J. Starruß, V. Jakovljevic, L. Søgaard-Andersen, A. Deutsch, and M. Bär, Phys. Rev. Lett. **108**, 098102 (2012).

4

NUMERICAL TREATMENT OF THE BOLTZMANN EQUATION

4.1 STARTING POINT OF THE PROJECT

The active Boltzmann equation, as discussed in the previous chapters, provides a versatile tool to set the mathematical framework for the investigation of systems of self-propelled particles. The main reason behind this is twofold: First, the Boltzmann equation explicitly incorporates a model of the system's dynamics at the level of single particles. Secondly, as an equation of motion for the one-particle distribution function it lends itself as a starting point to assess the system's macroscopic properties by taking appropriate averages. As a consequence, Boltzmann equation based approaches can play a pivotal role in establishing a connection between purely microscopic, agent based models on the one hand, and symmetry based, phenomenological theories on the other hand.

Although conceptually highly appealing, so far these potentials are of rather limited practical use. In previous analytical works on active systems [5, 20, 6, 4, 168, 21, 108, 107, 19, WTF13, TWF13], the main purpose of the Boltzmann equation has been to formulate the underlying physical model mathematically. Due to its intricate mathematical structure, however, progress toward a direct solution of this partial integro-differential equation has remained prohibitively difficult. The Boltzmann equation, therefore, mainly served as vehicle to derive a set of hydrodynamic equations for the systems under consideration. As has been discussed in chapters 1 – 3, a popular strategy to proceed an-

alytically, is to investigate the Boltzmann equation in Fourier space, where it transforms into an infinite hierarchy of coupled partial differential equations. To make this system of equations amenable to analytical methods, the Fourier space representation of the Boltzmann equation needs to be truncated so as to arrive at a finite number of equations.

Unfortunately, to this day such truncation schemes rely solely on physical intuition and have not yet been derived by any rigorous means. While the situation is under control in disordered systems, where the form of the one-particle distribution function can typically be inferred from the model definition and its respective symmetries, problems arise in regions of the parameter space where macroscopic order develops. In these cases, errors can barely be assessed and it is exceedingly difficult to estimate the range of parameters where such truncated equations constitute reasonable approximations to the underlying Boltzmann equation. Although it is generally believed that "appropriately" truncated systems of equations are capable to reproduce the properties of the Boltzmann equation right at the transition to macroscopic order, spurious instabilities of these equations have been reported for parameters even slightly beyond the transition line [107].

In our work *"Numerical treatment of the Boltzmann equation for self-propelled particle systems"* [TWF14], we propose an alternative, numerical approach to treat the Boltzmann equation in real space. For future reference, we will use the abbreviation *SNAKE* (solving numerically active kinetic equations) to refer to the corresponding computational scheme. This real space approach completely dispenses with a Fourier space transformation and, therefore, avoids complications resulting from an ad hoc truncation of an infinite hierarchy of equations. Instead, *SNAKE* is based on a direct discretization of the Boltzmann equation itself and thus naturally leads to a closed set of equations which is immediately amenable to numerical integration. In particular, *SNAKE* retains a plain connection to the original (continuous) Boltzmann equation and should be applicable even for parameters well beyond the onset of macroscopic order. *SNAKE*, therefore, allows us to exploit the full potential of the Boltzmann equation approach to

active systems and sets the stage for an in-depth analysis of a generic modeling framework for self-propelled particle systems.

While a complete exposition of the work, including a detailed description of the numerical scheme underlying *SNAKE*, is presented in the appended manuscript, section 4.4, a brief survey over the most pertinent physical results is given in the next section 4.2. Finally, potential future applications of *SNAKE* are highlighted in section 4.3.

4.2 SUMMARY OF MAIN RESULTS

The emergence of collective motion in active systems is probably best understood in terms of a competition between aligning particle interactions and the amount of randomness superimposed on single particle trajectories. Aligning particle interactions are at the heart of the formation of macroscopic order. On the other hand, correlations among particles are subject to finite memory times due to the erratic nature of particle motions. This finite memory can only be overcome if the frequency of particle collisions is sufficiently large, such that macroscopic order develops. As highlighted in the introduction, this notion has been implemented in the famous Vicsek model. [152], which serves as an archetypical framework to investigate the emergence of collective motion ever since.

At the level of the Boltzmann equation, a similar model has been proposed by Bertin et al. [20, 21] ("BDG model"); also cf. discussions in chapter 1. According to the BDG model, spherically shaped particles move at a constant speed v in a two dimensional space. To account for the randomness of particle trajectories, the model assumes a run-and-tumble motion, where each particle's ballistic motion is perturbed at a constant frequency λ, with perturbations causing the orientation θ of the particle to change instantaneously by a random amount ζ_0,

$$\theta \xrightarrow{\lambda} \theta + \zeta_0 \qquad (\text{modulo } 2\pi), \tag{16}$$

where ζ_0 is drawn from a zero-mean Gaussian distribution with variance σ_0^2. To model the aligning effect of particle interactions,

binary collisions are implemented according to following half angle alignment rule,

$$(\theta_1, \theta_2) \to (\bar{\theta} + \zeta, \bar{\theta} + \zeta), \qquad \bar{\theta} \equiv \frac{\theta_1 + \theta_2}{2}, \tag{17}$$

where $\theta_{1/2}$ denote the orientations of the two colliding particles prior to the actual collision, and where ζ adds a random amount of noise to the post-collision angle $\bar{\theta}$. Again, ζ is taken to be a zero-mean Gaussian random variable with variance σ^2.

We have implemented the BDG model as introduced above, using our newly developed *SNAKE* algorithm, and investigated its ordering behavior as the overall density (ρ_0) and the noise levels (σ, σ_0) were varied. Specifically, our focus is on the transition of the system between a spatially homogeneous, isotropic state at low overall densities ρ_0 (high noise levels) and a spatially homogeneous, polar ordered state at high densities (low noise levels), where the polar order parameter $\langle \boldsymbol{\varphi} \rangle_x$ (quantifying the spatially averaged macroscopic momentum) attains non-zero values. In our work [TWF14], we establish two novel key insights.

First of all, we observe that the order-disorder transition in the BDG model bears striking similarities to a liquid-gas transition in equilibrium systems. If the density of an equilibrium fluid in its gas phase is isothermally increased beyond the binodal threshold, the gas phase becomes metastable. In this regime, large enough density fluctuations initiate the nucleation and growth of high density liquid droplets, which eventually leads to phase segregation and spatial coexistence between the liquid and gas phase. At still larger densities, the gas phase becomes linearly unstable and spinodal decomposition occurs. In this case, arbitrarily small fluctuations in the local density are amplified and the system undergoes spontaneous density segregation with the mole fraction of the liquid phase (gas phase) increasing (decreasing) linearly with the system's specific volume, such that the liquid phase takes over the entire system at large enough densities. An analogous line of arguments applies in the reverse scenario, where the system's density is isothermally decreased, starting from a liquid state. Intriguingly, we observe the exact same behavior in the context of the order-disorder transition in the BDG

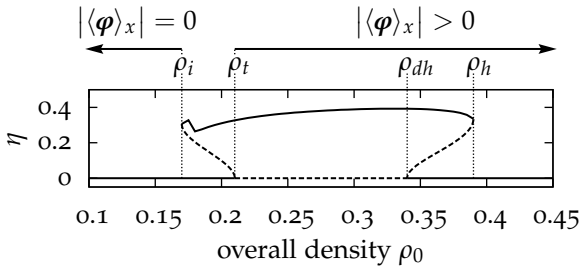

Figure 9.: Sketch of the bifurcation diagram for the bifurcation parameter ρ_0 (at $\sigma = \sigma_0 = 0.5$); cf. [TWF14]. Here η measures the difference between the system's maximum and minimum local density, and thus quantifies the degree of density segregation. Solid lines indicate stable fixed points of the system's dynamics and have been determined numerically. Dashed lines are drawn "by hand" and indicate the estimated position of unstable fixed points. ($\langle\boldsymbol{\varphi}\rangle_x$ denotes the spatially averaged polar order parameter which quantifies the system's net momentum).

model. If we fix the noise levels (σ, σ_0) to some finite values and then slowly increase the overall density ρ_0, starting from a spatially homogeneous and isotropic low-density state, we find the following ordering behavior, which is also summarized in Fig. 9. For densities up to a "binodal threshold" ρ_i, the isotropic "gas phase" is stable. For densities between the "binodal" and "spinodal" thresholds, $\rho_i < \rho_0 < \rho_t$, the spatially homogeneous, isotropic "gas state" becomes non-linearly unstable and becomes susceptible to large enough perturbations in the local density. If present, these perturbations lead to the formation of a density segregated state, where high-density polar ordered structures travel on an isotropic low-density "particle sea". Upon further increasing the density beyond the spinodal threshold ρ_t, the spatially homogeneous "gas state" turns linearly unstable and the aforementioned density segregation occurs spontaneously. A detailed explanation concerning the mechanics behind this formation of spatial inhomogeneities has been given in section 2.2. For densities $\rho_t < \rho_0 < \rho_h$, the surface fraction of the high-density, polar ordered phase is found to increase linearly with ρ_0 until the system transitions into a spatially homogeneous polar ordered

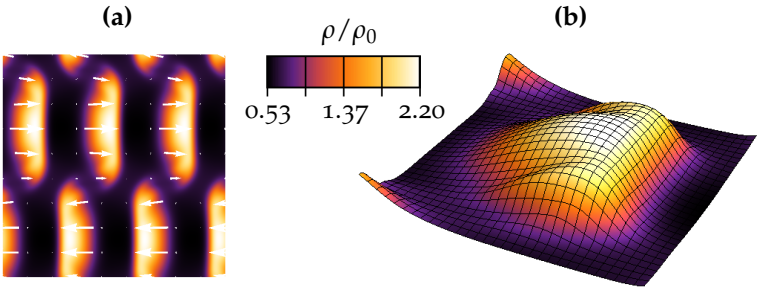

Figure 10.: **(a)** Typical snapshot of a cluster lane pattern in its stationary state. Lanes of polar clusters with opposite orientations render the system's large scale order nematic. **(b)** Three dimensional density profile of a single cluster moving to the right. The cluster's finite extent implies a non-trivial profile along the lateral direction. In the longitudinal direction, the cluster patterns exhibit an asymmetric shape which closely resembles that of the more familiar traveling wave patterns; cf. [TWF14]. Color code indicates local density ρ relative to overall density ρ_0.

state at $\rho_0 = \rho_h$. Again, the reverse scenario follows the same line arguments with the binodal and spinodal densities ρ_i and ρ_t replaced by their respective counterparts ρ_h and ρ_{dh}. Interestingly, the same overall picture has been reported recently in the context of active Ising spins with a discrete Z_2 symmetry in Ref. [133].

The second key result of this work concerns the specific formation of patterns inside the density segregated parameter regime of the BDG model. In previous works of this model and related approaches [21, 57, 31, 64, 65, 28], density segregation has been discussed in terms of solitary waves with "infinite" lateral extent. The respective states are purely polar ordered, i.e. macroscopic particle flows are strictly unidirectional. In our numerical solutions of the Boltzmann equation for the BDG model, however, we find one additional type of density segregated patterns consisting of polar clusters with finite spatial extent both, in longitudinal and in lateral directions. The clusters themselves are arranged in a number of parallel lanes, where each lane is made

up of cluster with the same polarity. In particular, consecutive cluster lanes are of opposite polarity such that the overall state of the system exhibits nematic order on large length scales, despite purely polar interactions on microscopic scales; cf. Fig. 10. In our numerical solutions of the BDG model, we observe parameter space coexistence between the more familiar solitary wave patterns, and this novel type of cluster lane patterns. Most intriguingly, however, preliminary studies on the selection frequency between these two types of patterns indicate a linear increase in the selection frequency of cluster lanes as the system size in the numerical computations increases. This entails a number of interesting questions concerning the genuine large scale properties of the BDG model, and, possibly, related models for active systems. In particular, the questions of whether or not the transverse correlation length in density segregated polar systems would actually diverge so as to give rise to the formation of solitary waves with infinite lateral extent would be worth of critical reexamination.

4.3 OUTLOOK

The flexibility of the Boltzmann equation to accommodate a great variety of different modeling approaches makes *SNAKE* a convenient and powerful platform to investigate a wide range of important questions in active matter research. Here, we give a brief overview over potential future applications of *SNAKE*.

Most studies on self-propelled particle systems have been conducted by means of simplified, generic modeling approaches like the BDG model discussed in this chapter. However, even *in silico* systems, like the simulation framework employed in section 3.4 to conduct a simple binary scattering analysis, exhibit a more subtle phenomenology at the microscopic, single particle level than is suggested by such generic approaches. Yet, to which extent system-specific differences in such microscopic details manifest themselves on macroscopic scales remains only poorly understood. Following our multi-scale approach proposed in section 3.4, and implementing the corresponding kinetic description by means of *SNAKE*, one may hope to make progress in this important direction.

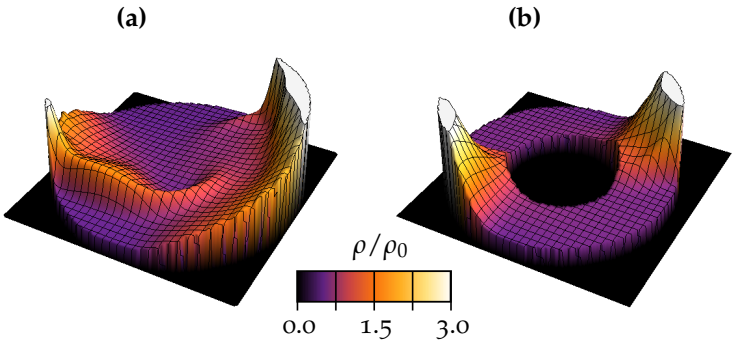

Figure 11.: **(a)** Sample computation of the BDG model with reflective boundary conditions and circular confinement geometry. Parameters: $\rho_0 = 0.3$, $\sigma = \sigma_0 = 0.5$. **(b)** Sample computation of the BDG model with reflective boundary conditions and ring-like confinement geometry. Parameters: $\rho_0 = 0.25$, $\sigma = \sigma_0 = 0.5$. Color code indicates local density ρ relative to overall density ρ_0.

Moreover, as has been demonstrated in section 2.4, the Boltzmann equation formalism is easily extended to the description of several distinct, mutually interacting particle species. It is well established that the transport of particles critically controls the emergence of spatial patterns in populations with chemical reactions or competition between different species. Examples of such systems include the famous Turing instability in reaction-diffusion systems [34], as well as the spatial coexistence in mobile populations with cyclic dominance between species [116]. Yet, the physical effects of active particle propulsion in conjunction with dissipative particle interactions and competitive and / or chemical interactions between members of different species remain largely elusive. The Boltzmann equation approach, as discussed in the present part of this thesis, provides a natural starting point for research in this direction. *SNAKE* then constitutes a powerful vehicle to directly access the actual solutions of the corresponding kinetic equations.

Finally, as will be detailed in the following section 4.4, the particular implementation of *SNAKE* lends itself to the incorpora-

tion of arbitrary boundary conditions and geometries; cf. Fig. 11. Since *SNAKE* is based on a kinetic description of the underlying system, boundary conditions can be formulated in terms of actual microscopic pictures of particle-wall interactions. Geometrical confinement is part and parcel of virtually any experimental measurement and has been recognized to play a vital role in the establishment of patterns of collective motion [159]. Understanding the impact of boundaries on the bulk behavior of active systems is, therefore, of utmost importance both, to properly interpret experimental data and to design meaningful experimental setups. Moreover, the large amount of flexibility *SNAKE* offers to model physical boundaries allows even for the implementation of more exotic confinement scenarios like moving or elastic boundaries. The latter case is especially relevant in the context of living cells, where interactions between an active gel (the cytoskeleton) and a flexible boundary (the cell's membrane) play a key role in the control of the cell's migratory behavior [1, 115, 46, 112]; cf. part ii of this thesis.

Numerical Treatment of the Boltzmann Equation for Self-Propelled Particle Systems

Florian Thüroff, Christoph A. Weber, and Erwin Frey

Arnold Sommerfeld Center for Theoretical Physics and Center for NanoScience, Department of Physics, Ludwig-Maximilians-University, Theresienstrasse 37, D-80333 Munich, Germany

(Received 2 April 2014; revised manuscript received 3 July 2014; published 14 November 2014)

Kinetic theories constitute one of the most promising tools to decipher the characteristic spatiotemporal dynamics in systems of actively propelled particles. In this context, the Boltzmann equation plays a pivotal role, since it provides a natural translation between a particle-level description of the system's dynamics and the corresponding hydrodynamic fields. Yet, the intricate mathematical structure of the Boltzmann equation substantially limits the progress toward a full understanding of this equation by solely analytical means. Here, we propose a general framework to numerically solve the Boltzmann equation for self-propelled particle systems in two spatial dimensions and with arbitrary boundary conditions. We discuss potential applications of this numerical framework to active matter systems and use the algorithm to give a detailed analysis to a model system of self-propelled particles with polar interactions. In accordance with previous studies, we find that spatially homogeneous isotropic and broken-symmetry states populate two distinct regions in parameter space, which are separated by a narrow region of spatially inhomogeneous, density-segregated moving patterns. We find clear evidence that these three regions in parameter space are connected by first-order phase transitions and that the transition between the spatially homogeneous isotropic and polar ordered phases bears striking similarities to liquid-gas phase transitions in equilibrium systems. Within the density-segregated parameter regime, we find a novel stable limit-cycle solution of the Boltzmann equation, which consists of parallel lanes of polar clusters moving in opposite directions, so as to render the overall symmetry of the system's ordered state nematic, despite purely polar interactions on the level of single particles.

DOI: 10.1103/PhysRevX.4.041030 Subject Areas: Soft Matter, Statistical Physics

I. INTRODUCTION

Developing a deeper understanding of active matter [1–4] has been the major focus of a considerable amount of theoretical work over the last few decades [5–20]. In recent years, kinetic theory has gained considerable popularity to assess the ordering behavior in systems of actively propelled particles [21–36]. In this context, the Boltzmann equation provides a particularly compelling approach to active matter systems. Apart from its inherent limitations, which are largely due to the assumptions of binary particle interactions and molecular chaos (see Refs. [28,34,37]), the following advantages of this framework are manifest: (i) The structure of the Boltzmann equation, relating convection and collision processes on the level of the one-particle distribution function, is ideally suited to explicitly implement a microscopic picture of particle dynamics. (ii) Because of its mesoscopic character, the Boltzmann equation provides an immediate connection to the system's hydrodynamic variables, which naturally arise in the form of the various moments of the one-particle distribution function. Therefore, the Boltzmann equation sets up a direct link between the microscopic dynamics of the system's constituent particles and the corresponding physics emerging on hydrodynamic length and time scales. Moreover, since the Boltzmann equation keeps track of all parameters used to formulate a particle-level description of the system under study, the resulting hydrodynamics can be studied explicitly in terms of those microscopic parameters.

The Boltzmann equation and related kinetic frameworks have been employed in a number of previous studies on two-dimensional systems of self-propelled particles [19,22,26–28,30,31,33,38], mainly to derive a hydrodynamic description. To this end, an expansion technique is used to derive an infinite hierarchy of coupled equations of motion for the Fourier modes of the angular degrees of freedom of the one-particle distribution function. Since the zeroth-, first-, second-, and higher-order Fourier modes are directly related to the local average particle-number, polar, nematic, and higher-symmetry order parameters, the Fourier-space description lends itself as a starting point to extract a hydrodynamic description. In general, the derivation of such a hydrodynamic description is achieved by truncating the hierarchy of Fourier-space equations by means of a perturbation ansatz for the Fourier modes, which itself typically depends on the system's symmetries.

Following a similar strategy, a numerical approach based on an Enskog-like kinetic theory has recently been proposed in Ref. [38].

While such Fourier-space approaches have been successfully applied to investigate the onset of collective motion, the validity of the underlying truncation schemes remains largely elusive for parameters deeper inside the ordered region. In this work, we propose a Boltzmann-equation-based approach which we will refer to as SNAKE (solving numerically active kinetic equations). SNAKE focuses on a direct numerical solution of the Boltzmann equation in real space, without any explicit recourse to the aforementioned coupled hierarchy of equations in Fourier space. Such a direct numerical approach offers a number of advantages in the study of active systems, which can be summarized as follows. First of all, the real-space Boltzmann equation constitutes a closed description for the dynamics of the one-particle distribution function. Consequently, the range of validity of this direct numerical strategy is restricted only by inherent limitations of the Boltzmann equation itself but is not principally confined to a parameter region around the onset of collective motion. Second, SNAKE provides full access to the flexibility of the Boltzmann equation in the implementation of specific model systems that are based on a concrete microscopic picture of particle dynamics. Third, this flexibility equips this approach with particularly powerful capabilities to incorporate physical boundary conditions, which can be formulated on the basis of actual particle-wall interactions rather than on the level of macroscopic, hydrodynamic field variables. Finally, since all pertinent hydrodynamic fields are easily computed from the one-particle distribution function by taking appropriate averages, this numerical approach allows us to fully exploit the Boltzmann equation's potential to mediate between the physics on microscopic and macroscopic scales.

To demonstrate the benefits of SNAKE, we will present a detailed study of an archetypical model for active particles subject to binary, polar particle interactions, which has been proposed originally by Bertin *et al.* [22,26] and which we will henceforth refer to as the "Bertin-Droz-Guillaume model" (BDG model). As has been established previously [26], the BDG model transitions from a spatially homogeneous, fully isotropic state at low densities or high noise levels to a collectively moving state at high densities or low noise levels. In the vicinity of this phase transition, the polar order-parameter field was shown to be susceptible to a longitudinal instability [26], which in turn has been linked to the emergence of stable solitary-wave patterns propagating on an otherwise isotropic low-density background [34,38]. Well beyond the transition line to collective motion, this longitudinal instability disappears from the Boltzmann equation [26] and a spatially homogeneous state of collective motion has been shown to emerge [34].

Our work is structured as follows. In Sec. II, we discuss a discretization scheme for the Boltzmann equation of self-propelled particles in two spatial dimensions. The central result of this section is an update rule [Eq. (21)] that lends itself to direct numerical implementation. This section also contains a discussion of the general strategy to implement virtually arbitrary boundary conditions and geometries. Readers not interested in the details of the actual discretization procedure underlying the SNAKE algorithm may skip Secs. II B–II D and proceed to Sec. III.

There, we will exploit SNAKE's capabilities to address the stationary states of the BDG model over a broad range in parameter space (Sec. III A). In particular, we will show that our implementation of SNAKE consistently reproduces previously established analytical results on this model [26]. In Sec. III B, we focus on the onset of collective motion, which is accompanied by the formation of density-segregated patterns and hysteresis effects, as previously reported in numerical studies of the Vicsek model [8,14,38]. Additionally, in Sec. III C, we extend previous results on the flocking transition in polar systems [26,28,38] well beyond the onset of order. Specifically, we demonstrate the presence of an additional first-order phase transition from a spatially inhomogeneous, density-segregated phase to a spatially homogeneous polar phase, taking place well inside the ordered, broken-symmetry parameter regime (Sec. III D). Overall, we find striking similarities between the flocking transition to spatially homogeneous polar order, on the one hand, and the features of liquid-gas phase transitions in equilibrium systems, on the other hand. Analogous observations have been made previously in the context of a lattice model of active Ising spins, where a discrete up-down symmetry is spontaneously broken in two spatial dimensions [20]. In Sec. III E, we shift our focus to a deeper discussion of density-segregated patterns and report on the emergence of previously unseen "cluster-lane patterns" that seem to occupy the same parameter region as the familiar solitary-wave patterns and to constitute a stable limit-cycle solution of the underlying Boltzmann equation. These patterns consist of parallel lanes of polar clusters moving in opposite directions; see Figs. 6(b), 6(c), 11(b), and 11(c) for snapshots. Intriguingly, the stability of such patterns provides a mechanism to establish states of nematic macroscopic order, arising from perfectly polar particle interactions on microscopic scales. Finally, in Sec. III F, we investigate the coarsening dynamics for both wave and cluster-lane patterns within the density-segregated phase.

Section IV, then, summarizes our numerical approach, discusses our main findings, and gives an outlook of potential applications of SNAKE. In particular, this section gives a comprehensive and self-contained discussion of the most pertinent results established in the more technical Secs. II and III and can be read independently of these technical parts. Section IV has been written to provide the reader with a direct and nontechnical accessibility to the core results of this work.

II. DISCRETIZATION OF THE BOLTZMANN EQUATION

Here and in the following, we focus on a kinetic description for two-dimensional systems of actively propelled particles in an overdamped environment. As a simplifying assumption, we consider particles moving at constant speed v but variable orientation θ, such that each particle's velocity vector $\mathbf{v}$ can be written as $\mathbf{v} = v\hat{\mathbf{e}}_\theta$. ($\hat{\mathbf{e}}_\theta$ is the unit vector.) For particles with nearly constant propelling forces, assuming constant particle speed is a reasonable approximation in the "Aristotelian regime" where the dynamics is governed by a balance between propelling and dissipative forces and inertial effects can be neglected. Moreover, for sufficiently dilute systems, binary particle interactions are believed to dominate over higher-order interactions and the spatiotemporal dynamics of the one-particle distribution function $f(\mathbf{x}, \theta, t)$ can be captured by means of the Boltzmann equation [39].

A. Boltzmann equation for active particles

The most general form of the Boltzmann equation reads

$$\partial_t f(\mathbf{x}, \theta, t) + v\hat{\mathbf{e}}_\theta \cdot \nabla f(\mathbf{x}, \theta, t) = I_{\text{source}}[f; \theta]. \tag{1a}$$

The density of particles in the phase-space element $\boldsymbol{\omega} = [\mathbf{x}, \mathbf{x} + d\mathbf{x}] \times [\theta, \theta + d\theta]$ is being convected due the particles' active propulsion (left-hand side) and is, simultaneously, subject to sudden changes due to particle collisions, chemical reactions, etc., which are captured on the right-hand side of Eq. (1a) in the form of source terms I_{source}. To make contact to previous works on the Boltzmann equation for active systems [22,26,30], we consider two separate contributions to the source term

$$I_{\text{source}}[f; \theta] = I_{\text{SD}}[f; \theta] + I_{\text{C}}[f; \theta], \tag{1b}$$

which take into account rotational diffusion due to a fluctuating background and/or noisy propelling mechanism I_{SD} and binary particle collisions I_{C}, respectively.

To be specific, rotational diffusion is implemented using a constant "tumbling" rate λ and drawing the corresponding angular shifts from a given probability distribution p_0. The self-diffusion integral I_{SD} then takes the following form (omitting any explicit reference to space and time coordinates for brevity):

$$I_{\text{SD}}[f; \theta] = -\lambda f(\theta) + \lambda \int_{-\pi}^{\pi} [d\phi]_{(m)} f(\phi) p_0(\theta - \phi + 2m\pi), \tag{1c}$$

where we introduce the shorthand notation

$$\int_{-\pi}^{\pi} [d\phi]_{(m)} \equiv \sum_{m=-\infty}^{\infty} \int_{-\pi}^{\pi} d\phi$$

to take into account the 2π periodicity of $f(\theta)$. In Eq. (1c), the two terms on the right-hand side quantify the diffusion-related loss and gain of particles in the phase-space element $\boldsymbol{\omega}$, respectively.

To assess the effect of binary particle collisions, we assume that the one-particle distribution function $f(\mathbf{x}, \theta, t)$ varies on time and length scales which are large compared to the typical time between particle collisions and typical interparticle separations, respectively. Therefore, on the scale of the Boltzmann equation (1a), the impact of collisions on the distribution of angles θ can be formulated locally in space. To capture the effect of binary collisions, we resort to a collision rule, i.e., a model-specific mapping $\boldsymbol{\theta}_w$ between pre- and postcollisional angles:

$$(\theta_1, \theta_2) \mapsto [\theta_w^{(1)}(\theta_1, \theta_2), \theta_w^{(2)}(\theta_1, \theta_2)].$$

Further, we assume that the collision process is subject to noise, which causes a rotation of the postcollisional angles $\theta_w^{(1/2)}$ by some random amount drawn from a probability distribution p. We then arrive at the following form of the collision integrals I_{C} (again, omitting any explicit reference to space and time coordinates):

$$\begin{aligned} I_{\text{C}}[f; \theta] = &-f(\theta) \int_{\theta-\psi}^{\theta+\psi} d\phi \Gamma(\theta - \phi) f(\phi) \\ &+ \int_{-\pi}^{\pi} [d\phi_1]_{(m)} \int_{\phi_1-\psi}^{\phi_1+\psi} d\phi_2 \Gamma(|\phi_2 - \phi_1|) f(\phi_1) f(\phi_2) \\ &\times \frac{1}{2}[p(\theta - \theta_w^{(1)} + 2m\pi) + p(\theta - \theta_w^{(2)} + 2m\pi)], \end{aligned} \tag{1d}$$

where $\Gamma(|\phi_1 - \phi_2|)$ is a phase-space factor ("Boltzmann Stoßzylinder"), quantifying the rate of collisions between particles with orientations ϕ_1 and ϕ_2. The first term on the right-hand side of Eq. (1d) gives the rate at which the phase-space element $\boldsymbol{\omega}$ loses particles due to binary collisions. Similarly, the second term quantifies the rate at which particles are scattered into $\boldsymbol{\omega}$. For the sake of greater generality, we further introduce the parameter $\psi \in [0, \pi]$ in Eq. (1d), to account for systems with limited angular interaction ranges [34].

Equations (1) have been investigated in a number of previous studies [22,26,30,31,33,34] by mapping the mesoscopic Boltzmann equation (1a) to a set of hydrodynamic equations of motion for the first few moments of the one-particle distribution function $f(\mathbf{x}, \theta, t)$. As discussed in the Introduction, this mapping is based on a truncation of terms in Fourier-space representation of the Boltzmann equation which itself rests on a perturbation ansatz for the Fourier modes around an isotropic base state. To which extent such an approach yields reliable results in the context of ordered systems remains an open question; see Ref. [38]. In the following sections, we take a different

route and focus on a kinetic description for active systems by a direct numerical solution of the Boltzmann equation (1).

Before we derive a discretized version of Eqs. (1), one last remark is in order: Since Eqs. (1b)–(1d) imply $\int_{-\pi}^{\pi} d\theta I_{\text{source}}[f;\theta] = 0$, Eq. (1a) gives rise to a conservation law for the local particle density $\rho(\mathbf{x},t) = \int_{-\pi}^{\pi} d\theta f(\mathbf{x},\theta,t)$:

$$\partial_t \rho(\mathbf{x},t) + \nabla \cdot \mathbf{g}(\mathbf{x},t) = 0, \tag{2}$$

where

$$\mathbf{g}(\mathbf{x},t) = v \int_{-\pi}^{\pi} d\theta \hat{\mathbf{e}}_\theta f(\mathbf{x},\theta,t) \tag{3}$$

denotes the local momentum density. In what follows, we will restrict ourselves to the discussion of closed systems in which the particle flux across its boundaries vanishes [40]. Equation (2) then entails conservation of the overall particle density

$$\rho_0 = \frac{1}{\|\Omega\|} \int_\Omega d^2x \rho(\mathbf{x},t) = \text{const}, \tag{4}$$

where Ω denotes the system's two-dimensional spatial domain, and $\|\Omega\|$ its volume.

B. Dimensionless Boltzmann equation

We start by rewriting Eqs. (1) in dimensionless form, in order to reduce the number of parameters. To this end, we measure time in units of the self-diffusion time scale λ^{-1}, distances in units of the "ballistic flight length" $v\lambda^{-1}$, and the one-particle distribution function f in units of the (constant) overall particle density ρ_0 [see Eq. (4)]. Finally, the phase-space factor Γ quantifies the rate of particle collisions and is, therefore, proportional to the particle speed v and the particle extension d. Dimensional analysis then dictates $\tilde{\Gamma} = dv$. We thus arrive at the following convention of units:

$$t \to t \cdot \lambda^{-1}, \tag{5a}$$

$$\mathbf{x} \to \mathbf{x} \cdot v\lambda^{-1}, \tag{5b}$$

$$f \to f \cdot \rho_0, \tag{5c}$$

$$\Gamma \to \Gamma \cdot dv, \tag{5d}$$

$$\rho \to \rho \cdot \lambda (dv)^{-1}, \tag{5e}$$

which will be used throughout this work. The Boltzmann equation (1a) then takes the dimensionless form

$$\partial_t f(\mathbf{x},\theta,t) + \hat{\mathbf{e}}_\theta \cdot \nabla f(\mathbf{x},\theta,t) = I_{\text{SD}}[f;\theta] + \rho_0 I_{\text{C}}[f;\theta]. \tag{6}$$

Here, the expressions for I_{SD} and I_{C} are given in Eqs. (1c) (with $\lambda = 1$) and (1d), respectively, with f and Γ in their dimensionless forms.

In the present system of units, the dimensionless density parameter ρ_0 measures the rate of collisions $[\rho_0 dv]$ relative to the rate of self-diffusion $[\lambda]$. As an aside, we note that in a regime of high densities and/or large ballistic flight lengths with $\rho_0 \gg 1$, the characteristic scales introduced above are no longer meaningful. In such cases, the characteristic time scale would be set by the typical time between subsequent collisions $(\rho_0 dv)^{-1}$, the characteristic length scale by the typical interparticle distance $(\rho_0 d)^{-1}$. In this limit, self-diffusion can be neglected and the problem becomes independent of the overall particle density.

C. Discretization scheme

Having established a dimensionless form for the Boltzmann equation for active, two-dimensional systems [Eq. (6)], this section is devoted to the derivation of a discretized version of Eq. (6). In order to keep the notation compact, we use "co- and contravariant indices" such that summation over repeated co- and contravariant index pairs is implied. Throughout this work, we reserve greek letters for spatial indices and latin letters for angular indices. Moreover, we use the symbol $\|\ldots\|$ to denote the measure of spatial domains and angular intervals.

To discretize the spatial domain Ω, we consider a general tessellation by means of an arbitrary set of connected domains $\{\mathfrak{s}^\alpha\}_{\alpha=1,\ldots,M}$ such that they are a partition of Ω, i.e., (δ^α_β is the Kronecker delta),

$$\mathfrak{s}^\alpha \subset \Omega, \tag{7a}$$

$$\|\mathfrak{s}^\alpha \cap \mathfrak{s}^\beta\| = \|\mathfrak{s}^\beta\| \delta^\alpha_\beta, \tag{7b}$$

$$\bigcup_{\alpha=1}^{M} \mathfrak{s}^\alpha = \Omega, \tag{7c}$$

for all $\alpha, \beta \in \{1,\ldots,M\}$. Similarly, to partition the angular range $A = (-\pi,\pi]$, we consider tessellations by means of a set of simply connected intervals $\{\mathfrak{a}_n\}_{n=1,\ldots,K}$, such that

$$\mathfrak{a}_n \subset A, \tag{8a}$$

$$\|\mathfrak{a}_n \cap \mathfrak{a}_m\| = \|\mathfrak{a}_m\| \delta^m_n, \tag{8b}$$

$$\bigcup_{n=1}^{K} \mathfrak{a}_n = A, \tag{8c}$$

for all $n, m \in \{1,\ldots,K\}$; see Fig. 1. The particular choices for the spatial tessellations are of no importance for the

general development of our discretization scheme. However, some care must be taken in the construction of the angular tessellations. To avoid creating an artificial angular bias, the angles $\{\theta_n\}_{n=1,\ldots,K}$, used to represent the partition $\{\mathfrak{a}_n\}_{n=1,\ldots,K}$, should sum up to 0. In addition, the angular partition should be constructed such that any special lattice found in the spatial tessellations (e.g., when space-filling, regular partitions are being used) should be reflected in any particular choice of angular tessellations. In what follows, we will use

$$\mathfrak{a}_n = \left(\theta_n - \frac{\pi}{K}, \theta_n + \frac{\pi}{K}\right], \qquad \theta_n = \frac{2\pi n}{K} \tag{9}$$

and choose $K \in 4\mathbb{N}$ such that (i) the angular partition $\{\mathfrak{a}_n\}_n \supset \{0, \pi, \pm\pi/2\}$ and (ii) for each angular domain $\mathfrak{a}_i \in \{\mathfrak{a}_n\}_n$, there exists a domain $\mathfrak{a}_j \in \{\mathfrak{a}_n\}_n$ such that $\theta_i = \theta_j + \pi$ (modulo 2π). These conditions then imply

$$\|\mathfrak{a}_n\| = \frac{2\pi}{K} \equiv \epsilon_\theta. \tag{10}$$

We proceed by defining indicator functions for the spatial partition of Ω

$$\mathcal{F}_\alpha(\mathbf{x}) \equiv \begin{cases} 1 & \text{if } \mathbf{x} \in \mathfrak{s}^\alpha \\ 0 & \text{otherwise} \end{cases} \tag{11}$$

and the angular partition of $(-\pi, \pi]$

$$\mathcal{F}^n(\theta) \equiv \begin{cases} 1 & \text{if } \theta \in \mathfrak{a}_n \\ 0 & \text{otherwise,} \end{cases} \tag{12}$$

which can be used to write

$$f(\mathbf{x}, \theta, t) \equiv f_k^\alpha(t) \mathcal{F}_\alpha(\mathbf{x}) \mathcal{F}^k(\theta). \tag{13}$$

Here, the time-dependent density matrix $f_k^\alpha(t) \geq 0$ constitutes a discrete representation of the continuous one-particle distribution function $f(\mathbf{x}, \theta, t)$. To assess the temporal evolution of the density matrix f_k^α, it suffices to establish a transformation law of this matrix under small time increments. This transformation law then provides us with an "update rule" to compute the temporal evolution $f_k^\alpha(t)$ iteratively, starting from some initial distribution $f_k^\alpha(0)$, and hence to numerically solve the Boltzmann equation (6). In the following, we restrict ourselves to considering the time evolution in the bulk of the system, postponing a detailed discussion of boundary conditions to Sec. II D.

1. Convective transport operator

Consider a small translation in the (rescaled) time coordinate $t \to t + \tau$, where $\tau \ll 1$. To assess the convective contribution to the time-transformation law for the density matrix f_k^α, we replace the convective derivative on the left-hand side of the Boltzmann equation (6) by finite differences. Using a forward difference to substitute for the partial time derivative, we get

$$\partial_t f(\mathbf{x}, \theta, t) \to \frac{f(\mathbf{x}, \theta, t + \tau) - f(\mathbf{x}, \theta, t)}{\tau}. \tag{14a}$$

Further, noting that $\hat{\mathbf{e}}_\theta \cdot \nabla f$ is the directional derivative of f along $\hat{\mathbf{e}}_\theta$, we write

$$\hat{\mathbf{e}}_\theta \cdot \nabla f(\mathbf{x}, \theta, t) \to \frac{f(\mathbf{x}, \theta, t) - f(\mathbf{x} - \tau \hat{\mathbf{e}}_\theta, \theta, t)}{\tau}, \tag{14b}$$

where now a backward difference is used to replace the spatial derivative in order to achieve cancellation of the terms $\propto f(\mathbf{x}, \theta, t)$. We choose equal step lengths in Eqs. (14a) and (14b) to account for the fact that the particles move at unit speed $v = 1$ according to our unit convention. To derive the time-transformation law for the density matrix f_k^α due to particle convection, we add Eqs. (14a) and (14b), substitute the discretization ansatz (13) for the one-particle distribution function $f(\mathbf{x}, \theta, t)$, and project the resulting expression onto the discretized phase-space volume $\boldsymbol{\omega}_n^\alpha = \mathfrak{s}^\alpha \otimes \mathfrak{a}_n$. Introducing the projection operator

$$\Pi_n^\alpha \equiv \frac{1}{\epsilon_\theta \|\mathfrak{s}^\alpha\|} \int_{\mathfrak{s}^\alpha} d^2x \int_{\mathfrak{a}_n} d\theta \equiv \int d\tilde{\omega}_n^\alpha, \tag{15}$$

we get

$$\begin{aligned} &\Pi_n^\alpha \{[\partial_t + \hat{\mathbf{e}}_\theta \cdot \nabla] f(\mathbf{x}, \theta, t)\} \\ &\quad \equiv \int d\tilde{\omega}_n^\alpha \mathcal{F}^k(\theta) [f_k^\gamma(t + \tau) \mathcal{F}_\gamma(\mathbf{x}) - f_k^\gamma(t) \mathcal{F}_\gamma(\mathbf{x} - \tau \hat{\mathbf{e}}_\theta)]/\tau \\ &\quad = [f_n^\alpha(t + \tau) - \mathcal{T}_{n\gamma}^{\alpha k} f_k^\gamma(t)]/\tau, \end{aligned} \tag{16a}$$

where we introduce the convective transport operator

$$\mathcal{T}_{n\gamma}^{\alpha k} = \delta_n^k \int d\tilde{\omega}_n^\alpha \mathcal{F}_\gamma(\mathbf{x} - \tau \hat{\mathbf{e}}_\theta), \tag{16b}$$

which quantifies the time propagation of the density matrix f_n^α, due to the convective transport of particles. From Eq. (16b), we can extract a direct geometrical interpretation for the implementation of convective transport processes via $\mathcal{T}_{n\gamma}^{\alpha k}$; see Fig. 1: The convective transport operator is computed by "convecting" the indicator function $\mathcal{F}_\gamma$ for the spatial domain $\mathfrak{s}_\gamma$ along θ_n and integrating the resulting function over the domain $\mathfrak{s}_\alpha$. Geometrically, Eq. (16b) therefore amounts to computing the area of intersection between $\mathfrak{s}_\alpha$ and a convected copy of $\mathfrak{s}_\gamma$ divided by the volume of the phase-space element $\boldsymbol{\omega}_n^\alpha$. The operator element $\mathcal{T}_{n\gamma}^{\alpha k}$ thus measures the number of particles being

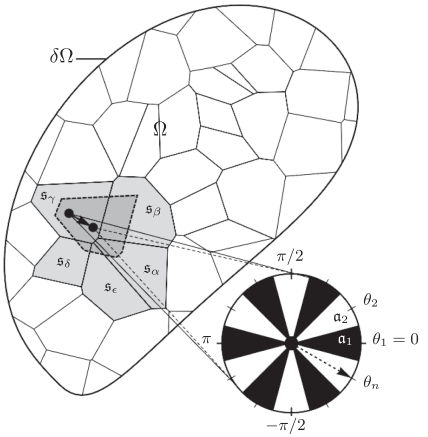

FIG. 1. Spatial and angular tessellations: The system's spatial domain Ω is discretized using an arbitrary tessellation $\{\mathfrak{s}^\alpha\}_\alpha$ obeying Eqs. (7). A set of angular channels according to the tessellation (9) is attached to each spatial cell $\mathfrak{s}^\gamma$. Spatial transport: Convection in the bulk of the system along the direction θ_n (indicated by the dashed arrow) amounts to translating each spatial cell $\mathfrak{s}^\gamma$ by the convection length τ. The convective transport operator $\mathcal{T}^{ak}_{n\gamma}$ [Eq. (16b)] then redistributes the current value of f^γ_n among all neighboring cells according to their intersection with the convected cell.

transported from $\boldsymbol{\omega}^\gamma_n$ to ω^α_n during $(t-dt,t)$. More precisely, $\mathcal{T}^{ak}_{n\gamma}$ gives the increase in particle density in the phase-space element ω^α_n relative to the particle density in the phase-space element $\boldsymbol{\omega}^\gamma_n$ at time $t-dt$ due to convective coupling between these elements in the time interval $(t-dt,t)$.

A few remarks on the properties of the convective transport operator are in order. First of all, since, in the absence of self-diffusion and collisions, the particles maintain their current orientation, the convective transport operator is diagonal with respect to the angular indices for convective processes in the bulk of the system. This observation is, however, no longer true for convection in the vicinity of a (nonperiodic) boundary, where particles generally reorient due to collisions with boundary walls. A corresponding redefinition of the convective transport operator will be given in Sec. II D, where we discuss the implementation of nonperiodic boundary conditions. Second, since $\mathcal{T}^{ak}_{n\gamma}$ reduces to the identity operator in the limit $\tau \to 0$, the convective transport operator becomes "quasidiagonal" in the spatial indices for sufficiently small time steps τ. More precisely, while the diagonal elements $\mathcal{T}^{an}_{n\alpha}$ are $\mathcal{O}(1)$, off-diagonal elements are $\mathcal{O}(\tau)$; i.e., convective coupling between neighboring elements becomes increasingly small as $\tau \to 0$. This effect, in turn, has important consequences for the computation of the angular self-diffusion and collision contributions to the time evolution of the density matrix f^α_n, which themselves are $\mathcal{O}(\tau)$, as will be shown below. Thus, up to linear order in τ, convective processes decouple from angular diffusion and collision, such that the latter processes can be computed independently inside each spatial domain $\mathfrak{s}_\alpha$.

2. Self-diffusion operator

To discretize the self-diffusion integral I_{SD}, we proceed along the same lines as in the preceding section and substitute the discrete representation of $f(\mathbf{x},\theta,t)$ [Eq. (13)] and project the resulting expression onto the phase-space volume $\boldsymbol{\omega}^\alpha_n$. Using the analytical form of the self-diffusion matrix [Eq. (1c)], we find

$$\begin{aligned}\Pi^\alpha_n I_{\mathrm{SD}} &\equiv -f^\alpha_n(t) + \int d\tilde{\omega}^\alpha_n \int_{-\pi}^{\pi}[d\phi]_{(m)} \\ &\quad\times \mathcal{F}^k(\phi) f^\gamma_k(t) \mathcal{F}_\gamma(\mathbf{x}) p_0(\theta-\phi+2m\pi) \\ &= \mathcal{D}^k_n f^\alpha_k(t), \end{aligned} \tag{17a}$$

where the matrix elements of the self-diffusion operator

$$\mathcal{D}^k_n = \int_{\mathfrak{a}_n} \frac{d\theta}{\epsilon_\theta} \int_{\mathfrak{a}_k} [d\phi]_{(m)} p_0(\theta-\phi+2m\pi) - \delta^k_n \tag{17b}$$

quantify the net gain of particles (per unit time) in the angular element $\mathfrak{a}_n$, by diffusive scattering from the angular element $\mathfrak{a}_k$.

3. Collision operator

Finally, the discretized version of the collision integral I_{C} defines the collision operator $\mathcal{C}^{kl}_n$, which can be calculated using the standard procedure outlined in the previous two subsections. Starting with the loss term in Eq. (1d), we obtain

$$\begin{aligned}\Pi^\alpha_n I^{(\mathrm{loss})}_{\mathrm{C}} &\equiv -\int d\tilde{\omega}^\alpha_n \int_{\theta-\psi}^{\theta+\psi} d\phi \Gamma(|\theta-\phi|) \\ &\quad\times \mathcal{F}_\gamma(\mathbf{x}) \mathcal{F}_\delta(\mathbf{x}) f^\gamma_k(t) f^\delta_l(t) \mathcal{F}^k(\theta) \mathcal{F}^l(\phi) \\ &= -f^\alpha_n(t) \mathcal{S}^l_n f^\alpha_l(t), \end{aligned} \tag{18a}$$

where the matrix elements

$$\mathcal{S}^l_n = \int_{\mathfrak{a}_n} \frac{d\theta}{\epsilon_\theta} \int_{\theta-\psi}^{\theta+\psi} d\phi \Gamma(|\theta-\phi|) \mathcal{F}^l(\phi) \tag{18b}$$

measure the loss of particles (per unit time) in the angular element $\mathfrak{a}_n$ due to collisions with particles in the element $\mathfrak{a}_k$.

Similarly, considering the gain term of Eq. (1d), we find

$$\Pi_n^{\alpha} I_C^{(\mathrm{gain})} \equiv \int d\tilde{\omega}_n^{\alpha} \int_{-\pi}^{\pi} [d\phi_1]_{(m)} \int_{\phi_1-\psi}^{\phi_1+\psi} d\phi_2 \Gamma(|\phi_2-\phi_1|) \times \mathcal{F}_{\gamma}(\mathbf{x}) \mathcal{F}_{\delta}(\mathbf{x}) f_k^{\gamma}(t) f_l^{\delta}(t) \mathcal{F}^k(\phi_1) \mathcal{F}^l(\phi_2) \times \frac{1}{2}[p(\theta-\theta_w^{(1)}+2\pi m)+p(\theta-\theta_w^{(2)}+2\pi m)] = f_k^{\alpha}(t) \mathcal{S}_n^{kl} f_l^{\epsilon}(t), \tag{19a}$$

where the matrix elements

$$\mathcal{S}_n^{kl} = \int_{\mathfrak{a}_n} \frac{d\theta}{\epsilon_\theta} \int_{\mathfrak{a}^k} [d\phi_1]_{(m)} \int_{\phi_1-\psi}^{\phi_1+\psi} d\phi_2 \Gamma(|\phi_2-\phi_1|) \mathcal{F}^l(\phi_2) \times \frac{1}{2}[p(\theta-\theta_w^{(1)}+2\pi m)+p(\theta-\theta_w^{(2)}+2\pi m)] \tag{19b}$$

count the number of particles (per unit time) being scattered into the angular element $\mathfrak{a}_n$ as a result of binary collisions between particles with angles $\phi_1 \in \mathfrak{a}_k$ and $\phi_2 \in \mathfrak{a}_l$.

Combining Eqs. (18) and (19), we find

$$\Pi_n^{\alpha} I_C \equiv f_k^{\alpha}(t) \mathcal{C}_n^{kl} f_l^{\alpha}(t), \tag{20a}$$

with the collision operator $\mathcal{C}_n^{kl}$ given by

$$\mathcal{C}_n^{kl} = \mathcal{S}_n^{kl} - \mathcal{S}_n^{l} \delta_n^{k}. \tag{20b}$$

4. Discrete time-transformation law and summation rules

Having discretized the various terms in the Boltzmann equation [Eq. (6)], we can now combine our findings from the previous three subsections, to arrive at the following transformation law, capturing the evolution of the density matrix $f_n^{\alpha}(t)$ under a small transformation in time $t \to t+\tau$

$$f_n^{\alpha}(t+\tau) = \{\mathcal{T}_{n\gamma}^{\alpha k} + \tau[\mathcal{D}_n^k + \rho_0 \mathcal{C}_n^{kl} f_l^{\alpha}(t)] \delta_{\gamma}^{\alpha}\} f_k^{\gamma}(t), \tag{21}$$

with the various operators, acting on the density matrix $f_n^{\alpha}(t)$, given in Eqs. (16b), (17b), and (20b). Equation (21) defines a recursive relation, which allows us to numerically compute the solutions of the Boltzmann equation [Eq. (6)], given initial conditions $f_n^{\alpha}(0)$. It, therefore, constitutes a discrete version of the Boltzmann equation for active systems, as introduced in Sec. II A.

We conclude the current section by demonstrating that the particle-conservation property, inherent in the original Boltzmann equation [Eq. (6)], is being preserved by the transformation law [Eq. (21)]. To this end, we use the following operator-summation rules, which themselves follow directly from the respective definitions of the corresponding operators:

$$\|\hat{\mathfrak{s}}_{\alpha}\| \|\mathfrak{a}^n\| \mathcal{T}_{n\gamma}^{\alpha k} = \|\hat{\mathfrak{s}}_{\gamma}\| \|\mathfrak{a}^k\|, \tag{22a}$$

$$\|\mathfrak{a}^n\| \mathcal{D}_n^k = 0, \tag{22b}$$

$$\|\mathfrak{a}^n\| \mathcal{C}_n^{kl} = 0. \tag{22c}$$

In particular, Eq. (22a) expresses the fact that convective streaming in the bulk conserves the volume of the phase-space elements $\boldsymbol{\omega}_{\gamma}^k = \hat{\mathfrak{s}}_{\gamma} \otimes \mathfrak{a}^k$. Equations (22b) and (22c) capture the particle-conserving properties of the self-diffusion and collision operators, by asserting that the total gain of particles in each angular element is balanced by the total loss of particles in all remaining angular elements, and vice versa. Now, using Eqs. (22), we find

$$N(t+\tau) = \|\hat{\mathfrak{s}}_{\alpha}\| \|\mathfrak{a}^n\| f_n^{\alpha}(t+\tau) = \|\hat{\mathfrak{s}}_{\alpha}\| \|\mathfrak{a}^n\| \{\mathcal{T}_{n\gamma}^{\alpha k} + \tau[\mathcal{D}_n^k + \rho_0 \mathcal{C}_n^{kl} f_l^{\alpha}(t)] \delta_{\gamma}^{\alpha}\} f_k^{\gamma}(t) = \|\hat{\mathfrak{s}}_{\gamma}\| \|\mathfrak{a}^k\| f_k^{\gamma}(t) = N(t), \tag{23}$$

i.e., conservation of the total number of particles.

Finally, we note that, without further simplification, the computation time for an algorithm based on Eq. (21) is of order $\mathcal{O}(K^3)$ [41] and is thus effectively set by the number of angular slices K. In the absence of collision noise, on the other hand, the transition probabilities in the definition of the collision operator [see Eq. (19b)] reduce to delta peaks about $\theta_w^{(1/2)}$, rendering the implementation of Eq. (21) of order $\mathcal{O}(K^2)$. Unless stated otherwise, we will use $K = 32$ in what follows. To test whether $K = 32$ is an appropriate choice for the angular resolution, we compute the spatially homogeneous solution of the density matrix f_n^{α} for a range of values $K \in \{32, \ldots, 128\}$ and a number of different density levels, using a 1×1 spatial grid. In fact, we observe no significant quantitative improvement upon increasing the number of angular slices in the presence of collision noise; see Fig. 2(a). The stationary, spatially homogeneous solution for the one-particle distribution function $f(\theta)$ as depicted in Fig. 2(a) has previously been observed numerically [21] and predicted analytically [23].

D. Boundary conditions

The analytical form of Eq. (21) applies equally well in the bulk and at the boundaries of the system. For nonperiodic boundaries, however, the convective transport operator $\mathcal{T}_{n\gamma}^{\alpha k}$ differs from its bulk form [Eq. (16b)] and has to be modified. In this section, we start by discussing these modifications in abstract terms and will later apply the generalized form of the convective transport operator to the specific case of reflective boundaries.

In the following, we shall confine ourselves to the discussion of fixed boundaries with a model-specific reflection rule. Specifically, we assume particles to undergo

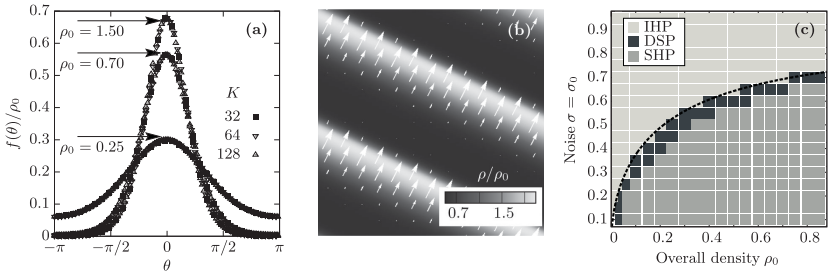

FIG. 2. (a) Stationary solution for the one-particle distribution function $f(\theta)$ according to Eq. (21) for a spatially homogeneous system with $L = 1$, $\sigma = \sigma_0 = 0.5$, and $K = 32$, 64, and 128 angular slices for various overall densities ρ_0 (indicated in the figure). (b) Representative snapshot of a stationary traveling-wave pattern for $\rho_0 = 0.25$ and $\sigma = \sigma_0 = 0.5$. The color code indicates local density; the length and direction of arrows indicate the magnitude and orientation of the local particle flow. (c) Phase diagram for different values of the overall density ρ_0 and noise amplitude $\sigma = \sigma_0$. The analytic result for the phase boundary [refer to Eq. (34)] is indicated by the dashed line. A DSP is observed all along the phase boundary between the IHP and the SHP. The system size $L = 100$, $\epsilon_x = 5$, and $K = 32$ for (b) and (c).

a spontaneous reorientation upon collisions with the boundary

$$\theta \to \theta_{\mathrm{BC}}(\theta), \tag{24}$$

where θ and $\theta_{\mathrm{BC}}(\theta)$ denote the particle's orientation before and after the boundary contact, and where θ_{BC} can be either a deterministic or a random variable. For the sake of clarity, we will discuss deterministic particle-boundary interactions. The treatment of stochastic boundary conditions follows along similar lines.

To the considered order, self-diffusion processes and particle-particle collisions are evaluated at a fixed point in space and time in Eq. (21). To account for the presence of boundaries, we are, therefore, led to reconsider the derivation of the convective transport operator $\mathcal{T}^{\alpha k}_{n\gamma}$; see Sec. II C 1. For small but finite values of the time shift τ, we have to redefine the convective derivative [Eqs. (14)] for all

$$\mathbf{x} \in \mathbb{B}_\tau = \{x; \min_{\mathbf{x}' \in \delta\Omega} |\mathbf{x} - \mathbf{x}'| < \tau\}. \tag{25}$$

Here, $\mathbb{B}_\tau$ denotes the set of all points in space which are within "convective reach" of the boundary $\delta\Omega$ of the system's domain Ω within the next time interval $[t, t+\tau]$. An appropriate redefinition of the convective transport operator can then be given using "inverse propagation functions":

$$\mathbf{c}_s^{-1}(\mathbf{x}, \theta; \tau) \equiv \text{particle position at time } t, \text{ given that the particle is located at } \mathbf{x} \text{ and oriented along } \hat{\mathbf{e}}_\theta \text{ at time } t+\tau, \text{ and} \tag{26a}$$

$$c_a^{-1}(\mathbf{x}, \theta; \tau) \equiv \text{particle orientation at time } t, \text{ given that the particle is located at } \mathbf{x} \text{ and oriented along } \hat{\mathbf{e}}_\theta \text{ at time } t+\tau. \tag{26b}$$

Using these inverse propagation functions, we redefine the finite difference approximation of the convective derivative (14) as follows:

$$[\partial_t + \hat{\mathbf{e}}_\theta \cdot \nabla] f(\mathbf{x}, \theta, t) \to \frac{f(\mathbf{x}, \theta, t+\tau) - f[\mathbf{c}_s^{-1}(\mathbf{x}, \theta; \tau), c_a^{-1}(\mathbf{x}, \theta; \tau), t]}{\tau}, \tag{27}$$

which reduces to the bulk form [Eq. (14)] upon substituting the inverse bulk propagation functions $\mathbf{c}_s^{-1}(\mathbf{x}, \theta; \tau) = \mathbf{x} - \tau\hat{\mathbf{e}}_\theta$ and $c_a^{-1}(\mathbf{x}, \theta; \tau) = \theta$. Using this generalized finite difference representation to replace the convective derivative, we can proceed along the same lines of Sec. II C 1 to arrive at the following, generalized form of the convective transport operator

$$\mathcal{T}^{\alpha k}_{n\gamma} = \int \frac{d\tilde{\omega}^\alpha_n}{\epsilon_\theta \|\tilde{\mathbf{s}}^\alpha\|} \mathcal{F}_\gamma[\mathbf{c}_s^{-1}(\mathbf{x}, \theta; \tau)] \mathcal{F}^k[c_a^{-1}(\mathbf{x}, \theta; \tau)]. \tag{28}$$

Since $c_a^{-1} = \theta_{\mathrm{BC}}^{-1} \neq \mathbb{1}$ for particles undergoing a collision with the system's boundary during $[t, t+\tau]$, $\mathcal{T}^{\alpha k}_{n\gamma}$ is no longer diagonal in the angular indices for $\mathbf{x} \in \mathbb{B}_\tau$.

The generalized convective transport operator [Eq. (28)] lends itself to implement virtually arbitrary boundary conditions that enter Eq. (28) by an appropriate definition of the inverse propagation functions (26). To illustrate the general concept, we conclude this section with a brief discussion of the implementation of reflective boundary conditions.

After the collision of a particle with a reflective boundary, the particle's orientation changes according to

$$\theta' = 2\phi_b(\mathbf{x}) - \theta, \tag{29a}$$

where $\phi_b(\mathbf{x})$ denotes the local orientation of the system's boundary, and where θ' and θ denote the particle's orientation before and after the collision with the reflective boundary, respectively. Moreover, if a particle's state is described by $(\mathbf{x},\theta)$ at time t and is known to have undergone a collision with the system's boundary in the time interval $(t-\tau, t]$, its spatial position $\mathbf{x}'$ at time $t-\tau$ is given by

$$\mathbf{x}' = R_{\phi_b}(\mathbf{x} - \tau\hat{\mathbf{e}}_\theta), \tag{29b}$$

where R_{ϕ_b} denotes a reflection with respect to the boundary's local tangent of orientation ϕ_b. In summary, the inverse propagation functions in the case of reflective boundary conditions read

$$\mathbf{c}_s^{-1}(\mathbf{x},\theta;\tau) = \begin{cases} R_{\phi_b}(\mathbf{x}-\tau\hat{\mathbf{e}}_\theta) & \overline{\mathbf{x}-\tau\hat{\mathbf{e}}_\theta,\mathbf{x}} \cap \delta\Omega \neq \emptyset \\ \mathbf{x}-\tau\hat{\mathbf{e}}_\theta & \text{otherwise} \end{cases} \tag{30a}$$

and

$$c_a^{-1}(\mathbf{x},\theta;\tau) = \begin{cases} 2\phi_b(\mathbf{x}) - \theta & \overline{\mathbf{x}-\tau\hat{\mathbf{e}}_\theta,\mathbf{x}} \cap \delta\Omega \neq \emptyset \\ \theta & \text{otherwise,} \end{cases} \tag{30b}$$

where $\overline{\mathbf{a},\mathbf{b}}$ denotes the line segment joining the points $\mathbf{a}$ and $\mathbf{b}$.

As a final remark, we mention that Eqs. (30) can be implemented straightforwardly using arbitrary boundary geometries. Although a detailed study on the impact of confining geometries on the behavior of active systems lies beyond the scope of our present work, SNAKE lends itself as a convenient starting point to address this important question. For sample simulations of active polar systems in circular and ringlike confinements, we refer the interested reader to the Supplemental Material [42].

III. POLAR SYSTEMS: PHASES AND TRANSITIONS

Having established a general framework to discretize the Boltzmann equation for active particles [Eq. (6)], we now discuss actual applications of SNAKE in the context of active polar systems. We will focus our considerations on a simple model system with a polar collision rule

$$(\theta_1,\theta_2) \mapsto \left(\theta_w^{(1)} = \frac{\theta_1+\theta_2}{2}, \theta_w^{(2)} = \frac{\theta_1+\theta_2}{2}\right) \tag{31}$$

and full angular interaction range. For the self-diffusion and collision-noise probability functions p and p_0, we choose zero-mean Gaussian probability distributions with variances σ_0^2 and σ^2, respectively.

This model has previously been proposed and studied by Bertin *et al.* [22,26] using mainly analytical methods. Our purpose here is twofold. First, we can resort to a number of well-established analytical results [26] for this model, as well as a number of previous studies of closely related systems [8,14,28,38], to test for the accuracy and reliability of our computational scheme. Second, we can use SNAKE to go beyond the hydrodynamic picture of the onset of collective motion, as discussed in Refs. [22,26], and study the nature of the various phases, as well as the ensuing transitions between them.

In the following sections, we will use the system of units introduced in Sec. II B; see Eqs. (5). Moreover, we will use spatial tessellations in the form of regular two-dimensional arrays of $L \times L$ rectangular grid sites with linear extensions $|\mathfrak{s}_\alpha| = \text{const} \equiv \epsilon_x$ and periodic boundary conditions. Some care must be taken for the appropriate choice of the size of one "Boltzmann element" ϵ_x: The spatial patterns typically formed by these systems at the onset of polar order are known to develop rather steep wave fronts, with density profiles varying on length scales comparable to the collision length (i.e., the typical length a particle travels between successive collisions) [14,38]. To be able to resolve such patterns with sufficient accuracy, we need $\epsilon_x \sim \rho_0^{-1}$. In all subsequent sections, we will use densities $\rho_0 = \mathcal{O}(0.1\text{–}1)$, such that $\epsilon_x = 5$ is an appropriate choice. Unless stated otherwise, $\epsilon_x = 5$ and $L = 100$ will be used throughout this work.

A. Phase diagram of stationary states

The simple model system referred to above [Eq. (31)] has been shown to exhibit a bifurcation, which separates a parameter regime at low density or high noise from one at high density or low noise levels. In the high-noise (low-density) regime, an isotropic, spatially homogeneous phase (IHP) is observed. This homogeneous and isotropic state can be seen as a dynamical attractor for the system's dynamics at low densities, which we will refer to as the "IHP fixed point" in the following. For low enough noise levels (and high enough densities), this IHP fixed point loses its stability and the system undergoes a transition toward polar order. The location of the corresponding bifurcation can be calculated directly from the Boltzmann equation [Eq. (6)] by performing an expansion in terms of the moments $f_k = \int_{-\pi}^{\pi} d\theta e^{ik\theta} f(\theta)$ of the one-particle distribution function $f(\theta)$ and studying the resulting dynamical equation for the polar order parameter f_1 (see Refs. [22,26] for details):

$$\partial_t f_1 = \mu_1 f_1 - \mu_2 |f_1|^2 f_1 + \cdots. \tag{32}$$

Here, the various coefficients are functions of ρ_0, σ, and σ_0, and the dots indicate higher-order and gradient terms.

Although a complete description of the dynamics of f_1 [Eq. (32)] contains couplings to an infinite number of higher-order moments f_n, the linear coefficient $\mu_1(\rho_0, \sigma, \sigma_0)$ can be calculated exactly within the Boltzmann-equation approach and does not depend on any approximation scheme used to truncate these couplings [26,34]. The condition

$$\mu_1(\rho_0, \sigma, \sigma_0)|_{\rho_0=\rho_t} = 0 \tag{33}$$

therefore provides us with an exact benchmark for the location of the bifurcation surface in parameter space. It is obtained by solving the above equation for ρ_t [26]:

$$\rho_t = \frac{\pi}{8}\frac{1 - e^{-\sigma_0^2/2}}{e^{-\sigma^2/2} - 2/3}. \tag{34}$$

For simplicity, we choose $\sigma = \sigma_0$ throughout this work. To test our implementation of SNAKE, we prepare different systems with varying values for the density ($0.0125 \leq \rho_0 \leq 0.85$) and noise levels ($0.1 \leq \sigma = \sigma_0 \leq 0.95$), starting from random initial conditions [43]. We perform the computations on a regular rectangular spatial grid with 100×100 grid sites and $K = 32$ angular slices and evaluate the systems' (stationary) states after a total computation time of $T = 15\,000$. The resulting phase diagram is shown in Fig. 2(c) along with the analytical result for the bifurcation line [Eq. (34)]. In accordance with previous analytical [26] and numerical results [14], we observe a phase transition between an IHP and a broken-symmetry density-segregated phase (DSP) upon crossing the bifurcation line $\rho_t(\sigma)$ [Eq. (34)]. A typical system snapshot inside the DSP is shown in Fig. 2(b). Deeper inside the symmetry-broken parameter domain, systems asymptotically reach a spatially homogeneous, polarized phase (SHP) after a transient episode of polar clustering and subsequent coarsening; see Sec. III F. In the subsequent sections, we will give a more detailed analysis of the various observed phases and the corresponding transitions in between.

B. First-order transition from disorder to polar order

The transition between the isotropic homogeneous phase toward the formation of polar order (IHP → DSP) is probably one of the most studied phase transitions in active polar systems. Despite prior beliefs that this transition is of second order [5], whereby polar order was assumed to build up continuously, a growing number of more recent agent-based [8,14,44] and kinetic studies [28,38] clearly indicates that the formation of density-segregated patterns at large enough system sizes renders this phase transition first order.

To check for consistency of our numerical Boltzmann approach with these previous results, we study the transition of the IHP toward polar for systems of varying linear sizes $L \in \{25, 50, 100\}$, subject to two different noise levels $\sigma = \sigma_0 \in \{0.35, 0.6\}$. For each choice of the system size and noise level, we prepare a set of systems at different overall densities $\rho_0 \in [0.05 < \rho_t(\sigma), 0.64 > \rho_t(\sigma)]$ using random initial conditions. To quantify the phase transition, we compute the local polar order parameter $\boldsymbol{\varphi}_\alpha$ from the numerical solution of the density matrix f_n^α

$$\boldsymbol{\varphi}_\alpha \equiv \frac{2\pi}{K}\sum_{n=1}^{K} e^{i\theta_n} f_n^\alpha. \tag{35}$$

From this expression, we then compute the spatially averaged polar order parameter

$$\langle \boldsymbol{\varphi} \rangle_x \equiv \frac{1}{L^2}\sum_{\alpha=1}^{L^2} \boldsymbol{\varphi}_\alpha, \tag{36}$$

after the systems have settled into a stationary state (which, here and in the following, shall include moving patterns of "stationary" shape, as observed inside the DSP).

The results of this study are shown in Fig. 3(a). Our results indicate a jump discontinuity of the polar order parameter $\langle \boldsymbol{\varphi} \rangle_x$ at the transition to polar order, which is accompanied by the formation of spatial heterogeneities, typically in the form of traveling-wave patterns [see Fig. 2(b); see also Sec. III E]. To within our chosen density resolution $\Delta\rho = 0.01$, the size of the observed jump discontinuity is virtually independent of the system size for $L \gtrsim 50$ but depends on the noise levels in the system. For the smallest system sizes considered, $L = 25$ and smaller (not shown), the size of the jump discontinuity

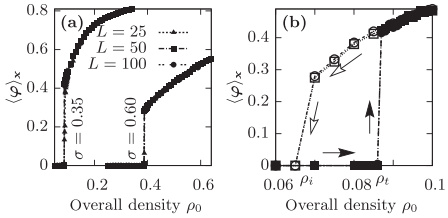

FIG. 3. (a) Average momentum against density ρ for two noise levels $\sigma = \sigma_0$ and three system sizes L; specific values are indicated in the figure ($\epsilon_x = 5$). The results indicate that the transition is first order. (b) Hysteresis study. The average momentum against overall density ρ_0 for $\sigma = \sigma_0 = 0.35$ and two system sizes $L \in \{50, 100\}$. Solid symbols (with the paths indicated by solid arrows) indicate the system's stationary state when starting from random initial conditions. Open symbols (with the paths indicated by open arrows) indicate the system's stationary states upon lowering the density quasistatically starting from a stationary wavelike pattern at $\rho_0 > \rho_t$. The system exhibits hysteresis, corroborating the assertion that the underlying ordering transition is first order.

shrinks down to 0, eventually rendering the observed phase transition continuous for system sizes below a critical size L^*. These observations are in agreement with previous studies on this phase transition in the context of the Vicsek model [8,14] and Enskog-like kinetic theories [28,38]. For a more detailed discussion of the critical system size L^*, we refer the reader to Refs. [28,38].

To scrutinize the subcritical nature of the bifurcation leading to the formation of polar order in large enough systems, we further check for the existence of hysteresis effects in this model system. To this end, we numerically compute the stationary solution of the density matrix f_n^α inside the DSP and then quasistatically reduce the overall density ρ_0 in small steps. Here and in the following, the term "quasistatic" change of the overall density refers to the fact that the system is given a sufficient amount of time to equilibrate in between successive adjustments in ρ_0. Two typical outcomes of such hysteresis experiments are shown in Fig. 3(b) for two different system sizes. There, closed symbols and arrows indicate the path a system follows in the ρ_0-$\langle\varphi\rangle_x$ plane, when starting from random initial conditions, exhibiting the familiar jump discontinuity at $\rho_0 = \rho_t$. Open symbols and arrows indicate the inverse situation, where systems evolve from an initial state inside the ordered DSP parameter regime. In this latter case, our results indicate that the corresponding dynamical fixed point is stable down to values of $\rho_0 = \rho_i < \rho_t$, well below the actual transition density ρ_t, thus corroborating the subcritical nature of the corresponding dynamical bifurcation. Similar hysteresis effects have been reported in Refs. [14,31,38].

C. Density-segregated polar phase

Since we have chosen to numerically solve the Boltzmann equation in real space, rather than in Fourier space, we expect SNAKE to be applicable even for parameters well inside the ordered phase, where Fourier-space approaches would have to include an exceedingly large number of modes. Therefore, we continue our study of polar systems by presenting a more detailed analysis of the DSP region in parameter space. In anticipation of our discussion in Sec. III E, we note that we frequently observe two distinct types of patterns within the DSP: traveling-wave patterns and cluster-lane patterns. While the former pattern shape is by now well known to occur in polar active systems with metric interactions [14,26,34,38], to our knowledge, the emergence of cluster-lane patterns has not yet been reported in the literature so far. We devote the separate Sec. III E to these novel patterns and restrict our present discussions to the well-known case of traveling waves.

After initial transients, during which "polar droplets" form and coalesce out of random initial conditions, the resulting stationary traveling-wave patterns (when viewed in a comoving frame) become translationally invariant in the lateral direction $x_\perp$ (perpendicular to the wave's velocity vector). The structure of these wave patterns can, therefore, be described by means of the longitudinal coordinate $x_\parallel$ (along the direction of the wave's velocity vector). Figure 4(a) shows typical density profiles of such polar waves as a function of the distance from the transition line at $\rho_t(\sigma)$. The observed wave profiles exhibit a characteristic front-rear asymmetry, similar to those reported in previous numerical studies [14], whereby the asymmetry becomes more pronounced as the parameters are chosen deeper inside the ordered region.

The waves themselves can be viewed as high-density structures, traveling on an isotropic, low-density background (see Appendix A and Fig. 10). To quantify the density segregation between the wave fronts and the isotropic background as function of the distance from the system's phase boundary, we introduce the following characteristic density scales:

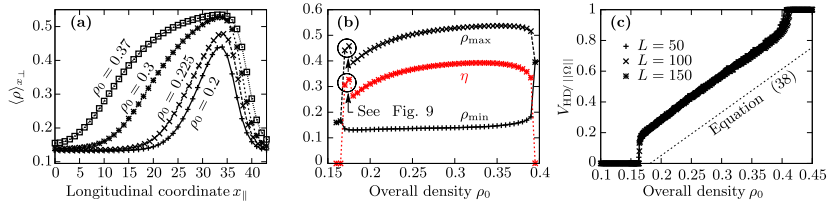

FIG. 4. Density variation inside the DSP parameter regime ($\sigma = \sigma_0 = 0.5$). (a) Typical profiles of wavelike patterns inside the density-segregated phase for various overall densities ρ_0. The asymmetry of the wave profiles increases with density. ($\rho_t \approx 0.21$ for the noise values considered.) (b) Density segregation as a function of the overall density ρ_0. Data points have been obtained by quasistatically changing ρ_0 starting at a stationary traveling-wave pattern at $\rho_0 = 0.25$. As a consequence of hysteresis effects [see Figs. 3(b) and 5], phase-space coexistence can be observed between the DSP and the IHP at low densities, as well as between the DSP and the SHP at higher densities. (c) Surface fraction of the HD phase as a function of the overall density ρ_0. Within the DSP, the surface fraction varies virtually linearly with ρ_0 in agreement with the mean-field picture [Eq. (38)]. At the transitions IHP → DSP and DSP → SHP, the surface fraction exhibits a discontinuous jump.

$$\rho_{\max} \equiv \max_{x_\parallel} \langle \rho(\mathbf{x}) \rangle_{x_\perp}, \tag{37a}$$

$$\rho_{\min} \equiv \min_{x_\parallel} \langle \rho(\mathbf{x}) \rangle_{x_\perp}, \tag{37b}$$

as measures for the density levels within the high-density, moving phase ("HD phase") and the low-density, isotropic background ("LD phase"), respectively. Figure 4(b) shows the characteristic density scales and the density-separation parameter

$$\eta \equiv \rho_{\max} - \rho_{\min}, \tag{37c}$$

as a function of the system's overall density ρ_0 at fixed noise levels. The data shown in Fig. 4 have been computed using the following simulation protocol: For a system well inside the DSP parameter regime, we follow its time evolution starting from a random initial condition until it reaches a stationary state with a traveling-wave pattern. The density matrix f_n^α corresponding to this stationary wave pattern is then used as the initial condition in subsequent numerical computations, during which the density level is quasistatically decreased or increased until the density-segregation parameter drops back to 0, i.e., until a spatially homogeneous state is reached.

This protocol allows us to explore the parameter range over which the "DSP fixed point" of the system's dynamics remains locally attracting. Before we embark on a more detailed discussion on the stability of the various dynamical fixed points and observed phase coexistence in parameter space in Sec. III D, we take a little detour and briefly comment on the observed wave profiles as the overall density is varied. First, we observe that the density level of the LD phase $\rho_{\min}$ is virtually independent of the overall density ρ_0 across the entire region of existence of the DSP. Any "surplus density" arising from an increase in ρ_0 must therefore be accommodated within the HD phase and, consequently, implies a change in the wave profiles. At the lowest densities ($\rho_0 < \rho_t$) where wave patterns are still stable, we observe wave profiles of relatively weakly pronounced front-rear asymmetry [see Fig. 4(a), $\rho_0 = 0.2$]. As the overall density is increased slightly above ρ_t, surplus density is being accommodated primarily by increasing the characteristic density $\rho_{\max}$, leaving the front-rear asymmetry virtually unchanged [see Fig. 4(a), $\rho_0 = 0.225$]. For still larger values of the overall ρ_0, the characteristic density $\rho_{\max}$ quickly saturates and surplus density is being accommodated by increasing the width of the solitary waves. This effect, in turn, leads to a drastic increase in front-rear asymmetry.

The latter regime of wave broadening can be understood intuitively by employing a simple mean-field picture that assumes constant density levels within the HD and LD phases, respectively. To this end, consider a system of arbitrary volume $\|\Omega\|$ in the DSP wave-broadening parameter regime. Since both characteristic densities $\rho_{\min}$ and $\rho_{\max}$ are constant by assumption, conservation of particle number $N \simeq V_{\mathrm{HD}}\rho_{\max} + V_{\mathrm{LD}}\rho_{\min}$ [$V_{\mathrm{HD(LD)}}$ are volumes occupied by the HD (LD) phase] dictates

$$\frac{V_{\mathrm{HD}}}{\|\Omega\|} = \frac{\rho_0 - \rho_{\min}}{\eta}. \tag{38}$$

Figure 4(c), where the surface fraction $V_{\mathrm{HD}}/\|\Omega\|$ is recorded as a function of ρ_0, confirms this linear dependence and thus corroborates the above mean-field picture. Moreover, since $V_{\mathrm{HD}} \leq \|\Omega\|$, Eq. (38) implies a crossover scale $\rho_h = \mathcal{O}(\rho_{\max})$, above which the LD phase gets depleted and the system becomes spatially homogeneous. We check that the mean-field picture conveyed by Eq. (38) is actually independent of the system size L and becomes quantitatively robust against changes in the system size for $L \gtrsim 50$; see Fig. 4(c). Interestingly, the composition of the system in terms of HD and LD phases as a function of the overall density ρ_0 exhibits qualitatively analogous behavior in the two-dimensional lattice model of active Ising spins of Ref. [20], where a Z_2 (up-down) symmetry is spontaneously broken. This observation strongly suggests that the qualitative features of the flocking transition toward spatially homogeneous polar order in active systems might actually be universal across different symmetry classes.

D. Transition to spatially homogeneous polar state and pattern selection

In the previous section, we investigated the evolution of systems inside the DSP regime, as the overall density ρ_0 is varied. We observed that the DSP parameter regime, which can be defined by nonzero values of the density-separation parameter η, is hallmarked by a linear variation of the surface fraction of the HD phase $V_{\mathrm{HD}}/\|\Omega\|$, with ρ_0. Importantly, the DSP regime is delimited by sharp jumps in η and $V_{\mathrm{HD}}/\|\Omega\|$ at both of its boundaries, i.e., at the transition toward a spatially homogeneous isotropic state (low densities) and at the transition toward a spatially homogeneous polar ordered state (high densities). As has been discussed before (e.g., Refs. [14,38] and Sec. III B), such nonregular behavior at the low-density limit of the DSP regime can be attributed to the first-order nature of the ordering transition between the IHP and DSP parameter regimes. However, for the transition between the DSP regime and the SHP regime, comparable results are not available, yet. The present section is devoted to fill this gap and to illuminate the nature of the phase transition between the DSP and SHP regimes. Similarly to the case of the IHP $\leftrightarrow$ DSP phase transition, we will observe hysteresis effects that are highly suggestive of a first-order transition between the DSP and SHP regimes.

To assess the nature of the DSP $\leftrightarrow$ SHP transition, we choose density and noise parameters inside the SHP regime ($\rho_0 = 0.415$, $\sigma = \sigma_0 = 0.5$) and let the system evolve until

it has reached a state of spatially homogeneous polar order. The corresponding stationary solution for the density matrix f_n^a is then used as the initial condition in subsequent computations. In contrast to the computation protocol in Sec. III B (where parameters are adjusted quasistatically), the system's overall density ρ_0 is then quenched to successively lower values $\rho_0 \in \{0.41, 0.405, \ldots, 0.25\}$ and the resulting pattern at asymptotically long times is recorded; for details of the numerical protocol, see Appendix C.

In Fig. 5(a), the corresponding results of this study are shown in terms of the surface fraction $V_{\mathrm{HD}}/\|\Omega\|$ occupied by the HD phase. There, open symbols and arrows indicate data points corresponding to initial conditions inside the SHP regime. Closed data points refer to initial conditions inside the DSP regime (where the overall density is then quasistatically increased). The data show that the transition between the DSP and SHP regimes is accompanied by hysteresis effects, supporting our initial claim that the corresponding transition is first order. Phase-space coexistence between both regimes can be observed for densities $\rho_{dh}(\sigma = \sigma_0 = 0.5) \approx 0.345 \lesssim \rho_0 \lesssim \rho_h(\sigma = \sigma_0 = 0.5) \approx 0.39$ [45]. Further evidence confirming the first-order nature of this transition comes from an analysis of the dynamics of the density-separation parameter η at the point where the actual transition DSP → SHP occurs [solid branch of the hysteresis loop in Fig. 5(a); $\rho_0 = 0.395$]. In the inset of Fig. 5(a), we show the dynamical evolution $\eta(t)$ (open data points), together with a numerically computed solution to a model equation for a subcritical bifurcation

$$\dot{\eta} = 0.15675\eta + 0.424\eta^3 - 0.3\eta^5, \qquad \eta(0) = \eta_0, \tag{39}$$

and find excellent agreement.

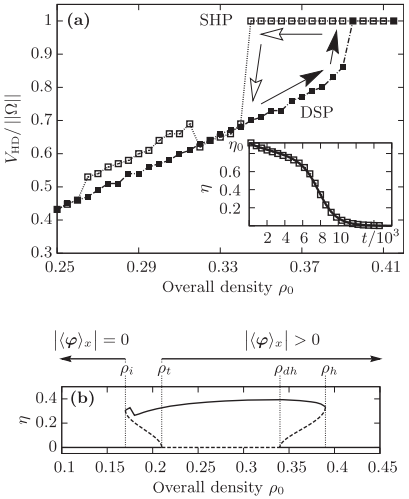

FIG. 5. (a) Hysteresis study ($\sigma = \sigma_0 = 0.25$). Surface fraction of the HD phase against overall density ρ_0. Solid symbols (with their paths indicated by solid arrows) indicate the system's stationary state upon increasing ρ_0 quasistatically, starting at a wavelike pattern at $\rho_0 = 0.25$. Open symbols (with their paths indicated by open arrows) indicate the system's stationary states upon quenching the density to successively lower values, starting from a stationary, spatially homogeneous state computed at $\rho_0 = 0.415$. The system exhibits hysteresis, corroborating the assertion that the underlying ordering transition is first order. Inset: Dynamics of the density-segregation parameter η (open data points) follows the subcritical bifurcation model [Eq. (39)] (solid line). (b) Sketch of the bifurcation diagram for the bifurcation parameter ρ_0 (at $\sigma = \sigma_0 = 0.5$). Solid lines indicate stable fixed points of the system's dynamics and have been determined numerically. Dashed lines are drawn "by hand" and indicate the estimated position of unstable fixed points.

Summarizing the results from Sec. III, we can now extend the picture conveyed by the phase-space diagram in Fig. 2(c), which has been recorded using random initial conditions at different points in parameter space. Our discussions in this and previous sections disclose regions in parameter space, where phase selection by the system is not uniquely related to the specific choice of parameters (i.e., density and noise levels). Instead, phase selection is sensitive to initial conditions in these parameter regions, and IHP and DSP coexistence at the low-density end and DSP and SHP coexistence at the high-density end of the DSP regime are observed. We condense these findings by sketching the corresponding bifurcation diagram in the ρ_0-η plane in Fig. 5(b). There, solid lines indicate the position of stable fixed points of the system's nonlinear dynamics, as measured by actual computations. Dashed lines are drawn "by hand" and indicate an estimate of the position of the corresponding unstable fixed points. Figure 5(b) corresponds to a horizontal cut through the phase diagram shown in Fig. 2(c) at $\sigma = \sigma_0 = 0.5$. Comparing both figures, we see that the phase diagram in Fig. 2(c) displays the DSP only in the relatively narrow window $\rho_t \lesssim \rho_0 \lesssim \rho_{dh}$ since initial conditions very close to the $\eta = 0$ fixed point are chosen. Because of the subcritical character of both transitions, IHP ↔ DSP and DSP ↔ SHP, density-segregated patterns can actually be observed over the much broader parameter range $\rho_i < \rho_0 < \rho_h$. Interestingly, an analogous extension of the existence region of density-segregated patterns has recently been reported in the context of nematic ordered active systems [31,35].

E. Phase-separated patterns

In previous works on polar systems with identical [26] or similar model properties [14,38], the emergence of

density-segregated states has been discussed in terms of traveling-wave patterns with "infinite" extent in the lateral direction [46]; see the snapshot in Fig. 2(b). However, in our numerical studies, we find an additional, genuinely distinct type of density-segregated pattern, which is fundamentally different from the familiar solitary-wave patterns. These patterns consist of a number of regularly shaped, moving high-density regions of finite lateral extent, where each such region carries a large net polarity. To emphasize their finite spatial extent, we will refer to these high-density polar regions as (polar) "clusters." Intriguingly, the polarities of these clusters are oriented along a common broken-symmetry axis with orientations distributed such that the overall symmetry of the system is nematic. More precisely, clusters are arranged in lanes, where each lane hosts a train of equally spaced clusters of parallel polarities. In our numerical studies, we observe two distinct types of cluster-lane pattern: First, we find antisymmetric cluster-lane solutions, where all cluster lanes have identical geometrical properties (same lane width and number and shape of polar clusters), except for a reflection of the cluster polarity from one lane to the next, thus rendering the overall symmetry of the system purely nematic. Typical snapshots of this first type of antisymmetric cluster-lane patterns are shown in Figs. 6(b), 6(c), and 11(b). Second, we observe asymmetric cluster-lane patterns where neither the number of clusters per lane nor the morphological properties of clusters in different lanes are symmetric; see Fig. 11(c). We note that the lane widths of this latter type of asymmetrical cluster are subject to a very slow but continuous drift during the computation times considered in this work. We, therefore, cannot exclude the possibility that this asymmetrical pattern would actually give rise to the more familiar wave pattern in the limit of long times (in which case the asymmetrical pattern would constitute an intermediate asymptote of the system's dynamics). In contrast, we find that the structural properties of the antisymmetric cluster-lane patterns do converge, which strongly suggests that these patterns constitute a genuine limit-cycle solution of the underlying Boltzmann equation [Eq. (6)]. In the following, we will, therefore, restrict ourselves to examine antisymmetric cluster-lane patterns that, moreover, are more frequently observed than their asymmetric counterparts. In particular, we give a detailed discussion highlighting the basic mechanisms stabilizing these remarkable patterns.

Before we embark on a more thorough discussion on the basic mechanisms stabilizing these nematic ordered patterns, we briefly comment on the observation statistics of antisymmetric cluster-lane patterns in our numerical solutions. As discussed in detail in Appendix B, the broken-symmetry axis in such cluster-lane patterns is effectively constrained to one of the two coordinate directions, due to the finite size of the computational grids used in our numerical studies. To obtain a counting statistics, we choose different sets of model parameters inside the DSP regime and use 350 different seeds per set of parameters to prepare independent systems with random initial conditions. We then let each of these systems evolve until a structurally stable, density-segregated state has developed. From all 350 patterns, we select those with a mean polar or nematic order along one of the coordinate axes and compute the observation frequency p of antisymmetric cluster-lane patterns among these "parallel patterns" [47]. While the observation frequency of antisymmetric cluster-lane patterns is rather low for the

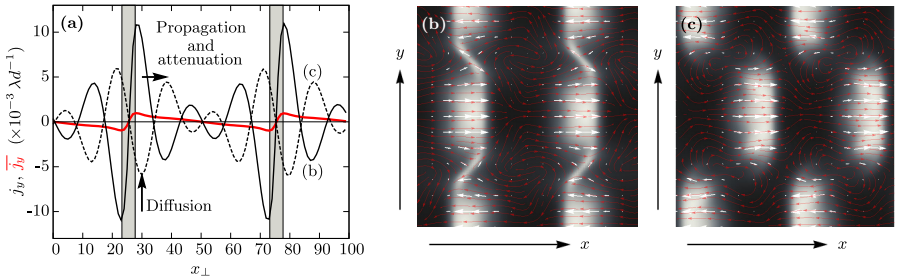

FIG. 6. Cluster-lane patterns. (a) Particle currents in the cluster-lane solution of the active Boltzmann equation. Black curves represent instantaneous realizations of the longitudinally averaged, transverse particle currents $j_y(y,t)$ as functions of the (transverse) y coordinate taken at different instances of time; see the snapshots in (b) and (c). The red curve represents the time-averaged transverse particle currents $\overline{j_y}(y)$. The gray shaded areas indicate the depletion zones where cluster grazing occurs, "feeding" the cluster zones (white areas). (b) Snapshot of a cluster-lane patten taken at the instant t_1 where the clusters of both lanes collide. (c) Snapshot of the same cluster-lane patten taken at some later instant $t_2 > t_1$ where the clusters of both lanes spread due to transverse diffusion. (b),(c) The color code indicates local density levels, white arrows indicate the magnitude and direction of the local momentum, and red streamlines indicate macroscopic flow patterns.

smallest system sizes considered in this work ($L = 50$; $p \approx 5\%$), these patterns make up a considerable fraction of all parallel patterns for system sizes $L \gtrsim 100$, in which case we find $p \approx 25\%$. (We find $p \approx 40\%$ if we count all cluster-lane patterns, including asymmetric cluster lanes.)

We shall now give a more precise definition of the term "cluster lane" and elucidate the dynamical mechanisms underlying their formation and stabilization. To this end, consider the antisymmetric cluster-lane pattern of Figs. 6(b) and 6(c) with the axis of nematic order along the x direction. To assess the particle-exchange dynamics between the various clusters, we record the transverse particle currents $g_y(\mathbf{x}, t)$ [Eq. (3)] and compute its longitudinal and time average according to

$$j_y(y,t) \equiv \frac{1}{L}\int_0^L dx g_y(\mathbf{x},t), \tag{40a}$$

$$\overline{j_y}(y) \equiv \frac{1}{\Delta T}\int_{t_0}^{t_0+\Delta T} dt j_y(y,t), \tag{40b}$$

where the time scales $t_0 = \Delta T = 10\,000\lambda^{-1}$ are chosen such that the computation of the time-averaged particle currents is done on the basis of a structurally stable cluster-lane pattern, i.e., in the limit of long times. Figure 6(a) shows $\overline{j_y}(y)$ along with the (instantaneous) particle currents $j_y(y,t)$ corresponding to two particular time instances, indicated by the snapshots in Figs. 6(b) and 6(c).

From inspection of the temporal average of the particle-current profile $\overline{j_y}(y)$ [red curve in Fig. 6(a)], we extract the following structural features: The overall functional form of $\overline{j_y}(y)$ resembles a sawtooth shape with large positive slopes (i.e., divergence of $\overline{j_y}$) in narrow depletion zones close to the cluster-lane boundaries and a shallow negative slope (i.e., convergence of $\overline{j_y}$) throughout the spatially extended cluster zones. The borders $y = y_b^i$ (with $i = 1, 2, \ldots$ labeling the different border lines) delineating adjacent cluster lanes are located at the 0s of the particle current inside the depletion zones, for which

$$j_y^{(s)}(y,t)|_{y=y_b^i} = 0 \quad \text{for all } t \text{ and } i \tag{41}$$

holds true in the stationary state (indicated by the superscript s). The sawtooth shape of the time-averaged current $\overline{j_y}$ therefore confers the following picture illustrating the balance of particle exchanges across different cluster lanes: The bulk of the clusters, i.e., the cluster zones inside each lane, receives particles at the expense of a narrow depletion zone at the cluster-lane borders. Within these depletion zones, large transverse, inwardly directed particle currents, "feeding" the bulk of the clusters, arise due to periodically recurring "cluster grazing"; see the solid black curve in Fig. 6(a) and the snapshot in Fig. 6(b). As time progresses, these particle currents propagate toward the center of the clusters. Concomitantly, rotational diffusion attenuates these propagative modes and gives rise to net diffusive currents at the tails of these modes that entail diffusive spreading of each cluster across the lane boundaries; see the dashed black curve in Fig. 6(a) and the snapshot in Fig. 6(c). In the steady state, these diffusive currents balance such that there is no net current across the lane boundaries. When the inwardly directed (attenuated) transverse currents eventually arrive at the cluster centers (which, again, correspond to the 0s of the transverse particle currents for all t), the aligning collision rule converts them into longitudinal currents, thus establishing a feedback mechanism to the macroscopic order parameter.

To demonstrate the structural stability of these antisymmetric cluster-lane patterns, we further compute the net particle exchanges [δC is the boundary delineating the right-moving cluster in Figs. 6(b) and 6(c)]

$$\dot{n} = \oint_{\delta C} d\mathbf{x} g_y(\mathbf{x},t) = L[j_y(y_b^1,t) - j_y(y_b^2,t)] \tag{42}$$

across the cluster-lane boundaries at y_b^2, y_b^1 ($y_b^2 > y_b^1$). Since in the stationary state $j_y^{(s)}(y_b^i,t) = 0$, we expect the magnitude of $j_y(y_b^i,t)$ to converge to 0 in the limit $t \to \infty$. In Fig. 7, the net rates $\dot{n}$ at which the left- and right-moving cluster lanes in Figs. 6(b) and 6(c) gain and lose particles are plotted as a function of time in the long-time regime $\lambda t \in [10\,000, 20\,000]$, where the cluster-lane pattern is virtually stationary. Because of overall particle conservation, the red and black curves in Fig. 7 sum up to 0. The net

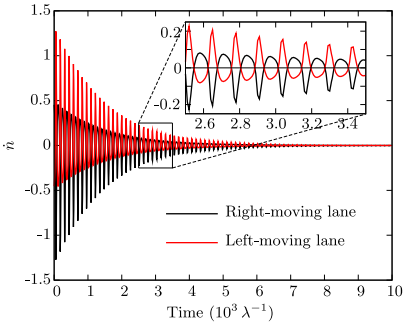

FIG. 7. Particle exchange across the cluster-lane boundaries in the long-time limit. In the plots, $t = 0$ corresponds to a simulation time of $t_{\text{sim}} = 10\,000\lambda^{-1}$, during which the cluster-lane pattern has developed from random initial conditions at $t_{\text{sim}} = 0$. Particle exchanges across the cluster-lane boundaries are driven by cluster grazing (spikes) and lateral diffusion of clusters (bumps); see the inset. In the long-time limit, the magnitude of the instantaneous value of the net particle exchange $\dot{n}$ across the cluster-lane boundaries converges to 0.

rates at which both cluster lanes gain and lose particles are extremely small in the displayed long-time limit and decay exponentially as $t \to \infty$. This exponential decay indicates that a balance of particle numbers is being established between both lanes, such that the corresponding cross-lane particle currents cancel in the limit of asymptotically long times. The close-up view in the inset of Fig. 7 reveals that this balancing process is driven by cluster-grazing events (spikes) during which the right-moving lane gives off particles to the left-moving lane and transverse diffusion (bumps), which leads to a net current of particles into the right-moving cluster lane. We stress, however, that even in the stationary state, large amounts of particles are transported laterally across the cluster-lane boundaries, and only the net exchange of particles vanishes due to a global cancellation of periodically oscillating particle currents that are constantly maintained by cluster grazing and transverse diffusion.

In summary, cluster-lane patterns constitute an intriguing, stable limit-cycle solution of the Boltzmann equation. The transport processes entailed by these cluster-lane patterns differ from those of the more familiar solitary-wave patterns in two important respects: First of all, in contrast to the solitary-wave solution, where a macroscopic transport of particles is confined to the longitudinal direction, the antisymmetric cluster-lane pattern approaches a stationary state in which macroscopic, periodically oscillating particle currents give rise to an interesting local net transport of particles in lateral directions, which is balanced only on global scales. Second, the global order of this limit-cycle solution is nematic rather than polar. The cluster-lane solution of the Boltzmann equation thus highlights a physical mechanism by which a system of self-propelled polar particles and purely polar interactions is capable of eliciting a macroscopic state of global nematic order. Put differently, clusters could be viewed as polar quasiparticles with only nematic interactions, thus rendering the system nematic on macroscopic scales. For a sample movie of a cluster-lane solution, refer to the Supplemental Material [42].

Before we conclude, some additional remarks are in order. Our numerical results, presented in this section, provide strong evidence for the actual stability of these novel cluster-lane patterns. Moreover, we check that the emergence of cluster-lane patterns is not a singular property of the specific features of the BDG model: As a matter of fact, we observe the formation of cluster-lane patterns over a large range of parameters for a class of more general collision rules (see Ref. [34]) deviating from the half-angle alignment rule [Eq. (31)] employed in the BDG model (data not shown). This observation suggests that the cluster-lane solution is of an even more general scope within the framework of the Boltzmann-equation approach to active polar systems. Nevertheless, it is important to keep in mind that the Boltzmann equation itself rests on a number of specific assumptions, including the absence of multiparticle interactions beyond binary collisions and the neglect of correlation effects among particle states as a consequence of the molecular chaos assumption. To which extent the emergence of cluster-lane patterns is hinged on such a hidden assumption constitutes an important question to be addressed in order to clarify the role of such cluster-lane patterns for actual active matter systems. We, therefore, hope that future studies employing alternative modeling approaches will shed light on this important question.

F. Coarsening dynamics

Having accessed the frequency of the stationary patterns of phase-segregated clusters and waves, in this section, we address the dynamics of the coarsening process for both patterns. For classical phase separation of fluid mixtures in the droplet regime (asymmetric quench [48]), the coarsening of structures is driven by Ostwald ripening [49] and Brownian coalescence [50]. Since both mechanisms rely on the diffusion of either droplet material or droplets, the corresponding growth laws exhibit identical scaling as a function of time, i.e., the characteristic size of structures (clusters or droplets) $\ell(t) \propto t^{1/3}$ [48]. Interestingly, the same coefficient is reported in a model of self-propelled particles exhibiting run-and-tumble dynamics on a lattice [51] and a similar (but slightly smaller) coarsening exponent has been found in actively propelled hard spheres [52,53] coinciding with theoretical predictions [54]. Here, we examine the question of whether there is dynamical scaling for the phase-segregated, polar-moving cluster and wave patterns.

To this end, the characteristic size of a structure $\ell(t)$ must be defined: We scan over the lattice along x while fixing y, and vice versa, and determine the corresponding probability distribution $p_{x(y)}(l)$ of connected areas l for which $\rho/\rho_0 > 1$, i.e., for which the density is larger than the homogenous density ρ_0. The characteristic length for scanning over x or y, respectively, is then defined as the first moment of the probability distribution

$$\ell_{x(y)}(t) = \int dl p_{x(y)}(l;t) l. \tag{43}$$

However, in contrast to a classical phase separation in fluid mixtures [48] or actively propelled hard spheres [52,53], the emerging phase-segregated patterns discussed in this manuscript are not isotropic. Consequently, the characteristic length has to be determined with respect to the mean polarity, i.e., transversal and longitudinal to it. In the following, we analyze the characteristic length transversal to the stationary polarity $\ell_\perp(t)$, whose long-time asymptote gives the lateral correlation length of the pattern, i.e., $\ell_\perp(t \to \infty) = \xi_\varphi$. Speaking in terms of Eq. (43), the transversal characteristic length $\ell_\perp(t)$ is equal to $\ell_{x(y)}(t)$ when the respective pattern moves along the y (x) axis. The corresponding results for wave patterns and cluster patterns

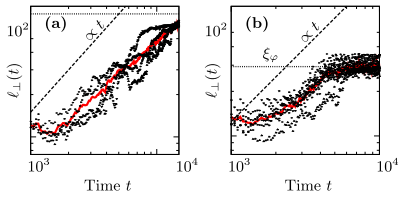

FIG. 8. Scaling of the coarsening dynamics inside the DSP regime at intermediate and long times. (a) Temporal evolution of $\ell_\perp(t)$ for a set of four different seeds (data points) of wave patterns. The length scale $\ell_\perp(t)$ roughly grows linearly with time and saturates at $\xi_\varphi \equiv \ell_\perp(t \to \infty) = L$. (b) Temporal evolution of $\ell_\perp(t)$ for a set of six different seeds (data points) of cluster-lane patterns. The length scale $\ell_\perp(t)$ roughly grows linearly with time and saturates at $\xi_\varphi \equiv \ell_\perp(t \to \infty) \approx 0.4L$. The solid red lines in (a) and (b) represent the averaged time evolution of $\ell_\perp$.

are shown in Fig. 8. Analyzing several random initial conditions, the characteristic transversal length follows roughly $\ell_\perp(t) \propto t^1$ for both wave and cluster-lane pattern morphologies. This linear scaling is compatible with previous results from agent-based simulations [14]. While $\ell_\perp(t)$ coarsens up to the system size L in the case of wave patterns [Fig. 8(a)], it saturates significantly below L for cluster patterns [Fig. 8(b)]. Moreover, the pronounced asymmetric fluctuations of the characteristic length in time for the cluster patterns correspond to configurations where antiparallel moving clusters are positioned directly transversal to each other.

Here, we would like to derive a simplified picture to explain the observed linear scaling for the domain size $\ell_\perp(t) \propto t^1$. In the following, we are led by the coarsening dynamics in classical binary mixtures [48]. Say all polar high-density domains move ballistically with a velocity of approximately 1 (measured in units of v_0) and are of characteristic size of approximately $\ell_\perp$. Moreover, we assume that the total surface coverage of high-density, polar domains is approximately conserved during the coarsening process and, especially, during each coalescence event of two polar domains. This conservation of surface coverage of the polar domains implies that the characteristic time scale between two coalescence events scales according to $\tau \sim \ell_\perp$. On average, coalescence causes the radius polar droplets to increase by a factor of $\sqrt{2}$ per coalescence event in 2D, where we assume colliding domains of approximately equal size. We then infer the following scaling picture for relative change of the polar domain size:

$$\frac{1}{\ell_\perp}\frac{d}{dt}\ell_\perp \sim \frac{\Delta \ln \ell_\perp}{\tau} \sim \frac{\ln 2}{2\tau} \sim \frac{1}{\ell_\perp}, \tag{44}$$

implying that $\ell_\perp(t) \sim t^1$.

Our analysis for the coarsening process within the phase-segregated regime of the phase diagram [see Fig. 2(c)] is, of course, limited by the system sizes investigated. (Here, $L = 150$.) We hope that future studies involving larger system sizes confirm our observation of dynamical scaling in the coarsening dynamics of polar-moving phase-segregated morphologies.

IV. CONCLUSION

In this work, we have developed a general numerical framework to solve the Boltzmann equation for two-dimensional systems of self-propelled particles, which we referred to as SNAKE. Since we have chosen to solve the Boltzmann equation in real space, our algorithm is applicable even far beyond the onset of macroscopic order, so long as the basic assumptions underlying the Boltzmann equation itself (e.g., molecular chaos) are fulfilled. Specifically, our numerical framework lends itself to the implementation of arbitrary boundary geometries, and we discussed how boundary conditions can be formulated directly in terms of microscopic particle-wall interactions.

We applied our algorithm to study an archetypal two-dimensional model system of actively propelled particles with binary, polar interactions, as previously proposed by Bertin *et al.* [22,26], and to which we refer as BDG model. The BDG model is a kinetic model that is inspired by Vicsek's agent-based model [5]. It considers a collection of spherical, self-propelled particles moving at a constant speed v such that each particle's state can be captured by a two-dimensional position vector and an angular variable characterizing the current particle orientation, i.e., the direction of its velocity vector. In the absence of noise, particle orientations change in response to binary particle collisions that cause the velocity vectors of both collision partners to align along the average orientation of both particles prior to their collision. In addition, noise effects are assumed to influence both the free motion of particles between subsequent collisions ("self-diffusion") as well as the alignment process of the binary collisions themselves.

We showed that our algorithm is fully consistent with previous analytical results on the BDG model itself [26], as well as with the most pertinent results from extensive simulation studies on the Vicsek model [14] at the onset of collective motion. In particular, our numerical results corroborate the first-order nature of the phase transition toward collective motion and reproduce hysteresis effects and, therefore, phase coexistence between a spatially homogeneous, isotropic state and the emergence of polar ordered, density-segregated patterns; see Refs. [14,38]. In the framework of our numerical investigations of the BDG model, we have established two novel key insights.

First, we have studied the emergence of macroscopic collective motion, including parameter regions well beyond the onset of macroscopic order. Our results convey a

comprehensive picture, highlighting the core features of the transition between a fully isotropic, disordered state at low densities or high noise values and a long-range-ordered, spatially homogeneous state at high densities or low noise values. We found that this ordering transition bears strong structural similarities to liquid-gas transitions in equilibrium systems. There, if the density of a gas is isothermally increased beyond the binodal, the gas phase becomes metastable and, therefore, susceptible to large-magnitude density fluctuations. If present, such large fluctuations lead to the nucleation and growth of high-density liquid droplets and eventually lead to phase separation into spatially coexisting liquid and gas phases. At still larger densities, the gas phase becomes unstable and spinodal decomposition occurs. In this case, arbitrarily small density fluctuations are amplified and the equilibrium system immediately separates into spatially coexisting low-density gas and high-density liquid phases. The mole fractions of these coexisting phases depend linearly on the system's specific volume such that the liquid phase completely takes over for large enough densities. The same line of arguments applies to the opposite case, where the density of a liquid system is being decreased. Intriguingly, we find the exact same overall behavior in the context of the ordering transition in the BDG model; see Fig. 5(b). At constant noise values ("temperature"), we identified binodal (ρ_i) and spinodal (ρ_t) density thresholds, beyond which the isotropic "gas" phase becomes metastable (susceptible to large enough density fluctuations) and unstable, respectively. Beyond the spinodal density threshold ρ_t, arbitrarily small density fluctuations give rise to the formation of polar droplets, whose size grows linearly over time until a macroscopic, density-segregated state has developed. Within this regime, well-ordered high-density waves or clusters ("liquid phase") are moving on a low-density, isotropic background ("gas phase"). Similarly to the equilibrium case, the surface fractions of both phases linearly depend on the system's overall density and the gas phase gets extinct at high enough overall densities. Conversely, any spatially homogeneous polar ordered system at high densities becomes metastable when the overall density falls below the second binodal density threshold ρ_h, and spinodal decomposition occurs upon further reduction of the overall density below the second spinodal density ρ_{dh}. An analogous discussion, highlighting the similarity between flocking and liquid-gas transitions, can be found in a recent work on a lattice model of active Ising spins [20]. Despite the fact that both the BDG model and the active Ising-spin model of Ref. [20] belong to different symmetry classes, the qualitative features of the flocking transition to spatially homogeneous polar order remain virtually unchanged. This observation, in turn, strongly suggests a universal character of the flocking transition to homogeneous polar order across different modeling classes and underlying symmetries.

Second, our results indicate the emergence of intriguing spatial structures after spinodal decomposition, which are genuinely distinct from wavelike patterns of infinite lateral extent. Inside the parameter regime where density-segregated patterns are found, we observed a novel type of patterns which we referred to as cluster-lane patterns. These patterns consist of parallel lanes of polar clusters, traveling in opposite directions. We gave a detailed discussion of the physical mechanisms underlying the stability of this limit-cycle solution of the Boltzmann equation in terms of the transverse cross-lane transport of particles. Most importantly, these cluster-lane patterns differ in two essential respects from the familiar solitary-wave patterns, with which they seem to coexist in the DSP regime of the parameter space: First of all, while the solitary-wave solution of the Boltzmann equation reflects the polar symmetry of the constituent particles and their mutual interactions, the cluster-lane solution of the Boltzmann equation renders the overall symmetry of the ordered state nematic. Second, while the solitary-wave solution gives rise to purely diffusive particle currents in the lateral direction which "die out" in the limit of long times, the cluster-lane solution is hallmarked by periodically recurring propagative lateral particle-transport modes that persist even for asymptotically long times. Regarding their potentially spectacular consequences, we hope that future research will further clarify the role of these intriguing patterns.

To conclude, the Boltzmann equation provides a convenient platform to implement particle-level descriptions of active model systems and to assess the ensuing spatiotemporal dynamics on macroscopic scales. While this latter step is prohibitively difficult to achieve in analytical treatments of the Boltzmann equation, our numerical framework allows us to study the macroscopic properties of active systems even far beyond the onset of collective order. SNAKE, therefore, provides the basis to study a countless variety of binary collision models with arbitrary interaction symmetries, which can be achieved by appropriately (re) defining the collision and diffusion operators; see Secs. II C 2 and II C 3. More general modeling classes can be constructed by redefining the convection operator (see Sec. II C 1), which, for instance, allows for the straightforward realization of density-dependent motilities [19]. In particular, the kinetic framework discussed in this work is easily extended to a multispecies description of active matter [33]. Therefore, SNAKE grants direct access to a wealth of new and exciting questions dealing with the spatiotemporal dynamics of actively propelled systems in conjunction with chemical reactions or in the context of mutually competing species both in free space and in arbitrary confinement geometries.

ACKNOWLEDGMENTS

We thank Hugues Chaté and Eric Bertin for stimulating discussions. This work was supported by the Deutsche

Forschungsgemeinschaft in the framework of the SFB 863 "Forces in Biomolecular Systems" (Project No. B2) and the German Excellence Initiatives via the program "NanoSystems Initiative Munich (NIM)."

APPENDIX A: WAVE PATTERNS REVISITED

In this Appendix, we briefly comment on momentum and velocity fields for wavelike patterns inside the DSP regime, as well as on their bending instability at the DSP → IHP transition.

In Sec. III C, we investigated the range of stability of wavelike patterns as the overall density of the system is gradually decreased or increased. In both cases, our results suggested a first-order transition toward a spatially homogeneous isotropic or polar state, respectively. Thereby, the former case, where the system undergoes a phase transition toward a spatially homogeneous, isotropic state upon decreasing the density below the threshold value ρ_i, is accompanied by a "reinforcement" of the wave pattern just before the DSP → IHP phase transition occurs; see the highlighted data points in Fig. 4(b) and corresponding data points in Fig. 10(b). This reinforcement effect can be explained by the finite system size and is illustrated by the sequence of snapshots displayed in Fig. 9. There, the initial state of the system corresponds to a wave pattern of relatively large lateral extent, which is wrapped around the torus (representing the system's domain Ω) twice (Fig. 9, left panel). As the overall density is decreased toward the transition threshold $\rho_0 \searrow \rho_i$, this laterally elongated pattern eventually becomes unstable toward a bending instability (Fig. 9, middle panel). However, on a periodic domain, this instability does not necessarily destroy the wave pattern but rather can lead to a reorientation of the wave, so as to contract its lateral extension (Fig. 9, right panel). This lateral contraction, in turn, leads to a reinforcement of the wave pattern, with both particle density and momentum across the contracted pattern being increased as compared to the initially elongated wave pattern; see Figs. 4(b) and 10(b). Note, however, that this reinforcement mechanism is an artifact of the finite system size and has no analog in infinite systems.

We conclude this Appendix by briefly reviewing the characteristics of the momentum and velocity fields for wave patterns inside the DSP regime. To this end, we have recorded the waves' momentum profiles at various overall density ρ_0 inside the DSP regime [Fig. 10(a)] and the characteristic particle velocities inside the LD phase ($v_{\min}$) and the HD phase ($v_{\max}$), together with the system's spatially averaged velocity $\langle v \rangle$ as a function of ρ_0 [Fig. 10(b)]. The waves' momentum profiles closely resemble their respective density profiles both with respect to their asymmetric shape and their growing asymmetry with increasing density. As for the characteristic velocities inside the DSP regime, we observe an approximately linear increase of the spatially averaged velocity $\langle v \rangle$ after an apparently discontinuous jump at the DSP → IHP transition. The characteristic velocity inside the HD phase remains virtually constant over the whole span of the DSP regime. In contrast, the characteristic velocity inside the LD phase is vanishingly small only up to densities $\rho_0 \lesssim 0.3 \equiv \rho_v$, in which case the wave patterns can, in fact, be characterized as high-density bands moving on an isotropic low-density sea of particles. For higher densities inside the DSP regime (i.e., $\rho_0 < \rho_h$), wave patterns persist but with increasing longitudinal extensions, such that the waves' tails start to infiltrate the LD phase. As a result of this infiltration, the characteristic velocity inside the LD phase is being increased to a density-dependent, finite value, although the corresponding characteristic density of the LD phase remains virtually unchanged at a subcritical value $\rho_{\min} < \rho_t$; see Figs. 4(a) and 4(b). One possible explanation for this observation of finite velocities inside the LD phase could be as follows: Since $\rho_{\min} < \rho_t$, the dynamics of the locally averaged momentum inside the LD phase is such that $|\mathbf{g}_{\min}|$ (and thus $v_{\min}$) decays exponentially. Above a certain threshold width of the density waves (i.e., for $\rho_0 > \rho_t$), however, the time scale between

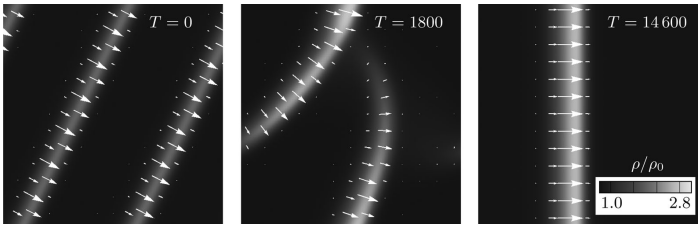

FIG. 9. Illustration of the bending instability in the vicinity of the transition DSP → IHP. Snapshots from left to right are taken at different times T. The left panel indicates the initial extended wave pattern, which becomes unstable toward a bending instability (middle panel); the right panel shows the reinforced stable wave pattern, which is contracted along the lateral dimension, as compared to the initial pattern.

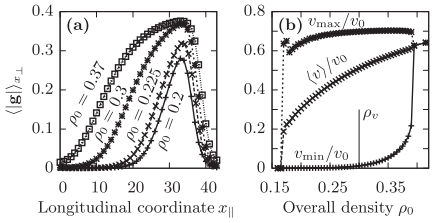

FIG. 10. Momentum and velocity for wavelike patterns within the DSP regime. (a) Momentum profiles corresponding to the density profiles displayed in Fig. 4(a). Velocity profiles morphologically resemble the corresponding density profiles and exhibit the same increase in asymmetry with increasing density. (b) Characteristic velocities inside the LD phase ($v_{\min}$) and the HD phase ($v_{\max}$), respectively. The middle curve gives the spatially averaged velocity $\langle v \rangle$. All velocities are measured in units of v_0. The velocity characterizing the LD phase $v_{\min}$ attains finite values for $\rho_0 \gtrsim \rho_v \approx 0.3$.

subsequent arrivals of wave maxima becomes comparable to the characteristic decay time scale for local momenta or velocities at $\rho = \rho_{\min}$. Hence, in the stationary limit, the LD phase attains nonvanishing average particle velocities, despite the fact that local conditions in the LD phase are such that polar order tends to be destroyed.

APPENDIX B: CLUSTER-LANE ORIENTATIONS

Here, we will give a brief account of possible cluster-lane orientations in systems with periodic boundary conditions. In particular, we will illustrate that the observation rates for cluster-lane patterns do strongly depend on cluster-lane orientations and, therefore, explain why only a small number of typical cluster-lane orientations is expected to be observed in simulations with finite system sizes.

For the sake of greater clarity, we will consider systems with a 1∶1 aspect ratio. Further, we will use the one-dimensional "midline" of each cluster lane [i.e., the 0 of the time-averaged particle current inside the cluster zone; see Fig. 6(a)] to represent the entire (two-dimensional) lane. Since clusters moving on different lanes (and antiparallel directions) must not collide, each cluster lane on the system's periodic domain Ω must be closed. This condition can be expressed by requiring

$$\frac{\Delta}{L} = \frac{w}{l} \leq 1, \qquad w \in \mathbb{N}, \qquad l \in \mathbb{N}\backslash\{0\}, \tag{B1}$$

where Δ denote the distance along the x axis between subsequent intersections of the cluster lane's midline with the lines $y = 0$ and $y = L$, and where w and l are coprime integers; see Fig. 11(a). Since all values of Δ with $\Delta_1/L = L/\Delta_2$ are equivalent upon interchanging the x and y axes, we can assert $\Delta \leq 1$ without loss of generality.

In Eq. (B1), the integers w and l characterize the topological and geometrical properties of the cluster lane, as is shown in Fig. 11(a). Specifically, w gives the cluster lane's winding number in the equatorial plane of the torus representing the periodic domain Ω; see Fig. 12. The length parameter l measures the total length of the cluster lane in units of the (orientation-dependent) length parameter $\ell(\alpha_{w,l}) = L/\cos(\alpha_{w,l})$, where

$$\alpha_{w,l} = \arctan(w/l) \tag{B2}$$

denotes the cluster lane's orientation with respect to the y axis.

According to Eq. (B1), the ratio Δ/L can take on arbitrary rational values. At first sight, this observation does not seem to imply a severe restriction, since the set of rational numbers is a dense subset of the real numbers. In other words, arbitrary cluster-lane orientations α are "infinitely close" to meeting the requirement Eq. (B1). While this statement is true in the hydrodynamic limit $L \to \infty$, finite-size effects considerably restrict the number of possible cluster-lane orientations $\alpha_{w,l}$. To see this, note

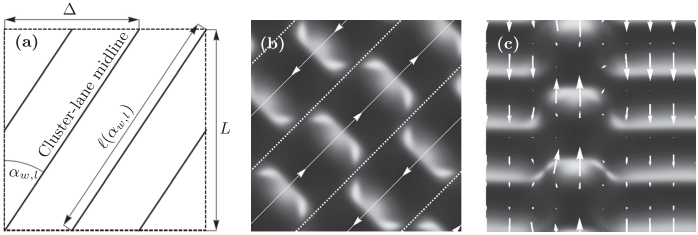

FIG. 11. Cluster-lane geometry in periodic systems. (a) Schematic of the position of a cluster lane's midline for winding number $w = 2$ and length parameter $l = 3$. (b) Illustration of a cluster-lane pattern with orientation $\alpha = \alpha_{1,1} = \pi/4$, observed in a system of linear extent $L = 125$. Cluster lanes are indicated by dashed white lines, cluster lanes' midlines indicated by thin solid lines. The direction of motion is indicated by arrows. (c) Asymmetric cluster-lane pattern observed in a system of linear extent $L = 150$. The parameters for (b) and (c) are $\sigma = \sigma_0 = 0.5$ and $\rho = 0.25$.

that the area $s_{\text{cluster}}(\alpha)$ each cluster lane of orientation α covers on Ω is given by (Λ is the cluster lane's transversal extension)

$$s_{\text{cluster}}(\alpha_{w,l}) = l \cdot \ell(\alpha_{w,l}) \cdot \Lambda. \tag{B3}$$

Since the total system size is finite $\|\Omega\| = L^2$, and since the minimum number of cluster lanes is 2 (one cluster lane alone corresponds to a wave pattern), we have

$$s_{\text{cluster}}(\alpha_{w,l}) \leq \frac{L^2}{2}. \tag{B4}$$

Therefore, noting that the cluster-lane width Λ is proportional to the transverse correlation length ξ_φ of the polar order parameter, and that $w \leq l$, we get

$$w \leq l \leq \frac{L^2}{2\ell(\alpha_{w,l})\Lambda} \propto \frac{L}{\Lambda} \propto \frac{L}{\xi_\varphi}. \tag{B5}$$

For the system sizes used in our numerical computations, we find $\xi_\varphi \sim L = \mathcal{O}(10^2)$. We, therefore, observe cluster-lane patterns characterized by $0 \leq w \leq l \sim 1$, i.e., $w/l \in \{0, 1\}$, amounting to cluster-lane orientations $\alpha_{w,l} \in \{\pi/2, \pi/4\}$; see Figs. 11(b) and 11(c). These orientations correspond to the cluster-lane geometries indicated in the top left plot in Fig. 12. Visual inspection of Fig. 12 illustrates the rapidly increasing space requirements for cluster-lane patterns with increasing values of w and l. These space requirements, in turn, directly affect the competition between cluster-lane and wave patterns during the pattern-selection process: Although Eq. (B1) has to be fulfilled for any line, representing the lateral extension of a wave pattern, as well, the resulting space requirements [as captured by Eqs. (B3) and (B4)] are far less restrictive for waves. More precisely, a single wave band can attain any orientation $\alpha_{w,l}$ such that

$$s_{\text{wave}}(\alpha_{w,l}) = l \cdot \ell(\alpha_{w,l}) \cdot \xi_\parallel \lesssim L^2, \tag{B6}$$

where $\xi_\parallel$ denotes the longitudinal extension of the wave. Since $\xi_\parallel \ll \Lambda = \mathcal{O}(\xi_\varphi)$, Eq. (B6) is, therefore, compatible with a much larger set of orientations $\alpha_{w,l}$ than Eqs. (B3) and (B4) (for finite system sizes L). Finite system sizes L, therefore, imply a bias in favor of the formation of wave patterns.

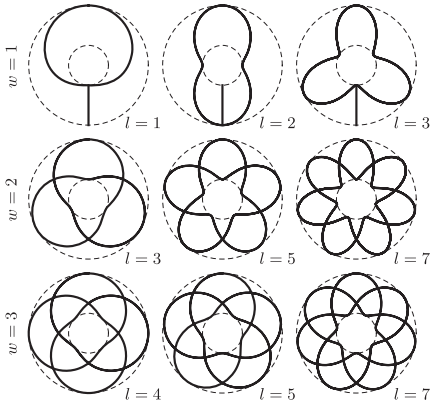

FIG. 12. Illustration of the winding number w and the length parameter l; see Eq. (B1). Each plot indicates the projection of the cluster lane's midline onto the torus's equatorial plane. (The system's extent in the equatorial plane is indicated by a pair of dashed, concentric circles.) The winding number w (rows) gives the number of full revolutions about the torus's midpoint in the equatorial plane. The special case $w = 0$ is indicated by the straight solid lines in the top row. The length parameter l (columns) gives the total length of the closed contour representing the cluster lane's midline.

APPENDIX C: NUMERICAL PROTOCOL TO MEASURE THE HIGH-DENSITY HYSTERESIS LOOP

In this Appendix, we briefly explain the numerical protocol used to obtain the data points shown in Fig. 5 (open symbols). Special care must be taken to properly assess the location of the density scale ρ_{dh}, where spatially homogeneous polar ordered states become linearly unstable toward the emergence of density-segregated patterns. At the point where the homogeneous system turns linearly unstable, the development of spatial heterogeneities out of a virtually homogeneous state is extremely slow. As a sensitive means to detect the buildup of spatial heterogeneities, we introduce the maximum absolute deviation

$$\Delta_f \equiv \max_{\alpha,n}\{|f_n^\alpha - \bar{f}_n|\} \tag{C1}$$

for the density matrix f_n^α, where

$$\bar{f}_n \equiv \langle f_n^\alpha \rangle_\alpha. \tag{C2}$$

This maximum absolute deviation approaches 0 for spatially homogeneous systems and attains finite values [typically of order $\mathcal{O}(10^{-1})$] for states inside the DSP regime.

To estimate the value of ρ_{dh}, we proceed as follows. We start from a spatially homogeneous base state, equilibrated at $\rho_0 = 0.415$ with $\Delta_f = \mathcal{O}(10^{-8})$. We then quench the overall density ρ_0 to successively lower values and let the system evolve for a time span of at least $T = 30\,000\lambda^{-1}$ [55]. During this time, we record the evolution of the quantity Δ_f. For all data points in Fig. 5 with $V_{\text{HD}}/\|\Omega\| = 1$, the maximum absolute deviation Δ_f is a monotonically decreasing function of time and the system

approaches a spatially homogeneous state. Conversely, in systems being represented by data points with $V_{\mathrm{HD}}/\|\Omega\| < 1$, Δ_f increases such that the spatially homogeneous initial states eventually give rise to density-segregated patterns.

As mentioned earlier, for density quenches down to final densities $\rho_0 \lesssim \rho_{dh}$ in the vicinity of ρ_{dh}, the actual buildup of spatial heterogeneities happens on a very large time scale. In actual computations, this time scale turns out to be much slower than the local "equilibration" of the density matrix f_n^α toward the new density level ρ_0. We, therefore, do not expect that the results shown in Fig. 5 should depend on whether they are obtained from a quasistatic protocol or a density quench protocol, as discussed here.

[1] J. Toner, Y. Tu, and S. Ramaswamy, *Hydrodynamics and Phases of Flocks*, Ann. Phys. (Amsterdam) **318**, 170 (2005).

[2] S. Ramaswamy, *The Mechanics and Statistics of Active Matter*, Annu. Rev. Condens. Matter Phys. **1**, 323 (2010).

[3] T. Vicsek and A. Zafeiris, *Collective Motion*, Phys. Rep. **517**, 71 (2012).

[4] M. C. Marchetti, J.-F. Joanny, S. Ramaswamy, T. B. Liverpool, J. Prost, M. Rao, and R. A. Simha, *Hydrodynamics of Soft Active Matter*, Rev. Mod. Phys. **85**, 1143 (2013).

[5] T. Vicsek, A. Czirók, E. Ben-Jacob, I. Cohen, and O. Shochet, *Novel Type of Phase Transition in a System of Self-Driven Particles*, Phys. Rev. Lett. **75**, 1226 (1995).

[6] J. Toner and Y. Tu, *Long-Range Order in a Two-Dimensional Dynamical XY Model: How Birds Fly Together*, Phys. Rev. Lett. **75**, 4326 (1995).

[7] J. Toner and Y. Tu, *Flocks, Herds, and Schools: A Quantitative Theory of Flocking*, Phys. Rev. E **58**, 4828 (1998).

[8] G. Grégoire and H. Chaté, *Onset of Collective and Cohesive Motion*, Phys. Rev. Lett. **92**, 025702 (2004).

[9] F. Peruani, A. Deutsch, and M. Bär, *Nonequilibrium Clustering of Self-Propelled Rods*, Phys. Rev. E **74**, 030904 (2006).

[10] S. Mishra and S. Ramaswamy, *Active Nematics Are Intrinsically Phase Separated*, Phys. Rev. Lett. **97**, 090602 (2006).

[11] A. Baskaran and M. C. Marchetti, *Hydrodynamics of Self-Propelled Hard Rods*, Phys. Rev. E **77**, 011920 (2008).

[12] A. Baskaran and M. C. Marchetti, *Enhanced Diffusion and Ordering of Self-Propelled Rods*, Phys. Rev. Lett. **101**, 268101 (2008).

[13] H. Chaté, F. Ginelli, G. Grégoire, F. Peruani, and F. Raynaud, *Modeling Collective Motion: Variations on the Vicsek Model*, Eur. Phys. J. B **64**, 451 (2008).

[14] H. Chaté, F. Ginelli, G. Grégoire, and F. Raynaud, *Collective Motion of Self-Propelled Particles Interacting without Cohesion*, Phys. Rev. E **77**, 046113 (2008).

[15] F. Ginelli, F. Peruani, M. Bär, and H. Chaté, *Large-Scale Collective Properties of Self-Propelled Rods*, Phys. Rev. Lett. **104**, 184502 (2010).

[16] S. Mishra, A. Baskaran, and M. C. Marchetti, *Fluctuations and Pattern Formation in Self-Propelled Particles*, Phys. Rev. E **81**, 061916 (2010).

[17] F. Peruani, T. Klauss, A. Deutsch, and A. Voss-Boehme, *Traffic Jams, Gliders, and Bands in the Quest for Collective Motion of Self-Propelled Particles*, Phys. Rev. Lett. **106**, 128101 (2011).

[18] A. Gopinath, M. F. Hagan, M. C. Marchetti, and A. Baskaran, *Dynamical Self-Regulation in Self-Propelled Particle Flows*, Phys. Rev. E **85**, 061903 (2012).

[19] F. D. C. Farrell, M. C. Marchetti, D. Marenduzzo, and J. Tailleur, *Pattern Formation in Self-Propelled Particles with Density-Dependent Motility*, Phys. Rev. Lett. **108**, 248101 (2012).

[20] A. P. Solon and J. Tailleur, *Revisiting the Flocking Transition Using Active Spins*, Phys. Rev. Lett. **111**, 078101 (2013).

[21] I. S. Aranson and L. S. Tsimring, *Pattern Formation of Microtubules and Motors: Inelastic Interaction of Polar Rods*, Phys. Rev. E **71**, 050901 (2005).

[22] E. Bertin, M. Droz, and G. Grégoire, *Boltzmann and Hydrodynamic Description for Self-Propelled Particles*, Phys. Rev. E **74**, 022101 (2006).

[23] E. Ben-Naim and P. L. Krapivsky, *Alignment of Rods and Partition of Integers*, Phys. Rev. E **73**, 031109 (2006).

[24] A. Baskaran and M. C. Marchetti, *Hydrodynamics of Self-Propelled Hard Rods*, Phys. Rev. E **77**, 011920 (2008).

[25] A. Baskaran and M. C. Marchetti, *Enhanced Diffusion and Ordering of Self-Propelled Rods*, Phys. Rev. Lett. **101**, 268101 (2008).

[26] E. Bertin, M. Droz, and G. Grégoire, *Hydrodynamic Equations for Self-Propelled Particles: Microscopic Derivation and Stability Analysis*, J. Phys. A **42**, 445001 (2009).

[27] I. S. Aranson, A. Sokolov, J. O. Kessler, and R. E. Goldstein, *Model for Dynamical Coherence in Thin Films of Self-Propelled Microorganisms*, Phys. Rev. E **75**, 040901 (2007).

[28] T. Ihle, *Kinetic Theory of Flocking: Derivation of Hydrodynamic Equations*, Phys. Rev. E **83**, 030901 (2011).

[29] Y.-L. Chou, R. Wolfe, and T. Ihle, *Kinetic Theory for Systems of Self-Propelled Particles with Metric-Free Interactions*, Phys. Rev. E **86**, 021120 (2012).

[30] A. Peshkov, S. Ngo, E. Bertin, H. Chaté, and F. Ginelli, *Continuous Theory of Active Matter Systems with Metric-Free Interactions*, Phys. Rev. Lett. **109**, 098101 (2012).

[31] A. Peshkov, I. S. Aranson, E. Bertin, H. Chaté, and F. Ginelli, *Nonlinear Field Equations for Aligning Self-Propelled Rods*, Phys. Rev. Lett. **109**, 268701 (2012).

[32] B. Ezhilan, M. J. Shelley, and D. Saintillan, *Instabilities and Nonlinear Dynamics of Concentrated Active Suspensions*, Phys. Fluids **25**, 070607 (2013).

[33] C. A. Weber, F. Thüroff, and E. Frey, *Role of Particle Conservation in Self-Propelled Particle Systems*, New J. Phys. **15**, 045014 (2013).

[34] F. Thüroff, C. A Weber, and E. Frey, *Critical Assessment of the Boltzmann Approach to Active Systems*, Phys. Rev. Lett. **111**, 190601 (2013).

[35] E. Bertin, H. Chaté, F. Ginelli, S. Mishra, A. Peshkov, and S. Ramaswamy, *Mesoscopic Theory for Fluctuating Active Nematics*, New J. Phys. **15**, 085032 (2013).

[36] X. Shi, H. Chaté, and Y. Ma, *Instabilities and Chaos in a Kinetic Equation for Active Nematics*, New J. Phys. **16**, 035003 (2014).
[37] T. Hanke, C. A. Weber, and E. Frey, *Understanding Collective Dynamics of Soft Active Colloids by Binary Scattering*, Phys. Rev. E **88**, 052309 (2013).
[38] T. Ihle, *Invasion-Wave-Induced First-Order Phase Transition in Systems of Active Particles*, Phys. Rev. E **88**, 040303 (2013).
[39] Here and in the following, we tacitly assume molecular chaos to apply to all systems considered in this work. For a critical assessment of the assumption of molecular chaos in the Boltzmann equation, refer to Refs. [34,37].
[40] Extension of the SNAKE algorithm to the situation of a nonvanishing flux at the boundaries is straightforward.
[41] The rate-limiting step here is the implementation of particle collisions. It takes $\mathcal{O}(K^2)$ operations to update each one of K angular channels of the local density matrix f_n^α.
[42] See Supplemental Material at http://link.aps.org/supplemental/10.1103/PhysRevX.4.041030 for videos and more information.
[43] Throughout this work, random initial conditions are chosen such that $f_n^\alpha = 0.95 + 0.1\zeta$, where the random variable ζ is uniformly distributed on the interval [0, 1].
[44] H. Chaté, F. Ginelli, and G. Grégoire, *Comment on "Phase Transitions in Systems of Self-Propelled Agents and Related Network Models,"* Phys. Rev. Lett. **99**, 229601 (2007).
[45] The small gap between the data points in Fig. 5(a) for $0.265 \leq \rho_0 \leq 0.295$ is due to a different pattern selection of the system on both branches of the hysteresis loop: While the solid branch refers to a single wave band wrapped around the donut, the density quench represented by the open symbols in the corresponding density range results in the formation of a two-banded pattern and thus occupies a slightly larger fraction of the overall volume.
[46] J.-B. Caussin, A. Solon, A. Peshkov, H. Chaté, T. Dauxois, J. Tailleur, V. Vitelli, and D. Bartolo, *Emergent Spatial Structures in Flocking Models: A Dynamical System Insight*, Phys. Rev. Lett. **112**, 148102 (2014).
[47] For the largest system sizes considered ($L = 150$), approximately 50–60 seeds out of a total of 350 seeds lead to parallel patterns.
[48] A. J. Bray, *Theory of Phase-Ordering Kinetics*, Adv. Phys. **43**, 357 (1994).
[49] I. M. Lifshitz and V. V. Slyozov, *The Kinetics of Precipitation from Supersaturated Solid Solutions*, J. Phys. Chem. Solids **19**, 35 (1961).
[50] K. Binder and D. Stauffer, *Statistical Theory of Nucleation, Condensation and Coagulation*, Adv. Phys. **25**, 343 (1976).
[51] A. G. Thompson, J. Tailleur, M. E. Cates, and R. A. Blythe, *Lattice Models of Nonequilibrium Bacterial Dynamics*, J. Stat. Mech. (2011) P02029.
[52] G. S. Redner, M. F. Hagan, and A. Baskaran, *Structure and Dynamics of a Phase-Separating Active Colloidal Fluid*, Phys. Rev. Lett. **110**, 055701 (2013).
[53] J. Stenhammar, D. Marenduzzo, R. J. Allen, and M. E. Cates, *Phase Behaviour of Active Brownian Particles: The Role of Dimensionality*, Soft Matter **10**, 1489 (2014).
[54] J. Stenhammar, A. Tiribocchi, R. J. Allen, D. Marenduzzo, and M. E. Cates, *Continuum Theory of Phase Separation Kinetics for Active Brownian Particles*, Phys. Rev. Lett. **111**, 145702 (2013).
[55] Systems with densities $0.3 < \rho_0 \leq 0.34$ have to be run for even longer time spans up to $T = 160\,000\lambda^{-1}$ in order to observe the formation of wave patterns. For $\rho_0 \in \{0.335, 0.34\}$, we observe a monotonic but extremely slow increase in Δ_f. To keep computation times at a tolerable level, we therefore perturb the system by setting $f_n^\alpha \to (0.995 + 0.01\zeta) f_n^\alpha$ at $T = 30\,000\lambda^{-1}$ (with the random variable ζ uniformly distributed on [0, 1]).

Part II

CELL MIGRATION: FROM SINGLE CELL MOTION TO COLLECTIVE DYNAMICS

5

A PRIMER ON THE CELLULAR POTTS MODEL

The theoretical studies discussed in the present part of this thesis are based on a cellular automaton model, which we have developed to capture the main features underlying the emergence of collective cell migration. The core framework underlying our simulation model is based on the so-called *cellular Potts model*, which has initially been proposed by Graner and Glazier [56, 55] to study cell sorting phenomena. To provide a frame of reference for subsequent discussions, this chapter will be devoted to an introduction of the main ideas underlying the *cellular Potts model*. While numerous modeling variants have been proposed to adapt the *cellular Potts model* to different biological situations, our focus here will be on the "standard version" of this model, as originally proposed in Refs. [56, 55]. A brief overview over some of the applications of the *cellular Potts model* will be given in section 6.2. A comprehensive discussion of our modeling approach, including details on its numerical implementation, as well as the biological basis underlying its definition will be given in sections 6.2 and 6.4, and in Appendix B.

The original design of the *cellular Potts model* aims at simulating the dynamical sorting of cells in heterogeneous tissues according to cell type. By the time the *cellular Potts model* has been proposed, such sorting behavior has been observed in a number of experimental studies [134, 51, 8], and has been hypothesized to be driven mainly by a difference in the strength of adhesive bonds between cells of different types [134, 45]. To put forward this idea of cell sorting due to differential adhesion, Graner and Glazier [56, 55] proposed a simulation framework based on the

so called Potts model [110, 160]. The Potts model has been introduced as an extension of the Ising model, and refers to a regular lattice of spins s_i (i: lattice index), where each spin can take any one out of N distinct values, $s_i \in \{1, \ldots, N\}$. The energy of each particular configuration of spins is given by the Hamiltonian

$$\mathcal{H}_{\mathrm{P}} = J \sum_{\langle i,j \rangle} \left(1 - \delta_{s_i s_j}\right), \tag{18}$$

where the sum is taken over neighboring spins, and where $J > 0$ quantifies the strength of interactions. According to Eq. (18), the growing lengths of domain boundaries between regions of unlike spins are energetically penalized. Graner and Glazier realized that this property could be used as a blueprint to model intercellular surface tensions, provided they proposed some suitable extension of the Potts model to incorporate the notion of biological cells.

To this end, Graner and Glazier proposed the following key extensions to complement the Potts model, in order to proceed from a set of spins to a collection of biological cells. First of all, they introduced the concept of a biological cell, which they defined to be a simply connected set of like spins. The spin variable s is thus used as identification number for individual cells. To conserve the simple connectedness of each cell, spin flips are only allowed at the cells' domain boundaries, but not in the bulk of the cells; cf. Fig. 12(a). Secondly, to account for varying strengths of adhesive bonds between different types of cells, they introduced an additional "quantum number" $\tau(s)$ associating each cell (identified via its spin s) with one particular cell type[1]. Using this notion of cell type, they then replaced the single coupling constant $J > 0$ by a matrix $J_{\tau,\tau'} > 0$ to model intercellular contact energies which depend on the particular cell types τ and τ'. Finally, to model realistic cell behavior, cell domain growth must be limited to prevent cells to attain unrealistically large surface areas. To achieve this, Graner and Glazier equipped each cell with a particular (possibly cell type specific) "target area" A_τ, which they

1 Thus, two or more cells can share the same cell type, but they cannot share the same spin value s, which is a unique identifier for each cell.

enforced via the introduction of a Lagrange multiplier λ in the definition of their extended (cellular) Potts model Hamiltonian, which then reads

$$\mathcal{H}_{\mathrm{CPM}} = \sum_{\langle i,j \rangle} J_{\tau(s_i),\tau(s_j)} \left(1 - \delta_{s_i s_j}\right) + \lambda \sum_s \left(A_s - A_{\tau(s)}\right)^2 . \quad (19)$$

Here A_s denotes the current area of cell s, and the Lagrange multiplier λ captures the elasticity of cells with respect to fluctuations of cell surface areas.

Equation (19) summarizes the standard *cellular Potts model*. Simulations of the standard *cellular Potts model* are based on a Monte-Carlo procedure and proceed via a succession of "atomic events" which allow cells in an initially well-mixed tissue comprising different cell types to move around and explore their environment. Atomic events are implemented as special kinds of spin flip trials during which the spin value s_i of a randomly selected lattice site is attempted to be copied to one of its next neighbors with spin $s_j \neq s_i$ prior to the flip. For each such atomic event, the corresponding "energy" change

$$\Delta\mathcal{H}_{\mathrm{CPM}} = \mathcal{H}_{\mathrm{CPM}}^{(\mathrm{after})} - \mathcal{H}_{\mathrm{CPM}}^{(\mathrm{before})} \quad (20)$$

is calculated and the attempted spin flip is accepted with probability[2]

$$p = \begin{cases} \exp\left(-\Delta\mathcal{H}_{\mathrm{CPM}}\right), & \Delta\mathcal{H}_{\mathrm{CPM}} > 0, \\ 1, & \Delta\mathcal{H}_{\mathrm{CPM}} \leq 0. \end{cases} \quad (21)$$

Time is measured in units of "Monte-Carlo steps" (MCS), where the length of one MCS is usually defined to comprise a number of atomic events which is comparable to the number of lattice sites in the simulation.

Figure 12 illustrates the basic concepts of the *cellular Potts model*. There, different colors indicate different cells (i.e. spins). Atomic events, as indicated by the arrow in Fig. 12(a), only occur across

2 Oftentimes, an effective "temperature" T is used in the definition of the spin flip probabilities in Eq. (21), such that $p = \exp\left(-\Delta\mathcal{H}_{\mathrm{CPM}}/T\right)$ for $\Delta\mathcal{H}_{\mathrm{CPM}} > 0$. Throughout this thesis, however, we set $T = 1$, which can be achieved by correspondingly rescaling the coupling constants in the system's "Hamiltonian".

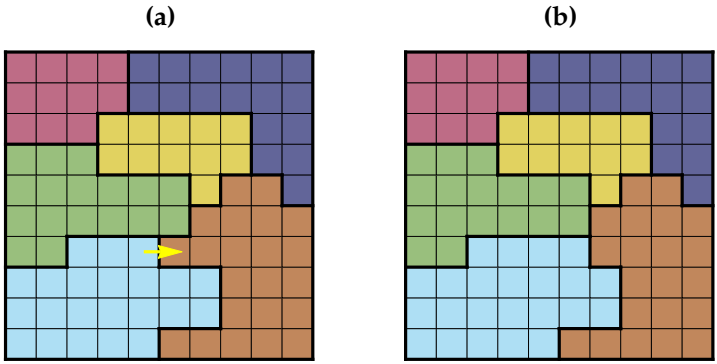

Figure 12.: Illustration of the standard *cellular Potts model*. Colors indicate cell number (spin). Atomic events (spin flips), as indicated by the yellow arrow in **(a)** can only occur across cell boundaries to preserve cell integrity. Trials of atomic events are accepted with a probability which is based on the change of adhesive and surface area "energies" associated with the attempted atomic event; cf. Eqs. (19) – (21). For instance, assume that cell-cell adhesion between the light blue and the green cells is stronger than the adhesion between either of these cells with the brown cell. Assume further that the indicated atomic event is energetically dominated by adhesion forces. Then the this attempted atomic event will be accepted with probability one since it increases the intercellular interface between the light blue and the green cell, and at the same time decreases the interface length between both these cells with the brown cell; cf. **(b)**.

the cells' membranes (i.e. domain boundaries between unlike spins). Eqs. (19) – (21) imply acceptance rates which tend to lower cell interface energies as the simulation progresses; cf. caption of Fig. 12.

In our simulation model, we will adopt the ideas put forward in the *cellular Potts model* to represent biological cells in numerical simulations, and we will resort to similar concepts to implement cell elasticity. In contrast to the standard version of the *cellular Potts model*, however, our focus of interest will be on the ability of cells to migrate and to elicit modes of collective motion

where several motile cells adhere to one another. Therefore, our computational approach comprises a number of modifications and extensions as compared to the standard *cellular Potts model*. Among others, we will exploit the representation of cells by (extended) sets of lattice sites, to equip each cell with a non-trivial internal structure representing a coarse grained model of the cytoskeleton. In particular, we will propose a rule based approach to capture the dynamical remodeling of the cytoskeleton, as well as mechanical crosstalk between cells in adhesive contact. A non-technical introduction to our computational model, along with a detailed study of the onset of collective cell migration will be given in the following chapter. A fully technical account, explaining the numerical implementation of our model can be found in Appendix B.

6

FROM SINGLE CELL MIGRATION TO COLLECTIVE DYNAMICS

6.1 STARTING POINT OF THE PROJECT

Living cells employ a variety of different motile machineries to propel themselves forward and to migrate to distant places. Leucocytes, for instance, employ the so called amoeboid mode of migration [46]. These highly flexible cells are able to squeeze through the narrow mesh of the extracellular matrix and form only very weak adhesive contacts, which allows them to move at very high migration speeds [49]. The same kind of migration strategy is also used by a number of tumor cells and makes such amoeboid cancers prone to the early formation of metastases [48]. In contrast, mesenchymal cells form tight integrin based focal adhesions with the substrate and, consequently, migrate at relatively slow speeds [48, 46]. Still other mechanisms are involved in the context of the collective migration of cell groups and entire tissues, where, additionally, the existence of stable cell-cell junctions and of various intercellular signaling processes has to be accounted for [47, 66].

These many different manifestations of cell motility are directly reflected in an enormous amount of theoretical literature, aiming at understanding the various aspects of cell migration at multiple levels of complexity and in different biological contexts. At the microscopic level, a solid body of mathematical modeling approaches addresses the sub-cellular basis of single cell motility [95, 36, 120, 72, 130, 96, 100, 129, 169, 167]. On the macroscopic level, the dynamics of extended tissues, comprising a large num-

ber of mutually adhesive cells, are typically captured theoretically by means of coarse grained models. In agent based simulations, for instance, cells are reduced to self-propelled point-like particles or to elastic objects with very simple geometrical properties, and the resulting tissue-wide dynamics is mainly a consequence of the particular assumptions used to model particle interactions [14, 87, 139, 12, 127]. Hydrodynamic approaches, on the other hand, capture tissues by means of macroscopic field variables such as the cell density and the stress tensor, and completely dispense with an explicit representation of single cells [15, 114, 78, 77, 86, 13].

Both limiting cases discussed above, cell migration at the scale of single cells and at the scale of tissues, have attracted considerable attention and seen impressive progress over the last years. However, a clear connection between both modeling regimes is still missing. There are two main reasons for this. First of all, the vast number of different cell types and, correspondingly, different biochemical implementations of cell motility, makes it difficult to find an appropriate level of description which, moreover, should be applicable over a large range of cell numbers. Secondly, the modeling paradigms pursued in both regimes are essentially incompatible. Microscopic modeling approaches are typically forbiddingly complex to allow for a straightforward generalization to the tissue level. In addition to restrictions due to limited computational resources, these models tend to view cells as isolated, autonomous objects and do not consider cells in their social context or take into account any mechanisms which would allow for crosstalk between cells. Conversely, macroscopic approaches rely on self-averaging properties of collections of a large number of individual cells and, therefore, discard cellular features which cannot be perceived in the bulk of extended tissues, but which might be essential in smaller systems.

In our work *"Bridging the gap between single cell migration and collective dynamics"* [TRS+14], we propose a computational framework which allows to establish a link between the migratory behavior of single cells and the large scale dynamical properties of adhesive groups of cells and tissues. This simulation model is then used to conduct an extensive investigation of the emergence

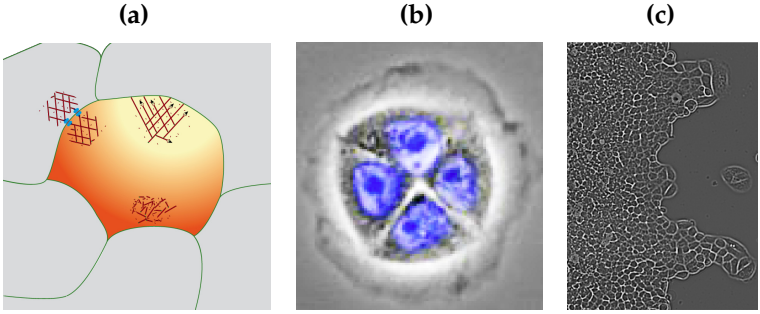

Figure 13.: **(a)** Illustration of high level cell functions accounted for in our simulation model. The cytoskeletal dynamics is captured in a rule based, but spatially resolved manner, and cell-cell signaling based on mechanical stimuli is taken into account. In addition, the dissipative effects brought about by cell-cell adhesion and cell-substrate adhesion (not shown), as well as cell elasticity are incorporated. **(b)** Coherent rotational motion in a small group of four cells confined on a circular micropattern [STFR14]. Courtesy of J. O. Rädler, LMU München. **(c)** Formation of fingering structures in an advancing cell front (image taken from Fig. 4E in Ref. [127], licensed under CC BY).

and the characteristics of collective cell migration in terms of single cellular properties. The main results of this study, as well as a brief introduction and motivation of our modeling approach will be summarized in the following section 6.2. Our focus there is on an exposition of the general spirit behind our modeling framework and on a spotlight on the most pertinent simulation results. A more comprehensive and technical description of our numerical model can be found in Appendix B. A complete discussion of our results is presented in the appended manuscript, section 6.4.

6.2 SUMMARY OF MAIN RESULTS

Our numerical model is based on the cellular Potts model [56, 55, 102], which has been introduced in chapter 5. The simulation framework provided by the cellular Potts model, has been used

in a number of previous works and has been successfully applied in both, the single cell and the tissue limit. In the context of single cells, the standard cellular Potts model has been complemented with an explicit description of a sub-cellular reaction diffusion network to study the polarization of motile keratocytes [85, 84]. Conversely, the standard cellular Potts model has been extended to include a number of kinetic rules, akin to those used in agent-based flocking models [87, 139], to study large scale cellular flows in tissues [89, 68, 138]. Also, the chemotactic migration of cells has been simulated in several biological contexts, including the aggregation of the slime mold *Dictyostelium discoideum* [121], the formation of vascular networks [91, 92, 103, 90, 88], the emergence of fingering structures in wound healing assays [101], and cell sorting phenomena [69]. Despite a large variety of different implementations [2, 137], however, typical tissue scale applications of the cellular Potts model are lacking an explicit description of essential cell features like the dynamics of the cytoskeleton and are, therefore, of only limited use in systems whose dynamics is governed by only a few cells. On the other hand, limited computational power essentially prevents the very sophisticated microscopic approaches [85, 84] to be amenable to the simulation of a larger number of cells.

In order to provide a connection between the single cell and the tissue levels, we, therefore, adopt a hybrid approach which lies in between the microscopic and the macroscopic modeling paradigms; cf. Fig. 13(a). In contrast to typical tissue level modeling approaches, we explicitly resolve the most pertinent features of cytoskeletal remodeling processes and implement feedback loops accounting for intra- and intercellular signaling based on mechanical stimuli. Unlike the more microscopic approaches, however, the design of our simulation model is based on high-level cell functions, rather than actual biochemical implementations in terms of various signaling pathways which might well differ from one cell-type to the next. In doing so, we exploit the fact that the same high-level cell functions are shared among a large variety of different cell types, despite the fact that the biochemical basis of these functions may be very different. Hence, rather than modeling the dynamics of cytoskeletal structures in

terms of complicated reaction-diffusion networks, we employ a strategy based on a relatively simple set of rules. The major upshots of this rule based approach are (i) a considerable gain in computational efficiency as compared to the more microscopic approaches and (ii) more realistic simulation results even in the limiting cases of single cell migration and small cell groups as compared to the more macroscopic approaches.

We emphasize that the different modeling approaches we discussed above, all provide answers to conceptually distinct questions. Typically, microscopic approaches revolve around questions addressing the actual emergence of high-level cell functions. Our simulations, in contrast, use these high-level functions as modeling input and, therefore, do not provide any answers in this particular direction. On the other hand, we do not expect our modeling approach to add novel insights in terms of the coarse grained bulk dynamics of extended tissues, where the reductionist's approach of macroscopic models should yield reliable results. However, we do expect our modeling approach to contribute substantially to the understanding of collective cell dynamics in all situations where the observed patterns of collective migration are a consequence of the orchestrated motion of a number of cells which is still too small for self-averaging to apply. Two important realizations of such situations will be discussed in our work [TRS+14]; see section 6.4, and Figs. 13(b,c): First, the emergence of coherent motion in small groups of cells on micropatterned surfaces [24, 63, 40, STFR14] (see also chapter 7), and secondly the evolution of cellular boundary layers as observed, for example, in typical wound healing assays [43, 111, 148, 109, 143, 128, 127].

Experimentally, micropatterns can be realized in the form of circular fibronectin islands which are surrounded by cell repellant surfaces [STFR14]. In simulations, the same confinement scenario is mimicked by exposing different levels of extra cellular matrix protein on the simulation grid, such that the formation of cell-substrate adhesions is effectively limited to a small circular region; see Appendix B for details. In experiments with MDCK cells [24, 63, STFR14], the cellular systems exhibit spontaneous cohort rotation about the center of the confining circle. While the

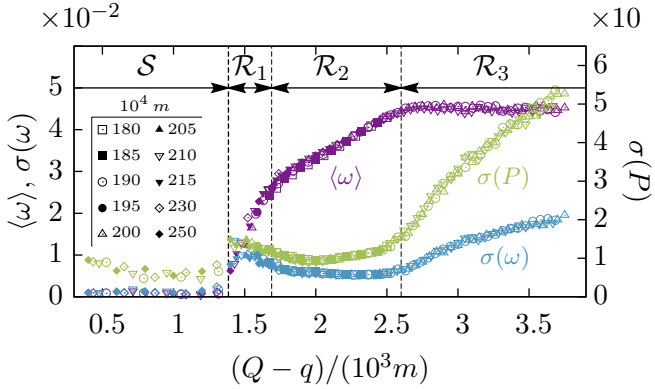

Figure 14.: Coherent motion of four cells in circular confinement as a function of the specific polarization $\Delta Q/m$; cf. [TRS+14]. The system exhibits an ordering transition to collective cell rotation for large enough specific polarizations, as indicated by the order parameter ξ. Based on the observed persistence times $\tau_p^{(c)}$ and cell shape variabilities $\mathrm{Var}(P)$, three distinct phases of collective rotation can be identified, where either elastic forces ($\mathcal{R}_1$-phase), or cytoskeletal forces ($\mathcal{R}_3$-phase) dominate the system's dynamics, or where both forces are in optimal balance ($\mathcal{R}_2$-phase).

details of the experimentally observed rotation statistics and its dependence on cell number is discussed in chapter 7, our focus here is on the identification of distinct phases of collective motion as cellular properties are varied.

To assess the overall features of collective cell rotation in our simulations, we quantify the statistics of rotation speeds observed in the cellular systems, as well as the variability of cellular shapes, which will be quantified by analyzing the statistics of cell perimeters P. To be specific, for any given combination of simulation parameters and for any given number of cells K, we prepare a set of N statistically independent simulation systems and measure the angular trajectory $\phi_\alpha^{(j)}(t)$ and cell perimeter history $P_\alpha^{(j)}(t)$ for each cell $\alpha = 1, \ldots, K$ within each simulation system $j = 1, \ldots, N$. We then define the (system-specific) mean trajectory $\Phi^{(j)}(t) \equiv$

$K^{-1}\sum_\alpha \phi_\alpha^{(j)}(t)$ and mean cell perimeter $P^{(j)}(t) \equiv K^{-1}\sum_\alpha P_\alpha^{(j)}(t)$, and compute the system-average of the rotation speed

$$\langle\omega\rangle \equiv \frac{1}{NT}\sum_{j=1}^{N}\sum_{t=1}^{T}|\dot{\Phi}^{(j)}(t)|, \tag{22a}$$

as well as the standard deviations

$$\sigma(\omega) \equiv \frac{1}{N(T-1)}\sum_{j=1}^{N}\sum_{t=1}^{T}\left(\dot{\Phi}^{(j)}(t) - \overline{\dot{\Phi}^{(j)}}\right)^2 \tag{22b}$$

and

$$\sigma(P) \equiv \frac{1}{N(T-1)}\sum_{j=1}^{N}\sum_{t=1}^{T}\left(P^{(j)}(t) - \overline{P^{(j)}}\right)^2, \tag{22c}$$

to assess rotation speed fluctuations and cell shape variabilities, respectively. Here T denotes the total simulation time, and $\overline{X^{(j)}} \equiv T^{-1}\sum_t X^{(j)}(t)$ denotes a time average of the system-specific observable $X^{(j)}$. We emphasize, however, that a statistical analysis based on the quantities introduced in Eqs. (22), is only meaningful in the context of sufficiently small cell numbers K, where only a single cell vortex is formed. Larger cell numbers escape a description in terms of the statistical quantities defined in Eqs. (22) due to the formation of multiple cell vortices, which call for a different strategy to quantify and describe the collective dynamics [40].

Figure 14, summarizes the overall features of collective cell rotation for varying strengths of the cells' cytoskeletal forces ΔQ and different cell elasticities m (more precisely, m controls the stiffness with respect to fluctuations of the cell's perimeter). Interestingly, the general statistical properties of collective cell rotations do not separately depend on the strength of cytoskeletal forces, ΔQ, and cell elasticity, m, but only on their ratio $\Delta Q/m$ which we will refer to as "specific polarity". For small values of the specific polarity, cells are immobile ($\langle\omega\rangle \approx 0$) and "condense" into a state of low elastic "energy" ($\mathcal{S}$-phase). For specific polarities above a certain threshold, the cells in the system become motile and collective cell rotation ($\langle\omega\rangle > 0$) is observed ($\mathcal{R}$-phases).

Based on the systems' rotation statistics, three distinct phases of collective cell rotation can be identified; cf. Fig. 14. For specific polarities $\Delta Q/m$ in the vicinity of the threshold to collective rotation, the system's dynamics is dominated by relatively large elastic forces which tend to arrest the system in a non-motile state of low elastic "energy" ($\mathcal{R}_1$-phase). Typical system trajectories in this regime are hallmarked by frequent changes in the direction of rotation and consist of finite episodes of collective cell rotation, interspersed by periods of stagnation. Conversely, for large specific polarities, the system's dynamics is dominated by relatively large cytoskeletal forces which imply a large variability of cell shapes, as quantified by the entity $\sigma(P)$ ($\mathcal{R}_3$-phase). Similar to the angular trajectories within the $\mathcal{R}_1$-phase, angular trajectories within the $\mathcal{R}_3$-regime exhibit finite (albeit larger) persistence times, and average rotation speeds saturating at a maximum value. We emphasize, however, that disruptions in cell rotations within the $\mathcal{R}_3$-phase arise as a consequence of unstable cellular shapes, rather than large "energetic" barriers entailed by strong elastic forces which are responsible for the frequent interruptions in cell rotations within the $\mathcal{R}_1$-regime. Finally, in between the $\mathcal{R}_1$- and $\mathcal{R}_3$-phases, we observe a parameter window of highly persistent[1], unidirectional collective cell rotations, which are sustained by an optimal balance of cytoskeletal and elastic forces and stable cell shapes ($\mathcal{R}_2$-phase). In this regime, average rotation speeds increase linearly with specific polarity $\Delta Q/m$.

Besides the emergence of coherent cell rotation in small groups of cells in confinement, we also applied our simulation model to study the expansion dynamics of an initially confined monolayer after the release of the spatial constraint. In experimental systems, such setups are often used as a model system to study cellular migration patterns during wound healing [43, 111, 148, 109, 143, 128]. Figure 15 shows typical morphologies of advancing cell fronts, along with the corresponding stress distributions in the bulk of the simulated tissues for two different modeling scenarios. The first row of Fig. 15 refers to a model system with

1 More precisely, for the simulation times considered in this work (T=10 000 MCS), we observed unidirectional cell rotations.

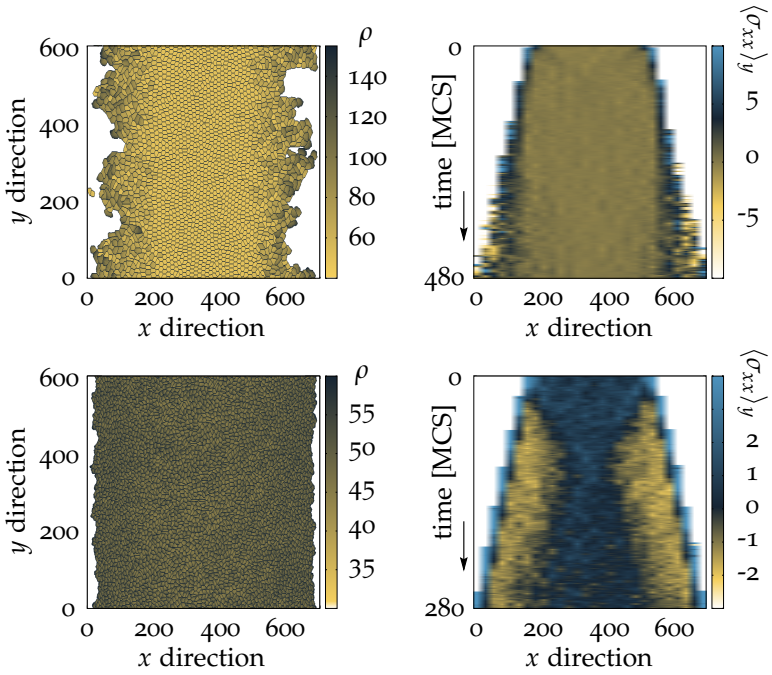

Figure 15.: Expansion of a confluent cell sheet driven by cell growth (upper row) and active cell migration (lower row), respectively; cf. [TRS+14]. Both, the snapshots (left column; color code: cell polarization ρ) and the kymographs (right column; color code: average stress in x-direction $\langle \sigma_{xx} \rangle_y$) highlight the markedly different extension dynamics in both scenarios.

a low homeostatic bulk pressure before the spatial constraint is lifted. In this system, cytoskeletal force generation, ΔQ, is assumed to be small and the dynamics of the advancing cell sheet is primarily driven by cell growth after the spatial constraint is released. The second row in Fig. 15 refers to the opposite situation. There, the homeostatic bulk pressure prior to the release of the spatial constraint is large, and cytoskeletal forces, ΔQ, are large during the expansion of the cell sheet. In what follows, we will refer to this latter modeling scenario as "scenario II", the former modeling scenario will be referred to as "scenario I".

Intriguingly, we observe markedly different morphologies of the leading edge of the expanding cell sheet in both scenarios. Specifically, in scenario I, where the progression of the monolayer boundary is primarily driven by cell growth, we observe the formation of finger like structures, akin to those observed in previous experimental studies [111, 109]. Due to the low homeostatic pressure in the tissue prior to the release of the spatial constraint, cell growth is essentially confined to the outer cell rows, where cells are exposed to free space. Concomitantly with cell growth, the maximum polarization of cells increases, which, in turn, implies a steep motility gradient across the outer boundary layers of the cell sheet; cf. Appendix B and section 6.4 for details. As a consequence, we observe the spontaneous formation of so called "leader cells" at the tips of the finger-like structures, which are significantly larger than the average size of cells in the system, and which can exert large pulling forces on "follower cells" by virtue of large cytoskeletal forces. The overall phenomenology is strikingly similar to previous experimental observations [111, 109]. In stark contrast, the expanding tissue in scenario II, where the homeostatic pressure across the cell layer before the release of the spatial constraint is large, exhibits a virtually straight advancing cell front as the spatial constraint is lifted; cf. Fig. 15, lower left plot. In this case, even cells in the bulk exhibit pronounced polarizations and actively contribute to the overall expansion dynamics of the tissue.

The essential differences in the tissue dynamics of both model scenarios clearly manifest themselves in the corresponding kymographs; Fig. 15, right column. While the generation of active stresses is confined to a narrow region at the tissue's boundary in scenario I, we observe a non-trivial stress distribution in scenario II, where a considerable amount of active stresses is concentrated in the bulk of the tissue. In particular, the observed "X-shaped" pattern of the stress distribution bears remarkable resemblance to the recent experimental measurements of Ref. [128]. We note, however, that unlike the experimental observations in Ref. [128], this X-shaped pattern in the kymograph of the simulated system is not reiterated in time.

6.3 OUTLOOK

In conclusion, we have proposed a numerical modeling framework which lends itself to the study of cell migration over a wide range of system sizes, spanning from the simulation of single cells up the order of $\mathcal{O}(10^4)$ cells. In our manuscript *"Bridging the gap between single cell migration and collective dynamics"* [TRS+14], we have demonstrated that our simulations are consistent with a large body of experimental evidence, including the migration of single cells in free space, and the collective migration at the level of extended cell sheets comprising thousands of cells. In particular, we have presented an extensive study on the cohort dynamics of cell groups on micropatterned surfaces and made testable predictions about the migratory behavior in such systems in terms of statistical quantities which are directly accessible to experimental measurements. A first benchmark of our computational model will be presented in chapter 7, where we compare the statistical properties of our simulation model to direct experimental measurements on MDCK cells [STFR14].

The major advantage of our numerical approach lies in its mesoscopic character, which makes it an ideal candidate to study a number of biologically and medically highly important processes which are driven by only a moderate number of cells. A particularly important example in this direction would be the early stages of cancer progression, but also a number of experimentally relevant developmental processes including, e.g., the migration of border cells during the oogenesis of the fruit fly *Drosophila* [118]. Moreover, in many biological contexts, developmental processes are a result of the interplay between a number of different cell types with distinct cellular properties. In cancer development, for instance, cancer cells are often significantly more compliant than their healthy counterparts [117], which can have important consequences for the migratory phenotype of these cells and, hence, their potential to invade healthy tissues [76]. So far, we have restricted ourselves to the study of homogeneous collections of cells, where the same cellular traits are shared among all individuals in the system, but a generalization of our model to include the simulation of different cellular phe-

notypes is straightforward. Therefore, the study of these and related biological systems presents exciting and promising future applications for the modeling approach proposed in this chapter.

Bridging the gap between single cell migration and collective dynamics

Florian Thüroff [*], **Matthias Reiter** [*], **Felix Segerer** [†], **Joachim O. Rädler** [†], **and Erwin Frey** [*]

[*]Arnold Sommerfeld Center for Theoretical Physics and Center for NanoScience, Ludwig-Maximilians-Universität München, Theresienstrasse 37, 80333 Munich, Germany, and [†]Faculty of Physics and Center for NanoScience, Ludwig-Maximilians-Universität München, Geschwister-Scholl-Platz 1, 80539 Munich, Germany

Submitted to Proceedings of the National Academy of Sciences of the United States of America

A large number of physiological functions in both, the development and maintenance of multi-cellular organisms, crucially depend on the ability of cells to migrate through their respective environments. To ensure impeccable health conditions, migratory responses must be specific to external stimuli and predefined physiological tasks. Loss of this specificity hallmarks a number of pathological processes of which metastasis during cancer progression is probably the most prominent one. Creating a more mechanistic understanding of how migratory responses are set into work thus appears to be a highly relevant endeavor. Here we propose a cellular automata modeling framework which focuses on the integration of "high-level cell functions" and their concerted effect on cellular migration patterns. In particular, we adopt a top-down approach to incorporate a coarse grained description of cell polarity and its response to mechanical cues, and address the effect of cell adhesion on collective migration in cell groups. We demonstrate that our model is capable to reproduce typical cell shapes and movements down to the level of single cells, and yet is computationally efficient enough to allow for the simulation of currently up to $\mathcal{O}(10^4)$ cells. To develop a mechanistic picture addressing the relation between cell-level function and collective migratory response, we present a detailed study on small groups of cells in circular confinement geometries, and discuss the emerging patterns of collective motion in terms of single cellular traits. Finally, we apply our computational model at the level of extended tissues, and investigate stress and velocity distributions as well as front morphologies in expanding cellular sheets.

2D cell migration | cellular automata | tissue dynamics | micropatterns

Cell migration comes in an overwhelming number of different varieties, and plays a vital role in such diverse processes as the inflammation induced migration of leukocytes [35] and the collective motion of entire tissues in response to wounding [14]. Depending on the biological context, different modes of cell migration are driven by a wide range of different microscopic mechanisms. For instance, while, on a single cell level, the motile machinery employed during amoeboid migration differs from the machinery that is used during the mesenchymal mode of migration, the collective dynamics of an adhesive group of cells is governed by yet additional microscopic regulators [30]. Despite this seemingly enormous diversity of microscopic details, however, the basic functionality implemented by these different subcellular designs, including, e.g., cell adhesions and the ability of cells to generate forces, is largely universal.

Our main objective here is to study the emergence of collective cell migration in two dimensions from an integrative perspective on such high-level cell functions. To this end, we propose a simulation model which is specifically designed to study cell migration at various scales, ranging from the dynamics of solitary crawling cells over the cohort migration in small cell groups, up to the collective dynamics at the scale of tissues. While a variety of very successful modeling approaches has been proposed both, on the scale of single cell dynamics [23, 19, 20] and on the scale of extended tissues [24, 21, 22], so far models from both branches can hardly be interconnected. Models with a focus on single cells are typically difficult to extend to larger cell numbers, largely due to issues related to computational power and the necessity to model interactions between cells. On the other hand, theoretical approaches which are designed to capture the dynamics at the scale of entire tissues generally adopt a rather coarse grained point of view and are, therefore, difficult to transfer to the scale of few or single cells.

The focus of our model is to capture essential cellular features even in the context of the migration of single cells and of very small cell numbers. At the same time, it is aimed at being computationally efficient enough to allow for the simulation of very large cell numbers [currently up to $\mathcal{O}(10^4)$ cells]. In the spirit of a cellular automaton approach, the simulation algorithm is, therefore, based on a set of (stochastic) rules, designed to account for essential high level cell functions. We will show that our model is capable to reproduce the most pertinent features of cell migration even in the limiting case of solitary cells, and is compatible with a wealth of experimental evidence both, in the context of small cell groups and in larger tissues made up of several thousand cells.

In the next section, we will give a largely non-technical introduction to our modeling approach, highlighting the biological motivations behind our modeling design. For a detailed and comprehensive account on how this functionality is actually implemented, we refer to the Supplemental Material [38]. In the following sections, we then apply our computational framework to investigate the emergence of collective cell migration at successively larger length scales. Starting with a discussion of the statistics of single cellular random walks, we progress up to the case of small cell groups confined in circular micropatterns [4, 5, 6, 7], and give a detailed analysis of the different phases of collective dynamics in terms of single cellular traits. Finally, at the tissue scale, we investigate the paradigmatic wound healing assay [14, 11, 13, 10] and discuss different modes of collective dynamics both, in the context of cell front progression and in the context of stress and velocity distributions across the tissue.

Computational model

The computational model, we propose in the following, is a cellular automaton approach, designed to capture the essential features of cell migration in a high-level, rule based fashion. The core framework of our computational approach is

Reserved for Publication Footnotes

based on the cellular Potts model, which has been . However, our simulation scheme differs from that of the original cellular Potts model in important respects. For the sake of greater clarity, we will, therefore, restrict ourselves to a direct description of our simulation model, and will dispense with an explicit comparison with the original cellular Potts model. For reviews to the original cellular Potts model, we refer the interested reader to many excellent accounts in the literature [25, 15, 16].

As a starting point for our computational model, we choose a regular, hexagonal lattice, with lattice vectors $\{\mathbf{x}_j\}_j$. This lattice hosts both, the cells and the substrate of the simulated biological system. The α^{th} cell is represented by a simply connected set of lattice sites $\{\mathbf{x}_k^{(\alpha)}\}_{k_\alpha}$. Cell motion and membrane deformations are implemented by the annexation and rejection of single lattice sites at the cellular boundaries, and are collectively referred to as "atomic events". Annexation events imply an expansion of the cell's body (by one lattice site) and are the numerical analogue of cellular protrusions. Conversely, rejection events correspond to cell retraction. In our numerical model, both, annexation and rejection are stochastic events with the corresponding statistics being controlled by high-level cell functions, which will be discussed below. In analogy to real biological systems [27, 28], cell migration is thus achieved by an orchestrated sequence of subsequent protrusions (annexations) and retractions (rejections) of the cell's body.

Cortical contractility and cytoskeletal structures are essential components determining the cell's mechanical integrity and shape, and play a vital role in the process of cell migration [29, 37, 30, 36]. In our computational framework, we model cortical contractility by statistically penalizing growing cell areas and perimeters, which we control by two elastic constants ("area stiffness" a and "perimeter stiffness" m). These elastic constants imply a tendency to shrink the cell's area and perimeter down to zero. To counteract this cell contraction, we introduce a scalar concentration field $\rho(\mathbf{x})$ of filamentous cytoskeletal structures, defined on the whole body of each cell α, $\mathbf{x} \in \{\mathbf{x}_k^{(\alpha)}\}_{k_\alpha}$, which provides a pushing force at the cell's boundary ("membrane") that keeps the cell from collapsing.

In real biological cells, these cytoskeletal structures are constantly remodeled [27, 23]. In the context of cell migration, these remodeling events play a crucial role and are tightly controlled by the integrated action of numerous regulatory components [28, 34]. Moreover, recent experiments on monolayers of migrating cells [26] reveal that the dynamics of cytoskeletal structures seem to be highly adaptive to external mechanical stimuli. In this work, our focus is on the mechanical aspects of cell migration. Following the biological picture outlined above, we therefore implemented a feedback mechanism from mechanical signals perceived by the cell at its membrane to the spatiotemporal evolution of cytoskeletal densities $\rho(\mathbf{x})$ in the cell body. At the level of our numerical model, mechanical stimuli manifest themselves in the form of atomic events, with annexations ultimately being caused by outward pushing forces, and rejections being caused by inward pushing forces. To model mechanical feedback on the spatiotemporal evolution of the cytoskeleton inside the α^{th} cell, we then apply the following rule: Let $\mathbf{x}_0^{(\alpha)}$ denote the lattice position annexed [rejected] by cell α. All lattice sites $\mathbf{x} \in \{\mathbf{x}_k^{(\alpha)}\}_{k_\alpha}$ with $||\mathbf{x} - \mathbf{x}_0^{(\alpha)}|| < R$ receive a chemical marker c_+ [c_-] supporting enhancement [degradation] of cytoskeletal structures. Here the "signaling radius" R captures the finite diffusion length of the various chemical signals (captured here, collectively, by the markers $c_\pm$). At completion of each time step, cytoskeletal structures at lattice position $\mathbf{x}$ are updated according to

$$\rho(\mathbf{x}, t + \Delta t) = \begin{cases} \rho(\mathbf{x}, t) + \mathfrak{t}\,[Q - \rho(\mathbf{x}, t)], & \text{predominantly } c_+, \\ \rho(\mathbf{x}, t) + \mathfrak{t}\,[q - \rho(\mathbf{x}, t)], & \text{else,} \end{cases} \qquad [1]$$

where Q and q denote maximum and minimum levels for $\rho(\mathbf{x})$, respectively. Higher levels of $\rho(\mathbf{x})$ favor the formation of cell protrusions. Conversely, lower levels of $\rho(\mathbf{x})$ facilitate cell retraction. Eq. [1], therefore, implies a positive feedback mechanism, between cellular protrusions / retractions and cytoskeletal remodeling. The polarization rule, Eq. [1], thus supports orchestration of a coherent succession of cell protrusions and retractions and thus lies at the heart of an efficient implementation of cell migration in our model.

In addition to cell internal remodeling events of the cytoskeleton, adhesion of cells both, to neighboring cells and to the substrate plays a key role in explaining observed migratory phenotypes [23, 31]. From a mechanical point of view, the implications of cell adhesion are two-fold. First, cell adhesions support growth of cell-cell and cell-matrix interfaces and can thus be modeled in terms of effective surface "energies". Secondly, once formed, adhesive bonds anchor the cell to the substrate and to neighboring cells. During the process of cell migration, these anchoring points must be continuously broken up and reassembled [32, 33] and, hence, provide a constant source of force dissipation. Our computational model is designed to capture both of these mechanical aspects of cell adhesion. There, cell-cell adhesion directly impacts atomic events in our simulation, since atomic events, in general, lead to a remodeling of cell-cell interfaces. To be specific, assume that cell α protrudes into the domain of cell β, such that α annexes one lattice site originally hosted by β, viz. $\mathbf{x}_n^{(\beta)} \to \mathbf{x}_n^{(\alpha)}$. As a result, the interfaces between all cells neighboring the lattice site $\mathbf{x}_n$ become remodeled. During this remodeling, contacts between pairs of cells are either newly formed, or torn apart. On a modeling level, the mechanical aspects of cell-cell adhesion can be captured by introducing an appropriate statistical bias for the actual occurrence of atomic events (and, hence, interface remodeling), based on the number of newly formed and broken cell contacts. Moreover, to explicitly capture the highly dissipative aspects of cell adhesion both, the number of newly formed and of broken contacts must contribute *independently* to this statistical bias. In our algorithm this is accomplished by the introduction of two parameters A and B, where increasing values of A lower the energy of cell-cell contacts, while increasing values of B reinforce cell-cell anchorage; for details see Supplemental Material [38].

Finally, to account for cell-substrate adhesion, we distribute a second scalar field $\rho_f(\mathbf{x})$ across the entire lattice, $\mathbf{x} \in \{\mathbf{x}_j\}_j$. The local level of $\rho_f(\mathbf{x})$ is taken to reflect the density of suitable substrate sites where focal adhesions between cell and substrate can be formed. Thereby, the value of the sum $\rho_f(\mathbf{x}) + \rho(\mathbf{x})$ is taken to represent the strength of such focal adhesions, with stronger focal adhesions statistically favoring successful protrusions (i.e. annexations) and impeding cell retraction (i.e. rejections). By allowing $\rho_f(\mathbf{x})$ to take negative values, we can, moreover, define lattice areas with cell repellant surfaces. The field variable $\rho_f(\mathbf{x})$ thus provides a natural means to implement arbitrary substrate micropatterns in our simulations.

Results

In the following, we will use the computational model introduced above to portray the emergence of collective cell migration in terms of high level cell functions. To this end, we proceed in multiple stages and discuss the pertinent aspects of

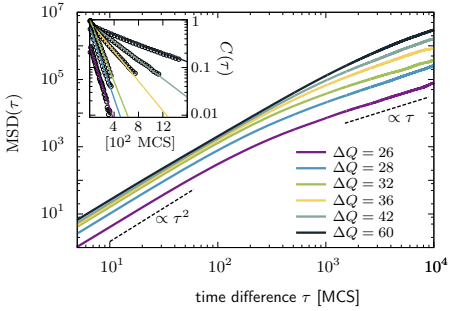

Fig. 1. Mean squared displacement (MSD) for single cell movements at different cytoskeletal polarities ΔQ (perimeter stiffness $m = 0.021$; signaling radius $R^2 = 24$). Single cells perform a persistent random walk, i.e. they move ballistically (MSD $\propto \tau^2$) on time scales smaller than the persistence time, $\tau \ll \lambda^{-1}$, and diffusively (MSD $\propto \tau$) on time scales larger than the persistence time, $\tau \gg \lambda^{-1}$. *Inset:* Tangent-tangent correlations of persistent random walks for cell parameters corresponding to those in the main figure. (Inverse) persistence times λ (slope of exponential fits) increase with increasing cytoskeletal polarity ΔQ.

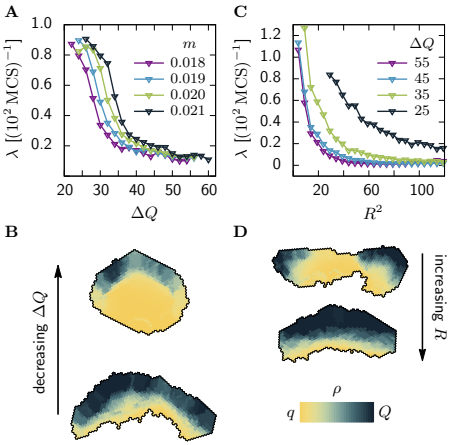

Fig. 2. Cell shape and persistence as function of the polarization parameters. **(A)** Persistence times of single cells' persistent random walks as function of cytoskeletal polarity, ΔQ, and perimeter stiffness, m (signaling radius $R^2 = 24$). The persistence of random walk increases with increasing cytoskeletal polarity and decreasing perimeter elasticity. **(B)** Cytoskeletal polarity also controls cell shapes, with crescent cell shapes (large persistence times) observed at large cytoskeletal polartities, and elongated cell shapes (small persistence times) at small cytoskeletal polarities. **(C)** Persistence times of single cells' persistent random walks as function of the cell's signaling radius at different values for the cytoskeletal polarity (perimeter stiffness $m = 0.021$). **(D)** The signaling radius critically determines the synchronicity of internal cytoskeletal remodeling efforts. Small signaling radii frequently lead to a transient formation of mutually independent lamellipodia at different places within the cell body, thereby interrupting persistent motion (small persistence times). Large signaling radii lead to structurally stable front-rear polarization profiles across the entire cell body (large persistence times). **(B)**, **(D)** Color code: cell polarization; cf. color bar in **(D)**.

(collective) cell migration at varying sizes of cell populations. We begin our considerations by studying the migratory behavior of only one single cell. Specifically, we investigate the random walk statistics as a function of cell elasticity and cytoskeletal dynamics, and discuss the connection between cell shape and cell persistency. Next, we present a detailed study of the collective migration in small adhesive groups of cells. To this end, we follow a confinement strategy and study the onset of collective cell motion in circular micropatterns. Similar setups have been used in recent experiments [4, 5, 6, 7] and have proven highly valuable in order to accentuate the emergence of collective effects. Finally, we transition to the tissue level and discuss the effects of collective cell dynamics in the context of cell front progression. In particular, we adopt a typical wound healing setup as previously used in a number of experimental works [14, 11, 13, 10], and study the morphology of the expanding cell fronts, as well as the distribution of stresses and velocities.

Single cell migration. To study the migration dynamics of single cells, we used a computational grid with $N = 9 \cdot 10^4$ sites and periodic boundary conditions. The distribution of adhesive substrate sites, $\rho_f(\mathbf{x}) = \text{const.} = 0$, is spatially homogeneous such that the substrate itself is devoid of any directional cues. Moreover, we fix the elastic constant a, controlling cell area fluctuations, at a value $a = 0.02$, and the maximum cytoskeletal density at $Q = 250$, such that the simulated cells typically cover a fraction $\mathcal{O}(10^{-2})$ of the entire computational grid. We then investigate the impact of varying cell stiffness m and varying levels of maximum cell polarities $\Delta Q \equiv Q - q$ on the properties of single cellular random walks.

To assess the random walk statistics, we record the cell's orientation $\hat{\mathbf{v}}(t) \equiv \mathbf{v}(t)/||\mathbf{v}(t)||$ ($\mathbf{v}$: cell velocity) and (geometrical) center of mass position $\mathbf{R}(t)$ during a total simulation time of $T = 10^4$ Monte-Carlo steps (MCS). For each set of parameters, we performed a total of 100 independent simulations, from which we computed the mean squared displacement

$$\text{MSD}(\tau) \equiv \langle [\mathbf{R}(t+\tau) - \mathbf{R}(t)]^2 \rangle, \qquad [2]$$

and the tangent tangent correlation function

$$C(\tau) \equiv \langle \hat{\mathbf{v}}(t+\tau) \cdot \hat{\mathbf{v}}(t) \rangle, \qquad [3]$$

where $\langle \dots \rangle$ denotes an average with respect to simulation time t and over all 100 independent simulations.

Figure 1 illustrates the statistics of simulated single cell randoms walks at varying levels of (maximum) cell polarity ΔQ. While small values of ΔQ render the simulated cells immobile (not shown), we observe persistent random walk statistics [1] for sufficiently large cell polarities. In this latter case, cells move ballistically, MSD $\propto \tau^2$, on small times scales, and diffusively, MSD $\propto \tau$, on large time scales. As is typical of persistent random walks, tangent tangent correlations $C(\tau) \sim e^{-\lambda t}$ decay exponentially at a rate $\lambda \sim \tau_p^{-1}$, which is inversely proportional to the persistence times τ_p of single cell trajectories; cf. inset of Fig. 1.

In Fig. 2(A), we have investigated the persistency of single cell motions at varying levels of cell polarity ΔQ and perimeter elasticities m. We observe a marked increase in persistence times $\tau_p \sim \lambda^{-1}$ with cell polarity ΔQ, i.e. cells with larger polarity exhibit extended episodes of ballistic motion. Likewise, persistence times decrease as cells get stiffer (by virtue of larger values of m), such that cell motion becomes more erratic. Interestingly, the simulated cell shapes are closely correlated to cell persistency; cf. Fig. 2(B). While highly persistent trajectories are observed for cells with crescent shapes, more erratic cell motions are typically associated with more rounded cell forms. Similar variations in cell shapes have been reported in experiments with keratocytes [2, 3]. In particular, the shapes of crawling keratocytes have been observed to de-

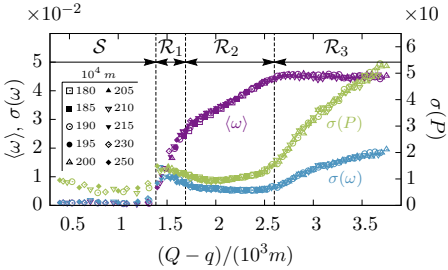

Fig. 3. Characteristic observables of collective cell rotation (4 cell systems, $R^2 = 24$, $A = 0$, $B = 7$) at different cell perimeter stiffness parameters m [mean ($\langle\omega\rangle$) and standard deviation ($\sigma(\omega)$) of the cells' angular velocities, and cell shape variability ($\sigma(P)$)]. The statistics of collective cell motion does not separately depend on cytoskeletal polarity, ΔQ, and cell contractility, m, but only on their ratio ("*specific polarity*"). Four phases can be identified: At small specific polarity, the cellular system freezes and no rotation occurs ($\mathcal{S}$-phase). At moderate values for the specific polarity, a transition to collective cell rotation occurs: A steep increase in the system's mean angular velocity $\langle\omega\rangle$ is accompanied by the formation of a local maximum in $\sigma(\omega)$ and $\sigma(P)$ ($\mathcal{R}_1$-phase). At intermediate specific polarities ($\mathcal{R}_2$-phase), both, fluctuations in angular velocities and cell shapes reach a minimum, and rotation speeds $\langle\omega\rangle$ increase linearly with $\Delta Q/m$. At large specific polarities ($\mathcal{R}_3$-phase), the system's rotation speed $\langle\omega\rangle$ saturates, while $\sigma(\omega)$ and $\sigma(P)$ both increase monotonically.

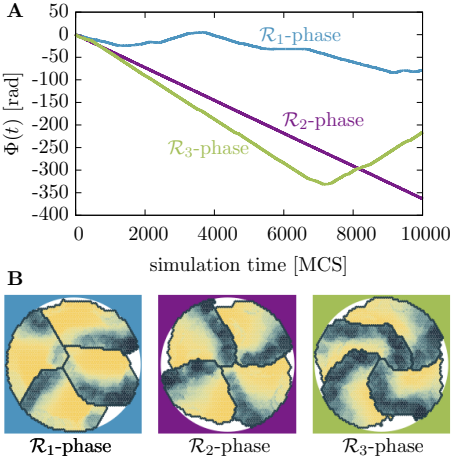

Fig. 4. Phases of collective motion: **(A)** Angular trajectories and **(B)** cell shapes (color code represents cell polarization; cf. Fig. 2(D)). $\mathcal{R}_1$-phase: Cellular lamellipodia start to form and phases of collective rotation, interspersed by phases of stagnation (plateaus in the angular trajectories) and changes in rotation direction are being observed. $\mathcal{R}_2$-phase: Strong lamellipodia are being sustained at the cells' leading edges by optimal, stable cell shapes, and cellular front-rear polarizations are perfectly synchronized across the entire system, leading to diverging persistent times (i.e. absence of phases of stagnation and changes in rotation direction for the observed simulation times used in this study). $\mathcal{R}_3$-phase: Unstable cell shapes interrupt phases of coherent rotation, and persistence times drop to finite values (non-zero probability of phases of stagnation and changes in rotation direction).

pend on the adhesive properties of the underlying substrate, with weak adhesion resulting in roundish cells, while cells at intermediate adhesion strengths typically attained more elongated, crescent shapes [3]. Moreover, cell-substrate adhesion has been reported to have measurable effects on the random walk statistics of cellular trajectories, with stronger adhesions supporting higher persistencies [1]. In the simulations underlying the data shown in Figs. 2(A,B), increasing ΔQ amounts to increasing the strength of focal adhesions at the cell's leading edge relative to those at the trailing edge. In this sense, our results are in qualitative agreement with experimental measurements. We note, however, that increasing cell-substrate adhesion uniformly across the cell body, e.g. by uniformly increasing the value of ρ_f, primarily increases the friction in our model and results in a decrease of observed cell speeds. While, this is consistent with the general observation that stronger cell-substrate adhesion tends to lower migration speeds [29], experimental studies on keratocytes report an increase in cell speeds upon increasing cell-substrate adhesions from low to intermediate strengths, and decreasing cell speeds for even higher levels of adhesion [3]. A fully mechanistic explanation of such subtle effects calls for more microscopic modeling approaches [3].

Finally, we investigated the influence of different signaling radii R on the persistence of single cell trajectories. In our computational model, R controls the spatial organization of lamellipodium formation and, therefore, strongly impacts cellular random walk statistics; cf. Fig. 2(C). At small values of the signaling radius R, the spatial coherence of cytoskeletal rearrangements is poor, which frequently results in the disruption of ballistic flights due to the formation of independent lamellipodia in different spatial regions of the cell body; cf. Fig. 2(D), upper snapshot. At larger values of R, spatial coherence is restored and the formation of one extended lamellipodium across the cell's leading edge maintains a distinct front-rear axis of cell polarity; cf. Fig. 2(D), lower snapshot.

Circular micro patterns. In the previous section, we have shown that simulated solitary cells in free space exhibit typical persistent random walk motions, with persistence times being controlled by cell polarity (cell-substrate adhesion) and cell elasticity. To assess the transition to collective cell motion, we now study the dynamics of a small group of 4 cells confined to a circular micropattern [4, 5, 6, 7]. Circular micropatterns of given radius r_0 have been implemented in silico by setting $\rho_f(\mathbf{x}) = 0$ for $||\mathbf{x} - \mathbf{x}_0|| \leq r_0$, and $\rho_f(\mathbf{x}) < -Q$ for $||\mathbf{x}-\mathbf{x}_0|| > r_0$, where $\mathbf{x}_0$ denotes the center of the circular pattern. During each single simulation, the number of cells has been fixed by deactivating cell division. We have employed this setup in a previous study to compare our numerical results to actual experimental measurements on small groups containing 2 – 8 cells, and have found very good agreement [7]. Here, we generalize these previous studies and present a detailed analysis of the statistical properties of the collective dynamics of such cell groups in terms of high level cell functions. As before, the parameter values $a = 0.02$ and $Q = 250$ remain fixed.

When adhesive groups of two or more motile cells are confined on a circular island, they arrange themselves in a state of spontaneous collective migration which manifests itself in the form of coordinated and highly persistent cell rotations about the island's midpoint $\mathbf{x}_0$ [4, 5, 6, 7]. The statistics of these states of rotational motion are ideally suited to study

the influence of cellular properties on the group's capabilities to coordinate cell movements. To quantify cell rotations in a system of K cells, we recorded the angular distance $\phi_\alpha(t)$, $\alpha = 1, \ldots, K$ of each cell α over time, and used the quantity $\Phi(t) \equiv K^{-1} \sum_\alpha \phi_\alpha(t)$ to obtain the average angular trajectory. To capture the statistics of collective cell rotation, we use the random variables $\omega(t) \equiv |\dot{\Phi}(t)|$ and $P(t) \equiv K^{-1} \sum_\alpha P_\alpha(t)$, where $P_\alpha(t)$ denotes the perimeter of cell α at time t. For each specific choice of simulation parameters, we record $\omega^{(j)}(t)$ and $P^{(j)}(t)$ $(j = 1, \ldots, N)$ for a set of $N = 10\,000$ statistically independent systems, where each system is observed over $T = 10\,000$ MCS. From these data, we then compute the "rotation speed"

$$\langle \omega \rangle \equiv \frac{1}{NT} \sum_{j=1}^{N} \sum_{t=1}^{T} \omega^{(j)}(t), \qquad [4]$$

its variance [denoting $\overline{X^{(j)}} \equiv T^{-1} \sum_t X^{(j)}(t)$]

$$\sigma^2(\omega) \equiv \frac{1}{N\,(T-1)} \sum_{j=1}^{N} \sum_{t=1}^{T} \left(\omega^{(j)}(t) - \overline{\omega^{(j)}} \right)^2, \qquad [5]$$

as well as the (squared) cell shape variability parameter

$$\sigma^2(P) \equiv \frac{1}{N\,(T-1)} \sum_{j=1}^{N} \sum_{t=1}^{T} \left(P^{(j)}(t) - \overline{P^{(j)}} \right)^2. \qquad [6]$$

As an aside we note that the statistical measures defined in Eqs. [4] and [5] are no longer well defined at cell numbers so large that the formation of multiple vortices may occur. For that reason, all subsequent discussions in this sections relate to moderate cell numbers.

Figure 3 illustrates the characteristic properties of collective cell rotations in systems of 4 cells at varying (maximum) cytoskeletal polarity ΔQ and varying cell contractility m. Plots corresponding to different (moderate) system sizes exhibit the same qualitative features (not shown). Remarkably, the statistical measures shown in Fig. 3 are not independent functions of cell elasticity m and maximum cytoskeletal polarity Q, but only depend on their ratio $\Delta Q/m$, which we will henceforth refer to as "specific polarity". Overall, we observe a typical transition toward a collectively moving state as the specific polarity is increased above a critical threshold at $\Delta Q/m \approx 1300$. Below this threshold the rotation speed $\langle \omega \rangle$ (purple curves in Fig. 3) equals zero and cells in the systems are immobile. Across the threshold, rotation speeds grow quickly, and cell shape and rotation speed fluctuations, $\sigma(P)$ and $\sigma(\omega)$, exhibit a local maximum. At intermediate values of the specific polarity, the cellular systems reach a regime of enduring rotational motion, where $\langle \omega \rangle$ varies linearly with the specific polarity, and where $\sigma(P)$ and $\sigma(\omega)$ form a local minimum. Finally, at large values of the specific polarity, the rotational speed $\langle \omega \rangle$ saturates at its maximum value, and cell shape instabilities (growing $\sigma(P)$; green curve in in Fig. 3) causes the rotational persistence of the cellular systems to decline (growing $\sigma(\omega)$; blue curve in in Fig. 3).

Building on these results, we identify four distinct phases of collective cell rotation, which are also illustrated in Fig. 4. $\mathcal{S}$-phase: At small specific polarities $\Delta Q/m$, cytoskeletal forces are too weak to initiate coherent cell rotation, and the system's dynamics is dominated by relatively strong contractile forces which tend to arrest the system in a "low energy" configuration. $\mathcal{R}_1$-phase: Upon crossing a critical threshold of the specific polarity, cytoskeletal forces become sufficiently large to establish actual membrane protrusions against the elastic forces, and cells start to rotate. In this regime contractile forces still dominate such that cellular interfaces are virtually straight and the formation of lamellipodia is only sustained over finite life times. Thus, due to the dominance of contractile forces, the systems frequently experience transient episodes of stagnation and repeatedly change direction. $\mathcal{R}_2$-phase: At intermediate values of the specific polarity, cytoskeletal and contractile forces are in optimal balance, so as to maintain ideal cell shapes and broadly extended lamellipodia. In this regime, persistence times diverge, rendering cellular rotations strictly unidirectional. $\mathcal{R}_3$-phase: At large values of the specific polarity, the system's dynamics is dominated by cytoskeletal forces. Due to relatively small elastic forces, cell shapes tends to become unstable which frequently leads to a loss of the positional coherence of cells. This loss of coherence in turn perturbs the system's dynamics which, therefore, undergoes temporary periods of disordered motion, causing persistence times to drop back to finite values.

Tissue level dynamics. As an application of the model on the tissue level we consider a setup where a confluent epithelial cell sheet expands into free space. In experiments such a setup is widely applied to simulate the process of wound closure. A certain region of the culture plate is masked by microfabricated stencils [9]. Cells are subsequently seeded on the accessible region of the culture plate, where they adhere and proliferate until reaching confluence. Then the stencils are removed and the confluent cell sheet may expand into to the free surface, the "model wound". As alternative to the microstencils a PDMS membrane can be used to initially confine the cell sheet to a rectangular region. Expansion is then observed after removal of the membrane [10] In our simulations this setup is realized by imposing periodic boundaries in y-direction and placing two fixed boundary lines at $x = 175$ and $x = 525$ (cf. Fig. 5(A)). Initially a confluent cell sheet is placed in the region $175 < x < 525$, and at $t = 0$ the boundary lines are removed, allowing the sheet to expand in positive and negative x-direction. We study this system for two different parameter configurations, highlighting the difference between a regime which is dominated by local cell growth in the region at the boundary and a regime in which the entire cell sheet is highly motile and contributes steadily to the expansion process.

In the first configuration, the number of cells is relatively small, such that the pressure in the sheet in confinement is not very high. In this simulation the cells change to a proliferating state if they exceed a certain size (cf. Supplemental Material [38] for details of this mechanism). Since the initial range $Q_0 - q$ for the cytoskeletal densities ρ is taken very small, all cells in the center of the sheet are only marginally motile and cannot increase considerably in size. However, cells in the region close to the edge of the epithelial sheet can stochastically exceed the threshold for cell growth upon removal of the confining boundaries. Growing cells then reinforce their cytoskeletal structures and at the same time direct their motion toward the epithelial border. Due to cellular adhesion forces, those cells which propagate outwards fastest start to pull their followers behind them. This results in a rather rough surface (epithelial border) exhibiting several finger-shaped structures which are led by large, fast-moving leader cells, as shown in Fig. 5(A). The form of these structures is in good agreement with experimental observations [10, 9, 13, 11]. While leader cells are defined explicitly in other numerical studies [9, 22], in our model they emerge from stochastic fluctuations in cellular growth and establishment of persistent motion and, therefore, their leading property is not permanent. Although our model includes mitosis, cell divisions do not seem to play a key role in the formation of the surface structure since only very few such events occur in the observed time window. The average cell density and x-component of velocity are shown as a function of the position x in the epithelial sheet in Fig. 5(B). The

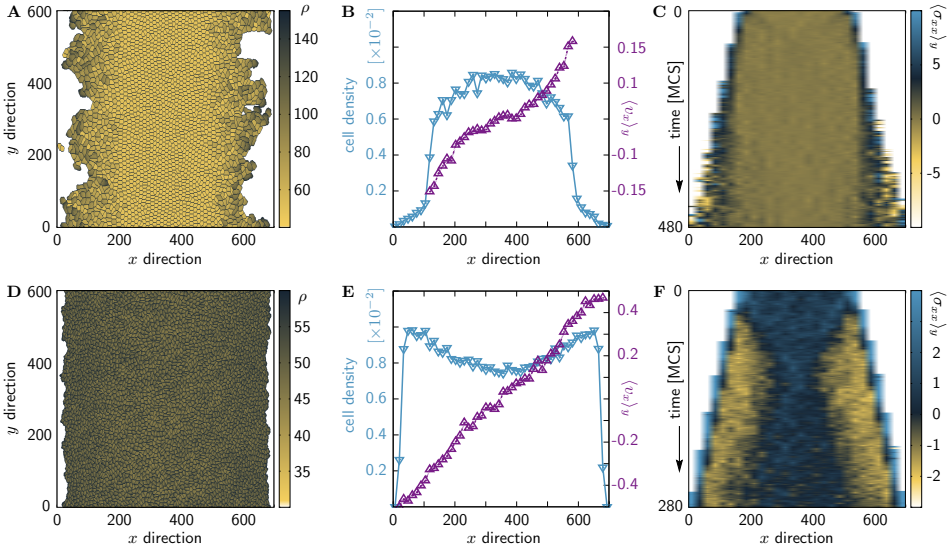

Fig. 5. Expansion of a confluent epithelial cell sheet in positive and negative x-direction after removal of two boundary lines positioned at $x = 175$ and $x = 525$ at time $t = 0$ for two different parameter settings. **(A-C)** include cell proliferation explicitely and use parameters $a = 0.02$, $m = 0.04$, $A_{\alpha,\beta} = B_{\alpha,\beta} = 8$, $\rho_f = 0$, $q = 45$, $Q_0 = 55$, $r = 0.93$, $g = 0.2$, $p_g = 0.015$, $T_r = 50$. The initial number of cells is 2200. **(A)** Snapshot of the density of cytoskeletal structures ρ at time $t = 480$. **(B)** Mean cell density and x-component of cellular velocity as a function of x at time $t = 480$. The data is averaged over the y-direction and additionally over 10 sample simulations. **(C)** Kymograph showing the component σ_{xx} of the stress tensor averaged over the y-direction for the simulation in **A**. See the supplementary material for information on the computation of the stress tensor (Make a footnote out of this!!). **(D-F)** are the corresponding graphs for a migration dominated setup without explicit cell growth and mitosis, using parameters $a = 0.02$, $m = 0.04$, $A_{\alpha,\beta} = B_{\alpha,\beta} = 8$, $\rho_f = 0$, $q = 20$, $Q = 50$ and a cell number of 3370. **(D)** and **(E)** show the system at time $t = 280$ in this case.

cell density is approximately constant in the center. Closer to the front, where cells are growing, it decreases linearly, followed by a sharp drop where the sheet looses confluency and a second zone of linear decrease at the position of the protruding fingers. Cell velocities turn out to be very high in the region where cells are proliferating and drop steeply to negligible values in the bulk of the cell sheet. The linear decrease of cell density and the steep drop of cell velocities agree with the experimental data in Ref. [9]. Fig. 5(C) reveals that fluctuations in the stress component in x-direction are confined to the irregular region at the surface. A broad region in the center is effectively devoid of any stress, which illustrates that those cells are in mechanical equilibrium and the mutual forces of neighboring cells balance.

Very contrasting features of the expansion process are illustrated in the second parameter configuration. Here the cells are very densely packed and a broader range for the polarization field ρ allows even the cells in the bulk to establish a higher persistence of motion. As illustrated in Fig. 5(D), the expansion process after removal of the confining boundaries is now dominated by the collective outward migration of the left and right halves of the cell sheet. In this simulation cell proliferation is not explicitly included in the model, and the cells uniformly approach their maximal size. Stochastic fluctuations are therefore less important and the surface of the monolayer remains rather smooth. Interestingly, the cell density indicated in Fig. 5(E) now exhibits a minimum in the center of the sheet. This is due to the stretching of the central group of cells evoked by the equally strong tractive forces from the migrating neighbors on both sides. The observation that the average cell velocities in x-direction increase approximately linear with the distance from the center confirms that the entire cell sheet contributes to the expansion in this configuration. As presented in Fig. 5(F), the kymograph for the mean stress component σ_{xx} shows a characteristic X-shaped pattern. While stress is distributed uniformly at $t = 0$, a region of negative stress emerges directly behind the propagating front. The width of this section where cells are compressed soon remains approximately constant, whereas the central region of positive stress, where cells are stretched, grows roughly linearly with time. This profile resembles the first period of the mechanical wave observed in corresponding experiments [10]. However, our model does not reproduce the periodicity of stress creation and degradation in the central region.

In summary, the study of tissue expansion illustrates that our model is computationally efficient enough to investigate systems with a large cell number. The model explains the emergence of large scale surface structures with stochastic fluctuations in the growth process of cells close to the edge of the cell sheet. Moreover it illustrates the transfer of stress toward the center of the monolayer in a regime where cells are highly motile and contribute collectively to the tissue expansion process.

ACKNOWLEDGMENTS. This work was supported by the Deutsche Forschungsgemeinschaft in the framework of the SFB 1032 "Nanoagent for Spatio-Temporal Control of Molecular and Cellular Reactions".

1. S. Kouvroukoglou, K. C. Dee, R. Bizios, L. V. McIntire, K. Zygourakis (2000) Endothelial cell migration on surfaces modified with immobilized adhesive peptides, Biomaterials 21:1725–1733.
2. K. Keren, Z. Pincus, G. M. Allen, E. L. Barnhart, G. Marriott, A. Mogilner, J. A. Theriot (2008) Mechanism of shape determination in motile cells, Nature 453:475–480.
3. E. L. Barnhart, K.-C. Lee, K. Keren, A. Mogilner, J. A. Theriot (2011) An Adhesion-Dependent Switch between Mechanisms That Determine Motile Cell Shape, PLoS Biol. 9:e1001059.
4. C. Brangwynne, S. Huang, K. K. Parker, D. E. Ingber (2000) Symmetry breaking in cultured mammalian cells, In Vitro Cell Dev. Biol. Animal 36:563–565.
5. S. Huang, C. P. Brangwynne, K. K. Parker, D. E. Ingber (2005) Symmetry-breaking in mammalian cell cohort migration during tissue pattern formation: role of random-walk persistence, Cell Motil. Cytoskelton 61:201–213.
6. K. Doxzen, S. R. K. Vedula, M. C. Leong, H. Hirata, N. S. Gov, A. J. Kabla, B. Ladoux, C. T. Lim (2013) Guidance of collective cell migration by substrate geometry, Integr. Biol. 5:1026–1035.
7. F. Segerer, F. Thüroff, A. P. Alberola, E. Frey, J. O. Rädler (2014) Coherent States of Cell Migration on Circular Micropatterns, in preparation.
8. W. T. Gibson, M. C. Gibson (2009) Cell topology, geometry, and morphogenesis in proliferating epithelia, Curr. Top. Dev. Biol. 89:87–114.
9. N. Sepúlveda, L. Petitjean, O. Cochet, E. Grasland-Mongrain, P. Silberzan, V. Hakim (2013) Collective cell motion in an epithelial sheet can be quantitatively described by a stochastic interacting particle model, PLoS Comput. Biol. 9:e1002944.
10. X. Serra-Picamal, V. Conte, R. Vincent, E. Anon, D. T. Tambe, E. Bazellieres, J. P. Butler, J. J. Fredberg, X. Trepat (2012) Mechanical waves during tissue expansion, Nat. Phys. 8:628–634.
11. M. Poujade, E. Grasland-Mongrain, A. Hertzog, J. Jouanneau, P. Chavrier, B. Ladoux, A. Buguin, P. Silberzan (2007) Collective migration of an epithelial monolayer in response to a model wound, Proc. Natl. Acad. Sci. U.S.A. 104:15988–15993.
12. A. J. Kabla (2012) Collective cell migration: leadership, invasion and segregation, J. R. Soc. Interface 9:3268–3278.
13. X. Trepat, M. R. Wasserman, T. E. Angelini, E. Millet, D. A. Weitz, J. P. Butler, J. J. Fredberg (2009) Physical forces during collective cell migration, Nat. Phys. 5:426–430.
14. R. Farooqui, G. Fenteany (2005) Multiple rows of cells behind an epithelial wound edge extend cryptic lamellipodia to collectively drive cell-sheet movement, J. Cell Sci. 118:51–63.
15. R. M. H. Merks, P. Koolwijk (2009) Modeling Morphogenesis in silico and in vitro: towards quantitative, predictive, cell-based modeling, Math. Model. Nat. Phenom. 4:149–171.
16. A. Szabo, R. M. H. Merks (2013) Cellular potts modeling of tumor growth, tumor invasion, and tumor evolution, Front. Oncol. 3:87.
17. J. A. Glazier, F. Graner (1993) Simulation of the differential adhesion driven rearrangement of biological cells, Phys. Rev. E 47:2128–2154.
18. F. Graner, J. A. Glazier (1993) Simulation of biological cell sorting using a two-dimensional extended Potts model, Phys. Rev. Lett. 69:2013–2016.
19. A. F. M. Marée, A. Jilkine, A. Dawes, V. A. Grieneisen, L. Edelstein-Keshet (2006) Polarization and movement of keratocytes: A multiscale modelling approach, Bull. Math. Biol. 68:1169–1211.
20. A. F. M. Marée, V. A. Grieneisen, L. Edelstein-Keshet (2012) How cells integrate complex stimuli: the effect of feedback from phosphoinositides and cell shape on cell polarization and motility, PLoS Comput. Biol. 8:e1002402.
21. A. Szabo, R. Unnep, E. Méhes, W. O. Twal, W. S. Argraves, Y. Cao, A. Czirok (2010) Collective cell motion in endothelial monolayers, Phys. Biol. 7:046007.
22. A. J. Kabla (2012) Collective cell migration: leadership, invasion and segregation, J. R. Soc. Interface 9:3268–3278.
23. A. Mogilner (2009) Mathematics of cell motility: have we got its number?, J. Math. Biol. 58:105-134.
24. B. Szabó, G. J. Szöllösi, B. Gönci, Zs. Jurányi, D. Selmeczi, T. Vicsek (2006) Phase transition in the collective migration of tissue cells: Experiment and model, Phys. Rev. E 74:061908.
25. J. A. Glazier, A. Balter, N. J. Poplawski (2007) Magnetization to Morphogenesis: A Brief History of the Glazier-Graner-Hogeweg Model. Single-Cell-Based Models in Biology and Medicine, eds A. R. A. Anderson, M. A. J. Chaplain, K. A. Rejniak (Birkhäuser, Basel), pp 79–106.
26. D. T. Tambe, C. C. Hardin, T. E. Angelini, K. Rajendran, C. Y. Park, X. Serra-Picamal, E. H. Zhou, M. H. Zaman, J. P. Butler, D. A. Weitz, J. J. Fredberg, X. Trepat (2011) Collective cell guidance by cooperative intercellular forces, Nat. Mater. 10:469–475.
27. T. D. Pollard, G. G. Borisy (2003) Cellular motility driven by assembly and disassembly of actin filaments, Cell 112:453–465.
28. D. A. Lauffenburger, A. F. Horwitz (1996) Cell migration: a physically integrated molecular process, Cell 84:359–369.
29. B. Alberts, A. Johnson, J. Lewis, M. Raff, K. Roberts, P. Walter (2008) Molecular Biology of the Cell, (Garland Science, New York).
30. P. Friedl (2004) Prespecification and plasticity: shifting mechanisms of cell migration, Curr. Opin. Cell Biol. 16:14–23.
31. P. Friedl, D. Gilmour (2009) Collective cell migration in morphogenesis, regeneration and cancer, Nat. Rev. Mol. Cell Biol. 10:445–457.
32. D. J. Webb, J. T. Parsons, A. F. Horwitz (2002) Adhesion assembly, disassembly and turnover in migrating cells – over and over and over again, Nat. Cell Biol. 4:E97–E100.
33. B. M. Gumbiner (2005) Regulation of cadherin-mediated adhesion in morphogenesis, Nat. Rev. Mol. Cell Biol. 6:622–634.
34. A. J. Ridley, M. A. Schwartz, K. Burridge, R. A. Firtel, M. H. Ginsberg, G. Borisy, J. T. Parsons, A. R. Horwitz (2003) Cell migration: Integrating signals from front to back, Science 302:1704–1709.
35. P. Friedl, B. Weigelin (2008) Interstitial leukocyte migration and immune function, Nat. Immunol. 9:960–969.
36. M. Prass, K. Jacobson, A. Mogilner, M. Radmacher (2006) Direct measurement of the lamellipodial protrusive force in a migrating cell, J. Cell Biol. 174:767–772.
37. D. Raucher, M. P. Sheetz (2000) Cell spreading and lamellipodial extension rate is regulated by membrane tension, J. Cell Biol. 148:127–136.
38. Supplemental Material online at – to be completed –

7

COHERENT CELL ROTATION ON CIRCULAR MICROPATTERNS

7.1 STARTING POINT OF THE PROJECT

As has been discussed in section 6.1, unraveling the core mechanisms underlying the emergence of collective motion in cellular systems is a highly delicate endeavor. Apart from complications arising from the intricate internal architecture and design of single cells, the sheer system sizes and, usually, immensely complex environmental conditions in typical biological settings present significant obstacles in identifying the key drivers of the system's dynamics. The main goal of *in vitro* experimental designs, therefore, lies in reducing the complexity of the systems under study and to put emphasis on the key features of interest. In the context of the study of collective cell migration, the advent of micropatterning techniques, which allowed to confine an arbitrary number of cells in purposefully designed micro environments, presents a major leap in this direction [24, 63, 67, 41, 82, 144, 151, 40, 80, 150].

In our work *"Coherent States of Cell Rotation on Circular Micropatterns"* [STFR14], we present an extensive experimental study on the statistical properties of coherent rotational motion in systems of MDCK cells confined on circular micropatterns. The analysis and interpretation of the experimental data is complemented by corresponding simulations based on the computational model introduced in chapter 6. Comparing experimental data sets to those obtained from numerical simulations, we find very good agreement. In section 7.2, we give a summary of the main results of our

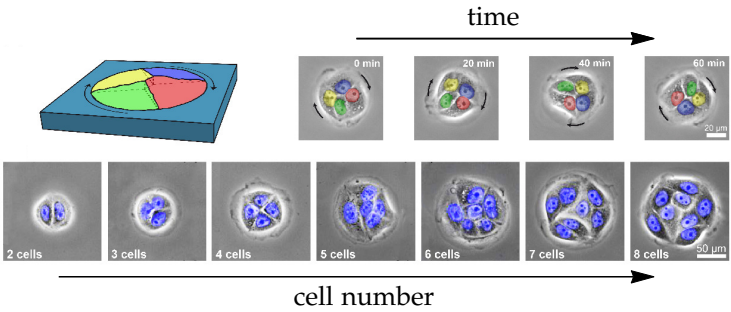

Figure 16.: Experimental setup; cf. [STFR14]. *Top left*: Illustration of the circular geometry of the micropatterns. *Top right*: Time series illustrating the coherent rotation of four cells on a circular micropattern at times $t \in \{0\,\text{min}, 20\,\text{min}, 40\,\text{min}, 60\,\text{min}\}$ (left to right; scale bar: $20\,\mu m$). *Bottom*: For increasing cell numbers, the dimensions of the circular islands have been adjusted such that the cell density remains constant (scale bar: $50\,\mu m$).

study, and conclude with a brief outlook in section 7.3. Details on experimental techniques, as well as a comprehensive discussion of our results can be found in the appended manuscript, section 7.4.

7.2 SUMMARY OF MAIN RESULTS

In the following, we study the rotation dynamics of small groups of MDCK cells confined on circular shaped fibronectin islands. Specifically, our focus will be on the statistical properties of coherent cell rotation, as well as their dependence on the system size. To this end, we consider cell groups hosting a varying number of cells, with cell numbers ranging from two to eight. The radii of the circular micropatterns used in the experiments were adjusted such that measurements on systems of different cell numbers could be performed at a constant cell density of 1200 cells/mm^2. The basic experimental setup used in our study is illustrated in Fig. 16.

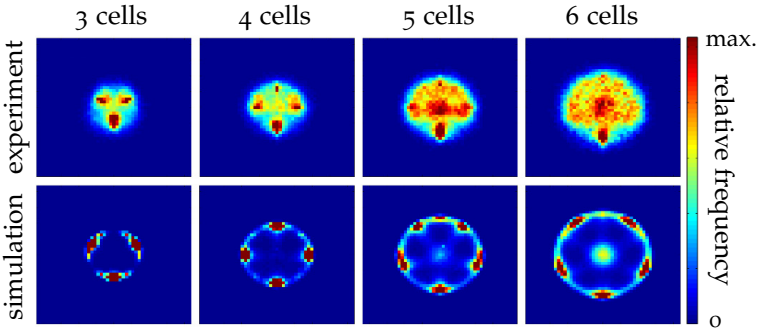

Figure 17.: Distribution of relative cell positions; cf. [STFR14]. The color code indicates the observation frequency of the cells' relative center of mass coordinates. In systems with four or less cells, relative center of mass positions are arranged in a quasi one-dimensional, ring-like configuration ("single lane" configuration). For larger cell numbers, a pronounced drop in the systems' persistence times is observed, which is accompanied by the emergence of two-dimensional "multi-lane" configurations.

The overall phenomenology of coherent cell migration in such circular confinement, as well as the appearance of typical cellular trajectories are identical to those discussed in sections 6.2 and 6.4. In particular, we note that the experimental measurements yield finite persistence times of coherent cell rotations and suggest that the motion of the MDCK cells can be associated with the R_1-PHASE identified in section 6.2[1].

Most strikingly, the experimental data exhibit a pronounced discontinuity in the persistency of the cell groups between 4- and 5-cell systems, despite a "global" tendency of increasing persistence times with increasing system sizes. This same discontinuity also naturally arises in our numerical simulations over a wide range of parameters inside the R_1-PHASE without the need of any further, specialized or artificial modeling assumptions. To under-

1 This statement is to be taken with a grain of salt. Due to complications to experimentally assess and quantify cell shape variability, it is rather difficult to distinguish between the R_1- and R_3-PHASES solely on the basis of measurements of the persistence times.

stand the physical origin of this discontinuity, we investigated the role of cell configurations in the establishment and maintenance of coherent group rotations. In Fig. 17, we show the distribution of the relative cell positions, averaged over an entire ensemble of measurements on independent systems and averaged over the entire observation time. More precisely, to assign cell positions, we used the geometrical center of mass of the cells for the data taken from the simulations, while in experimental measurements the position of the cells' nuclei have been used. Since the nucleus of each cell is itself subject to a certain amount of random motion, the heat maps corresponding to the experimental measurements appear more diffuse than the corresponding heat maps generated from the simulation data. Apart from this, however, both distributions share identical qualitative characteristics. Specifically, in both, numerical and experimental measurements, we observe the formation of quasi one-dimensional, "single-lane" cell configurations for systems containing only four cells or less. For larger cell numbers, in contrast, these single-lane configurations become unstable and cells start to organize themselves in genuinely two-dimensional "multi-lane" configurations.

In other words, our results show that the observed drop in the persistence times correlates with the formation of new lanes in the circular systems. Each time when an increase of the system size by one cell causes the formation of a new lane, the number of cells per lane decreases. This, in turn, suggests that the persistency of each lane, considered in isolation, is an increasing function of the number of cells per lane, so that the formation of new lanes causes a local drop in the system's persistency (as compared to "nearby" cell numbers). In addition, we note that an increasing number of cell lanes introduces further synchronization issues to achieve coherence across different lanes, which might well interfere with the system's capability to maintain a coherent state of collective rotation.

7.3 OUTLOOK

In conclusion, our results highlight the importance of local cell configurations in order to understand and interpret the forma-

tion of patterns of collective motion in cellular systems. Since it should be possible to control and vary relative cell positioning by means of well established micropatterning techniques, the study of collective cell migration in different topologies and confinement geometries presents fascinating future perspectives to advance our understanding in this important direction. In addition, as we have mentioned previously in section 6.3, we have made a number of experimentally testable predictions in Ref. [TRS+14] concerning the same experimental setup that has been discussed in the present chapter. To test these predictions, a promising next step would consist in an extension of the experimental investigations presented here, to study different cell types or different mutant strains of cells with varying mechanical and biochemical properties.

Cell Number and Local Arrangement Affect Collective Rotation on Micropatterns

Felix J. Segerer,[1] Florian Thüroff,[2] Alicia Piera Alberola,[1] Erwin Frey,[2,*] and Joachim O. Rädler[1,†]

[1] *Faculty of Physics and Center for NanoScience, Ludwig-Maximilans-Universität München, Geschwister-Scholl-Platz 1, D-80539 Munich, Germany*

[2] *Arnold-Sommerfeld-Center for Theoretical Physics and Center for NanoScience, Faculty of Physics, Ludwig-Maximilians-Universität München, Theresienstrasse 37, D-80333 Munich, Germany*

(Dated: November 12, 2014)

The spontaneous emergence of vortices is a hallmark of collective cellular activity. Here, we study the emergence of coherent angular motion (CAMo) as a function of the number of cells N confined in circular micropatterns. The persistence of CAMo increases with N, besides a distinct discontinuity, resulting from a topological transition of cell arrangement. Backed up by computer simulations, we suggest that the dipole nature of polarized, migrating cells accounts for the occurrence of vortex states, which reflect the instability of cell configurations that frustrate optimal dipole arrangement.

PACS numbers: 87.18.Gh,87.18.Fx,87.17.Rt

The ability of cells to coordinate their motion is essential in various biological contexts, notably morphogenesis [1–3] and tissue repair [4, 5]. In many recent studies two-dimensional cell monolayers of MDCK cells have been investigated as model systems for collective behavior in living systems. In these studies the occurrence of remarkably large scaled correlations and swirls in cell migration has been described using image correlation and traction force microscopy techniques [5–8]. The correlations are attributed to cell-cell coupling, and mechanotransduction mediated by the force generating cytoskeleton. In addition, migrating cells are known to exhibit an internal axis of front-rear polarization [9, 10]. These intrinsic properties result in swirls as natural modes of collective migration that preserve volume in densely packed cell layers. In fact, dynamic self-ordering into vortex states is well known in active systems such as driven filaments [11, 12], motile rod-like objects [13] or bacterial colonies [14, 15]. Yet in cell migration the spatial interactions are complex and parameter control is limited. To reduce degrees of freedom, boundary conditions can be implemented that enhance the selection of preferred dynamic states.

Micro-patterned surfaces have been used to study static adherence and intracellular cytoskeleton organization of individual cells in defined geometries [16]. Also, in small circular patterns occupied by only two cells, Huang et al. observed symmetry breaking in the direction of cell motion leading to a rotational state [17]. On large scale, Doxzen et al. [18] studied large numbers of cells confined in circular fields and found that the emergence of coherent angular motion [19] depends on cell density and cell-cell adhesion. Deforet et al. [20] observed stochastic global rotation reversals of the confined cells, on similar pattern size. However, the mechanisms underlying collective cell migration and the emergence of vortex states are poorly understood and its relationship to single cell properties remains unclear. In particular, a systematic study of the appearance and stability of small scale vortex states and the dynamic disorder-order transition leading to the emergence of collective migration as function of the number of involved cells has not been carried out so far.

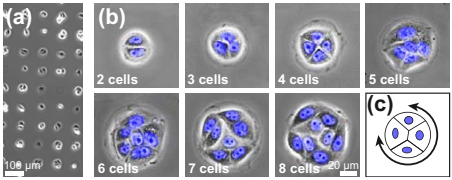

FIG. 1. (color online). (a) Array of MDCK cells seeded on circular micropatterns. (b) Circular patterns occupied by 2-8 cells. Circle size increases such that the average area per cell is constant at approximately 830 μm^2. Nuclei are labeled in blue. (c) Schematic of 4 cells rotating within a circular field.

In this letter, we investigate the emergence of collective rotational motion in small circular micropatterns as a function of the number of cells. The physical system consists of arrays of circular fields containing 2-8 cells. Cell density is kept constant by increasing field size in line with cell number. We find distinct transitions between states of disordered motion (DisMo) and states of coherent angular motion (CAMo) in the system. Furthermore, the survival time of the coherent state tends to increase with increasing cell number, but shows a pronounced drop between 4 and 5 cells, where the geometric cell arrangement changes from a conformation without a cell in the system center to one including a centered cell. By applying a computational model, based on the Cellular Potts Model (CPM) [21, 22], which we extend to incorporate internal polarization and cell-to-cell mechanotransduction [23], we are able to reproduce these features. Thus, the experimentally observed stepwise transition with increasing system size from the predominantly erratic motion of small cell groups to the directionally

persistent migration of larger assemblies is captured by the theory, underlining the role of polarity in the emergence of collective behavior.

Micro-patterns of the extracellular matrix protein fibronectin separated by PEGylated cell-repelling areas are fabricated using a plasma-induced patterning approach. Briefly, parts of a culture dish (Ibidi) are covered with a polydimethylsiloxan (PDMS) template of the desired pattern. The exposed parts are treated with O_2-plasma in a plasma cleaner (electronic diener) and overlaid for 30 min with 1 mg/mL PLL(20)-g[3.5]-PEG(2) (SuSoS). Afterwards, the template is removed and the whole surface is briefly exposed to a 50 μg/mL solution of fibronectin (Yo Proteins). MDCK cells are seeded on the structured surface and placed in a temperature controlled environmental chamber on the microscope stage. Arrays of circles are designed with increasing sizes to accommodate from 2 to 8 cells (Fig. 1(a), Fig. 1(b)). To ensure a constant cell density of 830 μm^2/cell, for each pattern size, only fields containing the appropriate number of cells are selected for analysis. Nuclei are stained using Leibowitz L-15 medium (c-c-pro) containing 15 ng/mL Hoechst 33342 (Invitrogen). Time lapse movies are recorded at a rate of 6 frames/hour over 50 h using an iMIC automated microscope (TILL Photonics). Individual nuclei are tracked using in-house image analysis software.

A typical array of circular adhesion sites occupied by MDCK cells is shown in Fig. 1(a). Cells exhibit spontaneous collective rotation within the circular areas (Fig. 1(c)). Periods of CAMo are seen to be interrupted by intervals of DisMo, after which rotation in an arbitrary direction is resumed (for movies see [24]). Increasing the system size cell by cell (Fig. 1(b)), we study the collective rotation and the associated switches as a function of cell number.

For each cell, the center of the nucleus is tracked and recorded in polar coordinates, and the individual angular positions $\varphi_i(t)$ with respect to the initial position $\varphi_i(0)$ are calculated (Fig. 2(a)) (for detailed description see section S1 [24]). Typical time courses of $\varphi_i(t)$ for a system of 7 cells are shown in Fig. 2(b). To filter out small fluctuations which result, for example, from displacements of the nucleus with respect to the geometric center of the cell, we calculate the system angular velocity $\Omega_N(t)$ as the mean over the individual angular velocities of the N-cell system smoothed over a number of frames n_f taken in discrete intervals of $T_f = 10$ min:

$$\Omega_N(t) = \frac{1}{N \cdot n_f^2 \cdot T_f} \sum_{i=1}^{N} \sum_{\tau=t}^{t+n_f} [\varphi_i(\tau) - \varphi_i(\tau - n_f)]. \quad (1)$$

We choose $n_f = 9$ as best trade-off between smoothing of fluctuations and temporal resolution [25]. For all N the probability distribution $P(\Omega_N)$ displays symmetry breaking into clockwise and counterclockwise rotations.

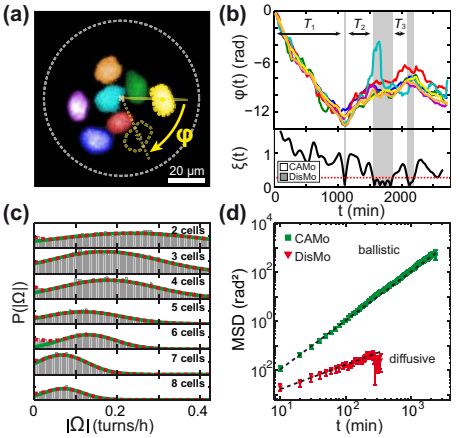

FIG. 2. (color). (a) False-color fluorescence image of the nuclei of seven cells within a circular micropattern. For each nucleus, the angular position $\varphi(t)$ is evaluated with respect to the circle center. (b) Angular positions $\varphi_i(t)$ of each cell (in colors correspond to the nuclei in (a)) and normalized total angular velocity $\xi(t)$. The classification threshold of $\xi_c = 1/4$ is indicated by the red dashed line. Periods of DisMo are highlighted by gray shaded areas. (c) Probability distribution of the mean angular velocity $|\Omega_N|$ for systems containing from 2 to 8 cells. The distributions are fitted by a single Gaussian (green) and a mixture of two Gaussians (dashed red). The deviation between the two curves reveals a local maximum at $|\Omega_N| = 0$. (d) Log-log plot of the angular MSD (Eq. 2) of CAMo (green) and DisMo (red) and its error for assemblies consisting of 8 cells. For other cell numbers see Fig. S3 [24].

Both directionalities are almost equally represented, with a small bias towards clockwise rotation (see Fig. S1 [24]). Similar asymmetries have been reported before [26, 27].

To distinguish periods of CAMo from periods of DisMo, we analyze the distribution of $|\Omega_N|$. Fig. 2(c) shows the distributions $P(|\Omega_N|)$ for each number of cells N. $|\Omega_N|$ is approximately Gaussian distributed with a maximum at a angular velocity $\bar{\Omega}_N$ and a standard deviation σ_N. $\bar{\Omega}_N$ as well as σ_N decrease with increasing cell number, displaying an almost constant coefficient of variation $\sigma_N/\bar{\Omega}_N = 0.74 \pm 0.13$. At $\Omega_N = 0$ the distribution $P(|\Omega_N|)$ exhibits a small second maximum, indicating a state of disordered, i.e. non-rotating, motion. Introducing a normalized variable $\xi_N(t) = \left|\Omega_N(t)/\bar{\Omega}_N\right|$, we define a common threshold for all N at $\xi_c = 1/4$, such that for $\xi_N(t) < \xi_c$ a migration state is classified as DisMo and for $\xi_N(t) \geq \xi_c$ as CAMo respectively (Fig. S1 [24]). (As seen in section S2 [24], an alternative approach to identifying collective motion gives the same results).

To verify that these two states are distinct in their mi-

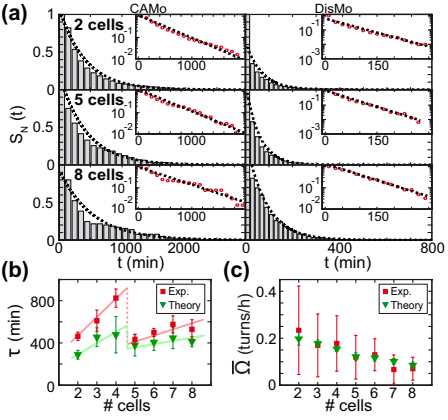

FIG. 3. (color online). (a) Survival function $S_N(t) = P_N(T > t)$ of CAMo and DisMo states. Insets show corresponding log-lin plots. Exponential fits are indicated by dashed lines (for other cell numbers see Fig. S4 [24]). (b) Persistence time τ as a function of cell number, derived from experiment and theory. Error bars indicate confidence bounds of 99 % within the fits. (c) Peak positions $\bar{\Omega}_N$ of the distribution of the angular velocity $P(\Omega_N)$ from experimental data and theory. Error bars indicate the standard deviation.

grational behavior we calculate the angular mean squared displacement (MSD) within each state:

$$\mathrm{MSD}(t) = \langle [\langle \varphi(t) \rangle_N - \langle \varphi(0) \rangle_N]^2 \rangle_{\mathrm{states}}. \qquad (2)$$

Here $t = 0$ indicates the starting point of an interval, $\langle\rangle_N$ indicates the average over all N cells within a system, and $\langle\rangle_{\mathrm{states}}$ indicates the average over all observed intervals of CAMo or DisMo, respectively. Consistently, the MSD of CAMo shows a slope 2 in a log-log plot, indicating ballistic angular motion for all cell numbers while the MSD of DisMo exhibits diffusive behavior (Fig. 2(d)).

Next we evaluate the lifetimes of the CAMo and DisMo states. Fig. 3(a) shows the survival function $S_N(t) = P_N(T > t)$, i.e. the fraction of CAMo/DisMo time periods T exceeding t, based on a sample size of over 600 analyzed systems (see Table S1 [24]). We find that the survival probabilities of both states decay exponentially, $S_N(t) \propto e^{-t/\tau}$. This finding indicates an underlying Poisson process for the emergence and collapse of both states. As seen in Fig. 3(b), the persistence time τ of the coherent state generally increases with increasing cell number, but a pronounced discontinuity between systems containing 4 and 5 cells is observed.

To further explore the mechanism underlying the discontinuity in persistence time, we monitored the spatial arrangement of cells within the pattern. Fig. 4(a) displays the relative positions of cells with respect to a reference cell. In systems containing two, three, and four cells, the cells are predominantly arranged in topologically equivalent positions in the outer regions of the circle. In this configuration, cells in the state of CAMo follow each other in a closed circle. As the number of cells increases to five, the packing geometry changes abruptly to a conformation in which a single cell is located at the system center. To connect this topological transition to the observed decrease in the persistence of the CAMo state, intrinsic cell properties have to be taken into consideration.

It is generally assumed that a migrating cell is highly polarized with respect to its internal signaling pathways and the polymerization of its cytoskeleton [9, 10]. In addition, since neighboring cells are coupled mechanically by cell-cell adhesion, a cell obtains directional guidance cues from migrating adjacent cells. This coupling suggests that adjacent cells tend to align their direction of internal front-rear polarization. Hence, a ring-like arrangement, as seen for 2-, 3-, and 4-cell systems, naturally provides a stable conformation during a period of CAMo (Fig. 4(b)). If, however, a cell is located in a central position, as in the case of 5 cells in a circle, this cell cannot establish a stable axis of internal polarization. It seems likely that this lack of orientation leads to the elevated instability we observe for CAMo states of such systems.

If this hypothesis is correct, the observed features should also emerge from theoretical migration models that include internal polarization and intercellular coupling. To this end, we set up a cellular automata model which is based on the CPM. Originally set up to model cell sorting phenomena [21, 22], the CPM has subsequently been extended and applied in various biological contexts. Cell motility has been addressed in a number of works, including studies on the "microscopic" level of single cells which couple rather sophisticated reaction diffusion networks to the dynamics of membrane protrusions [28, 29], as well as studies on the "macroscopic" level of large cell groups and tissues, where collective motion arises as a consequence of the alignment of "cell polarity vectors" [30, 31]. To describe the dynamics of small cell groups, we pursue an intermediate approach. Specifically, our simulation model uses a scalar polarization field within each cell to achieve the spatial resolution of microscopic models, and is entirely rule based (rather than being based on actual reaction-diffusion networks) to retain the computational efficiency of the more macroscopic models. To account for the effects of cell-cell communication via mechano-transduction, the local dynamics of the polarization field is coupled to the cells' membrane protrusions over a finite signaling range. This creates a positive feedback loop integrating intracellular fluctuations and external (mechanical) stimuli and gives rise to spontaneous cell polarization. To match the rotation

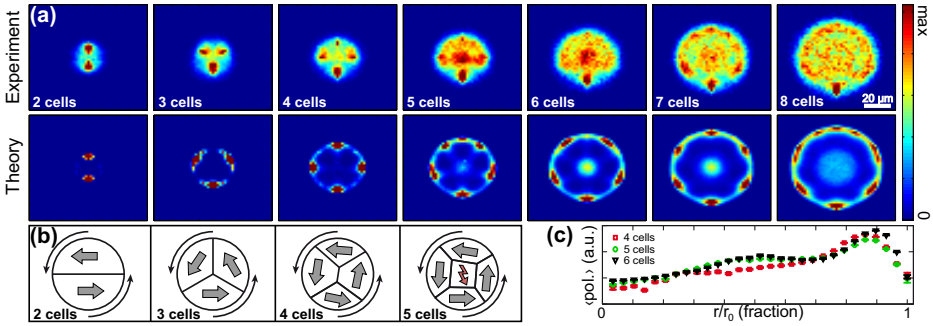

FIG. 4. (color). (a) Heat map of the relative nuclei positions with respect to a reference nucleus located at the lower border of the system from experimental and theoretical data (for details on the plot generation see section S7 [24]). (b) Schematic of possible polarization alignments during CAMo for different cell numbers. (c) For the CPM, mean magnitude of polarization and its error is plotted against the radial cell position r normalized by the maximal radial cell position r_0.

statistics to the experiments, we simulated cells of fixed (average) size on circular islands at fixed cell density. We then performed a parameter sampling by varying cell adhesion, the range of intracellular mechanical signaling, and the strength of cytoskeletal forces relative to contractile forces. For further details of the simulation model we refer the reader to a forthcoming publication [23].

The model reproduces the symmetry breaking into rotational states found by experiment (Supplement Movie [24]). Analyzing the theoretical cell tracks analogously to experimental data, we find CAMo as well as DisMo (see section S6 [24]). Monte Carlo Steps (MCS) were adjusted to real time by matching the CAMo peak positions $\bar{\Omega}_N$. As depicted in Fig. 3(c) we find the same steady decrease of $\bar{\Omega}_N$ with increasing cell number in the experimental as in the computational data. Moreover, simulation data exhibit the increase in CAMo persistence with increasing cell number for 2-,3- and 4-cell systems, and reproduce the discontinuity between 4- and 5-cell systems (Fig. 3(b)). (These observations are generic and appear also in alternative measures for persistence S5 [24].) The discontinuity in persistence is accompanied by the same topological transition in cell arrangement as found by experiment (Fig. 4(a) lower part). Assessing the characteristics of intrinsic cell polarization in the model, we find a systematic decrease of the mean magnitude of the front-rear polarization with decreasing distance to the system center (Fig. 4(c)). These findings clearly emphasize that a cell in the center of the pattern is unable to establish a stable axis of polarization and hence destabilizes collective behavior throughout the system.

Our results show that migration of small numbers of cells in circular patterns is well described in terms of two distinct states of disordered and coherent angular motion. In our experiments and simulations, the persistence of the ordered state increases with the number of confined cells for small cell numbers. Secondly, the geometry of cell arrangements within the circle has a critical influence on the alignment of cell polarization and hence the stability of rotational states. The dependence of state stability on both system size and relative cell arrangement is reminiscent of classical solid-state systems, where magnetization states depend on system size or coordination number [32, 33]. The behavior of cellular matter, however, appears more complex, as each unit is deformable and self-propelling. Hence our findings, in particular the discontinuity observed at the transition from states of four equally arranged cells to states of five cells including a central cell, reveals the decisive role of the local arrangement and orientation of neighboring cells in collective cell migration. As discussed by Doxzen et al. [18], defined boundary conditions as imposed by circular micropatterns can lead to the emergence of migrational states. Interestingly, they did not observe global changes in rotation direction for wild type MDCK cells on large scale patterns, while Deforet et al. [20] did. Since substrate stiffness can influence collective behavior significantly [7, 34], this discrepancy might be due to the different substrates used (PDMS/Glass). Here, we presented a mesoscopic experimental setup in which the emergence and persistence of collective behavior is analyzed for a small number of cells. We showed that it is possible to obtain controlled migrational cell states in confined geometries. Comparison of such states with computational simulations yields sets of intrinsic motility parameters. In future studies, this finding may help to evaluate and characterize migrational phenotypes and identify molecules that play a key role in cell-to-cell mechano-transduction and finally in the emergence of collective behavior.

This research was supported by the German Excellence

Initiative via the program 'NanoSystems Initiative Munich', and the Deutsche Forschungsgemeinschaft (DFG) via project B01 and project B02 within the SFB 1032.

* frey@lmu.de
† raedler@lmu.de

[1] A. J. Ewald, A. Brenot, M. Duong, B. S. Chan, and Z. Werb, Dev. Cell. **14**, 570 (2008).
[2] A. Vasilyev, Y. Liu, S. Mudumana, S. Mangos, P. Y. Lam, A. Majumdar, J. Zhao, K. L. Poon, I. Kondrychyn, V. Korzh, and I. A. Drummond, PLoS Biol. **7**, e9 (2009).
[3] V. Lecaudey and D. Gilmour, Curr. Opin. Cell. Biol. **18**, 102 (2006).
[4] T. J. Shaw and P. Martin, J. Cell. Sci. **122**, 3209 (2009).
[5] M. Poujade, E. Grasland-Mongrain, A. Hertzog, J. Jouanneau, P. Chavrier, B. Ladoux, A. Buguin, and P. Silberzan, Proc. Natl. Acad. Sci. U.S.A. **104**, 15988 (2007).
[6] L. Petitjean, M. Reffay, E. Grasland-Mongrain, M. Poujade, B. Ladoux, A. Buguin, and P. Silberzan, Biophys. J. **98**, 1790 (2010).
[7] T. E. Angelini, E. Hannezo, X. Trepat, J. J. Fredberg, and D. A. Weitz, Phys. Rev. Lett. **104**, 168104 (2010).
[8] A. K. Marel, M. Zorn, C. Klingner, R. Wedlich-Söldner, E. Frey, and J. O. Rädler, Biophys. J. , (to be published) (2014).
[9] N. Nishiya, W. B. Kiosses, J. Han, and M. H. Ginsberg, Nat. Cell. Biol. **7**, 343 (2005).
[10] A. J. Ridley, M. A. Schwartz, K. Burridge, R. A. Firtel, M. H. Ginsberg, G. Borisy, J. T. Parsons, and A. R. Horwitz, Science **302**, 1704 (2003).
[11] V. Schaller, C. Weber, C. Semmrich, E. Frey, and A. R. Bausch, Nature **467**, 73 (2010).
[12] Y. Sumino, K. H. Nagai, Y. Shitaka, D. Tanaka, K. Yoshikawa, H. Chate, and K. Oiwa, Nature **483**, 448 (2012).
[13] A. Kudrolli, G. Lumay, D. Volfson, and L. S. Tsimring, Phys. Rev. Lett. **100**, 058001 (2008).
[14] E. Ben-Jacob and H. Levine, J. R. Soc. Interface **3**, 197 (2006).
[15] H. Wioland, F. G. Woodhouse, J. Dunkel, J. O. Kessler, and R. E. Goldstein, Phys. Rev. Lett. **110**, 268102 (2013).
[16] M. Théry, J. Cell. Sci. **123**, 4201 (2010).
[17] S. Huang, C. P. Brangwynne, K. K. Parker, and D. E. Ingber, Cell Motil. Cytoskeleton **61**, 201 (2005).
[18] K. Doxzen, S. R. K. Vedula, M. C. Leong, H. Hirata, N. Gov, A. J. Kabla, B. Ladoux, and C. T. Lim, Integr. Biol. **5**, 1026 (2013).
[19] K. Tanner, H. Mori, R. Mroue, A. Bruni-Cardoso, and M. J. Bissell, Proc. Natl. Acad. Sci. U.S.A. **109**, 1973 (2012).
[20] M. Deforet, V. Hakim, H. G. Yevick, G. Duclos, and P. Silberzan, Nat. Commun. **5**, 3747 (2014).
[21] F. Graner and J. A. Glazier, Phys. Rev. Lett. **69**, 2013 (1992).
[22] J. A. Glazier and F. Graner, Phys. Rev. E **47**, 2128 (1993).
[23] F. Thüroff, M. Reiter, F. J. Segerer, J. O. Rädler, and E. Frey, (unpublished).
[24] See Supplemental Material at [URL will be inserted by publisher] for time lapse movies, plots, and detailed calculations..
[25] Data analysis using $n_f = 4$ or $n_f = 15$ respectively had no significant qualitative influence on the results (data not shown).
[26] L. Q. Wan, K. Ronaldson, M. Park, G. Taylor, Y. Zhang, J. M. Gimble, and G. Vunjak-Novakovic, Proc. Natl. Acad. Sci. U.S.A. **108**, 12295 (2011).
[27] L. N. Vandenberg and M. Levin, Dev. Biol. **379**, 1 (2013).
[28] A. F. M. Marée, A. Jilkine, A. Dawes, V. A. Grieneisen, and L. Edelstein-Keshet, Bull. Math. Biol. **68**, 1169 (2006).
[29] A. F. M. Marée, V. A. Grieneisen, and L. Edelstein-Keshet, PLoS Comput. Biol. **8**, e1002402 (2012).
[30] A. Szabó, R. Ünnep, E. Méhes, W. O. Twal, W. S. Argraves, Y. Cao, and A. Czirók, Phys. Biol. **7**, 046007 (2010).
[31] A. J. Kabla, J. R. Soc. Interface **9**, 3268 (2012).
[32] Y. Li, Y. Li, and T. Wang, J. Nano Mat. **2012**, 1 (2012).
[33] X. Wu, N. Izmailian, and W. Guo, Phys. Rev. E **87**, 022124 (2013).
[34] M. R. Ng, A. Besser, G. Danuser, and J. S. Brugge, J. Cell Biol. **199**, 545 (2012).

APPENDIX

—Supplementary Material—
A Critical Assessment of the Boltzmann Approach for Active Systems

Florian Thüroff,* Christoph A. Weber,* and Erwin Frey
*Arnold Sommerfeld Center for Theoretical Physics and Center for NanoScience, Department of Physics, Ludwig-Maximilians-University, Munich, Germany**

MICROSCOPIC MODELS FOR PROPELLED RODS

We consider (i) *hard-core rigid, propelled rods* as in [1], and (ii) a bead-spring model for *propelled polymers with a finite bending stiffness* as well as a *short-range polar alignment interaction*. For both models, we assume that each rod's dynamics is governed by over-damped equations of motion. The underlying equations for each model are given and discussed in the respective subsection below.

(i) Hard-core propelled rods

In our first microscopic model we consider rigid, rod-like particles of length L and diameter d moving in a effectively two-dimensional, over-damped fluid environment [1]. Each rod is driven parallel to its long axis by a constant driving force F^{d}. As interactions between the rods, we consider excluded volume forces, denoted as F^{ex}. The state of each rod is given by its position $\mathbf{x}$, and the rod's orientation θ, measured with respect to some fixed reference frame. The equations of motion for the orientation of the rod, θ, and it's motion parallel and perpendicular to the rod's long axis, $x_\parallel$ and $x_\perp$, are given by force and angular momentum balance [1]

$$\frac{d}{dt}x_\parallel = \mu_\parallel\left(F^{\mathrm{d}} + F_\parallel^{\mathrm{ex}}\right), \tag{S1a}$$

$$\frac{d}{dt}x_\perp = \mu_\perp F_\perp^{\mathrm{ex}}, \tag{S1b}$$

$$\frac{d}{dt}\theta = \mu_{\mathrm{r}} F_\perp^{\mathrm{ex}}\delta x_\parallel, \tag{S1c}$$

where $\mu_\parallel$, $\mu_\perp$ and μ_{r} denote the mobilities for translational and rotational motion in an over-damped fluid environment. $\delta x_\parallel$ denotes the length of the lever arm measured from the rod's center-of-mass to the point of contact with the collision partner. $F_\parallel^{\mathrm{ex}}$ and $F_\perp^{\mathrm{ex}}$ denote the projections of the excluded volume interaction forces along and perpendicular to the considered rod's long axis, respectively. The hard core potential is approximated by a harmonic spring with a very large spring constant, accounting for practically negligible penetrations distances [2]. In our scattering study presented in the main text we consider sphero-cylinders with aspect ratio $L/d = 10$. In the simulation we measure length in units of the rod's thickness d, and we rescale time as: $t \to t\,\mu_\parallel F^{\mathrm{d}}/d$. For the values of the mobilities we choose the hydrodynamic mobilities of a rod moving in three dimensions [3]: $\mu_\perp/\mu_\parallel = 0.5$ and $\mu_{\mathrm{r}}/\mu_\parallel = 6/L^2$. The non-dimensional spring constant of the excluded volume interactions is equal to 100.

(ii) Elastic propelled polymer with short-ranged aligning interactions

In our second microscopic model we consider propelled polymers with a finite bending stiffness which move in a two dimensional, over-damped fluid environment and which interact by a short-ranged polar alignment interaction. Each polymer is represented by a chain of beads i with spatial coordinates $\mathbf{x}_i$. The beads are coupled by harmonic springs for tangential stretching and bending, with the corresponding forces denoted as $\mathbf{F}^{\mathrm{stretch}}$ and $\mathbf{F}^{\mathrm{bend}}$. Tangential stretching forces are modeled via Hookian springs with a very large spring constant (to account for inextensibility, [2]) and with a rest position equal to the bead size d. To model bending forces, we use the *wormlike chain* model [4], with the bending force at bead i given by $\mathbf{F}_i^{\mathrm{bend}} = \frac{\mathcal{E}}{d}\frac{\partial}{\partial \mathbf{x}_i}\sum_j \mathbf{T}_j\cdot\mathbf{T}_{j+1}$, where $\mathbf{T}_i = (\mathbf{x}_i - \mathbf{x}_{i-1})/|\mathbf{x}_i - \mathbf{x}_{i-1}|$ denotes the i-th bead's tangent, and where $\mathcal{E}$ is the bending rigidity. Moreover, each bead is assumed to be propelled by a constant force $\mathbf{F}_i^{\mathrm{d}}$ pointing along each bead's tangent $\mathbf{T}_i$ [7]: $\mathbf{F}_i^{\mathrm{d}} = \alpha\mathbf{T}_i$, with α denoting the magnitude of the driving force.

As interaction between two colliding polymers, we consider excluded volume interactions between the beads, together with short-range, polar-aligning interactions. Excluded volume interactions are again described by harmonic springs

with a very large spring constant [2], with the corresponding force being denoted by $\mathbf{F}_i^{\mathrm{ex}}$. The alignment interactions are modeled as follows: If the distance between bead i and bead j, each belonging to a different polymer, is smaller than some critical distance ℓ_{a} (alignment radius), bead i feels a force $\mathbf{F}_i^{\mathrm{a}} = D^{\mathrm{a}}\mathbf{T}_j$, whereas bead j is subject to a force $\mathbf{F}_j^{\mathrm{a}} = D^{\mathrm{a}}\mathbf{T}_i$. The coefficient D^{a} denotes the alignment strength.

In summary, the dynamics of each bead i of e.g. polymer (1) is governed by the following set of equations [we introduce the short-hand notation $i(k)$, $k \in \{1,2\}$ to refer to bead i of polymer (k)]:

$$\begin{aligned}\frac{1}{\mu}\frac{d}{dt}\mathbf{x}_{i(1)}(t) \;=\; & \overbrace{\alpha\mathbf{T}_{i(1)}}^{\text{driving}} + \overbrace{\frac{\mathcal{E}}{d}\frac{\partial}{\partial\mathbf{x}_{i(1)}}\sum_{j(1)}\mathbf{T}_{j(1)}\cdot\mathbf{T}_{j(1)+1}}^{\text{bending}} + \sum_{j(1)}\mathbf{F}^{\mathrm{stretch}}_{i(1)j(1)} \\ & + \sum_{j(2)}\mathbf{F}^{\mathrm{ex}}_{i(1)j(2)} + \begin{cases}\sum_{j(2)} D^{\mathrm{a}}\mathbf{T}_{j(2)} & \text{if } |\mathbf{x}_{i(1)}-\mathbf{x}_{j(2)}| \le \ell_{\mathrm{a}}, \\ 0 & \text{otherwise,}\end{cases}\end{aligned} \tag{S2}$$

where μ denotes the mobility for a sphere with diameter d. Again, we measure length in units of the bead diameter d, and rescale time according to: $t \to t\mu\alpha/d$. To make sure that the polymer is semiflexible with respect to the alignment interactions, we choose the bending modulus, the alignment strength and alignment interaction radius in the scattering study presented in the main text as follows: $\mathcal{E}/(\alpha d^2) = 50.0$, $D^{\mathrm{a}}/\alpha = 0.15$ and $\ell_{\mathrm{a}} = 4d$. As in our first model, we consider polymers of length $L = 10d$. The values for the non-dimensional spring constants for stretching and excluded volume interactions are chosen as 5000 and 100, respectively.

Initialization of collision geometries

To perform scattering studies for each of these models, (i) and (ii), we prepare two rods with different relative pre-collisional orientations $\psi = \theta_1 - \theta_2 \in [0,\pi]$ ($\theta_{1/2}$: pre-collisional rod orientations) and different impact parameters b [for definition of b cf. Fig. 1], and observe the resulting values of the relative post-collisional orientations $\psi' = \theta_1' - \theta_2'$ ($\theta_{1/2}'$: post-collisional rod orientations). Specifically, we fix rod 1 and place rod 2 with relative angle ψ and impact parameter b. For model (i) we placed the rods in the considered collision geometries, direct at contact of the hard repulsive potential. For model (ii), rod 2 is placed at contact just as if rod 2 had a virtual diameter of $\ell_{\mathrm{a}} + d$, where ℓ_{a} denotes the alignment radius, and d is the diameter of the semi-flexible polymer.

EXISTENCE AND UNIQUENESS OF THE SOLUTION FOR $\bar{\rho}_t = \rho_t[\tilde{w}(\psi);\bar{\psi}] = \rho_t[\bar{w};\bar{\psi}]$ ($\bar{\rho}_t \ge 0$)

In the following, we briefly demonstrate that the manifold of deterministic collision rules $\tilde{w}(\psi)$, defined by

$$\rho_t[\tilde{w}(\psi);\bar{\psi}] = \rho_t[\bar{w},\bar{\psi}] = \bar{\rho}_t = \text{const.} \quad (\sigma = 0), \tag{S3}$$

contains one and only one constant function $\tilde{w}(\psi) = \bar{w} = \text{const.}$ for all non-negative transition densities $\bar{\rho}_t$.

Existence

Using the definition of $\rho_t[w(\psi);\bar{\psi}]$ [Eq. (5) in the main text] together with the definition of the integrals $\mathcal{I}_{n,k}$,

$$\mathcal{I}_{n,k} = \int_{-\bar{\psi}}^{\bar{\psi}} \frac{d\psi}{\pi}\,\mathcal{S}(L,\psi)\left\{e^{-(k\sigma)^2/2}\cos\Big[\Big(n - k\big(1-w(\psi)\big)\Big)\psi\Big] - \cos(n\psi)\right\}, \tag{S4}$$

the defining equation (S3) can be recast in the following explicit form:

$$\begin{aligned}&\int_{-\bar{\psi}}^{\bar{\psi}} \frac{d\psi}{\pi}\,\mathcal{S}(L,\psi)\left\{\cos\big[(1-\tilde{w}(\psi))\cdot\psi\big] + \cos\big(\tilde{w}(\psi)\cdot\psi\big) - \cos(\psi) - 1\right\} \\ &= \int_{-\bar{\psi}}^{\bar{\psi}} \frac{d\psi}{\pi}\,\mathcal{S}(L,\psi)\left\{\cos\big[(1-\bar{w})\cdot\psi\big] + \cos(\bar{w}\cdot\psi) - \cos(\psi) - 1\right\} = \frac{1-e^{-(\sigma_0)^2/2}}{\bar{\rho}_t} \equiv C \ge 0.\end{aligned} \tag{S5}$$

From the above equation we see that the "lower bound manifold", $C = 0$, contains exactly one constant function, viz. $\tilde{w}(\psi) = \bar{w}_{\rm low} = 1$. This manifold corresponds to the limiting case $\bar{\rho}_t \to \infty$. To obtain the "upper bound manifold", we compute the maximum of the functional in the first line of Eq. (S5) by considering the variation of Eq. (S5) with respect to $\tilde{w}(\psi)$. We get:

$$\int_{-\bar{\psi}}^{\bar{\psi}} \frac{d\psi}{\pi}\, \psi\, \mathcal{S}(L,\psi)\left\{\sin\big[(1-\tilde{w}(\psi))\cdot\psi\big] - \sin\big[\tilde{w}(\psi)\cdot\psi\big]\right\}\cdot\delta\tilde{w}(\psi) = 0, \tag{S6}$$

which has the constant solution $\tilde{w}(\psi) = \bar{w}_{\rm upp} = 1/2$, corresponding to the lowest physically possible value of the transition density $\rho_t[\bar{w} = 1/2]$. Since both, the upper and lower bound of Eq. (S5) can be represented in terms of the constant functions $\tilde{w}(\psi) = \bar{w}_{\rm low/upp}$, and since the integral in the second line of Eq. (S5) is a continuous function of $\bar{w}$, we can conclude that every physically possible choice of ρ_t is consistent with at least one constant representative $\tilde{w}(\psi) = \bar{w} \in [0.5, 1]$.

Uniqueness

To see that the solutions to Eq. (S5) are unique, it suffices to note that the integral in the second line of Eq. (S5) is strictly monotonically decreasing on the interval $\bar{w} \in (1/2, 1)$.

LINEAR-STABILITY OF FULL HYDRODYNAMIC EQUATIONS

In the main text, we stated that the instability of the fully isotropic and homogeneous state toward the emergence of polar order can be assessed by considering the dynamics of spatially uniform systems, *i.e.* that it occurs at zero wave-number. To demonstrate this, we extend the calculation in the main text, that led to the spatially uniform hydrodynamic equations (4), so as to include all gradient terms. We find:

$$\partial_t \rho = -\nabla\cdot\boldsymbol{\tau}, \tag{S7a}$$

$$\begin{aligned}\partial_t \boldsymbol{\tau} = {} & -\nu_1\boldsymbol{\tau} + \frac{\mathcal{I}_{1,2}(\mathcal{I}_{-1,1}+\mathcal{I}_{2,1})}{\nu_2}\,\boldsymbol{\tau}^2\,\boldsymbol{\tau} \\ & + \frac{1}{4\nu_2}\nabla^2\boldsymbol{\tau} - \frac{1}{2}\nabla\rho - \mu_-\left[\boldsymbol{\tau}(\nabla\cdot\boldsymbol{\tau}) - \frac{1}{2}\nabla\boldsymbol{\tau}^2\right] \\ & - \mu_+(\boldsymbol{\tau}\cdot\nabla)\boldsymbol{\tau} + \frac{\kappa}{4}\left[\nabla\boldsymbol{\tau} + \nabla\boldsymbol{\tau}^t - (\nabla\cdot\boldsymbol{\tau})\mathbb{1}\right]\nabla\rho \\ & - \mathcal{I}_{1,2}\kappa\left[\boldsymbol{\tau}(\boldsymbol{\tau}\cdot\nabla\rho) - \frac{1}{2}\boldsymbol{\tau}^2\nabla\rho\right],\end{aligned} \tag{S7b}$$

where we used the following abbreviations:

$$\nu_k = 1 - e^{-(k\sigma_0)^2/2} - \rho\,(\mathcal{I}_{0,k} + \mathcal{I}_{k,k})\,, \tag{S8a}$$

$$\mu_\pm = \frac{\mathcal{I}_{1,2}}{\nu_2} \pm \frac{\mathcal{I}_{-1,1}+\mathcal{I}_{2,1}}{2\nu_2}, \tag{S8b}$$

$$\kappa = \partial_\rho \nu_2^{-1} = \frac{\mathcal{I}_{0,2}+\mathcal{I}_{2,2}}{\nu_2^2}. \tag{S8c}$$

In Eqs. (S7) and (S8), variables have been rescaled as follows: $t \to t/\lambda$, $x \to x v_0/\lambda$, $\rho \to \rho\lambda/\bar{\mathcal{S}}$, $\boldsymbol{\tau} \to \boldsymbol{\tau} v_0\lambda/\bar{\mathcal{S}}$, $\mathcal{I}_{n,k} \to \mathcal{I}_{n,k}\bar{\mathcal{S}}$, where $\bar{\mathcal{S}} = (2\pi)^{-1}\int_{-\bar{\psi}}^{\bar{\psi}} \mathcal{S}(L,d,\psi)d\psi$ is the "total scattering cross section". The actual analytical form of $\mathcal{S}(L,d,\psi)$ can be determined from straightforward geometrical considerations [5]:

$$\mathcal{S}(L,d,\psi) = 4v_0 d\,\left|\sin\left(\frac{\psi}{2}\right)\right|\left(1 + \frac{L/d-1}{2}\,|\sin\psi|\right), \tag{S9}$$

where L denotes the rod length, d is the diameter and v_0 the constant velocity.

The fully isotropic state ($\rho = \rho_0 = $ const and $\boldsymbol{\tau} = 0$) obviously is a solution to Eqs. (S7). To assess the linear stability of this state, we assume our model system to extend out to infinity, and investigate the growth rates of

wavelike perturbations of the form $\rho(\mathbf{x},t) = \rho_0 + \delta\rho\, e^{st+i\mathbf{q}\cdot\mathbf{x}}$, and $\boldsymbol{\tau}(\mathbf{x},t) = \delta\boldsymbol{\tau}\, e^{st+i\mathbf{q}\cdot\mathbf{x}}$, with $\delta\rho, |\delta\boldsymbol{\tau}| \ll 1$. From Eqs. (S7), we then find:

$$s_\pm = \frac{1}{8\nu_2}\left[-(q^2+4\nu_1\nu_2) \pm \sqrt{(q^2+4\nu_1\nu_2)^2 - 32\nu_2^2 q^2}\right]. \tag{S10}$$

Since $\nu_2 > 0$, both branches of the growth rate s possess strictly negative real parts for $\nu_1 > 0$. At $\nu_1 = 0$ a bifurcation occurs, and for $\nu_1 < 0$ the largest growth rate is given by $s_+|_{q=0} > 0$. In fact, expanding $s_+(\nu_1 < 0)$ up to leading order in q, we obtain

$$s_+ = |\nu_1| - \frac{1}{4}\left(\frac{2}{|\nu_1|} + \frac{1}{\nu_2}\right) q^2 + \mathcal{O}(q^4), \tag{S11}$$

which corresponds to a typical long wavelength instability of type III_s [6].

DESCRIPTION OF VIDEO MATERIAL

We attached four videos: Two videos, corresponding to the two microscopic models for propelled rods (refer to the first section above), and two videos obtained from solving the full kinetic equations [see Eq. (2), main text]. In the latter case we show parameter sets that give rise to a polar state with a homogeneously distributed density field, and a polar-wave pattern, respectively.

Videos for microscopic models

(i) rigid, propelled rods with excluded volume interactions [1]: **hard_rods.mp4**,

(ii) propelled semiflexible polymers with excluded volume and short-ranged polar alignment interactions: **aligningrods.mp4**.

In both videos we show representative collision geometries, i.e. impact parameter b and relative angle ψ from the set: $\{b\}\times\{\psi\} = \{5, 5/3, -5/3, -5\}\times\{\pi/7, 2\pi/7, 3\pi/7, 4\pi/7, 5\pi/7, 6\pi/7\}$. In the simulation we numerically calculated the dynamics corresponding to each collision geometry until the relative orientation of both rods remain practically constant over time. However, for certain collision geometries, rods move quite are large distance $> \mathcal{O}(10L)$ until their orientations became stationary. Therefore, to keep movies within a reasonable bounds, we applied for the presented video material the following condition for each collision geometry: we switch to the next collision geometry if either both rods do not interact anymore, or if rod 1 (signaled in red) has moved a distance $25d$ away from its initial starting point.

Videos of the time-dependent solutions to the kinetic equation

Both videos correspond to a density $\rho = 0.15$ and a noise levels $\sigma = \sigma_0 = 0.15$. Moreover, time measured in λ^{-1} is indicated by "T" in the videos, while the normalized, averaged momentum is shown in the box at the bottom right. Black arrows correspond to the local polarization [only one out of 23 grid sites depicted; total number of grid sites: 10^4].

(i) Polar wave pattern developing for large times [$\bar{\psi} = \frac{3}{4}\pi$, $\bar{w} = 0.92$]: **polar_wave_pattern.mp4**,

(ii) Polar state with a homogeneously distributed density field emerging for large times [$\bar{\psi} = \frac{3}{4}\pi$, $\bar{w} = 0.8$]: **polar_homogenous_density_state.mp4**.

---

* F. Thüroff and C.A. Weber contributed equally to this work.

[1] F. Peruani, A. Deutsch, and M. Bär, Phys. Rev. E **74**, 030904 (2006).

[2] We checked that the observed results do not depend on the specific values of the chosen spring constant .
[3] J. K. Dhont, *An introduction to dynamics of colloids* (Elsevier Science B.V., Amsterdam, 1996), Chap. 6.
[4] J. d. Cloizeaux and G. Jannink, *Polymers in Solution: Their modelling and structure* (Clarendon Press, Oxford, New York, 1990).
[5] C. A. Weber, F. Thüroff, and E. Frey, arXiv:1301.7701 (2013).
[6] M. Cross and H. Greenside, *Pattern formation and dynamics in nonequilibrium systems* (Cambridge, New York, 2009), Chap. 2.
[7] To ensure that every bead is driven by a distinct tangential vector (note, there are N beads, but only $N-1$ tangents) we apply a slightly different definition for the tangent $\mathbf{T}_i$ to compute the propelling force, namely: $\mathbf{T}_i(t) = \mathbf{x}_i(t) - \mathbf{x}_i(t - \Delta t)/|\mathbf{x}_i(t) - \mathbf{x}_i(t - \Delta t)|$, where Δt denotes some small time-increment. We chose $\Delta t = 10dt$, where dt denotes the numerical time discretization.

Supplement: Bridging the gap between single cell migration and collective dynamics

Florian Thüroff,[1] Matthias Reiter,[1] Felix Segerer,[2] Joachim O. Rädler,[2] and Erwin Frey[1]

[1]*Arnold Sommerfeld Center for Theoretical Physics and Center for NanoScience, Department of Physics, Ludwig-Maximilians-University, Munich, Germany*

[2]*Faculty of Physics and Center for NanoScience, Ludwig-Maximilians-Universität München, Geschwister-Scholl-Platz 1, 80539 Munich, Germany*

Contents

I. COMPUTATIONAL MODEL

In this section, we describe the actual implementation of our computational model, which has been outlined briefly in the main text. While the biological rationale behind our modeling approach has been discussed in the main text, our focus here is on the technical aspects of our modeling approach. To facilitate subsequent discussions on implementation details, we start by introducing some model-specific terminology which will be used throughout this section to illustrate the mechanics of our model.

A. Computational grid

The basic data structure, our computational model resorts to, is referred to as the *grid*. The grid itself is implemented as a regular, space-filling lattice with lattice vectors $\{\mathbf{x}_i\}_{i=1,\dots,N}$. Each lattice vector $\mathbf{x}_i$ is understood to represent its associated Voronoi cell which will be referred to as *grid site*. To be specific, we will consider triangular tilings $\{\mathbf{x}_i\}_{i=1,\dots,N}$ in the following, such that each grid site is a hexagon, which is surrounded by 6 nearest neighbor sites, which define the neighborhood $\mathcal{N}_k$ of $\mathbf{x}_k$:

$$\mathcal{N}_k = \Big\{ \mathbf{x}_l \,\big|\, \mathbf{x}_l \text{ is nearest neighbor of } \mathbf{x}_k \Big\}. \tag{1}$$

Overall, the grid represents our general notion of (discretized) space, and each grid holds information specific to cells as well as to environmental factors. In what follows, distances on this spatial grid will be measured in units of the distance between the midpoints of neighboring lattice sites, i.e.

$$||\mathbf{x}_k - \mathbf{x}_l|| = 1 \Leftrightarrow l \in \mathcal{N}_k. \tag{2}$$

This then implies for the side length $\mathfrak{l}$ and the two-dimensional volume (area) $\mathfrak{a}$ of each hexagonal grid site: $\mathfrak{l} = 1/\sqrt{3}$ and $\mathfrak{a} = 3\sqrt{3}\,\mathfrak{l}^2/2$.

B. Representation of biological cells

In the spirit of the cellular Potts model [1, 2], each cell is represented by a simply connected set of lattice sites

$$\mathcal{D}^{(\alpha)} = \Big\{ \mathbf{x}_k \big|\, c(\mathbf{x}_k) = \alpha \Big\}, \tag{3}$$

where the indicator function $c(\mathbf{x}_k)$ gives the index of the cell occupying $\mathbf{x}_k$. Here and in the following, we use latin indices to reference lattice sites, and greek indices to reference cells. The set $\mathcal{D}^{(\alpha)}$ used to represent the spatial extension of cell α, will be referred to as the *domain* of cell α. In our model, each grid site, $\mathbf{x}_k$, can be occupied by at most one cell (i.e. we do not allow for overlapping cell domains). The absence of cells at $\mathbf{x}_k$ is indicated by negative values of the indicator function, $c(\mathbf{x}_k) < 0$. Following this terminology, the area and the perimeter of cell α is given by:

$$A^{(\alpha)} = \mathfrak{a} \sum_{k=1}^{N} \delta_{\alpha,c(\mathbf{x}_k)} = \frac{3\sqrt{3}}{2}\,\mathfrak{l}^2 \sum_{k=1}^{N} \delta_{\alpha,c(\mathbf{x}_k)}, \tag{4a}$$

$$P^{(\alpha)} = \mathfrak{l} \sum_{k=1}^{N} \sum_{\mathbf{x}_l \in \mathcal{N}_k} \delta_{\alpha,c(\mathbf{x}_k)} \big(1 - \delta_{\alpha,c(\mathbf{x}_l)}\big). \tag{4b}$$

C. Model dynamics

1. Protrusion and retraction of cells

Biological cells are highly dynamic entities which constantly change shape and move around in space. To reflect this dynamic behavior computationally, the domain $\mathcal{D}^{(\alpha)}$ of cell α changes over time. The evolution of

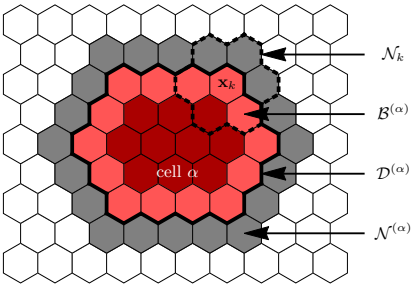

FIG. 1: Illustration of the various sets defined in the main text. Grid sites occupied by cell α, i.e. its domain $\mathcal{D}^{(\alpha)}$, are indicated in red colors. The cell's membrane sites, $\mathcal{B}^{(\alpha)}$, are indicated by the lighter red color, the cell's immediate neighborhood, $\mathcal{N}^{(\alpha)}$, is indicated in gray color. Elementary events involving cell α always involve one grid site in $\mathcal{B}^{(\alpha)}$ and one grid site in $\mathcal{N}^{(\alpha)}$. For the hexagonal lattices used in this work, each grid site $\mathbf{x}_k$ is surrounded by 6 nearest neighbors which we collectively denote by $\mathcal{N}_k$.

cell shape and position, as represented by $\mathcal{D}^{(\alpha)}$, proceeds via a succession of *elementary events*. In our numerical model, elementary events come in one of two basic flavors: *protrusion events* and *retraction events*. During a protrusion event, cell α (referred to as "source cell") incorporates one grid site $\mathbf{x}_t$ ("target grid site") from its neighborhood $\mathcal{N}^{(\alpha)}$,

$$\mathcal{D}^{(\alpha)}_{\text{old}} \to \mathcal{D}^{(\alpha)}_{\text{new}} = \mathcal{D}^{(\alpha)}_{\text{old}} \cup \{\mathbf{x}_t\}, \quad \mathbf{x}_t \in \mathcal{N}^{(\alpha)}, \tag{5}$$

thereby increasing its cellular domain by one grid site. Here, the neighborhood of cell α, $\mathcal{N}^{(\alpha)}$ is defined as

$$\mathcal{N}^{(\alpha)} = \Big\{ \mathbf{x}_l \,\Big|\, \min_{\mathbf{x}_k \in \mathcal{D}^{(\alpha)}} ||\mathbf{x}_l - \mathbf{x}_k|| = 1 \Big\}. \tag{6}$$

During a retraction event, source cell α expels one of its membrane grid sites $\mathbf{x}_s \in \mathcal{B}^{(\alpha)}$,

$$\mathcal{D}^{(\alpha)}_{\text{old}} \to \mathcal{D}^{(\alpha)}_{\text{new}} = \mathcal{D}^{(\alpha)}_{\text{old}} \setminus \{\mathbf{x}_s\}, \quad \mathbf{x}_s \in \mathcal{B}^{(\alpha)}_{\text{old}}, \tag{7}$$

where the set of membrane grid sites $\mathcal{B}^{(\alpha)}$ is defined as

$$\mathcal{B}^{(\alpha)} = \Big\{ \mathbf{x}_k \in \mathcal{D}^{(\alpha)} \,\Big|\, \min_{\mathbf{x}_l \in \mathcal{N}^{(\alpha)}} ||\mathbf{x}_k - \mathbf{x}_l|| = 1 \Big\}. \tag{8}$$

Protrusion and retraction events are the numerical analogs of cell protrusions and cell retractions.

In implementing the reassignment rules, Eqs. (5) and (7), we have to take into account that cellular domains must not overlap. For solitary cells moving in free space this does not imply any restrictions, and Eqs. (5) and (7) apply directly. In the bulk of a confluent monolayer of adhesive cells, however, any protrusion of source cell α into the domain of cell β (referred to as "target cell") must be accompanied by a retraction event $\mathcal{D}^{(\beta)}_{\text{old}} \to \mathcal{D}^{(\beta)}_{\text{new}} = \mathcal{D}^{(\beta)}_{\text{old}} \setminus \{\mathbf{x}_t\}$, where $\mathbf{x}_t$ denotes the target grid site annexed by cell α. We emphasize, however, that the reverse is not generally true. If source cell α retracts, i.e. loses one of its boundary grid sites $\mathbf{x}_s \in \mathcal{B}^{(\alpha)}$, the lost grid site $\mathbf{x}_s$ faces either one of two conceivable fates: If, on the one hand, cohesion among cells is sufficiently strong (cf. section I D 4 for a definition of the notion "sufficiently strong"), the retraction of cell α exerts a pulling force on one of its neighboring cells β (the "target cell"), which is then forced to fill the emerging void at $\mathbf{x}_s$, i.e. $\mathcal{D}^{(\beta)}_{\text{old}} \to \mathcal{D}^{(\beta)}_{\text{new}} = \mathcal{D}^{(\beta)}_{\text{old}} \cup \{\mathbf{x}_s\}$, where $\mathbf{x}_s$ denotes the grid site lost by cell α. On the other hand, if adhesion between cells is weak, retraction of the source cell α can lead to a rupture of pre-existing cell contacts between α and other cells at $\mathbf{x}_s$, such that the lost grid site $\mathbf{x}_s$ becomes free space $[c(\mathbf{x}_s) = \alpha \geq 0 \to c(\mathbf{x}_s) < 0]$. Details on the actual implementation of cell rupture are discussed in section I D 4.

2. *Monte-Carlo scheme*

In the spirit of a standard Monte-Carlo scheme, the actual simulation proceeds via a succession of *"Monte-Carlo steps"*, where each Monte-Carlo step (MCS) propagates the state of the simulated cell population from time t to time $t + 1$. One MCS consists in a series of attempts to perform elementary events, originating from randomly chosen membrane grid sites of randomly chosen cells. The length of one MCS, i.e. the actual number of attempted elementary events, is chosen such that each of the cells' membrane grid sites is given the opportunity to attempt, on average, one elementary event per MCS. During each MCS, cell domains $\mathcal{D}^{(\alpha)}$ as well as the numerical values of cell areas $A^{(\alpha)}$ and perimeters $P^{(\alpha)}$ are updated "on the fly", while the cells' cytoskelatal fields are updated only once at the end of each MCS; cf. section I D 2 for the details of this update rule. The simulation then proceeds along the following Monte-Carlo scheme:

1) Initialize the the cell population and define the duration of the simulation, i.e. the number of MCS N_{mcs} to be performed.

2) Set the simulation time $t = 0$.

3) Perform the next MCS; this step is further detailed below.

4) Update cytoskelatal fields (cf. section I D 2).

5) Set $t = t + 1$.

6) Repeat steps 3 – 5 while $t < N_{\text{mcs}}$.

The implementation of a MCS, i.e. the sequence of elementary events is based on the following general considerations:

(i) Choice of source and target grid sites. Each elementary event $\mathcal{T}$ originates from a membrane grid site $\mathbf{x}_s \in \mathcal{B}^{(\alpha)}$ of some cell α, referred to as *source cell*, which will be referred to as *"source grid site"*. In addition, each elementary event involves a second grid site which lies in the neighborhood of the source grid site $\mathbf{x}_s$ and which is not currently occupied by cell α: $\mathbf{x}_t \in \mathcal{N}_s \setminus \mathcal{D}^{(\alpha)}$. In what follows, this additional grid site $\mathbf{x}_t$ will be referred to as *"target grid site"*. This grid site may either be an empty substrate site or a membrane site of another cell β, in which case the respective cell will be referred to as *target cell*. While the source grid site determines the location of the attempted elementary event, the target grid site determines the direction along which the elementary events is bound to proceed.

(ii) Monte-Carlo method to generate the system's dynamics. As mentioned above, the actual dynamics of cells in our simulation model is driven by a succession of elementary events, whose cumulative effects over time allow cells to change shapes and to move relative the substrate and relative to each other. Following a standard Monte-Carlo procedure, the probability of occurrence of elementary events $\mathcal{T}$ is determined by a goal function $p(\mathcal{T})$ [cf. point (iii) below]. However, since elementary events come in two basic flavors, protrusions $\mathcal{T}_{\text{pro}}$ and retractions $\mathcal{T}_{\text{ret}}$, their actual occurrence is controlled by a three-step process, once source and target grid sites have been determined: In a first step, the goal function p is used to compute the occurrence probabilities of the two alternative scenarios where either the source cell protrudes toward $\mathbf{x}_t$ [$p(\mathcal{T}_{\text{pro}})$], or retracts from $\mathbf{x}_s$, [$p(\mathcal{T}_{\text{ret}})$]. In a second step, both probabilities $p(\mathcal{T}_{\text{pro}})$ and $p(\mathcal{T}_{\text{ret}})$ are compared and, based on this comparison, a decision is made as to whether to attempt $\mathcal{T}_{\text{pro}}$ or $\mathcal{T}_{\text{ret}}$. The actual decision making process underlying our simulation results is based on enhancing computational performance and is briefly discussed in point (iv) below. Finally, once a decision has been made on its specific nature, in the third step the elementary event $\mathcal{T}$ is being accepted with probability $p(\mathcal{T})$, or else rejected.

(iii) Choice of the goal function $p(\mathcal{T})$. As has been detailed above, we use a goal function $p(\mathcal{T})$ to control the occurrence and acceptance of elementary events $\mathcal{T}$. Following the standard cellular Potts model [1, 2], this goal function takes into account the effects of cell contractility and cell-cell adhesion, using, however, a slightly different implementation; cf. sections I D 1 and I D 3. In addition, we generalized the definition of the goal function $p(\mathcal{T})$ to explicitly take into account a simplified model of cytoskeletal structures and the ensuing polarization of cells. The actual definition of the goal function will be developed in section I D, where, moreover, details concerning the implementation of the cell polarization model will be discussed.

(iv) Optimization of the acceptance rate for elementary events. Finally, since elementary events come in two separate flavors, viz. protrusion and retraction events, we must decide which type of elementary event to attempt, once source and target grid sites have been determined. The least biased procedure to implement this decision would be to select one of the two possibilities with probability 0.5. However, given that cells are polarized, protrusion events should clearly be favored at the cell's leading edge, while retraction events should be preferred at the rear of the cell. Although our definition of the polarization contribution to the acceptance probability $p(\mathcal{T})$, Eq. (14), already takes this asymmetry into account, we can increase the efficiency of our algorithm (more precisely, its acceptance rate) if we choose among protrusion and retraction events based on the prospective acceptance probabilities $p(\mathbf{x}_s \to \mathbf{x}_t)$ [protrusion event] and $p(\mathbf{x}_s \leftarrow \mathbf{x}_t)$ [retraction event], respectively. Specifically, we choose the type of elementary event with the higher prospective acceptance probability, unless the lower of both acceptance probabilities is itself non-negligible, i.e. exceeds a finite probability threshold $p_{\min}$. In this latter case both types of elementary events are chosen with equal probability 0.5. A finite threshold probability $p_{\min}$ introduces an element of stochasticity in the selection process between protrusion and retraction events for cases where both events possess finite acceptance probabilities (typically at the weakly polarizes side portions of the cells' membranes). Throughout this work, we used $p_{\min} = 0.01$ to increase the efficiency of the algorithm.

The implementation of a single MCS loop is then given by the following simulation scheme:

3.A) Determine the current number of trials per Monte-Carlo step (MCS) $K = \sum_\alpha \sum_{\mathbf{x}_k \in \mathcal{B}^{(\alpha)}} 1$ and set the trial counter $n = 0$.

3.B) With equal probability, choose one source grid site $\mathbf{x}_s \in \bigcup_\alpha \mathcal{B}^{(\alpha)}$.

3.C) With equal probability, choose one target grid site index $\mathbf{x}_t \in \mathcal{N}^\alpha \cap \mathcal{N}_s$.

3.D) Compute the prospective acceptance probabilities $p(\mathcal{T}_{\text{pro}})$ and $p(\mathcal{T}_{\text{ret}})$ corresponding to a protrusion event and a retraction event, respectively, and decide whether to attempt a protrusion event or a retraction event on the basis of these probabilities (cf. discussion above).

3.E) Accept the attempted elementary event with probability $p(\mathcal{T}_{\text{pro}})$ or $p(\mathcal{T}_{\text{ret}})$, respectively.

3.F) If the attempted elementary event has been accepted, update the cellular domains of source cell α and opponent cell β; for details see section I E.

3.G) If $s < K$, set $s \to s + 1$ and then repeat steps B through F.

D. Implementation of cellular traits

In this section, we discuss the various contributions of cellular traits to the overall acceptance probability $p(\mathcal{T})$ of an elementary event $\mathcal{T}$. Specifically, our model takes into account cell contractility, the assembly and disassembly of cytoskeletal structures, cell-cell adhesion, and focal adhesions. We will assume that each of these cellular properties contributes independently to the acceptance probability p, such that

$$p = \min\{1,\ p_{\text{cont}} \cdot p_{\text{cyto}} \cdot p_{\text{adhesion}}\}. \tag{9}$$

Anticipating our discussions in section I D 2, the effects due to focal adhesions have been combined with the effects due to assembly and disassembly of cytoskeletal structures in $p_{\text{cyto}}(\mathcal{T})$. In the following sections, we give detailed discussions for each of these contributions, separately.

1. Cell contractility

In biological cells, membrane fluctuations are constrained by elastic forces and contractile cytoskeletal structures, which play a vital role in cell migration [9, 10, 12]. In our computational approach, we take cell contractility into account by assigning a contractile "energy"

$$\mathcal{H}_{\text{cont}} = \sum_{\alpha} \left[m_\alpha\, P_\alpha^2 + a_\alpha\, A_\alpha^2 \right], \tag{10}$$

with positive coupling constants a_α and m_α characterizing the contractility[1] of cell α; for empty substrate sites ($\alpha < 0$) we set $am_\alpha = a_\alpha = 0$. According to Eq.(10), the cell's "contractile energy" increases with increasing cell perimeter and increasing cell area. The model Hamiltonian $\mathcal{H}_{\text{cont}}$ can then be used to specify the contractile contribution to the goal function p. To this end, let $\Delta\mathcal{H}_{\text{cont}}(\mathcal{T})$ denote the contractile contribution to the energy difference entailed by accepting an elementary event $\mathcal{T}$. Following a standard Metropolis algorithm, we then define

$$p_{\text{cont}}(\mathcal{T}) := \exp\left[-\Delta\mathcal{H}_{\text{el}}(\mathcal{T})\right]. \tag{11}$$

The contractile "energy", Eq.(10), is similar to the corresponding energy model commonly used in cellular Potts models [11]. Unlike the standard cellular Potts model, however, where a target area and target perimeter is used to keep the simulated cells from collapsing, the energetic contribution in Eq.(10) strictly contracts the cell's body. As will be detailed in the next section, to counteract these contractile forces, we explicitly model cytoskeletal structures within each cell, which provide outward pushing forces to balance cell contraction.

2. Cytoskeletal structures and focal adhesion

The cytoskeleton plays key roles both, in maintaining the mechanical integrity of the cell, and in the process of active cell migration [8–10]. Our model design aims at achieving high computational efficiency to allow for the simulation of very large cell numbers[2] and, at the same time, to capture the essential effects of cytoskeletal dynamics to attain meaningful results down to the level of single cells. Thus, instead of accounting for a detailed biochemical description by means of reaction-diffusion networks [3, 4], we resort to a simplified implementation of the most pertinent features of cytoskeletal dynamics. Specifically, we propose a rule based algorithm to model cytoskeletal structures, and to assess the integrated effects of cell polarity, cell contractility and adhesion on the collective dynamics of cells as parts of larger groups.

To this end, we define a scalar field $\rho(\mathbf{x}_n)$, $\mathbf{x}_n \in \mathcal{D}^{(\alpha)}$, on the domain of each cell α. The local quantity $\rho(\mathbf{x}_n)$ will be referred to as *cytoskelatal field* and is taken to be a measure for the density of cytoskeletal structures at position $\mathbf{x}_n$ within the cell's body. The field variable $\rho(\mathbf{x}_n)$ is dynamically updated as the simulation progresses, reflecting cytoskeletal remodeling. To set up a system of rules underlying the actual implementation of these cytoskeletal remodeling processes, we resort to the following biologically motivated premises:

(i) The scalar cytoskeletal field ρ is bounded: The dynamics of cytoskeletal remodeling not only depends on the local number (density) of actin monomers and polymers, but also on a multitude of accessory proteins controlling cytoskeleton assembly and disassembly. Several biological factors, including the action of sequestering proteins like profilin, which act to suppress actin polymerization, and limited amounts of nucleating proteins like the Arp 2/3 complex, keep the local density of actin filaments bounded. We, therefore, introduce bounds for the *cytoskeletal field*: $q \le \rho(\mathbf{x}_n) \le Q$. These bounds are cell-type specific. While the upper bound Q mainly reflects the limited availability of protein resources, the lower bound q serves to prevent cells from collapsing.

(ii) Regulatory proteins affect assembly and disassembly of cytoskeletal structures: The assembly and disassembly of cytoskeletal structures, numerically encoded by $\rho(\mathbf{x}_n)$, is regulated by a myriad of accessory proteins. In our computational model we simplify these complex processes by resorting to a single "bookkeeping variable"

[1] To compute the energy numerically, we choose our units such that $\mathfrak{l} = 1$. This amounts to a rescaling of the contractile constants such that $\mathfrak{l}^2\, m_\alpha \to m_\alpha$ and $\mathfrak{l}^4\, a_\alpha \to a_\alpha$.

[2] Currently, cell numbers up to $\mathcal{O}(10^4)$ can be achieved at acceptable computation times.

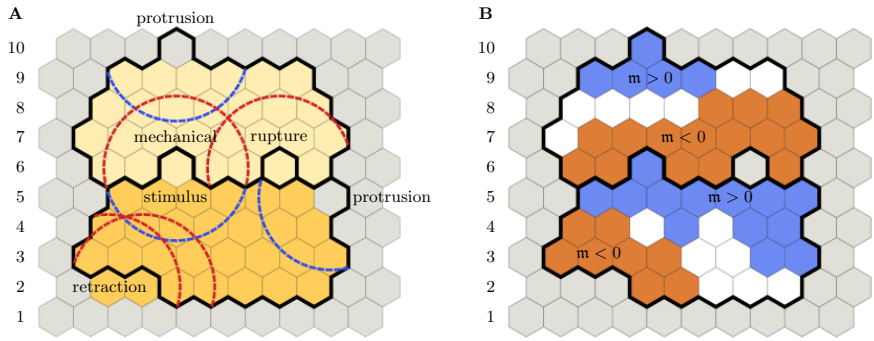

FIG. 2: Distribution of regulatory factors on the basis of accepted elementary events. For ease of reference, grid rows have been numbered from 1 to 10. *Left*: Solid black line indicate cells' membrane positions *after* acceptance of the respective elementary event; colors indicate cellular domains *before* the respective elementary event has been accepted (gray: substrate; shades of yellow: cells). Blue and red circular arcs (of radius R) delineate areas of local increase or decrease in the level of regulatory factors, respectively. The following elementary events are depicted: (i) lower cell retracts (two grid sites in row 2); (ii) lower cell protrudes (row 5); (iii) upper cell protrudes (row 10). In addition, the following elementary events occur across the cell-cell boundary: (iv) retraction of upper cell leads to rupture of cell-cell contact (row 6, right event); (v) either the lower cell protrudes and pushes the upper cell or the upper cell retracts and pulls on the lower cell (row 6, left event). Specifically, event (v) entails mechanical signaling between the upper and lower cell and, therefore, affects the distribution of regulatory factors in *both* cells. *Right*: Identical copy of the left image. Colors indicate local levels of regulatory factors $\mathfrak{m}$ (blue: $\mathfrak{m}$ positive; white: $\mathfrak{m}$ zero; red: $\mathfrak{m}$ negative; gray: substrate site). Note, in particular, that a substrate grid site has been inserted where cell rupture occurred (row 6, right pixel). The following cases can be distinguished: (i) Grid site $\mathbf{x}_k$ lies in the zone of influence of only positive (blue circles) or negative (red circles) chemical feedback, in which case the level of regulatory factors is positive or negative, respectively (e.g. red grid sites in row 2, or blue grid sites in row 5). (ii) Grid site $\mathbf{x}_k$ lies outside of any zone of influence, in which case the level regulatory factors is zero (e.g. white grid sites in row 2). (iii) Grid site $\mathbf{x}_k$ lies in the zone of influence of equally many positive and negative feedbacks, in which case the level of regulatory factors remains zero (e.g. fourth grid sites in row 4). (iv) Grid site $\mathbf{x}_k$ lies in a zone of predominantly positive or negative feedback, in which case the level of regulatory factors is positive or negative, respectively (e.g. third grid site in row 4). Recall that only the sign of $\mathfrak{m}$ is of significance to update the cells' cytoskelatal fields; cf. Eq. (13).

which we will refer to as "regulatory factors". Its local level is stored as an integer variable $\mathfrak{m}(\mathbf{x}_n)$ for each grid site $\mathbf{x}_n \in \mathcal{D}^{(\alpha)}$. We use $\mathfrak{m}(\mathbf{x}_n)$ to implement the overall action of regulatory cytoskeletal proteins in an effective and collective manner. Specifically, since the formation of lamellipodial structures depends on active nucleation promoting factors [5], we assume that positive levels, $\mathfrak{m}(\mathbf{x}_n) > 0$, reflect local conditions in support of network-assembly, whereas non-positive levels, $\mathfrak{m}(\mathbf{x}_n) \leq 0$, represent predominantly degrading (or disassembly) conditions.

(iii) Feedback between cytoskeletal structures and regulatory factors: The activities of accessory cytoskeletal proteins which regulate the local levels of cytoskeletal structures are themselves controlled by a number of mechanical and chemical signals received by the cell. Here and in the following, our focus will be on mechanical signals. For example, important regulatory proteins like the Arp 2/3 complex are activated locally at the cell membrane, from where they diffuse into the bulk of the cell until they are bound by actin [5–7]. Adopting a coarse level of description, this diffusion-degradation dynamics entails a finite range of regulatory proteins, which are activated at the cell's membrane. In our model, we use the integer variable variable $\mathfrak{m}(\mathbf{x}_n) > 0$ to implement this propagation of mechanical information, perceived by cell α at its periphery $\mathcal{B}^{(\alpha)}$, across a certain spatial distance R. The local levels of $\mathfrak{m}(\mathbf{x}_n)$ are continuously updated as the MCS loop progresses. The actual update procedure is given by the following set of rules; cf. Fig. 2:

- If a *protrusion event* has been accepted at the source site $\mathbf{x}_s \in \mathcal{B}^{(\alpha)}$ (source cell: α; target cell: β), then for all sites $\mathbf{x}_n$ within a range R (i.e. $||\mathbf{x}_n - \mathbf{x}_s|| < R$) the integer variable signifying regulatory factors is incremented up and down for the protruding and the retracting cell, respectively:

$$\mathfrak{m}(\mathbf{x}_n) \to \begin{cases} \mathfrak{m}(\mathbf{x}_n) + 1, & \mathbf{x}_n \in \mathcal{D}^{(\alpha)}, \\ \mathfrak{m}(\mathbf{x}_n) - 1, & \mathbf{x}_n \in \mathcal{D}^{(\beta)}. \end{cases} \tag{12a}$$

- Similarly, if a *retraction event* has been accepted at the source site $\mathbf{x}_s \in \mathcal{B}^{(\alpha)}$, and the (local) cell contact between source cell α and target cell β has

remained intact, then within a range R one applies the inverse update rule:

$$\mathfrak{m}(\mathbf{x}_n) \to \begin{cases} \mathfrak{m}(\mathbf{x}_n) - 1, & \mathbf{x}_n \in \mathcal{D}^{(\alpha)}, \\ \mathfrak{m}(\mathbf{x}_n) + 1, & \mathbf{x}_n \in \mathcal{D}^{(\beta)}. \end{cases} \tag{12b}$$

- If a *retraction event* has been accepted at the source site $\mathbf{x}_s \in \mathcal{B}^{(\alpha)}$, and in addition the (local) cell contact between source cell α and target cell β has *ruptured*, then the regulatory factors are reduced only within a range R in the retracting cell:

$$\mathfrak{m}(\mathbf{x}_n) \to \begin{cases} \mathfrak{m}(\mathbf{x}_n) - 1, & \mathbf{x}_n \in \mathcal{D}^{(\alpha)}, \\ \text{no update}, & \text{otherwise}. \end{cases} \tag{12c}$$

Finally, if the target grid site $\mathbf{x}_t$ is not occupied by any cell ($\beta \geq 0$) prior to the elementary event, only the first lines in the above update scheme apply.

By virtue of the above update scheme, Eq. (12), "regulatory factors" are continuously distributed across each cell's domain $\mathcal{D}^{(\alpha)}$ as the current MCS progresses. At the end of each MCS, the accumulated (local) values of $\mathfrak{m}(\mathbf{x}_n)$ are used to update the local values of the cytoskelatal fields $\rho(\mathbf{x}_n)$ inside each cell $\alpha \geq 0$ ($\mathbf{x}_n \in \mathcal{D}^{(\alpha)}$): We assume that for positive values, $\mathfrak{m} > 0$, there is assembly of cytoskeletal structures and ρ is increased by an amount proportional to the distance of ρ from its upper bound Q:

$$\rho(\mathbf{x}_n, t + \Delta t) = \rho(\mathbf{x}_n, t) + \mathfrak{t}\,[Q - \rho(\mathbf{x}_n, t)]. \tag{13a}$$

Thereby Q is a fixed point of this map and limits the build-up of cytoskeletal structures. In contrast, for negative values, $\mathfrak{m}(\mathbf{x}_n) \leq 0$, disassembly prevails, and we assume that ρ then tends towards its lower bound q:

$$\rho(\mathbf{x}_n, t + \Delta t) = \rho(\mathbf{x}_n, t) + \mathfrak{t}\,[q - \rho(\mathbf{x}_n, t)]. \tag{13b}$$

The parameter $\mathfrak{t}$ signifies the rate at which cytoskeletal structures respond to the regulatory factors $\mathfrak{m}$. To obtain meaningful results, the time scale of the cytoskelatal field to traverse the interval $[q, Q]$ should be comparable to the time it takes a simulated cell to travel one cell diameter. For the parameters and cell sizes used in this work ($q, Q = \mathcal{O}(100)$; each cell occupying ~ 1000 grid sites) we set $\mathfrak{t} = 0.1$.

After this update procedure for $\rho(\mathbf{x}_n, t)$ is completed, all regulatory factors are reset, $\mathfrak{m}(\mathbf{x}_n) = 0,\ \forall n$. This prevents "spurious memory effects" which may arise once the cell's rear reaches its initial leading edge position as time goes on. In essence, resetting regulatory factors upon completion of one MCS implies that the diffusion-degradation dynamics, underlying the distribution of regulatory factors, is fast on the scale of one MCS.

We emphasize that the cytoskelatal field $\rho(\mathbf{x}_n)$ is defined only for grid sites $\mathbf{x}_n \in \mathcal{D}^{(\alpha)}$ occupied by an actual cell ($\alpha \geq 0$). To allow for spatial variations of substrate properties, we therefore introduce a second scalar field variable $\varphi(\mathbf{x}_n)$, which is defined on the entire computational grid. The scalar field $\varphi(\mathbf{x}_n)$ is taken to measure the local density of anchoring points, a cell might use to form focal adhesions. Although one might consider to treat φ as a time-dependent field variable, in this work φ is used to implement static substrate patterns, only. The field $\varphi(\mathbf{x}_n)$ is thus initialized once at the beginning of the simulation and kept fixed throughout the entire simulation.

Having introduced the fields $\rho(\mathbf{x}_n)$ and $\varphi(\mathbf{x}_n)$, we now discuss their impact on the system's dynamics by giving their contribution to the goal function $p(\mathcal{T})$. Assume that the elementary event $\mathcal{T}$ is attempted by a source cell α at source grid site $\mathbf{x}_s \in \mathcal{B}^{(\alpha)}$. Further, let denote $\mathbf{x}_t$ the target grid site and β denote the index of the target cell (where as ususal $\beta \geq 0$ indicates that $\mathbf{x}_t$ is occupied by an actual cell, $\beta < 0$ means $\mathbf{x}_t$ exposes substrate). We then define the *"polarization energy"* $\Delta\mathcal{H}_p(\mathcal{T})$ as follows:

$$\Delta\mathcal{H}_p(\mathcal{T}) \equiv \begin{cases} \rho(\mathbf{x}_t) - \rho(\mathbf{x}_s), & \mathcal{T} \mathrel{\widehat{=}} \mathcal{T}_{\text{pro}} \wedge \beta \geq 0, \\ \rho(\mathbf{x}_s) - \rho(\mathbf{x}_t), & \mathcal{T} \mathrel{\widehat{=}} \mathcal{T}_{\text{ret}} \wedge \beta \geq 0, \\ -\big[\rho(\mathbf{x}_s) + \varphi(\mathbf{x}_t)\big], & \mathcal{T} \mathrel{\widehat{=}} \mathcal{T}_{\text{pro}} \wedge \beta < 0, \\ \rho(\mathbf{x}_s) + \varphi(\mathbf{x}_t), & \mathcal{T} \mathrel{\widehat{=}} \mathcal{T}_{\text{ret}} \wedge \beta < 0, \end{cases} \tag{14a}$$

where the characteristic "energy scale" for $\Delta\mathcal{H}_p$ is set by the polarization bounds q and Q. In the above equation, the last two rows reflect the anchoring properties of focal adhesions, whose strength is taken to be measured by the sum $\rho+\varphi$. Note, in particular, that the first two rows can be obtained from a combined evaluation of the lower two rows. For example, if cell α annexes $\mathbf{x}_t$ starting from $\mathbf{x}_t$, two things need to happen: First, focal adhesions formed by cell β must be broken, implying a contribution $\Delta\mathcal{H}_p = \rho(\mathbf{x}_t) + \varphi(\mathbf{x}_t)$ by virtue of line 4. Secondly, new focal adhesions are formed by cell α, implying a contribution $\Delta\mathcal{H}_p = -\left[\rho(\mathbf{x}_s) + \varphi(\mathbf{x}_t)\right]$ by virtue of line 3. Taking the sum of both contributions gives the expression in line 1. An analogous line of arguments leads to the expression in line 2. The contribution to the goal function $p(\mathcal{T})$ due to the *polarization energy* $\Delta\mathcal{H}_p(\mathcal{T})$ is then defined by

$$p_{\text{cyto}}(\mathcal{T}) \equiv \exp\big[-\Delta\mathcal{H}_p(\mathcal{T})\big]. \tag{14b}$$

3. *Cell adhesion*

To implement the ability of cells to establish cell adhesions across cell-cell interfaces, we use a special form for the respective contribution to the goal function p, which is designed to distinguish between the formation of new and the breakage of existing cell-cell adhesion sites.

To this end, we define *adhesion matrices* $A_{\alpha,\beta}$ and $B_{\alpha,\beta}$ quantifying the system's change in "energy" upon forming a new contact between cells α and β [$A_{\alpha,\beta}$] and upon breaking a pre-existing contact between those cells by an "intruder cell" $\gamma \neq \alpha, \beta$ [$B_{\alpha,\beta}$]. In our computational model, we assume that formation of new cell-cell contacts is energetically favored, and that breaking of pre-existing

contacts by intruder cells is energetically penalized. The matrix entires of $A_{\alpha,\beta}$ and $B_{\alpha,\beta}$, therefore, have a definite sign, which we take to be positive. The ordering of the cell index pair of $A_{\alpha,\beta}$ and $B_{\alpha,\beta}$ is of no physical significance, i.e. the adhesion matrices are symmetric. We also assume that a given cell α does not interact with itself, such that the diagonal elements of the adhesion matrices vanish. Finally, there is no adhesion between cells and empty substrate sites, such that all matrix elements containing a negative cell index vanish. In summary, the adhesion matrices $A_{\alpha,\beta}$ and $B_{\alpha,\beta}$ exhibit the following properties:

$$A_{\alpha,\beta} = A_{\beta,\alpha} \geq 0, \tag{15a}$$
$$B_{\alpha,\beta} = B_{\beta,\alpha} \geq 0, \tag{15b}$$
$$A_{\alpha,\alpha} = B_{\alpha,\alpha} = 0, \tag{15c}$$
$$A_{\alpha,\beta} = B_{\alpha,\beta} = 0, \qquad \text{if } \alpha < 0 \vee \beta < 0. \tag{15d}$$

In addition, we assume that the energy cost associated with the breakage of a given cell-cell contact exceeds the energetic benefit of its initial formation, i.e.

$$B_{\alpha,\beta} \geq A_{\alpha,\beta}, \tag{15e}$$

where equality of both quantities would reproduce the assumption underlying the standard cellular Potts model [1, 2]. We shall refer to this property as the "dissipative nature of cell-cell adhesion".

To implement the effects of cell-cell adhesion, we compute the "energy difference" $\Delta\mathcal{H}_a(\mathcal{T})$ for any given elementary event $\mathcal{T}$ according to the scheme illustrated in Fig. 3. One has to distinguish between *protrusion* and *retraction* events. First, say that a cell α attempts a protrusion event $\mathcal{T}_{\rm pro}$, involving the source grid site $\mathbf{x}_s \in \mathcal{B}^{(\alpha)}$ and the target grid site $\mathbf{x}_t \in \mathcal{B}^{(\beta)}$, as illustrated in Fig. 3A. In this case, cell α acts as intruder cell, since the depicted protrusion event affects three pre-existing contacts between the target cells β and a "third party" cell γ. Acceptance of the depicted protrusion event would have the following energetically relevant effects: (i) All pre-existing contacts between the target cell β and third party cell $\gamma \neq \alpha, \beta$ at the target grid site $\mathbf{x}_t$ are torn apart. (ii) New contacts between the source cell α and third party cell $\gamma \neq \alpha, \beta$ are being established. (iii) The length of the cell contact line between source cell α and target cell β is changed. Altogether, these three effects lead to the following cell adhesion energy difference,

$$\begin{aligned}\Delta\mathcal{H}_a(\mathcal{T}_{\rm pro}) \equiv &- \sum_{\mathbf{x}_j \in \mathcal{N}_t} \left[A_{\alpha,c(\mathbf{x}_j)} - \delta_{\alpha,c(\mathbf{x}_j)}\, A_{\alpha,\beta}\right] \\ &+ \sum_{\mathbf{x}_j \in \mathcal{N}_t} B_{\beta,c(\mathbf{x}_j)}(1 - \delta_{\alpha,c(\mathbf{x}_j)}).\end{aligned} \tag{16a}$$

The first term in this expression accounts for the (energetically favored) formation of new cellular contacts, as well as for the remodeling of the interface between source cell α and target cell β [points (ii) and (iii)]. The second term measures the (energetically penalized) breaking of pre-existing cell contacts [point (i)] and, therefore, impedes cell α's ability to intrude. Conversely, if source cell α attempts a retraction event $\mathcal{T}_{\rm ret}$, the same reasoning leading to Eq. (16a) applies, only this time the elementary event proceeds in reverse, i.e. from the target site $\mathbf{x}_t$ to the source site $\mathbf{x}_s$; cf. Fig. 3A:

$$\begin{aligned}\Delta\mathcal{H}_a(\mathcal{T}_{\rm ret}) \equiv &- \sum_{\mathbf{x}_j \in \mathcal{N}_s} \left[A_{\beta,c(\mathbf{x}_j)} - \delta_{\beta,c(\mathbf{x}_j)}\, A_{\alpha,\beta}\right] \\ &+ \sum_{\mathbf{x}_j \in \mathcal{N}_s} B_{\alpha,c(\mathbf{x}_j)}(1 - \delta_{\beta,c(\mathbf{x}_j)}).\end{aligned} \tag{16b}$$

We may now use Eqs. (16)(a,b) to illustrate the "dissipative nature" of adhesive interactions by means of two archetypical examples. First, consider the adhesive energy contribution to any cyclic process. By a cyclic process we mean a sequence of two mutually inverse elementary events, e.g. a protrusion event $\mathcal{T}_{\rm pro}$, which is immediately followed by its inverse retraction event $\mathcal{T}_{\rm ret}$, such that the system's final configuration is identical to its initial configuration. Using Eqs. (16) we find for the total adhesive energy contribution to a cyclic process:

$$\Delta\mathcal{H}_a^{(\rm cycl)} = \sum_{\mathbf{x}_j \in \mathcal{N}_t \setminus \left(\mathcal{D}^{(\alpha)} \cup \mathcal{D}^{(\beta)}\right)} \left[\Delta_{\alpha,c(\mathbf{x}_j)} + \Delta_{\beta,c(\mathbf{x}_j)}\right] \geq 0, \tag{17}$$

$$\Delta_{\alpha,\beta} := B_{\alpha,\beta} - A_{\alpha,\beta} \geq 0 \quad \text{[Eq. (15e)]}, \tag{18}$$

where $\mathcal{N}_t$ denotes the neighborhood of the grid site which temporarily changes its cell index, and where α and β are the indices of the source and target cells involved in the cyclic process; cf. Fig. 3A. Since $\Delta_{\alpha,\beta} \geq 0$, the above adhesive energy contribution is non-negative, thus leading to an amount of energy equal to $\Delta\mathcal{H}_a^{(\rm cycl)}$ being dissipated as the cyclic process completes. This leads us to refer to the parameter matrix $\Delta_{\alpha,\beta}$ as *"dissipation matrix"*. Second, consider two (infinitely extended) rows of cells in adhesive contact, sliding past each other. This situation is depicted in Fig. 3B, where the top row of cells moves (as a whole) to the right by one grid site, while the bottom row of cells remains stationary. To assess the adhesive energy contribution along the contact line connecting both cell rows, note that the depicted transformation can be implemented by letting each cell in the top row protrude its leading (i.e. right) edge by one grid site. For each protruding (source) cell α, this transformation entails to the following energetic effects (cf. discussion above): (i) Two of the pre-existing cell-cell contacts between the source cell's right neighbor in the top row (target cell β) and the corresponding cell in the bottom row (third party cell γ) get torn apart, leading to an energetic contribution $2\,B_{\beta,\gamma}$. (ii) In return, two new contacts between the protruding (source) cell α and cell γ are being established, leading to a contribution $-2\,A_{\alpha,\gamma}$. (iii) Since the length of the contact line between cells in the top row (i.e. between protruding source cell α and retracting target cell β) remain unchanged, there's no further energetic contribution due to adhesive contacts

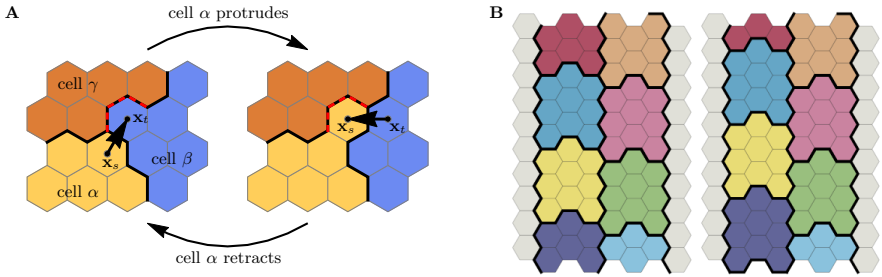

FIG. 3: Cell-cell adhesion. **A)** Adhesive energy contribution in a cyclic process, where a protrusion of source cell α against target cell β is followed by the inverse retraction event. Both events involve a third party cell γ, leading to net energy dissipation after the cyclic process has been completed. *Protrusion:* (i) Three pre-existing cell-cell contacts between β and γ are torn apart (red dashed contacts); (ii) three new contacts between α and γ are formed; (iii) the contact length between source cell α and target cell β increases by one unit of length. This implies $\Delta\mathcal{H}_a(\mathcal{T}_{\rm pro}) = 3B_{\beta,\gamma} - 3A_{\alpha,\gamma} - A_{\alpha,\beta}$. *Retraction:* (i) Three pre-existing cell-cell contacts between α and γ are torn apart (red dashed contacts); (ii) three new contacts between β and γ are formed; (iii) the contact length between source cell α and target cell β decreases by one unit of length. This implies $\Delta\mathcal{H}_a(\mathcal{T}_{\rm ret}) = 3B_{\alpha,\gamma} - 3A_{\beta,\gamma} + A_{\alpha,\beta}$. Altogether, this leads to $\Delta\mathcal{H}_a^{(\rm cycl)} = \Delta\mathcal{H}_a(\mathcal{T}_{\rm pro}) + \Delta\mathcal{H}_a(\mathcal{T}_{\rm ret}) = 3\Delta_{\alpha,\gamma} + 3\Delta_{\beta,\gamma} \geq 0$, i.e. a (non-negative) dissipative contribution, whose magnitude depends on the dissipation matrix $\Delta_{\alpha,\beta} = B_{\alpha,\beta} - A_{\alpha,\beta} \geq 0$.
B) Shear viscosity due to cell-cell adhesion. Consider two rows of adhesive cells sliding past each other as indicated in the figure (left row of cells moves up by one gird site; colors indicate different cells). The associated adhesion energy (per cell) reads $\Delta\mathcal{H}_a/n_c = 2\,(B - A) \geq 0$, where n_c denotes the number of cells sliding past each other, and where we assumed cells of like type, i.e. $A_{\alpha,\beta} \equiv A$ and $B_{\alpha,\beta} \equiv B$ ($\alpha \neq \beta$). The condition $B > A$, Eq. (15e), thus implies positive friction associated with cellular shear flows, whose magnitude is proportional to the number of cells sliding past each other. Note that this shear viscosity vanishes for $A = B$, i.e. for zero dissipation matrix.

between cells in the top row. Assuming that all cells in the system are of equal types, we write $A_{\alpha,\beta} \equiv A$ and $B_{\alpha,\beta} \equiv B$ ($\alpha \neq \beta$) and, therefore, find

$$\Delta\mathcal{H}_a^{(\rm visc)} = 2(B - A) \equiv 2\Delta \geq 0, \tag{19}$$

i.e. a non-negative dissipative contribution per cell. The size of the dissipation parameter Δ thus introduces a natural means to tune the system's *shear viscosity*.

With the above definitions of the adhesive energy changes, Eqs. (16), we define the contribution of cell adhesion to the goal function $p(\mathcal{T})$ as follows:

$$p_{\text{cell-adhesion}}(\mathcal{T}) \equiv \exp\big[-\Delta\mathcal{H}_a(\mathcal{T})\big]. \tag{20}$$

4. *Rupture of cell contacts*

By now, we have introduced all components making up the total acceptance probability $p(\mathcal{T})$, Eq. (9). To conclude our discussions concerning the implementation of cellular traits, we highlight one additional aspect of elementary events. So far, the notion of an elementary event can be summarized as follows: Once source and target grid sites, $\mathbf{x}_s$ and $\mathbf{x}_t$, have been selected, acceptance of a protrusion [retraction] event causes (among other things like the distribution of regulatory factors) the cell index to be copied from $\mathbf{x}_s$ to $\mathbf{x}_t$ [from $\mathbf{x}_t$ to $\mathbf{x}_s$]. In other words, the domain $\mathcal{D}^{(\alpha)}$ of source cell α annexes $\mathbf{x}_t$ [loses $\mathbf{x}_s$], while the domain $\mathcal{D}^{(\beta)}$ of source cell β is forced to let go $\mathbf{x}_t$ [accommodate $\mathbf{x}_s$]. However, if both, source and target cells are actual cells, i.e. $\alpha, \beta \geq 0$, and if the source cell attempts a retraction event, there is one additional possible outcome: If cell cohesion is weak, the pulling force exerted by the retracting source cell α on its neighboring cells might also result in rupture of all pre-existing contacts between the retracting source cell and its neighboring cells at $\mathbf{x}_s$, rather than forcing one of its neighboring cells (the target cell) to fill the void created at $\mathbf{x}_s$ once α retracts; cf. rupture event depicted in Fig. 2. To test for the occurrence of cell rupture, the total energetic cost of each attempted retraction event between two actual cells is evaluated under two different assumptions: First, we assume that the pulling force exerted by the retracting source cell α on target cell β is strong enough to force β to fill the void created at $\mathbf{x}_s$ (i.e. to accommodate $\mathbf{x}_s$), and call this a regular retraction event $\mathcal{T}_{\rm ret}$. Secondly, we assume that the retraction of source cell α causes all pre-existing cell-cell contacts of cell α at $\mathbf{x}_s$ to rupture, leaving a free substrate site at $\mathbf{x}_s$ after the retraction event has been accepted. This latter event will be referred to as rupture event $\mathcal{T}_{\rm rup}$. We then

compute the total energy differences

$$\Delta\mathcal{H}(\mathcal{T}_{\rm ret}) = \Delta\mathcal{H}_{\rm el}(\mathcal{T}_{\rm ret}) + \Delta\mathcal{H}_{p}(\mathcal{T}_{\rm ret}) + \Delta\mathcal{H}_{a}(\mathcal{T}_{\rm ret})$$

and

$$\Delta\mathcal{H}(\mathcal{T}_{\rm rup}) = \Delta\mathcal{H}_{\rm el}(\mathcal{T}_{\rm rup}) + \Delta\mathcal{H}_{p}(\mathcal{T}_{\rm rup}) + \Delta\mathcal{H}_{a}(\mathcal{T}_{\rm rup})$$

under both assumptions[3] and compare the respective outcomes. Then, if the rupture event is energetically favored over the regular retraction event, i.e. $\Delta\mathcal{H}(\mathcal{T}_{\rm rup}) < \Delta\mathcal{H}(\mathcal{T}_{\rm ret})$, cohesion between cells is weak. In this case, the rupture event $\mathcal{T}_{\rm rup}$, rather than the regular retraction event $\mathcal{T}_{\rm ret}$ will be attempted. Otherwise, cohesion is strong and a regular retraction event $\mathcal{T}_{\rm ret}$ will be attempted.

E. Cell domain update routine

Having discussed the implementation concerning the two basic types of elementary events, viz. protrusion events $\mathcal{T}_{\rm pro}$ and retraction events $\mathcal{T}_{\rm ret}$, as well as the two subtypes of regular retraction events and rupture events $\mathcal{T}_{\rm rup}$, we can now summarize the cell domain update routine, point 3.F in section I C 2. To this end, and in accordance with our previous notation, we use the cell indices α and β to denote source and target cell, and $\mathbf{x}_s$ and $\mathbf{x}_t$ to denote source and target grid site. Moreover, equal signs "=" in the following listing are to be interpreted as assignment operators, where the value of the variable on the left hand side of the operator is assigned to the value of the variable on the right hand side. With these preliminary remarks in mind, the cell update routine can be summarized as follows:

- If the accepted elementary event is a protrusion event:
  1. Set $\rho(\mathbf{x}_t) = \rho(\mathbf{x}_s)$ and $\mathfrak{m}(\mathbf{x}_t) = \mathfrak{m}(\mathbf{x}_s)$.
  2. Set $\mathcal{D}^{(\alpha)} \to \mathcal{D}^{(\alpha)} \cup \{\mathbf{x}_t\}$.
  3. Set $\mathcal{D}^{(\beta)} \to \mathcal{D}^{(\beta)} \setminus \{\mathbf{x}_t\}$.
  4. Distribute regulatory factors according to Eq. (12a).
- If the accepted elementary event is a regular retraction event:
  1. Set $\rho(\mathbf{x}_s) = \rho(\mathbf{x}_t)$ and $\mathfrak{m}(\mathbf{x}_s) = \mathfrak{m}(\mathbf{x}_t)$.
  2. Set $\mathcal{D}^{(\alpha)} \to \mathcal{D}^{(\alpha)} \setminus \{\mathbf{x}_s\}$
  3. Set $\mathcal{D}^{(\beta)} \to \mathcal{D}^{(\beta)} \cup \{\mathbf{x}_s\}$
  4. Distribute regulatory factors according to Eq. (12b).
- If the accepted elementary event is a rupture event:
  1. Set $\rho(\mathbf{x}_s) = 0$ and $\mathfrak{m}(\mathbf{x}_s) = 0$.
  2. Set $\mathcal{D}^{(\alpha)} \to \mathcal{D}^{(\alpha)} \setminus \{\mathbf{x}_s\}$
  3. Distribute regulatory factors according to Eq. (12c).

F. Cell proliferation and mitosis

While cell proliferation and mitosis play no role in the experimental setup of rotating cell clusters, cell growth and division are observed experimentally in a setup where a sheet of cells expands into free space after removal of a stencil. Therefore it is essential to include proliferation of cells in the numerical model. How this is done is described in the following section.

For the given value of the upper bound for cell polarizability Q_0 and the number of anchorage sites of the underlying substrate (represented by ρ_s) there exists an equilibrium size (area) a single cell can reach on this substrate. This size is the equilibrium point at which the perimeter and area constraints balance with the focal adhesion term. It can be measured numerically by fixing $\rho = Q_0$ for the entire domain of the cell and waiting until the cell area ceases to change. This maximal size is referred to as $A_{\rm ref}$.

In a simulation including proliferation of cells, several additional steps take place:
Before the simulation is started, $A_{\rm ref}$ is measured for the specified parameters as described above.
A state variable $s^{(\alpha)}$ is assigned to each cell α. $s = 0$ indicates the non-growing state, $s = 1$ indicates the growing state.
At the start of the simulation, all cells are in the non-growing state $s^{(\alpha)}(t = 0) = 0$ and start with $Q^{(\alpha)}(t = 0) = Q_0$.
The lower bound for cell polarizability q is kept fixed. The difference $Q_0 - q$ can therefore be interpreted as the range over which the density of cytosceletal elements may vary in a non-proliferating cell.

At each time step t, the following updates are performed on the cell state and the polarizability of each cell α:

- If $s^{(\alpha)}(t) = 0$ and $A^{(\alpha)}(t) > rA_{\rm ref}$ for a fixed parameter r, the cell enters the growing state: $s^{(\alpha)}(t+1) = 1$. A typical parameter choice is $r \lesssim 1$.

  This area constraint models the contact inhibition of cell proliferation [14, 15]. When the tissue reaches a state where each cell has formed adhesive contacts with the substrate and is completely surrounded by neighbours, the cells stop proliferating. In addition it has been proposed that the pressure or local density in the tissue has a negative impact

[3] The energy difference associated with accepting $\mathcal{T}_{\rm rup}$ can be computed by standard means, simply using the substrate $\beta = -1$ as new target cell.

on the local growth rate [16, 17]. These phenomena could alternatively be captured in the model by introducing a direct dependence of cell growth on the local cell density or on the membrane length which is in contact with neighbour cells. However, the use of a critical cell size is numerically advantageous and produces similar effects, since the area of a cell depends mainly on the tissue pressure.

More specifically, cells living in a densely packed environment will not exceed the area threshold rA_{ref} due to the pressure exerted on them by neighboring cells and can therefore not grow. Conversely, cells exposed to free space are more likely to reach this threshold and proliferate.

- If $s^{(\alpha)}(t) = 1$, the upper bound for cell polarizability is increased with a given probability p_g:

$$Q^{(\alpha)}(t+1) = Q^{(\alpha)}(t) + g\,Q_0. \tag{21}$$

With probability $1-p_g$ the value of Q is unchanged. While the product $p_g \cdot g$ fixes the average growth speed, p_g determines the level of stochastic fluctuations in the growth process.

As long as the substrate is homogeneous with respect to the density of anchorage sites, it is equivalent to either reduce the area coupling constant a_α or to increase the average cell polarization $[Q^{(\alpha)} + q^{(\alpha)}]/2$ in order to simulate cell growth. We here choose the second method. Keeping the lower bound for cell polarizability constant during cell growth leads to an increasing persistence of cellular motion with increasing size. This choice is based on the natural assumption that the cytosceletal density may vary stronger across a cell if its body is larger (I don't know any references which would support this assumption). A reorganisation of structural elements therefore takes more time and makes the direction of cell migration less flexible.

- If $Q^{(\alpha)}(t) \geq 3Q_0$, cell α divides into the two descendant cells α and β. Even though there exists experimental evidence that the orientation of the cleavage plane along which cells divide depends on local cell geometry and possibly the direction of stress in a tissue [13] (also add references therein on pages 97-100, maybe Lynch1997, but it deals with plant development), we here pursue the most general approach to choose the axis along which the cell divides in a random direction through the geometric center of the mitotic cell. By disregarding any mechanisms which propose a preferential direction for the division axis, we ensure that the observed features in a simulation do not depend on such effects. In case of irregular cell shapes a separation of the cellular domain into more than 2 connected components can occur. To prevent violation of topological constraints, in this case the two largest components are considered as descendant cells and the residual pixels are replaced by substrate pixels.
After mitosis the state variables and polarization bounds are reset: $Q^{(\alpha)}(t+1) = Q^{(\beta)}(t+1) = Q_0$, $s^{(\alpha)}(t+1) = s^{(\beta)}(t+1) = 0$. To ensure that the polarization field ρ relaxes to the range $[q, Q_0]$, the cell state may not change in the next T_r time steps: $s^{(\alpha)}(t') = s^{(\beta)}(t') = 0$ for $t' \in [t+1, t+T_r]$.

G. Numerical computation of stress in a tissue

In the section describing the numerical results on tissue expansion, the stress distribution in the tissue is shown in the kymographs Figs. 6(C,F). Hereafter is explained how the stress tensor for each cell in the tissue can be computed from the forces acting on the cell's membrane pixels in the monte carlo simulation. The mean value of the stress tensor in a deformed body can be calculated numerically from the formula

$$\bar{\sigma}_{ij}^{(\alpha)} = \frac{\mathfrak{l}}{2A^{(\alpha)}} \sum_{\mathbf{x}_k \in \mathcal{B}^{(\alpha)}} \left(f_k^i x_k'^j + f_k^j x_k'^i \right), \tag{22}$$

which is a discretized version of the surface integral in (cite landau lifshitz). Here $\mathbf{f_k}$ is the force acting on the membrane element $\mathbf{x_k}$ of cell α, $\mathbf{x'_k} = \mathbf{x_k} - \mathbf{x}_{\mathrm{com}}^{(\alpha)}$ is the position of the element with respect to the center of mass $\mathbf{x}_{\mathrm{com}}^{(\alpha)}$ of the cell, and the superscripts i and j are Cartesian indices. The forces $\mathbf{f_k}$ can be computed from the energy differences of all possible protrusion and retraction events originating from $\mathbf{x}_k$,

$$\begin{aligned} \mathbf{f_k} = &- \sum_{\mathbf{x}_l \in \mathcal{N}_k} \frac{\Delta\mathcal{H}(\mathcal{T}_{\mathrm{pro}})}{\|\mathbf{x_l} - \mathbf{x_k}\|} \frac{\mathbf{x_l} - \mathbf{x_k}}{\|\mathbf{x_l} - \mathbf{x_k}\|} \\ &- {\sum_{\mathbf{x}_l \in \mathcal{N}_k}}' \frac{\Delta\mathcal{H}(\mathcal{T}_{\mathrm{ret}})}{\|\mathbf{x_k} - \mathbf{x_l}\|} \frac{\mathbf{x_k} - \mathbf{x_l}}{\|\mathbf{x_k} - \mathbf{x_l}\|}, \end{aligned} \tag{23}$$

where ${\sum}'_{\mathbf{x}_l}$ indicates a sum only over substrate pixels, i.e. pixels with $c(\mathbf{x}_l) < 0$, and where $\Delta\mathcal{H} \equiv \mathcal{H}_{\mathrm{cont}} + \mathcal{H}_a + \mathcal{H}_p$.

[1] J. A. Glazier, F. Graner (1993) *S*imulation of the differential adhesion driven rearrangement of biological cells, Phys. Rev. E 47:2128–2154.

[2] F. Graner, J. A. Glazier (1993) *S*imulation of biologi-

cal cell sorting using a two-dimensional extended Potts model, Phys. Rev. Lett. 69:2013–2016.

[3] A. F. M. Marée, A. Jilkine, A. Dawes, V. A. Grieneisen, L. Edelstein-Keshet (2006) *P*olarization and movement of keratocytes: A multiscale modelling approach, Bull. Math. Biol. 68:1169–1211.

[4] A. F. M. Marée, V. A. Grieneisen, L. Edelstein-Keshet (2012) *H*ow cells integrate complex stimuli: the effect of feedback from phosphoinositides and cell shape on cell polarization and motility, PLoS Comput. Biol. 8:e1002402.

[5] T. D. Pollard, G. G. Borisy (2003) *C*ellular motility driven by assembly and disassembly of actin filaments, Cell 112:453–465.

[6] E. M. Kovacs, M. Goodwin, R. G. Ali, A. D. Paterson, A. S. Yap (2002) *C*adherin-Directed Actin Assembly: E-Cadherin Physically Associates with the Arp2/3 Complex to Direct Actin Assembly in Nascent Adhesive Contacts, Curr. Biol. 12:379–382.

[7] D. E. Leckband, Q. le Duc, N. Wang, J. de Rooij (2011) *M*echanotransduction at cadherin-mediated adhesions, Curr. Opin. Cell Biol. 23:523–530.

[8] A. Mogilner (2009) *M*athematics of cell motility: have we got its number?, J. Math. Biol. 58:105-134.

[9] B. Alberts, A. Johnson, J. Lewis, M. Raff, K. Roberts, P. Walter (2008) *M*olecular Biology of the Cell, (Garland Science, New York).

[10] P. Friedl (2004) *P*respecification and plasticity: shifting mechanisms of cell migration, Curr. Opin. Cell Biol. 16:14–23.

[11] N. B. Ouchi, J. A. Glazier, J.-P. Rieu, A. Upadhyaya, Y. Sawada, Y (2003) *I*mproving the realism of the cellular Potts model in simulations of biological cells, Physica A 329:451–458.

[12] D. Raucher, M. P. Sheetz (2000) *C*ell spreading and lamellipodial extension rate is regulated by membrane tension, J. Cell Biol. 148:127–136.

[13] W. T. Gibson, M. C. Gibson (2009) *C*ell topology, geometry, and morphogenesis in proliferating epithelia, Curr. Top. Dev. Biol. 89:87–114.

[14] J. F. Li, J. Lowengrub (2014) *T*he effects of cell compressibility, motility and contact inhibition on the growth of tumor cell clusters using the Cellular Potts Model., J. Theor. Biol. 343:79–91.

[15] B. Alberts, A. Johnson, J. Lewis, D. Morgan, M. Raff, K. Roberts, P. Walter (2014) *M*olecular Biology of the Cell, (Garland Science, New York).

[16] B. I. Shraiman (2005) *M*echanical feedback as a possible regulator of tissue growth, Proc. Natl Acad. Sci. U.S.A. 102:3318–3323.

[17] J. Ranft, M. Basan, J. Elgeti, J.-F. Joanny, J. Prost, F. Jülicher (2010) *F*luidization of tissues by cell division and apoptosis, Proc. Natl Acad. Sci. U.S.A. 107:20863–20868.

"Cell Number and Local Arrangement Affect Collective Rotation on Micropatterns" Supplemental Information

Felix J. Segerer,[1] Florian Thüroff,[2] Alicia Piera Alberola,[1] Erwin Frey,[2] and Joachim O. Rädler[1]

[1] *Faculty of Physics and Center for NanoScience, Ludwig-Maximilans-Universität München, Geschwister-Scholl-Platz 1, D-80539 Munich, Germany*

[2] *Arnold-Sommerfeld-Center for Theoretical Physics and Center for NanoScience, Faculty of Physics, Ludwig-Maximilians-Universität München, Theresienstrasse 37, D-80333 Munich, Germany*

S1. EVALUATION AND DISTRIBUTION OF NORMALIZED ANGULAR VELOCITIES

In the main text we briefly described the calculation of the smoothed total angular velocity $\Omega_N(t)$ from the individual angular positions $\varphi_i(t)$ with respect to a initial position at $t = 0$ of each nucleus $i \in \{1...N\}$ within a pattern. In this section we want to show the calculations in more detail. From the individual cell positions $\mathbf{r}_i(t)$, the center of mass of a system is calculated as $\mathbf{r}_{CM} = \langle\langle \mathbf{r}_i(t)\rangle_t\rangle_N$, where $\langle\rangle_t$ and $\langle\rangle_N$ indicate the mean over the observation time and all cells within a pattern respectively. From the angular shifts $\Delta\varphi_i(t)$ between two successive frames, the angular position at time t is calculated as $\varphi_i(t) = \sum_{\tau=0}^{t} \Delta\varphi_i(\tau)$ for each cell. Here, $t = 0$ indicates the start of the observation. Note that due to the time lapse resolution of one frame per 10 min, time is a discrete quantity in our analysis. A direct crossing of the origin location $\mathbf{r}_{CM}$ leads to artifacts in the rotation angle $\varphi_i(t)$. This can for example be seen for the cyan colored cell in Fig. 2(a) and (b) at around 1600 min. The pronounced peak at around 1600 min results from a direct transition of the rotation axis. For this reason, the cell closest to $\mathbf{r}_{CM}$ is dynamically excluded when calculating Ω_N according to Eq. 1. This calculation is conducted for an overall sample size of over 600 systems distributed among the system sizes according to Table S1. Finally, we normalize the distribution of Ω_N according to $\xi_N(t) = \left|\Omega(t)/\bar{\Omega}_N\right|$. Here, $\bar{\Omega}_N$ denotes the peak position corresponding to CAMo in $P(|\Omega_N|)$(Fig. 2(c)). The distribution of ξ_N for different numbers of cells within the pattern is shown in Fig. S1.

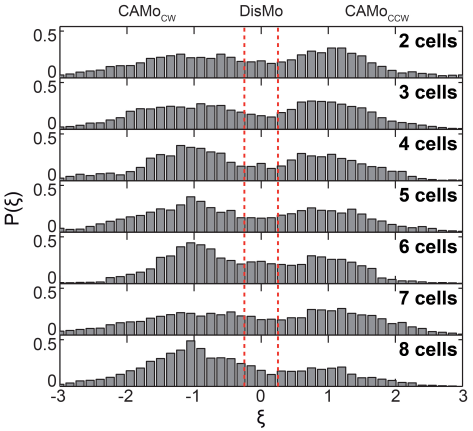

FIG. S1. Probability distribution of the normalized angular velocity $\xi_N(t)$ for different cell numbers N.

TABLE S1. Number of analyzed systems for different cell numbers

Cells per system	2 cells	3 cells	4 cells	5 cells	6 cells	7 cells	8 cells
Number of analyzed systems	124	115	95	89	64	63	56

S2. ALTERNATIVE DISMO-CAMO CLASSIFICATION SCHEME

In order to check if if our observations are robust to different data analysis approaches, we also test an alternative way [1] to discriminate collective behavior from disordered motion than that described in the main text. This alternative approach is only based on an analysis of the correlation of cell orientation and is therefore independent of the individual cell velocities. For each cell i, we introduce a cell orientation γ_i which is defined as the smaller angle between the moving vector of a nucleus in two successive frames and a line from the system center to the position of the nucleus in the first frame (Fig. S2(a)). For clockwise rotation γ_i is defined negative whereas for counterclockwise rotation γ_i is defined as a positive angle. The overall alignment of motion is calculated for each time step as

$$\Gamma_N(t) = \frac{2}{\pi \cdot N} \sum_{i=1}^{N} \gamma_i(t), \tag{S1}$$

where N denotes the number of cells within the pattern. Defined like this, a value of $\Gamma(t) = \pm 1$ would correspond to a perfect circular alignment of the motion of all cells within a pattern, whereas $\Gamma(t) = 0$ would correspond to no alignment in azimuthal direction or no motion at all. The distribution $P(\Gamma_N)$ shows a clear bimodal character consisting of states corresponding to clockwise and counterclockwise rotation as it can be seen in Fig. S2(c). We define a threshold of $\Gamma_c = \pm 0.3$ where a state of $|\Gamma_N(t)| < |\Gamma_c|$ a migration state is classified as DisMo and for $|\Gamma_N(t)| \geq |\Gamma_c|$ as CAMo respectively. Note that the choice of $\Gamma_c = \pm 0.3$ is heuristically estimated from the distribution $P(\Gamma)$ (Fig. S2(c)). A choice of $\Gamma_c = \pm 0.2$ and $\Gamma_c = \pm 0.4$, respectively, had only little influence on the results though (data not shown). A typical time course of $\Gamma_N(t)$ for a system consisting of seven cells is shown in Fig. S2(b). It can be seen that the classification via Γ_N results in very similar intervals of CAMo and DisMo as the method via ξ_N. Also the survival frequencies of Γ_N exhibit an exponential distribution (data not shown). For the dependence of the mean persistence time τ_Γ on the cell number N we find the same characteristics as for the mean persistence time τ_ξ calculated via ξ_N (Fig. S1(c)).

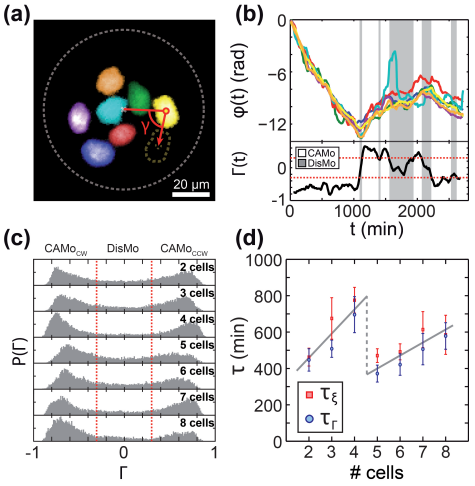

FIG. S2. (a) False-colored fluorescence image of the nuclei of seven cells confined in a circular micro-pattern. We define γ_i as the smaller angle between the moving vector of a nucleus in two successive frames and a line from the system center to the position of the nucleus in the first frame. (b) Angular positions $\varphi_i(t)$ of each cell (marked in color of the corresponding nuclei in (a)) and the average orientation Γ_N (Eq. S1). The classification threshold of $\Gamma_c = \pm 0.3$ is indicated by the red dashed lines. Periods of DisMo are highlighted by gray shaded areas. (c) Probability distribution of Γ_N for systems containing from 2 to 8 cells. $\Gamma_c = 0.3$ is indicated by the red dashed line. (d) Persistence times τ obtained by exponential fits of the survival frequencies of CAMo calculated via ξ_N and Γ_N. Error bars indicate confidence bounds of 99 % within the fits.

S3. FULL DATA SET OF ANGULAR MEAN SQUARED DISPLACEMENT

In the main text we calculated the angular mean squared displacement (MSD) according to

$$MSD(t) = \langle [\langle \varphi(t) \rangle_N - \langle \varphi(0) \rangle_N]^2 \rangle_{\text{states}} \tag{S2}$$

(Eq. 2 of the main text) for each cell number separately. Here $t = 0$ indicates the starting point of an interval, $\langle\rangle_N$ indicates the mean over all N cells within a system, and $\langle\rangle_{\text{states}}$ indicates the mean over all observed intervals of CAMo or DisMo respectively. Due to restricted space, we only showed the MSD-plot for systems containing $N = 8$ cells. The MSD-plots for $N = 2...8$ are shown in Fig. S3.

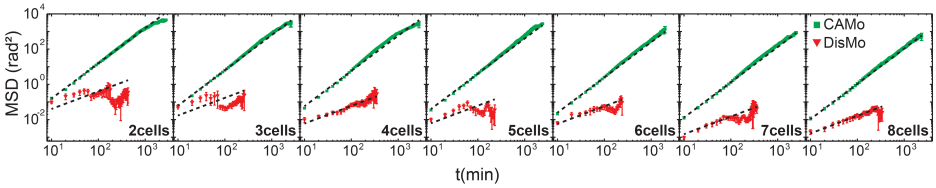

FIG. S3. Log-log plot of the angular MSD and its error calculated separately for each number of cells and periods of CAMo and DisMo according to Eq. 2. While periods of CAMo show a slope of 2 corresponding to ballistic motion in azimuthal direction, periods of DisMo exhibit a slope around 1 corresponding to the diffusive regime.

S4. FULL DATA SET OF DISMO/CAMO SURVIVAL FUNCTIONS

In the main text we analyzed the life time of states of CAMo and DisMo in terms of their survival function $S_N(t) = P_N(T > t)$, where T denotes the time a state persists. Due to restricted space, we only showed the survival functions for systems containing $N = 2, 5, 8$ cells. The survival functions for all analyzed cell numbers are shown in Fig. S4.

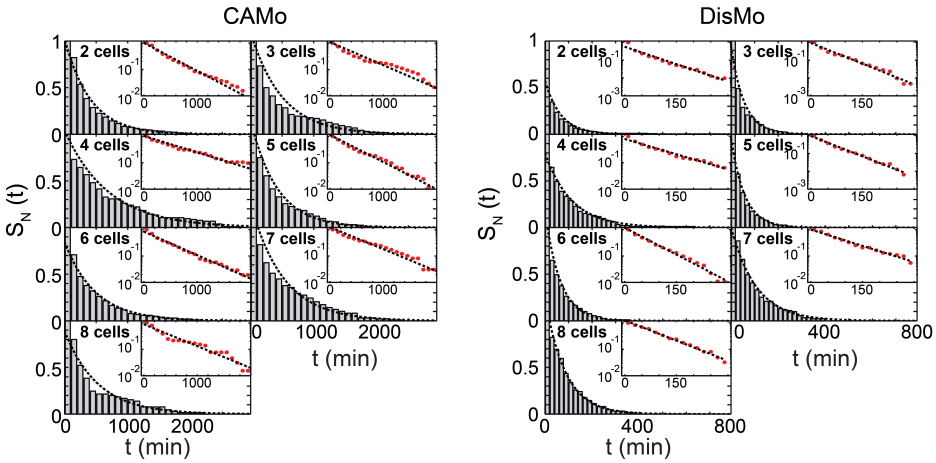

FIG. S4. Survival function $S_N(t) = P_N(T > t)$ of CAMo and DisMo states. Insets show corresponding log-lin plots. Exponential fits are indicated by dashed lines. For all numbers of cells, we find the persistence time to be distributed exponentially.

S5. ALTERNATIVE MEASURE FOR PERSISTENCE

In the main text we measured the life time of CAMo-periods to compare the persistence of the state among different cell numbers. Since all pattern sizes are analyzed at a constant number of cells N, in experiment, the time span between two cell divisions in general limits the period over which a system can be analyzed. Periods of CAMo exceeding this time of observation can therefore not be taken into account when calculating the mean persistence time τ. In order to check whether this limitation influences the found correlations between cell number and CAMo-persistence, we introduce an alternative method to measure the persistence of CAMo. For this reason we constrain the interval over which each system is analyzed to a time span $\tau_{\mathrm{obs}} = 1750$ min. This procedure excludes the effects of stochastic cell division events on the statistics of CAMo-persistence. In doing so, systems which were originally observed for less than τ_{obs} are removed from statistics (τ_{obs} is chosen such, that a good trade-off between long track lengths and a large number of analyzed systems is achieved). Furthermore, we introduce an order parameter for the persistence of CAMo as:

$$\bar{\tau}_N = \left\langle \frac{\tau_{\mathrm{tot}}}{N_{\mathrm{CAMo}} \cdot \tau_{\mathrm{obs}}} \right\rangle_{\mathrm{systems}} . \tag{S3}$$

Here, τ_{tot} denotes the total amount of time a specific system exhibits CAMo, N_{CAMo} stands for the total number of periods of CAMo system, and $\langle\rangle_{\mathrm{systems}}$ indicates the mean over all systems with same cell number N. Defined like this, $\bar{\tau}_N \to 0$ would correspond to a case in which the intervals exhibiting CAMo are very short (there is always at least one period of CAMo within τ_{obs}), whereas the case $\bar{\tau}_N = 1$ would correspond to the case where no period of DisMo occurs within τ_{obs}. We find that $\bar{\tau}_N$ exhibits the same characteristic features when plotted against the cell number as the mean persistence time τ. $\bar{\tau}_N$ shows the overall increase with increasing cell number as well as the discontinuity between systems containing 4 and such containing 5 cells as shown in Fig. S5. Since $\bar{\tau}_N$ is not influenced by the stochastic occurrence of cell division, these features seem to be a generic property of CAMo persistence within the system. Note that the qualitatively better match of experimental and numerical results from the artificially limited observation time in the model as also discussed in section S6.

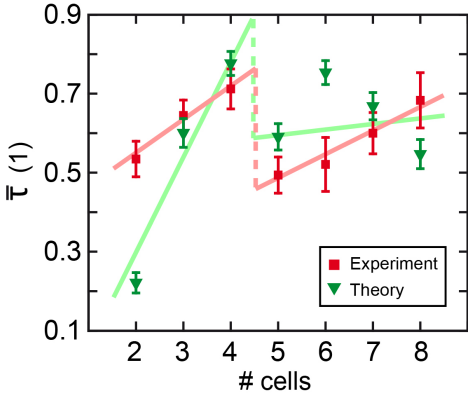

FIG. S5. Mean of the measure for persistence $\bar{\tau}$ (Eq. S3) and its error plotted as a function of cells within the system for experiment and theory. Lines are plotted to guide the eye and illustrate the discontinuity between 4 and 5 cell systems.

S6. ANALYSIS OF NUMERICAL DATA

As described in the main text, we set up computational model, based on the Cellular Potts Model, which is extended to incorporate local mechano-transduction and intracellular polarization. In analogy to experiment, we simulate cell migration of different numbers of cells within a circular confinement. Finally, we analyze the numerical cell tracks

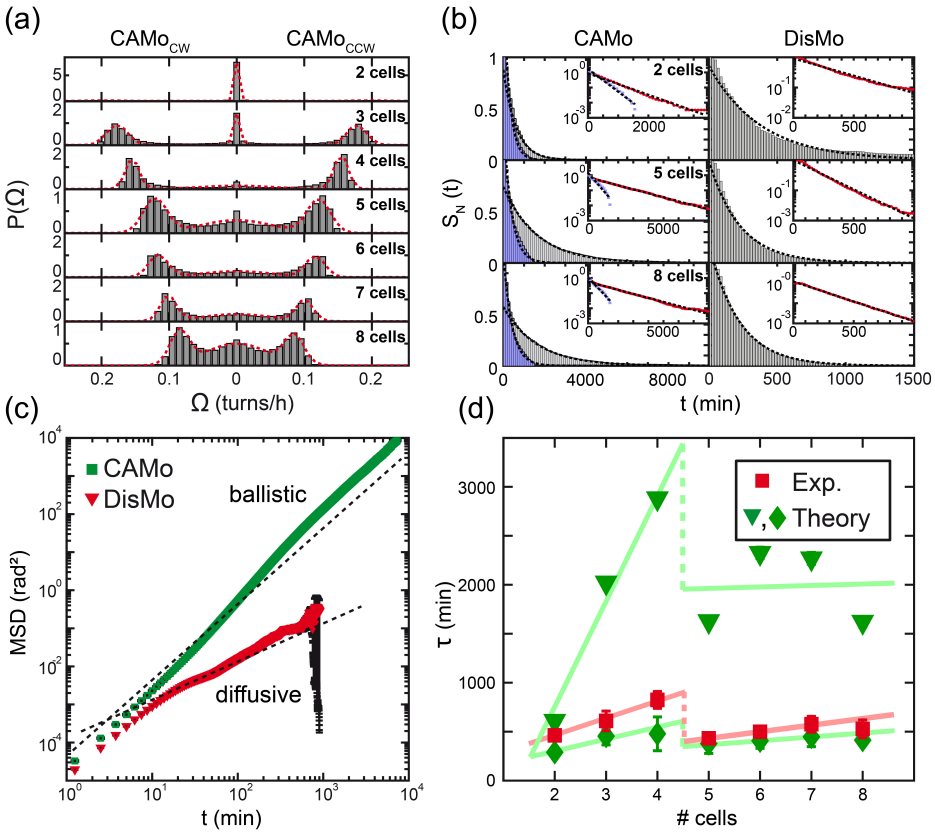

FIG. S6. Results from the Cellular Potts model. (a) Probability distribution of the smoothed total angular velocity Ω. (b) Survival function $S_N(t) = P_N(T > t)$ of CAMo and DisMo states exemplarily shown for systems containing 2,5, and 8 cells. Insets show corresponding log-lin plots. Exponential fits are indicated by dashed lines. Results for theoretical observation times constrained to the average observation times for each cell number according to Table S2 are indicated in blue. (c) Angular MSD calculated according to Eq. 2 for periods of CAMo and DisMo exemplarily shown for systems containing 8 cells. Dashed lines indicate ballistic (slope 2) and diffusive (slope 1) regime. (d) Persistence time τ as a function of cell number, derived from experiment and theory. Green diamonds indicate the persistence times of theoretical tracks constrained to the limited observation times of experiment. Error bars (comparable to symbol size) indicate confidence bounds of 99 % within the fits.

in the same way as the experimental data. In agreement with experiment, we find a trimodal distribution for the smoothed total angular velocity $\Omega_N(t)$ which consists of two CAMo states (clockwise/counterclockwise) and a state of DisMo at $\Omega_N = 0$ (Fig. S6(a)). Also for the theoretical data, the peak position corresponding to CAMo shifts to lower absolute angular velocities as the cell number increases. Applying the distinction algorithm into CAMo and DisMo periods described in the main text, we find the persistence time of both states to be exponentially distributed (Fig. S6(b)). In order to estimate the effect of the limited observation time in experiment, we artificially constrain theoretical observation times to the experimental ones given in Table S2. Analog to the long-time tracks, these constrained tracks exhibit exponential distribution of the persistence time but display faster decay rates. Also the

TABLE S2. Average time a system is observed in experiment

Cells per system	2 cells	3 cells	4 cells	5 cells	6 cells	7 cells	8 cells
Mean observation time [h]	29.4	30.9	30.3	27.8	26.1	32.4	28.0

angular MSD calculated according to Eq. 2 of the main text shows clearly ballistic behavior (in azimuthal direction) for CAMo as well as diffusive character for periods of DisMo (Fig. S6(c)).

S7. CALCULATION OF RELATIVE CELL POSITIONS

For Fig. 4(a) of the main text, we calculate relative cell positions with respect to a reference cell at the lower center of the patterns as follows. For all systems containing the same amount of cells, the heat plots are generated separately by the following procedure. For each frame, all cell positions are rotated by an angle α around $\mathbf{r}_{CM}$ such that the azimuth of the cell with the second largest radial coordinate becomes zero (the choice of the cell for the definition of α is arbitrary, using another cell as reference has no qualitative influence on the result). Afterwards, the cell positions of the successive frame are commonly rotated to the best match of these positions by applying an iterative closest point (ICP) algorithm. The best match now contributes to the location statistics and consequently to the final heat map. This procedure is conducted for every frame in each system using an in house algorithm implemented in MATLAB.

[1] J. Buhl, D. J. Sumpter, I. D. Couzin, J. J. Hale, E. Despland, E. R. Miller, and S. J. Simpson, Science **312**, 1402 (2006).

LITERATURE

[1] B. Alberts, A. Johnson, J. Lewis, M. Raff, K. Roberts, and P. Walter. *Molecular Biology of the Cell*. Garland Science, 2008.

[2] A. R. A. Anderson, M. A. J. Chaplain, and K. A. Rejniak. *Single-Cell-Based Models in Biology and Medicine*. Birkhäuser, 2007.

[3] E. Anon, X. Serra-Picamal, P. Hersen, N. C. Gauthier, M. P. Sheetz, X. Trepat, and B. Ladoux. Cell crawling mediates collective cell migration to close undamaged epithelial gaps. *Proc. Natl Acad. Sci. U.S.A.*, 109(27):10891, 2012.

[4] I. S. Aranson, A. Sokolov, J. O. Kessler, and R. E. Goldstein. Model for dynamical coherence in thin films of self-propelled microorganisms. *Phys. Rev. E*, 75(4):040901, 2007.

[5] I. S. Aranson and L. S. Tsimring. Pattern formation of microtubules and motors: Inelastic interaction of polar rods. *Phys. Rev. E*, 71(5):050901, 2005.

[6] I. S. Aranson and L. S. Tsimring. Theory of self-assembly of microtubules and motors. *Phys. Rev. E*, 74(3):031915, 2006.

[7] I. S. Aranson, D. Volfson, and L. S. Tsimring. Swirling motion in a system of vibrated elongated particles. *Phys. Rev. E*, 75(5):051301, 2007.

[8] P. B. Armstrong. Cell sorting out: The self-assembly of tissues in vitro. *Crit. Rev. Biochem. Mol. Biol.*, 24(2):119, 1989.

[9] M. D. Baker, P. M. Wolanin, and J. B. Stock. Signal transduction in bacterial chemotaxis. *BioEssays*, 28(1):9, 2005.

[10] M. Ballerini, N. Cabibbo, R. Candelier, A. Cavagna, E. Cisbani, I. Giardina, V. Lecomte, A. Orlandi, G. Parisi, A. Procaccini, M. Viale, and V. Zdravkovic. Interaction ruling animal collective behavior depends on topological rather than metric distance: Evidence from a field study. *Proc. Natl Acad. Sci. U.S.A.*, 105(4):1232, 2008.

[11] E. L. Barnhart, K.-C. Lee, K. Keren, A. Mogilner, and J. A. Theriot. An Adhesion-Dependent Switch between Mechanisms That Determine Motile Cell Shape. *PLoS Biol.*, 9(5):e1001059, 2011.

[12] M. Basan, J. Elgeti, E. Hannezo, W.-J. Rappel, and H. Levine. Alignment of cellular motility forces with tissue flow as a mechanism for efficient wound healing. *Proc. Natl Acad. Sci. U.S.A.*, 110(7):2452, 2013.

[13] M. Basan, J.-F. Joanny, J. Prost, and T. Risler. Undulation instability of epithelial tissues. *Phys. Rev. Lett.*, 106(15):158101, 2011.

[14] M. Basan, J. Prost, J.-F. Joanny, and J. Elgeti. Dissipative particle dynamics simulations for biological tissues: rheology and competition. *Phys. Biol.*, 8(2):026014, 2011.

[15] M. Basan, T. Risler, J.-F. Joanny, X. Sastre-Garau, and J. Prost. Homeostatic competition drives tumor growth and metastasis nucleation. *HFSP J.*, 3(4):265, 2009.

[16] A. Baskaran and M. C. Marchetti. Enhanced Diffusion and Ordering of Self-Propelled Rods. *Phys. Rev. Lett.*, 101(26):268101, 2008.

[17] A. Baskaran and M. C. Marchetti. Hydrodynamics of self-propelled hard rods. *Phys. Rev. E*, 77(1):011920, 2008.

[18] S. Bazazi, J. Buhl, J. J. Hale, M. L. Anstey, G. A. Sword, S. J. Simpson, and I. D. Couzin. Collective Motion and Cannibalism in Locust Migratory Bands. *Curr. Biol.*, 18(10):735, 2008.

[19] E. Bertin, H. Chaté, F. Ginelli, S. Mishra, A. Peshkov, and S. Ramaswamy. Mesoscopic theory for fluctuating active nematics. *New J. Phys.*, 15(8):085032, 2013.

[20] E. Bertin, M. Droz, and G. Grégoire. Boltzmann and hydrodynamic description for self-propelled particles. *Phys. Rev. E*, 74(2):022101, 2006.

[21] E. Bertin, M. Droz, and G. Grégoire. Hydrodynamic equations for self-propelled particles: microscopic derivation and stability analysis. *J. Phys. A: Math. Theor.*, 42(44):445001, 2009.

[22] D. L. Blair, T. Neicu, and A. Kudrolli. Vortices in vibrated granular rods. *Phys. Rev. E*, 67(3):031303, 2003.

[23] L. Boltzmann. Weitere Studien über das Wärmegleichgewicht unter Gasmolekülen. *Sitzungsberichte der Akademie der Wissenschaften Wien*, 66:275, 1872.

[24] C. Brangwynne, S. Huang, K. Parker, and D. Ingber. Symmetry breaking in cultured mammalian cells. *In Vitro Cell Dev. Biol. Animal*, 36(9):563–565, 2000.

[25] J. Buhl, D. J. T. Sumpter, I. D. Couzin, J. J. Hale, E. Despland, E. R. Miller, and S. J. Simpson. From disorder to order in marching locusts. *Science*, 312(5778):1402, 2006.

[26] T. Butt, T. Mufti, A. Humayun, P. B. Rosenthal, S. Khan, S. Khan, and J. E. Molloy. Myosin Motors Drive Long Range Alignment of Actin Filaments. *J. Biol. Chem.*, 285(7):4964, 2010.

[27] I. Buttinoni, J. Bialké, F. Kümmel, H. Löwen, C. Bechinger, and T. Speck. Dynamical Clustering and Phase Separation in Suspensions of Self-Propelled Colloidal Particles. *Phys. Rev. Lett.*, 110(23):238301, 2013.

[28] J.-B. Caussin, A. Solon, A. Peshkov, H. Chaté, T. Dauxois, J. Tailleur, V. Vitelli, and D. Bartolo. Emergent Spatial Structures in Flocking Models: A Dynamical System Insight. *Phys. Rev. Lett.*, 112(14):148102, 2014.

[29] P. M. Chaikin and T. C. Lubensky. *Principles of condensed matter physics*. Cambridge University Press, 2006.

[30] H. Chaté, F. Ginelli, G. Grégoire, F. Peruani, and F. Raynaud. Modeling collective motion: variations on the Vicsek model. *Eur. Phys. J. B*, 64(3-4):451, 2008.

[31] H. Chaté, F. Ginelli, G. Grégoire, and F. Raynaud. Collective motion of self-propelled particles interacting without cohesion. *Phys. Rev. E*, 77(4):046113, 2008.

[32] H. Chaté, F. Ginelli, and R. Montagne. Simple Model for Active Nematics: Quasi-Long-Range Order and Giant Fluctuations. *Phys. Rev. Lett.*, 96(18):180602, 2006.

[33] Y.-L. Chou, R. Wolfe, and T. Ihle. Kinetic theory for systems of self-propelled particles with metric-free interactions. *Phys. Rev. E*, 86(2):021120, 2012.

[34] M. Cross and H. Greenside. *Pattern Formation and Dynamics in Non-Equilibrium Systems*. Cambridge University Press, 2009.

[35] A. Czirók, H. E. Stanley, and T. Vicsek. Spontaneously ordered motion of self-propelled particles. *J. Phys. A: Math. Gen.*, 30(5):1375, 1997.

[36] G. Danuser, J. Allard, and A. Mogilner. Mathematical Modeling of Eukaryotic Cell Migration: Insights Beyond Experiments. *Annu. Rev. Cell Dev. Biol.*, 29:501, 2013.

[37] J. Deseigne, O. Dauchot, and H. Chaté. Collective Motion of Vibrated Polar Disks. *Phys. Rev. Lett.*, 105(9):98001, 2010.

[38] J. Deseigne, S. Léonard, O. Dauchot, and H. Chaté. Vibrated polar disks: spontaneous motion, binary collisions, and collective dynamics. *Soft Matter*, 8(20):5629, 2012.

[39] C. Dombrowski, L. Cisneros, S. Chatkaew, R. E. Goldstein, and J. O. Kessler. Self-Concentration and Large-Scale Coherence in Bacterial Dynamics. *Phys. Rev. Lett.*, 93(9):098103, 2004.

[40] K. Doxzen, S. R. K. Vedula, M. C. Leong, H. Hirata, N. S. Gov, A. J. Kabla, B. Ladoux, and C. T. Lim. Guidance of collective cell migration by substrate geometry. *Integr. Biol.*, 5(8):1026, 2013.

[41] A. D. Doyle, F. W. Wang, K. Matsumoto, and K. M. Yamada. One-dimensional topography underlies three-dimensional fibrillar cell migration. *J. Cell Biol.*, 184(4):481, 2009.

[42] M. Enculescu and H. Stark. Active Colloidal Suspensions Exhibit Polar Order under Gravity. *Phys. Rev. Lett.*, 107(5):058301, 2011.

[43] R. Farooqui and G. Fenteany. Multiple rows of cells behind an epithelial wound edge extend cryptic lamellipodia to collectively drive cell-sheet movement. *J. Cell Sci.*, 118(1):51, 2005.

[44] F. D. C. Farrell, M. C. Marchetti, D. Marenduzzo, and J. Tailleur. Pattern Formation in Self-Propelled Particles with Density-Dependent Motility. *Phys. Rev. Lett.*, 108(24):248101, 2012.

[45] R. A. Foty and M. S. Steinberg. Cadherin-mediated cell-cell adhesion and tissue segregation in relation to malignancy. *Int. J. Dev. Biol.*, 48(5-6):397, 2004.

[46] P. Friedl. Prespecification and plasticity: shifting mechanisms of cell migration. *Curr. Opin. Cell Biol.*, 16(1):14, 2004.

[47] P. Friedl and D. Gilmour. Collective cell migration in morphogenesis, regeneration and cancer. *Nat. Rev. Mol. Cell Biol.*, 10(7):445, 2009.

[48] P. Friedl and K. Wolf. Tumour-cell invasion and migration: diversity and escape mechanisms. *Nat. Rev. Cancer*, 3(5):362, 2003.

[49] P. Friedl, K. S. Zänker, and E.-B. Bröcker. Cell Migration Strategies in 3-D Extracellular Matrix: Differences In Morphology, Cell Matrix Interactions, and Integrin Function. *Microsc. Res. Tech.*, 43(5):369, 1998.

[50] B. M. Friedrich and F. Jülicher. Chemotaxis of sperm cells. *Proc. Natl Acad. Sci. U.S.A.*, 104(33):13256, 2007.

[51] D. R. Garrod and M. S. Steinberg. Tissue-specific Sorting-out in Two Dimensions in Relation to Contact Inhibition of Cell Movement. *Nature*, 244(5418):568, 1973.

[52] J. Gautrais, P. Michelena, A. Sibbald, R. Bon, and J.-L. Deneubourg. Allelomimetic synchronization in merino sheep. *Anim. Behav.*, 74(5):1443, 2007.

[53] F. Ginelli and H. Chaté. Relevance of Metric-Free Interactions in Flocking Phenomena. *Phys. Rev. Lett.*, 105(16):168103, 2010.

[54] F. Ginelli, F. Peruani, M. Bär, and H. Chaté. Large-Scale Collective Properties of Self-Propelled Rods. *Phys. Rev. Lett.*, 104(18):184502, 2010.

[55] J. A. Glazier and F. Graner. Simulation of the differential adhesion driven rearrangement of biological cells. *Phys. Rev. E*, 47(3):2128, 1993.

[56] F. Graner and J. A. Glazier. Simulation of Biological Cell Sorting Using a Two-Dimensional Extended Potts Model. *Phys. Rev. Lett.*, 69(13):2013, 1992.

[57] G. Grégoire and H. Chaté. Onset of Collective and Cohesive Motion. *Phys. Rev. Lett.*, 92(2):025702, 2004.

[58] G. Grégoire, H. Chaté, and Y. Tu. Active and passive particles: Modeling beads in a bacterial bath. *Phys. Rev. E*, 64(1):011902, 2001.

[59] G. Grégoire, H. Chaté, and Y. Tu. Comment on "Particle Diffusion in a Quasi-Two-Dimensional Bacterial Bath". *Phys. Rev. Lett.*, 86(3):556, 2001.

[60] T. Hanke, C. A. Weber, and E. Frey. Understanding collective dynamics of soft active colloids by binary scattering. *Phys. Rev. E*, 88(5):052309, 2013.

[61] C. W. Harvey, M. Alber, L. S. Tsimring, and I. S. Aranson. Continuum modeling of myxobacteria clustering. *New J. Phys.*, 15(3):035029, 2013.

[62] K. Huang. *Statistical Mechanics*. Wiley, 1987.

[63] S. Huang, C. P. Brangwynne, K. K. Parker, and D. E. Ingber. Symmetry-Breaking in Mammalian Cell Cohort Migration During Tissue Pattern Formation: Role of Random-Walk Persistence. *Cell Motil. Cytoskelton*, 61(4):201, 2005.

[64] T. Ihle. Kinetic theory of flocking: Derivation of hydrodynamic equations. *Phys. Rev. E*, 83(3):030901, 2011.

[65] T. Ihle. Invasion-wave-induced first-order phase transition in systems of active particles. *Phys. Rev. E*, 88(4):040303, 2013.

[66] O. Ilina and P. Friedl. Mechanisms of collective cell migration at a glance. *J. Cell Sci.*, 122(18):3203, 2009.

[67] X. Jiang, D. A. Bruzewicz, A. P. Wong, M. Piel, and G. M. Whitesides. Directing cell migration with asymmetric micropatterns. *Proc. Natl Acad. Sci. U.S.A.*, 102(4):975, 2005.

[68] A. J. Kabla. Collective cell migration: leadership, invasion and segregation. *J. R. Soc. Interface*, 9(77):3268, 2012.

[69] J. Käfer, P. Hogeweg, and A. F. M. Marée. Moving Forward Moving Backward: Directional Sorting of Chemotactic Cells due to Size and Adhesion Differences. *PLoS Comput. Biol.*, 2(6):e56, 2006.

[70] E. Karsenti. Self-organization in cell biology: a brief history. *Nat. Rev. Mol. Cell Biol.*, 9(3):255, 2008.

[71] K. Keren, Z. Pincus, G. M. Allen, E. L. Barnhart, G. Marriott, A. Mogilner, and J. A. Theriot. Mechanism of shape determination in motile cells. *Nature*, 453(7194):475, 2008.

[72] M. M. Kozlov and A. Mogilner. Model of Polarization and Bistability of Cell Fragments. *Biophys. J.*, 93(11):3811, 2007.

[73] A. Kudrolli. Concentration Dependent Diffusion of Self-Propelled Rods. *Phys. Rev. Lett.*, 104(8):o88001, 2010.

[74] A. Kudrolli, G. Lumay, D. Volfson, and L. S. Tsimring. Swarming and Swirling in Self-Propelled Polar Granular Rods. *Phys. Rev. Lett.*, 100(5):058001, 2008.

[75] E. Lauga and T. R. Powers. The hydrodynamics of swimming microorganisms. *Rep. Prog. Phys.*, 72(9):096601, 2009.

[76] F. Lautenschläger, S. Paschke, S. Schinkinger, A. Bruel, M. Beil, and J. Guck. The regulatory role of cell mechanics for migration of differentiating myeloid cells. *Proc. Natl Acad. Sci. U.S.A.*, 106(37):15696, 2009.

[77] P. Lee and C. Wolgemuth. Advent of complex flows in epithelial tissues. *Phys. Rev. E*, 83(6):061920, 2011.

[78] P. Lee and C. W. Wolgemuth. Crawling Cells Can Close Wounds without Purse Strings or Signaling. *PLoS Comput. Biol.*, 7(3):e1002007, 2011.

[79] F. Y. Leong. Physical Explanation of Coupled Cell-Cell Rotational Behavior and Interfacial Morphology: A Particle Dynamics Model. *Biophys. J.*, 105(10):2301, 2013.

[80] M. C. Leong, S. R. K. Vedula, C. T. Lim, and B. Ladoux. Geometrical constraints and physical crowding direct collective migration of fibroblasts. *Commun. Integr. Biol.*, 6(2):e23197, 2013.

[81] U. Lopez, J. Gautrais, I. D. Couzin, and G. Theraulaz. From behavioural analyses to models of collective motion in fish schools. *Interface Focus*, 2(6):693, 2012.

[82] G. Mahmud, C. J. Campbell, K. J. M. Bishop, Y. A. Komarova, O. Chaga, S. Soh, S. Huda, K. Kandere-Grzybowska, and B. A. Grzybowski. Directing cell motions on micropatterned ratchets. *Nat. Phys.*, 5(8):606, 2009.

[83] M. C. Marchetti, J.-F. Joanny, S. Ramaswamy, T. B. Liverpool, J. Prost, M. Rao, and R. A. Simha. Hydrodynamics of soft active matter. *Rev. Mod. Phys.*, 85(3):1143, 2013.

[84] A. F. M. Marée, V. A. Grieneisen, and L. Edelstein-Keshet. How Cells Integrate Complex Stimuli: The Effect of Feedback from Phosphoinositides and Cell Shape on Cell Polarization and Motility. *PLoS Comput. Biol.*, 8(3):e1002402, 2012.

[85] A. F. M. Marée, A. Jilkine, A. Dawes, V. A. Grieneisen, and L. Edelstein-Keshet. Polarization and Movement of Keratocytes: A Multiscale Modelling Approach. *Bull. Math. Biol.*, 68(5):1169, 2006.

[86] S. Mark, R. Shlomovitz, N. S. Gov, M. Poujade, E. Grasland-Mongrain, and P. Silberzan. Physical Model of the Dynamic Instability in an Expanding Cell Culture. *Biophys. J.*, 98(3):361, 2010.

[87] E. Méhes and T. Vicsek. Collective motion of cells: from experiments to models. *arXiv:1403.1127*, 2014.

[88] R. M. H. Merks, S. V. Brodsky, M. S. Goligorksy, S. A. Newman, and J. A. Glazier. Cell elongation is key to in silico replication of in vitro vasculogenesis and subsequent remodeling. *Dev. Biol.*, 289(1):44, 2006.

[89] R. M. H. Merks and J. A. Glazier. A cell-centered approach to developmental biology. *Physica A*, 352(1):113, 2005.

[90] R. M. H. Merks and J. A. Glazier. Dynamic mechanisms of blood vessel growth. *Nonlinearity*, 19(1):C1, 2006.

[91] R. M. H. Merks and P. Koolwijk. Modeling Morphogenesis in silico and in vitro: Towards Quantitative, Predictive, Cell-based Modeling. *Math. Model. Nat. Phenom.*, 4(4):149, 2009.

[92] R. M. H. Merks, E. D. Perryn, A. Shirinifard, and J. A. Glazier. Contact-Inhibited Chemotaxis in De Novo and Sprouting Blood-Vessel Growth. *PLoS Comput. Biol.*, 4(9):e1000163, 2008.

[93] N. D. Mermin and H. Wagner. Absence of Ferromagnetism or Antiferromagnetism in One- or Two-Dimensional

Isotropic Heisenberg Models. *Phys. Rev. Lett.*, 17(22):1133, 1966.

[94] S. Mishra, A. Baskaran, and M. C. Marchetti. Fluctuations and pattern formation in self-propelled particles. *Phys. Rev. E*, 81(6):o61916, 2010.

[95] A. Mogilner. Mathematics of cell motility: have we got its number? *J. Math. Biol.*, 58(1-2):105, 2009.

[96] A. Mogilner and B. Rubinstein. Actin disassembly 'clock' and membrane tension determine cell shape and turning: a mathematical model. *J. Phys.: Condens. Matter*, 22(19):194118, 2010.

[97] M. Moussaïd, D. Helbing, and G. Theraulaz. How simple rules determine pedestrian behavior and crowd disasters. *Proc. Natl Acad. Sci. U.S.A.*, 108(17):6884, 2011.

[98] V. Narayan, N. Menon, and S. Ramaswamy. Nonequilibrium steady states in a vibrated-rod monolayer: tetratic, nematic and smectic correlations. *J. Stat. Mech.*, 2006:P01005, 2006.

[99] S. I. Nishimura, M. Ueda, and M. Sasai. Cortical Factor Feedback Model for Cellular Locomotion and Cytofission. *PLoS Comput. Biol.*, 5(3):e1000310, 2009.

[100] N. Ofer, A. Mogilner, and K. Keren. Actin disassembly clock determines shape and speed of lamellipodial fragments. *Proc. Natl Acad. Sci. U.S.A.*, 108(51):20394, 2011.

[101] G. Y. Ouaknin and P. Z. Bar-Yoseph. Stochastic Collective Movement of Cells and Fingering Morphology: No Maverick Cells. *Biophys. J.*, 97(7):1811, 2009.

[102] N. B. Ouchi, J. A. Glazier, J.-P. Rieu, A. Upadhyaya, and Y. Sawada. Improving the realism of the cellular Potts model in simulations of biological cells. *Physica A*, 329(3-4):451, 2003.

[103] M. M. Palm and R. M. H. Merks. Vascular networks due to dynamically arrested crystalline ordering of elongated cells. *Phys. Rev. E*, 87(1):012725, 2013.

[104] F. Peruani and M. Bär. A kinetic model and scaling properties of non-equilibrium clustering of self-propelled particles. *New J. Phys.*, 15(6):065009, 2013.

[105] F. Peruani, A. Deutsch, and M. Bär. Nonequilibrium clustering of self-propelled rods. *Phys. Rev. E*, 74(3):030904, 2006.

[106] F. Peruani, J. Starruß, V. Jakovljevic, L. Søgaard-Andersen, A. Deutsch, and M. Bär. Collective Motion and Nonequilibrium Cluster Formation in Colonies of Gliding Bacteria. *Phys. Rev. Lett.*, 108(9):098102, 2012.

[107] A. Peshkov, I. S. Aranson, E. Bertin, H. Chaté, and F. Ginelli. Nonlinear Field Equations for Aligning Self-Propelled Rods. *Phys. Rev. Lett.*, 109(26):268701, 2012.

[108] A. Peshkov, S. Ngo, E. Bertin, H. Chaté, and F. Ginelli. Continuous Theory of Active Matter Systems with Metric-Free Interactions. *Phys. Rev. Lett.*, 109(9):098101, 2012.

[109] L. Petitjean, M. Reffay, E. Grasland-Mongrain, M. Poujade, B. Ladoux, A. Buguin, and P. Silberzan. Velocity Fields in a Collectively Migrating Epithelium. *Biophys. J.*, 98(9):1790, 2010.

[110] R. B. Potts. Some Generalized Order-Disorder Transformations. *Math. Proc. Camb. Phil. Soc.*, 48(1):106, 1952.

[111] M. Poujade, E. Grasland-Mongrain, A. Hertzog, J. Jouanneau, P. Chavrier, B. Ladoux, A. Buguin, and P. Silberzan. Collective migration of an epithelial monolayer in response to a model wound. *Proc. Natl Acad. Sci. U.S.A.*, 104(41):15988, 2007.

[112] M. Prass, K. Jacobson, A. Mogilner, and M. Radmacher. Direct measurement of the lamellipodial protrusive force in a migrating cell. *J. Cell Biol.*, 174(6):767, Sept. 2006.

[113] S. Ramaswamy. The Mechanics and Statistics of Active Matter. *Annu. Rev. Condens. Matter Phys.*, 1:323, 2010.

[114] J. Ranft, M. Basan, J. Elgeti, J.-F. Joanny, J. Prost, and F. Jülicher. Fluidization of tissues by cell division and apoptosis. *Proc. Natl Acad. Sci. U.S.A.*, 107(49):20863, 2010.

[115] D. Raucher and M. P. Sheetz. Cell Spreading and Lamellipodial Extension Rate Is Regulated by Membrane Tension. *J. Cell Biol.*, 148(1):127, 2000.

[116] T. Reichenbach, M. Mobilia, and E. Frey. Mobility promotes and jeopardizes biodiversity in rock-paper-scissors games. *Nature*, 448(7157):1046, 2007.

[117] T. W. Remmerbach, F. Wottawah, J. Dietrich, B. Lincoln, C. Wittekind, and J. Guck. Oral Cancer Diagnosis by Mechanical Phenotyping. *Cancer Res.*, 69(5):1728, 2009.

[118] P. Rørth. Initiating and guiding migration: lessons from border cells. *Trends Cell Biol.*, 12(7):325, 2002.

[119] P. Rørth. Collective guidance of collective cell migration. *Trends Cell Biol.*, 17(12):575, 2007.

[120] B. Rubinstein, K. Jacobson, and A. Mogilner. Multiscale two-dimensional modeling of a motile simple-shaped cell. *Multiscale Model. Simul.*, 3(2):413, 2005.

[121] N. J. Savill and P. Hogeweg. Modelling Morphogenesis: From Single Cells to Crawling Slugs. *J. theor. Biol.*, 184(3):229, 1997.

[122] S. C. Schaffner and J. V. José. Biophysical model of self-organized spindle formation patterns without centrosomes and kinetochores. *Proc. Natl Acad. Sci. U.S.A.*, 103(30):11166, 2006.

[123] V. Schaller, C. Weber, E. Frey, and A. R. Bausch. Polar pattern formation: hydrodynamic coupling of driven filaments. *Soft Matter*, 7(7):3213, 2011.

[124] V. Schaller, C. Weber, C. Semmrich, E. Frey, and A. R. Bausch. Polar patterns of driven filaments. *Nature*, 467(7311):73, 2010.

[125] V. Schaller, C. A. Weber, B. Hammerich, E. Frey, and A. R. Bausch. Frozen steady states in active systems. *Proc. Natl Acad. Sci. U.S.A.*, 108(48):19183, 2011.

[126] F. Schwabl. *Statistische Mechanik*. Springer, 2004.

[127] N. Sepúlveda, L. Petitjean, O. Cochet, E. Grasland-Mongrain, P. Silberzan, and V. Hakim. Collective Cell Motion in an Epithelial Sheet Can Be Quantitatively Described by a Stochastic Interacting Particle Model. *PLoS Comput. Biol.*, 9(3):e1002944, 2013.

[128] X. Serra-Picamal, V. Conte, R. Vincent, E. Anon, D. T. Tambe, E. Bazellieres, J. P. Butler, J. J. Fredberg, and X. Trepat. Mechanical waves during tissue expansion. *Nat. Phys.*, 8(8):628, 2012.

[129] D. Shao, H. Levine, and W.-J. Rappel. Coupling actin flow, adhesion, and morphology in a computational cell motility model. *Proc. Natl Acad. Sci. U.S.A.*, 109(18):6851, 2012.

[130] D. Shao, W.-J. Rappel, and H. Levine. Computational Model for Cell Morphodynamics. *Phys. Rev. Lett.*, 105(10):108104, 2010.

[131] A. F. Siekmann and N. D. Lawson. Notch signalling limits angiogenic cell behaviour in developing zebrafish arteries. *Nature*, 445(7129):781, 2007.

[132] A. Sokolov, I. S. Aranson, J. O. Kessler, and R. E. Goldstein. Concentration Dependence of the Collective Dynamics of Swimming Bacteria. *Phys. Rev. Lett.*, 98(15):158102, 2007.

[133] A. P. Solon and J. Tailleur. Revisiting the Flocking Transition Using Active Spins. *Phys. Rev. Lett.*, 111(7):078101, 2013.

[134] M. S. Steinberg. Does Differential Adhesion Govern Self-assembly Processes in Histogenesis? Equilibrium Configurations and Emergence of a Hierarchy Among Populations of Embryonic Cells. *J. Exp. Zool.*, 173(4):395, 1970.

[135] Y. Sumino, K. H. Nagai, Y. Shitaka, D. Tanaka, K. Yoshikawa, H. Chaté, and K. Oiwa. Large-scale vortex lattice emerging from collectively moving microtubules. *Nature*, 483(7390):448, 2012.

[136] R. Suzuki, C. A. Weber, E. Frey, and A. R. Bausch. *unpublished*, 2014.

[137] A. Szabó and R. M. H. Merks. Cellular Potts modeling of tumor growth, tumor invasion, and tumor evolution. *Front. Oncol.*, 3:87, 2013.

[138] A. Szabó, R. Ünnep, E. Méhes, W. O. Twal, W. S. Argraves, Y. Cao, and A. Czirók. Collective cell motion in endothelial monolayers. *Phys. Biol.*, 7(4):046007, 2010.

[139] B. Szabó, G. J. Szöllösi, B. Gönci, Z. Jurányi, D. Selmeczi, and T. Vicsek. Phase transition in the collective migration of tissue cells: Experiment and model. *Phys. Rev. E*, 74(6):061908, 2006.

[140] J. Taktikos, H. Stark, and V. Zaburdaev. How the Motility Pattern of Bacteria Affects Their Dispersal and Chemotaxis. *PLOS ONE*, 8(12):e81936, 2013.

[141] J. Taktikos, V. Zaburdaev, and H. Stark. Modeling a self-propelled autochemotactic walker. *Phys. Rev. E*, 84(4):041924, 2011.

[142] J. Taktikos, V. Zaburdaev, and H. Stark. Collective dynamics of model microorganisms with chemotactic signaling. *Phys. Rev. E*, 85(5):051901, 2012.

[143] D. T. Tambe, C. C. Hardin, T. E. Angelini, K. Rajendran, C. Y. Park, X. Serra-Picamal, E. H. Zhou, M. H. Zaman, J. P.

Butler, D. A. Weitz, J. J. Fredberg, and X. Trepat. Collective cell guidance by cooperative intercellular forces. *Nat. Mater.*, 10(6):469, 2011.

[144] M. Théry. Micropatterning as a tool to decipher cell morphogenesis and functions. *J. Cell Sci.*, 123(24):4201, 2010.

[145] J. Toner and Y. Tu. Long-Range Order in a Two-Dimensional Dynamical XY Model: How Birds Fly Together. *Phys. Rev. Lett.*, 75(23):4326, 1995.

[146] J. Toner and Y. Tu. Flocks, herds, and schools: A quantitative theory of flocking. *Phys. Rev. E*, 58(4):4828, 1998.

[147] J. Toner, Y. Tu, and S. Ramaswamy. Hydrodynamics and phases of flocks. *Ann. Phys.*, 318(1):170, 2005.

[148] X. Trepat, M. R. Wasserman, T. E. Angelini, E. Millet, D. A. Weitz, J. P. Butler, and J. J. Fredberg. Physical forces during collective cell migration. *Nat. Phys.*, 5(6):426–430, 2009.

[149] Y. Tu, J. Toner, and M. Ulm. Sound Waves and the Absence of Galilean Invariance in Flocks. *Phys. Rev. Lett.*, 80(21):4819, 1998.

[150] S. R. K. Vedula, H. Hirata, M. H. Nai, A. Brugués, Y. Toyama, X. Trepat, C. T. Lim, and B. Ladoux. Epithelial bridges maintain tissue integrity during collective cell migration. *Nat. Mater.*, 13(1):87, 2014.

[151] S. R. K. Vedula, M. C. Leong, T. L. Lai, P. Hersen, A. J. Kabla, C. T. Lim, and B. Ladoux. Emerging modes of collective cell migration induced by geometrical constraints. *Proc. Natl Acad. Sci. U.S.A.*, 109(32):12974, 2012.

[152] T. Vicsek, A. Czirók, E. Ben-Jacob, I. Cohen, and O. Shochet. Novel Type of Phase Transition in a System of Self-Driven Particles. *Phys. Rev. Lett.*, 75(6):1226, 1995.

[153] T. Vicsek and A. Zafeiris. Collective motion. *Phys. Rep.*, 517(3-4):71, 2012.

[154] C. A. Weber, C. Bock, and E. Frey. Defect-Mediated Phase Transitions in Active Soft Matter. *Phys. Rev. Lett.*, 112(16):168301, 2014.

[155] C. A. Weber, T. Hanke, J. Deseigne, S. Léonard, O. Dauchot, E. Frey, and H. Chaté. Long-Range Ordering of Vibrated Polar Disks. *Phys. Rev. Lett.*, 110(20):208001, 2013.

[156] C. A. Weber, V. Schaller, A. R. Bausch, and E. Frey. Nucleation-induced transition to collective motion in active systems. *Phys. Rev. E*, 86(3):030901, 2012.

[157] H. H. Wensink, J. Dunkel, S. Heidenreich, K. Drescher, R. E. Goldstein, H. Löwen, and J. M. Yeomans. Meso-scale turbulence in living fluids. *Proc. Natl Acad. Sci. U.S.A.*, 109(36):14308, 2012.

[158] H. H. Wensink and H. Löwen. Emergent states in dense systems of active rods: from swarming to turbulence. *J. Phys.: Condens. Matter*, 24(46):464130, 2012.

[159] H. Wioland, F. G. Woodhouse, J. Dunkel, J. O. Kessler, and R. E. Goldstein. Confinement Stabilizes a Bacterial Suspension into a Spiral Vortex. *Phys. Rev. Lett.*, 110(26):268102, 2013.

[160] F. Y. Wu. The Potts model. *Rev. Mod. Phys.*, 54(1):235, 1982.

[161] X.-L. Wu and A. Libchaber. Particle Diffusion in a Quasi-Two-Dimensional Bacterial Bath. *Phys. Rev. Lett.*, 84(13):3017, 2000.

[162] X.-L. Wu and A. Libchaber. Wu and Libchaber Reply. *Phys. Rev. Lett.*, 86(3):557, 2001.

[163] Y. Wu, Y. Jiang, D. Kaiser, and M. Alber. Social Interactions in Myxobacterial Swarming. *PLoS Comput. Biol.*, 3(12):e253, 2007.

[164] D. Yamada, T. Hondou, and M. Sano. Coherent dynamics of an asymmetric particle in a vertically vibrating bed. *Phys. Rev. E*, 67(4):040301, 2003.

[165] Y. Yang, V. Marceau, and G. Gompper. Swarm behavior of self-propelled rods and swimming flagella. *Phys. Rev. E*, 82(3):031904, 2010.

[166] H. P. Zhang, A. Be'er, E.-L. Florin, and H. L. Swinney. Collective motion and density fluctuations in bacterial colonies. *Proc. Natl Acad. Sci. U.S.A.*, 107(31):13626, 2010.

[167] F. Ziebert and I. S. Aranson. Effects of Adhesion Dynamics and Substrate Compliance on the Shape and Motility of Crawling Cells. *PLOS ONE*, 8(5):e64511, 2013.

[168] F. Ziebert, I. S. Aranson, and L. S. Tsimring. Effects of cross-links on motor-mediated filament organization. *New J. Phys.*, 9(11):421, 2007.

[169] F. Ziebert, S. Swaminathan, and I. S. Aranson. Model for self-polarization and motility of keratocyte fragments. *J. R. Soc. Interface*, 9(70):1084, 2012.

[170] A. Zöttl and H. Stark. Nonlinear Dynamics of a Microswimmer in Poiseuille Flow. *Phys. Rev. Lett.*, 108(21):218104, 2012.

[171] A. Zöttl and H. Stark. Hydrodynamics Determines Collective Motion and Phase Behavior of Active Colloids in Quasi-Two-Dimensional Confinement. *Phys. Rev. Lett.*, 112(11):118101, 2014.

Ich versichere, die Arbeit selbstständig angefertigt
und dazu nur die im Literaturverzeichnis
angegebenen Quellen benutzt zu haben.

München, den 20. Mai 2014